# Fluid-particle interactions: from the simple pendulum to collective effects in turbulence

Martin Obligado

## To cite this version:

Martin Obligado. Fluid-particle interactions: from the simple pendulum to collective effects in turbulence. Fluids mechanics [physics.class-ph]. Université de Grenoble, 2013. English. NNT : . tel-01454681v1

**HAL Id: tel-01454681**

**https://hal.science/tel-01454681v1**

Submitted on 7 Feb 2017 (v1), last revised 15 Jan 2018 (v2)

UNIVERSITÉ DE GRENOBLE

# THÈSE

Pour obtenir le grade de

## DOCTEUR DE L'UNIVERSITÉ DE GRENOBLE

Spécialité : **Mécanique des fluides, Energétique, Procédés**

Arrêté ministériel : 23 avril 2009

Présentée par

**Martín Obligado**

Thèse dirigée par **Mickaël Bourgoin**

préparée au sein du **Laboratoire des Écoulements Géophysiques et Industriels**
et de l'école doctorale **I-MEP2**

# Fluid-particle interactions:

## from the simple pendulum to collective effects in turbulence

Thèse soutenue publiquement le **30 septembre 2013**,
devant le jury composé de :

**M. Jan Dušek**
Professeur des Universités, Université de Strasbourg, Président
**M. Markus Uhlmann**
HDR, Karlsruhe Institute of Technology, Rapporteur
**M. Romain Volk**
HDR, ENS Lyon, Rapporteur
**M. Haitao Xu**
Profeseur Étranger, Max Planck Institute for Dynamics and Self-Organization, Examinateur
**M. Alberto Aliseda**
Profeseur Étranger, University of Washington, Examinateur
**M. Mickaël Bourgoin**
HDR, CNRS, Directeur de thèse
**M. Cristophe Baudet**
Professeur des Universités, Université Joseph Fourier, Co-Directeur de thèse

*This dissertation is dedicated to my grandfather Alberto.*

# Acknowledgements

This thesis would not have been possible without the help, support and friendship of many people. First, I would like to mention the reviewers of this thesis, Markus Uhlmann and Romain Volk, for revising this work carefully. I would also like to thank the rest of the jury that honoured me accepting and considering my work; Jan Dŭsek, Haitao Xu and Alberto Aliseda. I appreciate as well the constant support of the co-director of this thesis, Christophe Baudet, during these years.

During my stay in LEGI I have known many wonderful friends: Diego, Manolo, Nicolas, Sylvain, Corinne, Martin, Antoine among many others. Also the "filial vasca": Ibai, Igor, Jon, Mickel and Iván. In particular, I would like to mention Ibai for helping me with hot-wire measurements and Iván for sharing his knowledge in Fluent simulations.

Mickaël Bourgoin, one of the best experimental physicist I have ever met, taught me that the work in the laboratory can be a funny game. Without his scientific creativity and generosity in sharing his ideas, any of the results of this thesis would have been possible. His constant help and support has been essential during all the steps of this thesis and made my stay in Grenoble a very pleasant time.

I would like to thank Nicolas Mordant, who came recently to LEGI and worked with me for the experiments discussed in chapters 7 and 8. Without his great experimental skills (and greater patience) none of those experiments would have been possible. Romain Volk, for let me use his "french washing machine" and sharing his enthusiasm for physics.

During this thesis I had the pleasure of visiting two others laboratories for very fruitful collaborations. In Karsruhe, Markus Uhlmann and his team gave me a wonderful reception and the possibility to participate of many interesting discussions. The experiments performed in chapter 4 have been performed during this visit. Then, during my stay in Buenos Aires, Pablo Mininni and all the turbulence group in the University of Buenos Aires helped me to spend a great time. Pablo kindly taught me to use his DNS code, which has been fundamental for obtaining the results reported in this work.

I would like to mention Alain Cartellier and Yves Gagne for being part of many fruitful discussions. Finally, I would also like to thank all the technicians in LEGI for his support in all the experiments, specially Stephan, Joseph, Tristan and Laure.

También agradezco a mis viejos y a mi hermana Lucía. A Francisco por su apoyo fortinero y a edu por permitirlo. A mis amigos que quedaron en Buenos Aires pero siempre me apoyaron. Un agradecimiento muy especial para Clara, Roco, Julieta y Camila por siempre recibirme en Madrid y hacerme sentir en casa. A Silvia por su apoyo para venir a Grenoble. A Alejandra, Ricardo, los chicos y mecha por su presencia constante; a Daniela y Florencia por su compañía y finalmente a mi abuelo tata que no llegó a leer estas palabras.

Y por último la persona más importante, Natalia, por acompañarme siempre, por estos cuatro años. Por su amor y por darle sentido y substancia a cada minuto de mi vida.

*Martín*

# Résumé en français

Cette thèse est organisée en deux parties. Après une brève discussion présentant la soufflerie du LEGI et des techniques expérimentales utilisées (chapitre 2), une première partie étudie les effets individuels des particules dans les écoulements tantôt laminaires et turbulents. Les propriétés d'un pendule immergé dans une écoulement moyen sont analysées dans le chapitre 3. Les chapitres 4, 5 et 6 abordent ensuite la question de la dynamique d'objets tractés. Le Chapitre 4 concerne les instabilités de sillage d'une sphère tractée dans un réservoir d'eau tandis que les autres chapitres portent sur la dynamique d'objets tractés dans la soufflerie sous un écoulement laminaire (chapitre 5) et turbulent (chapitre 6), pour lesquels les instabilités aéroélastiques jouent un rôle prépondérant.

Dans une seconde partie je me suis intéressé aux effets collectifs d'une population dense d'inclusions en interaction avec un champ turbulent. Trois chapitres traitent la question de la concentration préférentielle: des bulles d'air dans un canal à eau (chapitre 7), des particules solides dans un écoulement en eau de von Kármán (chapitre 8) et des gouttelettes d'eau en turbulence de grille active dans la soufflerie (chapitre 9). Le premier chapitre de cette partie (chapitre 7) propose une introduction générale de la problématique de la concentration préférentielle de particules en turbulence, alors que le dernier chapitre (chapitre 9), présente quelques conclusions générales.

# Chapitre 1: Introduction

Ce chapitre offre une introduction sur les différents modes d'interaction entre une particule et un fluide, en commençant par une description de la force de traînée, et de la difficulté à modéliser les coefficients aérodynamiques, notamment en conditions turbulentes.

La dynamique des particules dans un écoulement est ensuite étudiée. L'équation de Maxey-Riley-Gatignol [61, 36], qui reste à ce jour le modèle le plus abouti dont nous disposons (malgré un certain nombre d'approximations nécessaires pour sa validité), est détaillée. Les simulations numériques et les modèles théoriques utilisent en général une version minimale de cette équation, dans laquelle le force de traînée est le terme principal. Ces modèles minimalistes (dit Stokésiens) sont néanmoins incapables de prédire certaines observations expérimentales, notamment pour des particules de tailles finies, dont le diamètre est supérieur aux échelles de dissipation visqueuse de l'écoulement. Ceci a motivé l'intérêt porté au cours de cette thèse envers un système semi-contraint, où une importante vitesse relative est imposée entre l'écoulement et la particule, de sorte à garantir un rôle important de la force de traînée agissant sur la particule. Ces questions sont abordés dans les chapitres 4, 5 et 6. Nous espérons ainsi pouvoir reproduire, du moins partiellement, certaines prédictions des modèles Stokésiens.

En fin de chapitre, une bref description des effets collectifs est présentée. Ceux-ci sont attendus lorsque la concentration volumique en particule augmente, tout en restant dans des conditions suffisamment diluées afin d'éviter les effets de rétroaction des particules sur l'écoulement, qui vont au-delà du cadre de cette thèse. Nous nous intéressons tout particulièrement à la remarquable tendance des particules inertielles dans un écoulement turbulent à se regrouper en amas (phénomène connu sous le nom de concentration préférentielle). Les mécanismes physiques potentiellement responsables de ce phénomène (notamment la turbophorèse et les mécanismes de type "stick-sweep") sont discutés :

- *Réponse aux structures d'écoulement:* ce mécanisme est aussi référé comme turbophorèse. En raison de leur inertie, les particules plus denses que le fluide ont tendance à être éjectées des structures tourbillonnaires alors qu'elles sont facilement piégées dans les régions convergentes de l'écoulement. Le comportement inverse est prévu pour des particules moins denses que le fluide porteur (des bulles dans l'eau par exemple). Si ces comportements sont facilement observables et bien compris pour des écoulements réguliers simples, le cas des écoulements turbulents (même homogènes et isotropes) est bien plus complexe, du fait du caractère multi-échelle (en temps et en espace) des structures tourbillonnaires. Certaines études expérimentales et numériques sur la question sugèrent que l'effet de centrifugation, généralement invoqué pour expliquer la turbophorèse, n'est peut-être pas pertinent lorsque le nombre de Stokes des particules (défini comme le rapport entre le temps de relaxation visqueuse des particules $\tau_p$ et l'échelle de temps caractéristique de la turbulence) est de l'ordre de l'unité ou supèrieur.

- *Mécanisme "sweep-stick":* ou mécanisme de balayage-adhérence. Vassilicos et collaborateurs ont mis au point au cours des cinq dernièrres annés, une nouvelle vision de la formation des clusters de particules en turbulence homogène et isotrope. Dans leur premier travail en turbulence $2D$ [38], ils montrent l'existence d'une forte corrélation, sur une large gamme d'échelles, entre les distributions de particules inertielles lourdes et les points d'accélération nulle du champ turbulent porteur. Depuis, ils ont étendu leurs conclusions à la turbulence $3D$ et développé une description rigoureuse et quantitative du mécanisme sous-jacent (dit "stick-sweep") [15, 39, 20].

Le mécanisme de base s'explique de la façon suivante : d'une part, les points d'accélération nulle sont balayés par le fluide et se déplacent (statistiquement) à la vitesse locale du fluide (c'est la phase "sweep" du mécanisme); d'autre part, les particules plus denses que le fluide tendent à coller aux poins d'accélération nulle (c'est la phase "stick" du mécanisme).

Les études expérimentales présentées dans les chapitres 7, 8 et 9 visent en particulier à explorer la pertinence de ces mécanismes.

# Chapitre 2: la Soufflerie

Dans ce chapitre nous présentons le principal dispositif expérimental utilisé au cours de cette thèse: la soufflerie à faible turbulence (SFT1) située à Grenoble, au laboratorie LEGI. Nous rappelons que lors de l'élaboration de cette thèse, la soufflerie SFT1 a été hors service pendant 12 mois, ce qui a motivé l'utilisation d'autres dispositifs expérimentaux (qui seront détailles dans les chapitres correspondants). Toutefois la soufflerie restant l'installation principale de ce travail, un chapitre lui est dédié, notamment en vue de présenter les propriétés de la turbulence engendrée par la nouvelle grille active dont la mise en opération effective a été réalisée au cours de cette thèse.

La technique du fil-chaud, qui reste probablement la méthode expérimentale la plus utilisée et la plus précise pour caractériser les paramètres de turbulence d'un écoulement, est expliquée, tout comme les principes physiques sous-jacents. Ensuite, nous nous attardons sur les propriétés générales de l'écoulement engendré dans la soufflerie en l'absence de grille d'abord puis en présence d'une grille produisant en aval une turbulence homogène et isotrope. Deux types de grille ont été utilisés:

- Une grille passive composée de 10 barreaux verticaux et 10 barreaux horizontaux. Le taux de fluctuations (défini comme le rapport $\sigma_u/U$, où $U$ est la vitesse moyenne de l'écoulement et $u$ ses fluctuations) est constante et de l'ordre de 3%. Le nombre de Reynolds (basé sur l'échelle de Taylor) maximal atteint avec cette grille est de l'ordre de $R_\lambda \sim 200$.

- Une grille active est ensuite présentée. Elle est composée de 16 axes de rotation (huit horizontaux et huit verticaux) sur lesquelles sont montés des volets carrées. Chaque axe est entraîné indépendamment par un moteur pas à pas dont la vitesse et la direction de rotation peut être modifiée de façon dynamique. Ce type de grille produit une turbulence dont le niveau de fluctuation est bien plus élevé (de l'ordre de 20%). Le nombre de Reynolds maximal est alors de l'ordre de $R_\lambda \sim 1000$, bien que nous nous soyons limités à 500 pour les premières études dont cette thèse a fait l'objet.

# Chapitre 3: Pendule dans un écoulement

Le pendule simple reste l'un des systèmes les plus fondamentaux étudiés en physique. Il est couramment utilisé comme modèle pour illustrer un large éventail de mécanismes dans un large éventail de domaines. Cependant, malgré sa popularité, de nombreux comportements subtiles de ce système restent à être explorés, notamment lorsque le pendule est fortement couplé à un fluide. Ceci est par exemple illustré par des études récentes [78, 11] mettant en évidence l'impact du lâcher de tourbillons dans le sillage d'un pendule simple ainsi que les effets de masse ajoutée. Nous montrons dans ce chapitre que l'équilibre d'un disque pendulaire faisant face à un écoulement présentant une vitesse moyenne présente un comportement bi-stable et hystérétique. Nous donnons une interprétation simple de ce comportement en termes d'une description par deux puits de potentiel, nécessitant uniquement de connaître la dépendance angulaire du coefficient de traînée normale d'une plaque statique inclinée. Nous étudions l'influence de la turbulence sur l'équilibre du pendule en général et sur la bi-stabilité observée en particulier. Nos résultats ont des conséquences fondamentales et pratiques potentiellement importantes:

(*i*) ils étendent l'attractivité du pendule comme modèle pour étude de questions génériques relatives aux processus stochastiques bi-stables.

(*ii*) ils mettent en évidence des mécanismes de dynamique des fluides importants, y compris l'augmentation turbulente du coefficient de traînée et des problèmes d'interaction fluide-structure.

Au-delà de la configuration actuelle (notamment avec la grille passive, où un bruit additif est introduit par une turbulence modérée), la polyvalence de notre système devrait permettre d'étudier à l'avenir l'influence de plusieurs paramètres tels que l'amplitude et la couleur de bruit (qui peut être simplement introduit par une force mécanique aléatoire contrôlant le pendule), mais aussi de la forme du puits de potentiel lui-même (qui peut être adaptée par l'ajout d'un ressort de torsion ou d'une force magnétique par exemple). La capacité du pendule bi-stable à subir une résonance stochastique est également un aspect intéréssant qui sera prochainement étudié.

Enfin, des simulations effectuées avec Ansys Fluent nous permettent de comprendre la structure de l'écoulement et de retrouver des résultats compatibles avec les mesures expérimentales. Un résultat intéressant concerne l'observation numérique de la formation de tourbillons dans la région de bistabilité qui sera vérifiée dans des mesures futures.

# Chapitre 4: Instabilités sur une sphère tractée à vitesse constante

La dynamique des objets tractés dans un environnement fluide est d'intérêt pour de nombreuses situations pratiques. Ce chapitre et les deux chapitres suivants concernent l'étude expérimentale de l'équilibre et de la stabilité de la trajectoire d'une sphère tractée à vitesse constante.

Dans le cadre de certaines applications, il est d'une importance cruciale de garantir la stabilité de la trajectoire de l'objet tracté (à l'extrémité du câble) ce qui est un problème fondamental de dynamique des fluides intéressant et complexe. La dynamique des particules tractées résulte en effet de plusieurs contributions:

(*i*) les forces aéro/hydro-dynamiques exercées par le fluide environnant directement sur l'objet lui-même (dont principalement la traînée et la portance, mais peut-être aussi des effets de masse ajoutée et des gradients de pression lorsque l'environnement est turbulent, etc).

(*ii*) la tension du câble de remorquage (qui est lui-même soumis à des forces aero/hydro-dynamiques).

(*iii*) la gravité.

En conséquence, l'objet tracté est couplée au fluide à la fois directement et aussi indirectement par l'intermédiaire du câble. L'étude du couplage entre le câble et le fluide est donc également d'une importance cruciale. Dans ce chapitre, nous allons étudier les instabilités de sillage qui peuvent apparaître du fait du couplage directe de la particule en mouvement avec le fluide environnant. Dans les deux chapitres suivants, nous allons nous concentrer sur l'influence du câble de remorquage dans le développement d'instabilités aéroélastiques pouvant apparaître lorsque la vitesse de traction est suffisamment élevée (le chapitre 5, aborde le cas d'un écoulement laminaire tandis que le chapitre 6 traîte le cas turbulent).

L'étude présentée dans ce chapitre suit la ligne directrice suivante : nous notons d'abord que les résultats présentés ici concernent un travail préliminaire, effectué lors d'une visite d'une semaine dans le Groupe de Turbulences de l'Institut d'Hydromécanique du Karlsruhe Institute of Technology, en collaboration avec Pr. Markus Uhlmann. Malgré la simplicité de l'expérience mise en place à cette occasion, les résultats obtenus au cours de cette courte visite, apportent un aperçu complémentaire intéressant concernant l'apparition d'instabilités de sillage par rapport au cas de sphères en chute libre qui a fait l'objet de nombreuses études par le passé. La situation d'une sphère tractée à une vitesse constante peut en effet être reliée au cas d'une sphère en chute libre à sa vitesse terminale. Ce problème a déjà été examiné par Newton [79], alors qu'il étudiait la traînée de sphères tombant dans un liquide. Avec les simulations numériques directes (DNS) à plus grand nombre de Reynolds et grâce aux techniques d'imagerie à haute vitesse, ce problème a reçu une attention renouvelée au cours des dernières 15 années, et une grande variété de mouvements a été dévoilée pour un système si simple en apparence. Une étude sur ce sujet peut être trouvée dans [29].

Dans ce chapitre, nous considérons une particule tracté à une vitesse constante $U$ (de l'ordre de 2.2 cm/s), significativement plus faible que les vitesses de sédimentation correspondantes pour ces mêmes objets. Le système est donc un cas intermédiaire entre la sphère fixe et la sphère en chute libre. Alors que dans le cas de la chute libre la vitesse de sédimentation est contrôlée par la densité de la particule $\rho_p$ et le nombre de Reynolds $Re_p$ (défini comme $Re_p = Ud_p/\nu$, avec $d_p$ le diamètre de la sphère et $\nu$ la viscosité cinématique), dans notre cas, cette vitesse est maintenue constante, et ces paramètres peuvent être variés indépendamment. Cette situation offre un nouveau scénario dans lequel ce deux paramètres peuvent être combinés de façon nouvelle, jamais explorées auparavant dans le contexte de l'étude de l'influence des instabilités de sillage sur la trajectoire de la sphère. Comme cela a été souligné dans [29], dans le cas d'une sphère en chute libre l'instabilité de sillage est en effet le seul mécanisme pouvant génerer des oscillations. Par conséquent, certaines instabilités analogues doivent apparaître dans le cas tracté (bien que l'influence de la tension du câble de traction sur le mouvement doive être également pris en compte).

Le but de ce chapitre est d'étudier un tel système tracté en essayant d'identifier les valeurs critiques de nombre de Reynolds $Re_{pc}$ et/où de densité $\Gamma_c$ (avec $\Gamma = \rho_p/\rho_0$ ou $\rho_0$ est la densité du fluide). Pour cela, nous étudions la stabilité de la trajectoire de différentes classes de particules, avec différents rapports de densité et de nombre de Reynolds. Nous mettons en évidence l'apparition d'une instabilité de sillage se traduisant par un mouvement périodique hélicoïdal de la sphère tractée au-delà d'un certain seuil en nombre de Reynolds.

# Chapitre 5: Équilibre et stabilité de longs câbles tractés. Partie I: instabilités en écoulement laminaire

Dans ce chapitre nous poursuivons l'étude de la stabilité de particules tractées, par l'étude de la trajectoire d'une sphère tractée à vitesse constante, à l'extrémité d'un long câble avec un rapport longueur sur diamètre inédit, supérieure à $10^4$. La configuration de tractage est artificiellement obtenue en considérant un câble en équilibre dans la soufflerie SFT1 (avec une extrémité fixe et l'autre bougeant librement avec la possibilité d'y attacher un particule). Nous considérons trois configurations différentes:

(*i*) le câble tracté par lui-même.

(*ii*) une sphère millimétrique, légère (en polystyrène expansé) attachée à l'extrémité du fil.

(*iii*) une sphère millimétrique en plomb attachée à l'extrémité du fil.

La trajectoire de l'extrémité du câble est enregistrée par imagerie haute-vitesse (ce qui nous permet de reconstruire la trajectoire Lagrangienne de la particule), en vue de caractériser la position moyenne ainsi que les fluctuations dynamiques de l'objet tracté. Nous montrons que la position moyenne d'équilibre est bien prédite par un modèle simple décrivant les forces aérodynamiques agissant sur le câble et sur la sphère tractée.

En ce qui concerne les questions de stabilité, nous constatons que la particule la plus lourde (en plomb) est toujours tractée dans des conditions stables (dans la gamme de vitesses accessibles) avec seulement de très faibles oscillations liées à un faible mouvement pendulaire. Au contraire, l'extrémité libre et la sphère légere deveniennent instables lorsque la vitesse de tractage dépasse un certain seuil. L'analyse spectrale montre une instabilité oscillante de type "flutter" pour la sphère légere, tandis que le câble seul développe une instabilité de type “divergence” avec des fluctuations aléatoires.

# Chapitre 6: Équilibre et stabilité de longs câbles tractés. Partie I: instabilités en écoulement turbulent

Dans ce chapitre, le même système expérimental que dans le chapitre précédent est utilisé. La principale différence consiste en la nature de l'écoulement qui est désormais rendu turbulent, par l'introduction d'une grille passive placé à l'entrée de la veine d'essai de la soufflerie. Nous comparons d'une part la dynamique de la sphère tractée en régime laminaire et turbulent et d'autre part, la dynamique turbulente de la sphère tractée et d'une sphère librement advectée (ayant fait l'objet d'études antérieures à cette thèse dans l'équipe).

Concernant la comparaison tractée versus advection libre, les études numériques et théoriques sur le transport turbulent de particules matérielles modélisent généralement le couplage entre la dynamique du fluide et celle de la particule par une simple force de traînée. Des expériences récentes ont montré que cette approche échoue à prédire des propriétés pourtant élémentaires de la dynamique de particules de taille finie. Ceci a donc motivé une série d'expériences cherchant à accentuer le rôle de la force de traînée agissant sur la particule afin de tester si certaines prédictions des modèles en question étaient alors mieux vérifiées. Ceci est réalisé en considérant la dynamique de la particule tractée du dernier chapitre dans un écoulement turbulent. Dans ce chapitre, nous nous concentrons sur l'influence de l'inertie de la particule sur ses statistiques Lagrangiennes de vitesse et d'accélération. Nos résultats sont compatibles avec un mécanisme de filtrage dû au temps de réponse visqueux fini de la particule dont le couplage avec le fluide environnant résulte essentiellement de la force de traînée.

Concernant la comparaison tractée laminaire versus turbulent, nous montrons que la turbulence tend à masquer les instabilités précédemment décrite (tant de sillage qu'aéroélastiques) et à engendrer des trajectoires de l'objet tracté dont les propriétés statistiques présentent une certaine universalité reflétant celle de la turbulence proteuse. La dynamique pour un écoulement laminaire est ainsi paradoxalement beaucoup plus riche, du fait des diverses instabilités possibles (dépendant des conditions initiales et des propriétés des particules tractées entre autre). Le cas turbulent, malgré son caractère fortement aléatoire, impose certaines propriétés universelles qui rendent la dynamique des particules finalement plus prédictible (d'un point de vue statistique) que dans le cas laminaire.

# Chapitre 7: Étude du champ de concentration d'une population de bulles d'air en turbulence de grille dans un canal a eau

Le chapitre 7 ouvre la partie de ce manuscrit dédié à l'étude des effets collectifs d'une population dense de particules en interaction avec un champ turbulent porteur. La présence de particules dans un écoulement turbulent est une situation fréquente dans la nature comme dans l'industrie: la dispersion des polluants dans l'atmosphère, la sédimentation des rivières, la formation de la pluie dans les nuages chauds, la dispersion de plancton dans l'océan, l'optimisation des réacteurs chimiques et de divers procédés industriels, y compris la combustion du liquide carburant ne sont que quelques exemples. Nous nous intéressons ici au cas de particules dont la densité diffère de celle du fluide et qui de ce fait ne se comporte *a priori* pas comme des traceurs de l'écoulement. L'apparition fréquente de cette classe d'écoulement chargé en inclusion mérite des études fondamentales approfondies car aucune modélisation pertinente ou pratique n'est encore disponible. Jusqu'à présent, les équations qui régissent la dynamique des particules inertielles ont été obtenues sous des hypothèses fortes valables dans des situations très limitées ([61, 36], voir chapitre 1) et la plupart des travaux numériques récents utilisent des modèles encore plus simples (modèles stokésiens).

Une caractéristique frappante des écoulements turbulents chargés de particules inertielles est la concentration préférentielle ("clustering") qui conduit à de très fortes hétérogénéités du champ de concentration en particules, à différentes échelles. Ce phénomène a désormais été observé dans de nombreuses configurations expérimentales et numériques de turbulence homogène et isotrope (voir [114, 31, 105, 68, 32]). Les particules qui interagissent avec un écoulement turbulent sont alors généralement caractérisées par leur nombre de Stokes (voir chapitre 1), qui est le rapport entre le temps de relaxation visqueuse des particules $\tau_p$ et une échelle de temps caractéristique de l'écoulement.

Ce nombre sans dimension est souvent utilisé en comme paramètre clé pour caractériser la dynamique des particules en turbulence, ainsi que pour quantifier l'importance de la concentration préférentielle. Les modèles Stokésiens prédisent en effet une concentration préférentielle pour des particules dont le nombre de Stokes est non nul, avec un effet maximal pour $St$ de l'ordre de l'unité [8, 20]. Ce comportement est confirmé, au moins qualitativement, dans des expériences avec des particules petites (i.e. $\phi = d_p/\eta < 1$) et lourdes (i.e. $\Gamma = \rho_p/\rho_f > 1$ [68]). Fiabane *et al.* [32] ont étudié le cas de particules de taille finie (à la fois des particules avec une flottabilité neutre et des particules plus lourdes que le fluide). Ils ont montré que les particules neutres n'engendre pas de concentration préférentielle, quelque soit leur nombre de Stokes, contrairement aux particules lourdes. Ce dernier travail suggère que le nombre de Stokes par lui-même ne peut pas être considéré comme suffisant pour caractériser le clustering. La validité de ce paramètre est donc un champ ouvert et actif d'investigation et il est important d'explorer des particules de différentes tailles et de différentes densités dans différents types des écoulements. Finalement, Aliseda et collaborateurs [2] ont montré que l'augmentation locale de la concentration pouvait être responsable de l'augmentation mesurée de la vitesse de sédimentation des particules dans des écoulements turbulents. Ceci constitue un autre exemple justifiant la nécéssité de mieux comprendre et mieux quantifier le phénomène de concentration préférentielle.

Au cours de ces dernières années, le groupe s'est spécialisé dans une technique particulière, qui consiste à analyser ce phénomène via une analyse en diagrammes de Voronoï. Cette technique a été récemment présentée sur une étude de concentration préférentielle de petites gouttelettes d'eau dans un écoulement d'air modérément turbulent [68] et s'est avérée particulièrement robuste et efficace pour diagnostiquer et quantifier la formation des amas. Les diagrammes de Voronoï représentent une décomposition particulière d'un espace métrique déterminée par les distances à un ensemble discret d'objets de l'espace, en général un ensemble discret de points. C'est une diagramme d'un espace à deux dimensions (il existe aussi une représentation tridimensionnelle) où chaque cellule du diagramme est lié à une particule détectée, avec tous les points d'une cellule plus proche de sa particule associée qu'à tout autre particule. Ainsi, l'aire de chacune des cellules de Voronoï est l'inverse de la concentration locale de particules. Ces aires sont donc une mesure des champs de concentration locaux à une échelle de longueur interparticulaire. Pour comparer les résultats des expériences faites avec différentes quantités de particules détectées par image, la cellule de Voronoï est normalisé en utilisant l'aire moyenne des cellules de Voronoï $\bar{A}$ définie comme l'inverse de la concentration moyenne en particule, indépendamment de l'organisation spatiale des particules. Par conséquent, nous nous concentrons dans le reste de cette thèse sur l'analyse statistique des aires de Voronoï normalisées $\mathcal{V} = A/\bar{A}$. Les propriétés des clusters sont quantifiées en comparant la fonction de densité de probabilité (PDF) des aires des celulles de Voronoï obtenues à partir des expériences à celle d'un procèssus de Poisson aléatoire (RPA) dont la forme est bien approchée par une distribution Gamma [30].

Trois systèmes ont été étudiés:

- *Bulles d'air dans un canal à eau* (chapitre 7) : particules moins denses que le fluide, avec une taille de l'ordre de l'échelle de Kolmogorov. Le nombre de Reynolds de l'écoulement porteur est de l'ordre de $Re_\lambda = 100$.
- *des particules solides dans une "french washing machine" en eau (écoulement de von Kármán)* (chapitre 8) : Les particules (en PMMA) sont légèrement plus denses que l'eau (rapport de densité de 1.4) et leur diamètre est supérieur à l'échelle de Kolmogorov ($d_p > \eta$). Le clustering dans un écoulement turbulent inhomogène est ainsi explorée. Le nombre de Reynolds ($Re_\lambda$) de l'écoulement varie entre 300 et 800.
- *Goutelettes d'eau en soufflerie* (chapitre 9) : les particules sont ici beaucoup plus denses que le fluide porteur (rapport de densité de l'ordre de 800) et leur diamètre inférieur à l'échelle de Kolmogorov ($d_p < \eta$). Le nombre de Reynolds de l'écoulement turbulent, produit en aval d'une grille active, varie dans la gamme $234 < Re_\lambda < 400$.

Dans le chapitre 7, nous proposons une analyse simultanée de la concentration préférentielle de bulles dans une turbulence de grille en canal à eau, et des propriétés de l'écoulement (obtenu par vélocimétrie par images de particules (PIV)). Notre étude abouti à l'absence de concentration préférentielle (cohérent avec le faible nombre de Stokes des bulles que nous avons pu produire dans le canal). L'étude simultanée du champ de vitesse montre par ailleurs que dans les conditions expérimentales considérées la présence des bulles n'affecte pas les propriétés locales ou globales de la turbulence.

# Chapitre 8: Concentration préférentielle de particules solides dans un écoulement turbulent de von Kármán

Dans ce chapitre, nous étudions (par la méthode de tesselation de Voronoï) la concentration préférentielle de particules solides dans un écoulement de von Kármán en eau. Une étude simultanée par PIV permet également de caractériser l'écoulement porteur. La principale différence par rapport au chapitre précédent concerne le rapport de densité et la taille des particules, ainsi que la nature hétérogène et anisotrope de l'écoulement de von Kármán à grande échelle.

Les particules sont des sphères de PMMA ($\rho_p = 1,4$ kg/m$^3$ et $2.8 < d_p/\eta < 6.3$ pour $340 < Re_\lambda < 810$). Dans ces conditions la dimension des particules les place au voisinage du seuil communément admis comme limite de validité de l'approximation de particules ponctuelles ($d_p/\eta = 5$). La gamme de nombre de Stokes correspondante va de $St \sim 0.8$ à $St \sim 4$. Nous observons la formation d'amas de particules. L'analyse de Voronoï nous permet non seulement de diagnostiquer l'apparation des amas, mais également d'identifier les amas (ainsi que les zones de déplétion) et d'analyser leur structure. Nous observons que les amas et les zones déplétées ont une structure géométrique similaire. Les PDF des aires des clusters ($A_c$) et des zones dplétées ($A_v$) se confondent quand elles sont normalisées par leur valeur moyenne et présentent un maximum de $A_{c,v}/ < A_{c,v} >\sim 0.15$. La nature fractale de ces structures est mise en évidence.

Les mesures PIV ne sont correctement résolues que pour l'écoulement le plus lent ($Re_\lambda$ le plus bas). Nous n'avons pas réussi pour le moment à identifier une corrélation claire entre la concentration préférentielle et des points particuliers de l'écoulement porteur. Bien qu'une légère tendance des particules à explorer préférentiellement les zones de faible accélération et faible vorticité (en accord avec un effet de type stick-sweep et de turbophorèse au même temp) semble présente.

# Chapitre 9: Concentration préférentielle de goutelettes d'eau en turbulence de grille active dans une soufflerie

Poursuivant notre étude de la concentration préférentielle de particules inertielles en turbulence, nous abordons dans ce chapitre la cas de particules avec un grand rapport de densité et bien plus petites que l'échelle de Kolmogorov: à savoir des gouttelettes d'eau de dimension typique de l'ordre de 100 $\mu$m dans une turbulence de grille active en soufflerie. Ce chapitre constitue également un prolongement d'un travail précédent mené il y a quelques années dans la même soufflerie [68] mais utilisant une grille passive comme générateur de turbulence. Ces études précédentes étaient donc limitées à des nombres de Reynolds modérés (jusqu'à $Re_\lambda \sim 120$). Ces études passées laissaient entrevoir de possibles effets du nombre de Reynolds sur la concentration préférentielle. Toutefois, la gamme limitée de $Re_\lambda$ alors accessible n'avait pas permis d'approfondir cet aspect de l'étude. Grâce à notre nouvelle grille active (détaillée au chapitre 2), nous avons exploré au cours de cette thèse une large gamme de nombres de Reynolds (allant jusqu'à $Re_\lambda \sim 400$).

L'analyse des statistiques des aires de Voronoï montre que la PDF s'écarte fortement de celle d'une distribution aléatoire, traduisant ainsi l'existence de concentration préférentielle. Cette PDF est relativement bien décrite par une distribution lognormale, en accord avec les études antérieures à des nombre de Reynolds plus faibles. Le clustering est trouvé fortement dépendant du nombre de Reynolds. Cette dépendance affecte davantage les zones de forte concentration, tandis que les régions déplétées semblent être essentiellement indépendantes de ce paramètre. Ceci est cohérent avec les observations antérieures pour des nombres de Reynolds inférieurs, et peut être interprété comme le fait que les grandes zones de déplétion sont associées à des structures à grande échelle de l'écoulement porteur, qui restent peu affectées lorsque le nombre de Reynolds est augmenté.

Une motivation importante de ce travail est liée à l'investigation de la pertinence du mécanisme de sweep-stick. Des simulations de DNS ont été effectuées (en collaboration avec Pablo Mininni de l'Université de Buenos Aires) dans des conditions similaires aux expériences. Les points d'accélération nulle de l'écoulement sont identifiées, et les diagrammes de Voronoï correspondants sont calculés. Nous trouvons que les aires de Voronoï de ces points présentent des statistiques presque identiques a celles obtenus dans l'expérience pour les gouttelettes. Une comparaison avec d'autres modèles, comme la turpophorèse est également proposée en considérant les statistiques des aires de Voronoï des points de vorticité nulle de l'écoulement. La comparaison va en faveur d'un rôle dominant des points d'accélération nulle.

Enfin, nous proposons une nouvelle méthode de reconstruction des champs de concentration en particule dans les expériences par analogie avec le fonctionnement des caméras linéaire, et en exploîtant l'hypothèse de Taylor dans la soufflerie. Cette nouvelle approche nous permet de reconstruire des champs de particules de plusieurs mètres de long (alors que seules des dimensions de quelques centimètres etaient accessibles auparavant). Ces champs permettent d'analyser un ensemble complet et sans précédent des interactions de longue échelle, telle que la formation des superclusters. Nous montrons en effet que les clusters tendent eux-mêmes à s'organiser en superclusters (amas d'amas). L'influence de la turbulence pour la formation de telles structures pourrait notamment avoir un impact pour la compréhension des mécanismes de formation de superamas galactiques et ouvre des perspectives nouvelles et passionnantes pour l'étude des interactions particules-turbulence.

Dans un futur proche, une analyse plus détaillée des champs reconstruits à grande échelle par cette méthode sera menée. Il s'agit notamment d'étudier les propriétés de corrélation spatiale entre les clusters ainsi que de calculer des champs de vitesse par PIV entre les cellules de Voronoï définissant les clusters et les superclusters (plutôt que les cellules carrées habituellement utilisées en PIV). Ceci peut être réalisé par la reconstruction de deux champs de particules en utilisant deux modèles de caméra linéaire par image (au lieu d'une), permettant de reconstrurie deux champs à grande échelle légèrement décalés dans le temps afind d'obtenir les corrélations de PIV. L'estimation de ces propriétés dynamiques conditionnées aux propriétés du champ de concentration revêt une importance particulière en vue d'aider à la compréhension des mécanismes collectifs affectant par exemple la vitesse de sédimentation de particules au sein des clusters comme observé par Aliseda *et al.* [2].

# Contents

**1 Introduction** **1**
- 1.1 Turbulence . . . 3
  - 1.1.1 The Notion of Scales . . . 4
  - 1.1.2 Kolmogorov's phenomenology of turbulence . . . 6
- 1.2 Free advection of inertial particles in turbulence . . . 9
  - 1.2.1 Particles equation of motion . . . 9
  - 1.2.2 Usual minimal model . . . 11
  - 1.2.3 Drag Force . . . 12
  - 1.2.4 On the limits of Stokesian models for freely advected particles . . . 15
- 1.3 Inertial particles with constrained dynamics . . . 16
- 1.4 Collective effects . . . 18
- 1.5 A quick overview of this thesis . . . 20

**2 Wind tunnel** **23**
- 2.1 Hot-wire anemometry . . . 25
- 2.2 Passive grid . . . 26
- 2.3 Active grid . . . 28
- 2.4 Conclusion . . . 30

## I Single particle-flow interaction 32

**3 Pendulum in a flow** **33**
- 3.1 Introduction . . . 33
- 3.2 Experimental setup . . . 34
- 3.3 Results . . . 36
  - 3.3.1 Laminar case . . . 36
  - 3.3.2 Origin of the bi-stability . . . 36
- 3.4 Numerical simulations . . . 41
  - 3.4.1 Inclined plate . . . 44

3.5 Influence of turbulence intensity . . . . . . . . . . . . . . . . . . 46
3.5.1 Discussion . . . . . . . . . . . . . . . . . . . . . . . . . . 50
3.6 Conclusion . . . . . . . . . . . . . . . . . . . . . . . . . . . . . . 52

**4 Instabilities on a sphere towed at constant speed 53**
4.1 Introduction . . . . . . . . . . . . . . . . . . . . . . . . . . . . . 53
4.2 Experimental setup . . . . . . . . . . . . . . . . . . . . . . . . . . 57
4.3 Equation of movement . . . . . . . . . . . . . . . . . . . . . . . . 60
4.4 Results . . . . . . . . . . . . . . . . . . . . . . . . . . . . . . . . 63
4.4.1 Instability diagnoses . . . . . . . . . . . . . . . . . . . . . 63
4.4.2 Discussion . . . . . . . . . . . . . . . . . . . . . . . . . . 64
4.4.3 Traces of a chaotic regime? . . . . . . . . . . . . . . . . . 71
4.4.4 3D tracking . . . . . . . . . . . . . . . . . . . . . . . . . . 71
4.5 Conclusions . . . . . . . . . . . . . . . . . . . . . . . . . . . . . . 75

**5 Equilibrium and stability of long towed cable systems. Part I: instabilities under a laminar flow 76**
5.1 Introduction . . . . . . . . . . . . . . . . . . . . . . . . . . . . . 76
5.2 Experimental setup . . . . . . . . . . . . . . . . . . . . . . . . . . 78
5.2.1 Lagrangian tracking . . . . . . . . . . . . . . . . . . . . . 80
5.3 Results . . . . . . . . . . . . . . . . . . . . . . . . . . . . . . . . 82
5.3.1 Mean height . . . . . . . . . . . . . . . . . . . . . . . . . 82
5.3.2 Dynamical fluctuations and stability . . . . . . . . . . . 86
5.3.3 A second instability towards toroidal trajectories. . . . 95
5.3.4 Discussion . . . . . . . . . . . . . . . . . . . . . . . . . . 96
5.4 Conclusion . . . . . . . . . . . . . . . . . . . . . . . . . . . . . . 103

**6 Equilibrium and stability of long towed cable systems. Part II: the role of turbulence 105**
6.1 Introduction . . . . . . . . . . . . . . . . . . . . . . . . . . . . . 105
6.2 Experimental setup . . . . . . . . . . . . . . . . . . . . . . . . . . 106
6.3 Post-processing . . . . . . . . . . . . . . . . . . . . . . . . . . . . 108
6.3.1 Trajectories . . . . . . . . . . . . . . . . . . . . . . . . . . 108
6.3.2 Spectral analysis . . . . . . . . . . . . . . . . . . . . . . . 109
6.3.3 “Empirical Large Eddy Simulation” (E-LES): a new estimator of variances and correlation functions . . . . 110
6.3.4 Transfer functions . . . . . . . . . . . . . . . . . . . . . . 113
6.4 Results on the turbulent dynamics of towed spheres . . . . . . 114
6.4.1 Statistical Analysis . . . . . . . . . . . . . . . . . . . . . 114
6.4.2 Transfer functions analysis . . . . . . . . . . . . . . . . . 115
6.5 Advected sphere in turbulence: the role of filtering effects. . . 118

  - 6.5.1 Dynamical model for the attached particles motion . . 118
  - 6.5.2 Inhibition of intermittency . . . . . . . . . . . . . . . . 123
  - 6.5.3 Turbulent versus laminar towing . . . . . . . . . . . . 124
- 6.6 Results . . . . . . . . . . . . . . . . . . . . . . . . . . . . 126
- 6.7 Physics of sports . . . . . . . . . . . . . . . . . . . . . . . 131
- 6.8 Conclusions . . . . . . . . . . . . . . . . . . . . . . . . . . 133

**II Collective effects 135**

**7 Air bubbles in a water tunnel 136**
- 7.1 Introduction . . . . . . . . . . . . . . . . . . . . . . . . . . 136
- 7.2 Experimental setup. . . . . . . . . . . . . . . . . . . . . . . 138
  - 7.2.1 SprayTec . . . . . . . . . . . . . . . . . . . . . . . . 141
- 7.3 PIV . . . . . . . . . . . . . . . . . . . . . . . . . . . . . . 142
- 7.4 Preferential concentration analysis . . . . . . . . . . . . . . . 146
  - 7.4.1 Post-processing to quantify clustering . . . . . . . . . . 146
  - 7.4.2 Voronoï analysis of bubble concentration field . . . . . 148
  - 7.4.3 Conditioned statistics . . . . . . . . . . . . . . . . . . 148
- 7.5 Conclusions . . . . . . . . . . . . . . . . . . . . . . . . . . 154

**8 Preferential concentration of finite solid particles in a swirling von Kármán flow of water 156**
- 8.1 Introduction . . . . . . . . . . . . . . . . . . . . . . . . . . 156
- 8.2 Experimental setup. . . . . . . . . . . . . . . . . . . . . . . 156
- 8.3 Results . . . . . . . . . . . . . . . . . . . . . . . . . . . . 161
  - 8.3.1 Clusters . . . . . . . . . . . . . . . . . . . . . . . . 163
  - 8.3.2 Voids . . . . . . . . . . . . . . . . . . . . . . . . . 166
  - 8.3.3 Fractal structure of clusters and voids . . . . . . . . . . 168
- 8.4 PIV . . . . . . . . . . . . . . . . . . . . . . . . . . . . . . 169
- 8.5 Conclusions . . . . . . . . . . . . . . . . . . . . . . . . . . 174

**9 Preferential concentration of sub-Kolmogorov dense particles in active grid generated turbulence 176**
- 9.1 Introduction . . . . . . . . . . . . . . . . . . . . . . . . . . 176
- 9.2 Experimental setup . . . . . . . . . . . . . . . . . . . . . . . 176
- 9.3 Voronoï analysis of particles spatial distribution . . . . . . . . 180
- 9.4 Clustering evidence . . . . . . . . . . . . . . . . . . . . . . . 180
- 9.5 Cluster geometry . . . . . . . . . . . . . . . . . . . . . . . . 184
- 9.6 Numerical simulations. . . . . . . . . . . . . . . . . . . . . . 186
  - 9.6.1 Motivations . . . . . . . . . . . . . . . . . . . . . . . 186

  - 9.6.2 Simulation details. . . . . . . . . . . . . . . . . . . . . . 187
  - 9.6.3 Determination of “zero-acceleration” points. . . . . . . 188
  - 9.6.4 Voronoï analysis of zero-acceleration points. . . . . . . 191
  - 9.6.5 Voronoï analysis of other characteristic points of the turbulent field. . . . . . . . . . . . . . . . . . . . . . . 192
- 9.7 Beyond clustering. . . . . . . . . . . . . . . . . . . . . . . . . . 194
- 9.8 Superclustering . . . . . . . . . . . . . . . . . . . . . . . . . . 199
- 9.9 Discussion and conclusions . . . . . . . . . . . . . . . . . . . . . 201

# Chapter 1

# Introduction

Flows transporting particles are ubiquitous in natural and human-made systems. The study of material inclusions interacting with a carrier flow is therefore an activity of scientific interest by itself, but it is also related with lots of natural processes and has many industrial applications. In the first group, we can mention the formation of rain droplets in warm clouds [91], the coexistence of plankton species [103], the sporing of pollen or dust in the atmosphere [21], sediment deposition, planet formation in accretion disks, etc. Regarding to industrial applications, spray combustion in Diesel engines [95] and some rocket propellers [126], mixing of catalytic powders, separative methods in oil industry, etc. are just a few examples (figure 1.1). In most of these situations the carrier flow is turbulent, and the coupling between the particle dynamics and the flow is further complexified by the random and multi-scale nature of turbulence and by the inertia of the particles.

These complex interactions result in fascinating phenomena as for instance the preferential concentration of inertial particles, whose investigation is one of the main goals of this thesis. However the complexity revealed by previous works on particle-laden flows, motivated to consider several simpler situations, trying to separate different physical mechanisms coupling the dynamics of a particle and a flow, before addressing the problem of collective effects for freely advected particles in turbulent flows.

In this first chapter, I therefore first describe some aspects of the state of the art on inertial particles in turbulence research, starting with a brief description of turbulence itself. This will lead me to introduce basic concepts of the turbulence-particle interaction problem, in particular regarding the role of the drag force acting on the particle, which in turn motivates the investigation of simpler configurations prior to addressing the case of freely advected particles in turbulence.

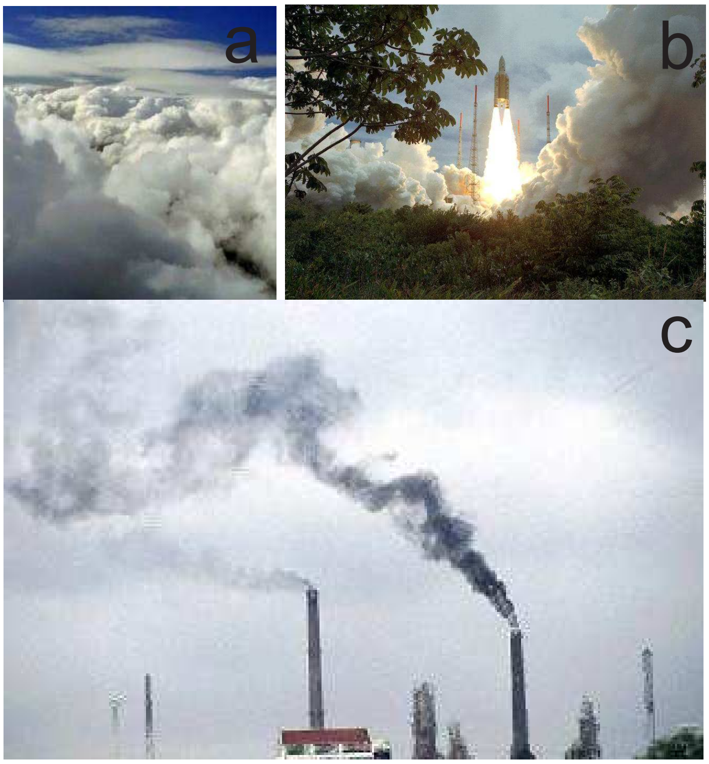

Figure 1.1: Typical examples of material inclusions interacting with a carrier flow: clouds in the atmosphere (a), rocket propellers (b) and pollutants emitted to the atmosphere by a factory (c).

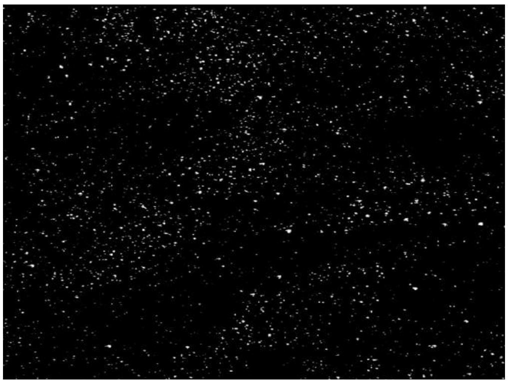

Figure 1.2: Experimental image of preferential concentration of water droplets in air (image taken from [2]).

## 1.1 Turbulence

Everyday life gives us an intuitive knowledge of turbulence in fluids: the smoke of a cigarette, the chaotic motion of a river, turbulence in an airplane etc. In spite of its constant presence, we have not found an appropriate definition of a turbulent flow. Lesieur [56] propose tentatively the following definition of turbulence:

- Firstly, a turbulent flow is unpredictable, in the sense that a small uncertainty as to its knowledge at a given initial time will amplify so as to render impossible a precise deterministic prediction of its evolution.
- Secondly, it satisfies the increased mixing property. The readily available supply of energy in turbulent flows tends to accelerate the homogenization (mixing) of fluid mixtures. The characteristic which is responsible for the enhanced mixing and increased rates of mass, momentum and energy transports in a flow is called "turbulent diffusivity".
- Thirdly, it involves a wide range of spatial and temporal scales.

The third condition is maybe the one that represents the biggest experimental challenge when dealing with turbulent flows: its multi-scale nature. Since the pioneering work by Richardson in the 1920', the usual phenomenology of turbulence considers that mechanical energy is injected at some large scale (the integral scale $L_0$) and then cascades down the smallest scales up to the viscous dissipation scale $\eta$ [120]. Turbulent eddies exist over the entire range of scales between $L_0$ and $\eta$ (known as the inertial range of turbulence), for which specific statistical properties prevail due to local spatial and temporal correlations between eddies. At small scales (below $\eta$), the flow is dominated by viscous effects and becomes smooth, while at larger scales (above $L_0$) eddies are fully uncorrelated and follow a Brownian like dynamics.

Turbulent flows are governed by the Navier-Stokes equation:

$$\partial_t \vec{u} + (\vec{u} \cdot \vec{\nabla})\vec{u} = -\frac{1}{\rho}\vec{\nabla} p + \nu \triangle \vec{u}, \tag{1.1}$$

$$\vec{\nabla} \cdot \vec{u} = 0,$$

where $\vec{u}$ is flow velocity, $\rho$ its density and $p$ its static pressure. This equation with appropriate boundary condition contains all the turbulent phenomena (at least for classical systems). The problem is that Navier-Stokes equation is highly non-linear (as a consequence of the term $(\vec{u} \cdot \vec{\nabla})\vec{u}$) and analytical solutions are extremely scarce. On the other hand, the multi-scale nature of turbulence (both in time and space), makes numerical analysis extremely expensive, considering that short and long time and space scales must be resolved simultaneously.

Using $L$, $U$ and $\rho U^2$ as reference length, reference velocity and reference pressure respectively, the normalized variables for fluid velocity, position, time and pressure are defined as $\vec{u_+} = \vec{u}/U$, $\vec{x_+} = \vec{x}/L$, $t_+ = t\frac{U}{L}$ and $p_+^* = p/(\rho U^2)$ respectively. The non-dimensional form of equation 1.1, now can be written as:

$$\partial_{t+}\vec{u_+} + (\vec{u_+} \cdot \vec{\nabla}_+)\vec{u_+} = -\vec{\nabla}_+ p_+^* + Re^{-1}\triangle_+\vec{u_+}, \tag{1.2}$$

$$\vec{\nabla}_+ \cdot \vec{u_+} = 0,$$

The above equation is completely non-dimensional, where the only parameter taking into account the flow characteristics is the Reynolds number $Re = UL/\nu$. It can be noticed that a greater Reynolds number leads to the decay of viscous dissipation term as compared with non linear convective term on the left hand side, hence the flow becomes turbulent due the diminution of viscous damping. The Navier-Stokes equation holds true even for high Reynolds numbers, even when the flow becomes highly unpredictable and chaotic. Turbulence is an hydrodynamic instability, where the symmetries on the basis of which Navier-Stokes equations were developed are broken, but where these symmetries are somehow regained in a statistical sense [34].

### 1.1.1 The Notion of Scales

The concept of scales in turbulence was first introduced by Lewis Fry Richardson in 1922 [102]. He attributed turbulence as a multiple scale phenomenon which contains eddies of different sizes and scales. According to him, in turbulent flows the energy is injected through large eddies which are named as energy containing eddies or also known as large scale structures. As these eddies become unstable, they split into many small eddies hence transferring their energy to the smaller ones, this process goes on until the Reynolds number of smallest scale structures becomes unity, resulting in the stability of eddies and hence, their energy is damped through viscous dissipation (figure 1.3).

Although Richardson model gives a conceptually valid vision of turbulence, several fundamental questions remain unanswered: what is the size of the smallest eddies that are responsible for dissipating the energy? How many degrees of freedom does a turbulent flow have?

The idea of multiple scale nature of turbulence was formulated in the form of a theory by A.N. Kolmogorov in 1941 [51]. Using only three hypothe-

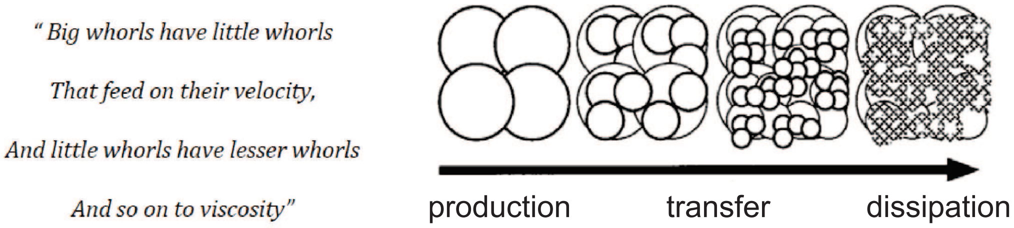

Figure 1.3: *Left:* Richardsons verses describing the notion of scales in turbulence inspired from a Jonathan Swift's verse. *Right:* Kolmogorovs illustration of Richardsons idea as cascade of scales (image taken from [60])

ses he devised a phenomenological theory which is known as Kolmogorov Phenomenology of turbulence. A detailed discussion on this theory and its limitations may be found in [34]. Before going into the discussion on the Kolmogorov phenomenology, which was actually based upon the Richardsons cascade theory, it is essential to define few characteristic length scales that are present in turbulent flows (in the next chapter this parameters will be further discussed).

- *Flow length scale or large scale ($L$):* this length scale is the characteristic of turbulence generation mechanism and mostly based upon the flow geometry. For example, while studying wakes behind a cylinder or sphere, this scale is the diameter of cylinder or sphere; in case of grid generated wind tunnel flow it is the mesh size of the grid etc.
- *Integral length scale ($L_0$):* in the developed turbulent flow region the integral length scale corresponds to the size of the largest eddy present therein.
- *Dissipative or Kolmogorov length scale ($\eta$)*: this length scale is considered to be the smallest length scale present in turbulent flows at which all the injected energy that was transferred through the intermediate scales dissipates due to viscous dissipation.
- *Taylor microscale:* an intermediate length scale which is much smaller than integral length scale and much greater than dissipative length scale.

Most of the complexities and the richness of turbulence lie in the range of scales between the integral and dissipative lengths. In this range also known as inertial range, multiscale structures coexist and interplay in the energy cascade process.

### 1.1.2 Kolmogorov's phenomenology of turbulence

The theory advanced by Kolmogorov is based on the hypothesis. Kolmogorov's first hypothesis of local isotropy, states that in the case of fully developed turbulence the small scale statistics $l << L_0$ are independent of their generation mechanisms [46]. This implies the statistical restoration of symmetries which actually were broken by the turbulence generation mechanisms. This is valid for small scale structures away from boundaries. According to this proposition the large scales may still be anisotropic but the isotropy is recovered at inertial and dissipative scales.

Furthermore, in his first similarity hypothesis Kolmogorov stated that in the limit of high Reynolds number, the statistics of turbulent structures having scales much smaller than integral length scale can be universally determined only by viscosity $\nu$ and mean dissipation rate $\epsilon$. In Kolmogorov's phenomenology the characteristic length, time and velocity scales below which the viscous effects dominate are determined through classical dimensional analysis as:

$$\eta = \left(\frac{\nu^3}{\epsilon}\right)^{\frac{1}{4}}, \tag{1.3}$$

$$\tau_\eta = \sqrt{\frac{\nu}{\epsilon}}, \tag{1.4}$$

$$u_\eta = (\epsilon\nu)^{1/4}. \tag{1.5}$$

These dissipative length, time and velocity scales are often named after his name as Kolmogorov length scale $\eta$, Kolmogorov time scale and Kolmogorov velocity scale respectively. The Reynolds number based upon these length and velocity scales verifies the relation:

$$Re_\eta = \frac{\eta u_\eta}{\nu} = 1. \tag{1.6}$$

Note, that the above mentioned length, time and velocity are known to be the smallest scales present in any turbulent flow and these represent the smallest eddies which dissipate in the form of heat, all of the energy they have received from larger structures. The Reynolds number based on these scales is unity which conforms to the energy cascade idea of Richardson.

The second similarity hypothesis of Kolmogorov, states that in every turbulent flow at sufficiently high Reynolds number, the statistics of the motions at inertial range scales $L_0 >> l >> \eta$ have a universal form independent of viscosity $\nu$ and uniquely determined by the energy dissipation rate $\epsilon$.

It remains to be determined how the turbulent kinetic energy is distributed among the eddies of differents sizes. For this purpose we consider homogeneous turbulence and the wavenumber $k = 2\pi/l$. The energy in the wavenumber range $[k_a, k_b]$ is defined as:

$$\mathbf{k_{k_a,k_b}} = \int_{k_a}^{k_b} E(k)dk. \tag{1.7}$$

It can be shown [94] that the contribution to the dissipation rate $\epsilon$ from motions in the range $(k_a, k_b)$ is

$$\epsilon_{k_a,k_b} = \int_{k_a}^{k_b} 2\nu k^2 E(k)dk. \tag{1.8}$$

It follows from Kolmogorov's first similarity hypothesis that, in the universal equilibrium range ($k > k_{IR} = 2\pi/l_{IR}$) the spectrum is a universal function of $\epsilon$ and $\nu$. From the second hypothesis it follows that, in the inertial range the spectrum is:

$$E(k) = C\epsilon^{2/3}k^{-5/3}, \tag{1.9}$$

where $C$ is a universal constant. Sreenivasan *et al.* [115] studying different types of flows, with the Reynolds number based in the Taylor microscale (defined as $Re_\lambda = \frac{u_{rms}\lambda}{\nu}$, with $u_{rms}$ the rms value of velocity fluctuation) ranging from 28 to 18000 found, for high enough Reynolds numbers ($Re_\lambda > 50$) a value of $C = 0.53 \pm 0.033$. A typical turbulence spectrum with the inertial range can be observed in figure 1.4.

For a length scale in the inertial subrange such that $\eta << l << L_0$, Kolmogorov's second hypothesis of similarity implies that the statistics of second order velocity increments depends only on mean dissipation rate $\epsilon$. The velocity increments (longitudinal component) are defined as the velocity difference between two points separated by a distance $l$, given by:

$$\delta_l u = u(\vec{x} + l \cdot \widehat{e}_x) - u(\vec{x}). \tag{1.10}$$

Thus according to K41, the second order longitudinal velocity increments (also known as second order structure function) must be independent of viscosity and follows:

$$S_2(l) =< (\delta_l u)^2 >= C_2\epsilon^{2/3}l^{2/3}, \tag{1.11}$$

where, $C_2$ is a universal constant of proportionality. Similarly, according to K41 for the higher order moments the velocity structure functions must follow:

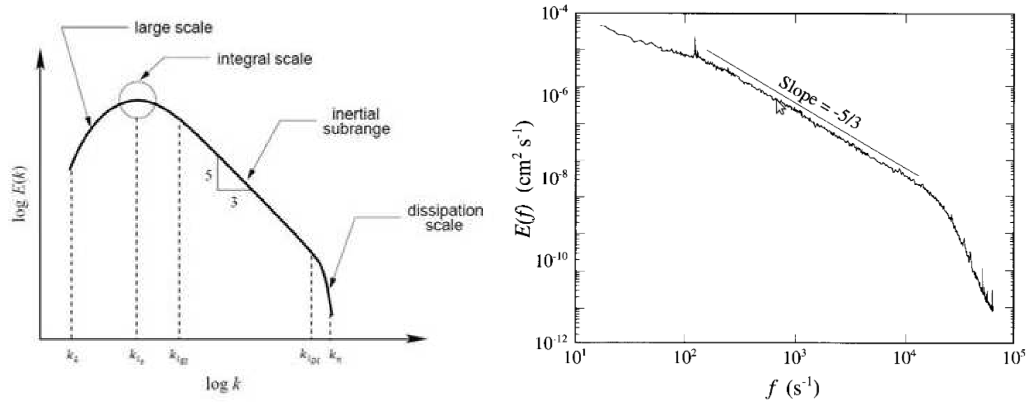

(a) (b)

Figure 1.4: (a) Schema of a turbulence spectrum an the different ranges. (b) Turbulence spectrum obtained experimentally (image taken from [34]).

$$S_p(l) =< (\delta_l u)^p >\sim \epsilon^{p/3} l^{\zeta_p}, \tag{1.12}$$

where $\zeta_p = p/3$ according to Kolmogorov phenomenology. For the particular case $p = 3$, Kolmogorov derived the famous four-fifth law, where $S_3(l) = -\frac{4}{5}\epsilon l$.

In the case of higher order velocity structure functions, if K41 phenomenology is to be considered exact, the exponent $\zeta_p$ must vary linearly with the order $p$. The experimental measurements of the velocity increments have shown deviations from K41 scaling for orders higher than 3 [34]. This departure from K41 behavior is named as intermittency. This phenomenon may also be attributed to the difference in statistical signature of velocity increments with respect to their increments or in other words the statistics of velocity increment change with the spatial increment itself. In other words, the statistics of velocity increment change with the spatial increment itself. Kolmogorov and Obukhov in 1962 [83] refined the K41 theory to include intermittency effects, by defining a dissipation rate which was not averaged globally but locally over the volume of sphere having a radius equal to spatial increment $l$.

## 1.2 Free advection of inertial particles in turbulence

As previously mentioned the transport of dispersed inclusions by turbulence is a question of primary importance. One of the difficulties in studying the turbulent dynamics of particles is that a general framework is still lacking in order to write a proper equation of motion for a particle forced by a turbulent environment. Several situations must be distinguished depending on the nature of the particle. If the particle is neutrally buoyant and small compared to the dissipative scale of the flow, it is considered to behave as a tracer of the flow. Such tracers are commonly used for instance to seed a flow for visualization purposes (PIV, PTV, LDV, etc.). On the other hand, particles which are much denser or lighter than the flow and/or whose size is much larger than the dissipation scale [99, 20, 69, 19] do not behave as tracers and have a dynamics which deviates from that of fluid particles. Such particles are generally called *inertial particles*. An equation for the motion of such particles has only been derived for the specific case of very small particles (point particle limit), as described in the following sub-section.

In the recent years, with the development of new technologies (high speed cameras, holographic imaging techniques), the experimental study of turbulent transport has been revolutionized. The new experimental information has shown that the theoretical models need to be revised and corrected.

### 1.2.1 Particles equation of motion

Originally Basset, and later Boussinesq and Oseen, examined the motion of a sphere settling out under gravity in a fluid that was otherwise at rest ([7, 12, 85]). The disturbance flow produced by the motion of the sphere was assumed to have sufficiently low Reynolds number so that the fluid force on the sphere could be calculated from the results of unsteady Stokes flow. Tchen extended this work to a sphere settling under gravity in an unsteady and nonuniform flow, with a view to application to turbulent flows. The resulting model (known as BBOT, Basset-Boussinesq-Oseen-Tchen) has been revisited in 1983, simultaneously by Maxey & Riley [61] and by Gatignol [36]. To date the equation of motion derived by Maxey-Riley-Gatignol is considered as the reference for the motion of small inertial particles in a turbulent environment. It can be written as

$$
\begin{aligned}
m_p \frac{d\vec{v}}{dt} = 3\pi \mu_f d_p (\vec{u} - \vec{v}) + \frac{1}{2} m_f \frac{d(\vec{u} - \vec{v})}{dt} + m_f \frac{D\vec{u}}{Dt} + \\
\frac{3}{2} d_p^2 \sqrt{\pi \rho_f \mu_f} \int_{-\infty}^{t} \frac{d(\vec{u} - \vec{v})}{dt} \frac{d\tau}{\sqrt{t - \tau}} + (m_p - m_f)\vec{g},
\end{aligned}
\tag{1.13}
$$

where $\vec{v}$ is the particle velocity, $\vec{u}$ is the carrier flow velocity field, $d_p$ is the particle diameter, $\rho_p$ is the particle density, $\rho_f$ is the carrier fluid density, $m_f = \rho_f \pi \frac{d_p^3}{6}$ is the mass of the fluid displaced by the particle and $\mu_f$ is the carrier fluid dynamic viscosity. The terms on the right hand side are, in order of appearance:

- The Stokes drag force, which is due to the relative velocities of particle and fluid. In the expression above, particle is supposed to have a viscous response time $\tau_p = m_p / 3\pi \mu_f d_p$, which corresponds to a low particulate Reynolds number limit ($Re_p = d_p \|\vec{u} - \vec{v}\|)/\nu << 1$). More generally the drag term can be written as $(\vec{u} - \vec{v})/\tau_p$, where the response time $\tau_p$ can be empirically corrected from non-linear particulate Reynolds effects, as detailed in section 1.2.3.

- The added mass force (also known as virtual mass force), which is purely inertial, is the force exerted by the displaced fluid caused by the particle that resists particles acceleration and deceleration.

- The pressure gradient term, which is equivalent to the fluid particle acceleration at the position of the particle center.

- The history term, which takes into account the entire history of the particle motion in the carrier fluid up to an instant $t$ and it mainly takes into account the interaction of the particle with its own wake.

- The Archimedes force, which is the net force due to gravity and buoyancy.

The derivatives $\frac{d\vec{v}}{dt}$ and $\frac{d\vec{u}}{dt}$ are taken along the material particle trajectories, whereas $\frac{D\vec{u}}{Dt}$ is the material or Lagrangian derivative representing the fluid element acceleration along fluid particles. This equation assumes point particles as it neglects non-uniformities of the fluid field around the particles. Second order corrections in $d_p$, known as Faxen correction, have been introduced by Maxey-Riley and Gatignol to account for simple finite size effects. However, recent numerical studies [14, 42] suggests that this corrections may only be relevant for particles marginally larger than the turbulence dissipation scale.

Even in the point particle approximation, the Maxey-Riley-Gatignol equation for point particles is very complex to deal with, therefore, numerical resolution of the complete equation coupled to direct numerical simulation (DNS) of the carrier fluid has only been performed for moderate Reynolds numbers [28]. Different groups doing DNS have proposed simplified models taking into account only the Stokes drag force and, in some cases, also the added mass and pressure gradients [127]. Eliminating the history term responds mainly to simulations feasibility issues and the relevance of this approximation remains an open question, while gravity is also generally neglected assuming that particles terminal settling velocity is negligible compared to characteristic turbulent velocities (small Rouse number approximation). This simplifications reduce equation (1.13) to

$$\frac{d\vec{v}}{dt} = \beta \frac{D\vec{u}}{Dt} + \frac{1}{\tau_p}(\vec{u} - \vec{v}), \tag{1.14}$$

where $\beta = 3\rho_f/(\rho_f + 2\rho_p)$ is the coefficient that takes into account the added mass and pressure gradient forces and $\tau_p = d_p^2/12\beta\nu_f$ is the particle viscous response time.

### 1.2.2 Usual minimal model

In the simplest limit, only the drag force is conserved, a final simplification supposed to be valid when the density ratio $\Gamma = \rho_p/\rho_f$ is much larger than one (*i.e.* $\Gamma >> 1$). This simpler case has been extensively investigated, starting from the seminal work by Tchen and Hinze in the late 40' and reduces the equation of motion of the particle to :

$$\frac{d\vec{v}}{dt} = \frac{1}{\tau_p}(\vec{u} - \vec{v}). \tag{1.15}$$

This equation is particularly attractive for its simplicity. Though it is expected to be valid only in the limit of point particles with $\Gamma = \rho_p/\rho_f >> 1$, it is traditionally invoked as being *the* equation of motion of inertial particles transported by a turbulent velocity field $\vec{u}$. The exact range of validity of this equation (in terms of particles size and density) remains an open question which has motivated many recent experimental investigations [98, 127, 14, 129]. In this standard framework particles inertia is entirely governed by its viscous time $\tau_p$, easily deduced from equations 1.21 and 1.23:

$$\tau_p = \frac{8m_p}{\pi d_p \mu_f Re_p C_D(Re_p)}, \tag{1.16}$$

for a particle with a given size and mass (or density) as a function of its particulate Reynolds number $Re_p$. The dimensionless equivalent of $\tau_p$, the Stokes number, is defined as:

$$St = \tau_p/\tau_\eta, \tag{1.17}$$

where $\tau_\eta$ is the viscous dissipation time scale of the carrier flow

Taking the temporal Fourier transform, equation 1.15 can be written as

$$\widehat{v} = \frac{1}{1 + i\omega\tau_p}\widehat{u}. \tag{1.18}$$

where $\widehat{u}$ represents the Fourier transfom of the fluid velocity along the particles trajectory. The transfer function $H = \frac{1}{1+i\omega\tau_p}$ acts as a first order low-pass filter on the carrier flow velocity fluid. In particular it predicts that velocity fluctuations of inertial particle can be simply deduced from that of the carrier flow by a simple filtering process. By integrating the square of equation (1.18) over $\omega$ and assuming an exponential correlation function for the carrier fluid velocity along particles trajectory, Tchen [119] showed that particles *rms* velocity can be related to fluid's by :

$$v_{rms} = \frac{1}{1 + \tau_p/T_L}u_{rms}, \tag{1.19}$$

where $T_L$ is the Lagrangian correlation time of the carrier flow. According to this relation particles fluctuations are expected to be reduced as their inertia increases (*i.e.* as $\tau_p$ increases), consistently with the filtering effect just mentioned.

Recently, DNS coupled to the simple model (1.15) have also suggested an important influence of inertia on particles acceleration statistics [9]: while acceleration probability functions for fluid tracers are highly non Gaussian [54], inertial particles whose dynamics is ruled by equation (1.15) tend to have Gaussian acceleration statistics as their inertia increases (with much less extreme acceleration events compared to fluid Lagrangian particles), also as a consequence of the filtering effect introduced with the increasing particles response time.

### 1.2.3 Drag Force

The discussion in the previous sections shows the leading role of the drag force in transport of particles in flows. Resistance was evidently the first fluid-dynamic force, arising from an obstacle placed against a stream of air or water, to become obvious to man. This force is nowadays related to drag forces, and is still the leading force in many fluid-structure interaction models and is the force that will be more carefully studied in this work.

The drag force is a good example of the richness of fluid-particle interactions. There is not a drag force, but several forces named in this way: skin friction drag force, pressure drag force, induced drag, parasite drag; even lift forces may be considered as a special case of these resistance forces. As this thesis covers mainly spheres with medium or high *Re*, only the lift and pressure drag force are relevant. Although written almost 50 years ago, the book by Hoerner [41], Fluid-Dynamic Drag, still remains the most complete and documented work on the subject.

Let us consider the case of an object facing a mean stream with velocity $\vec{U}$ The aerodynamic forces acting on the object are generally decomposed in the *drag* $F_D$ (component alined with $\vec{U}$) and the *lift* $F_L$ (component perpendicular to $\vec{U}$), expressed as follow:

$$F_{D,L} = \frac{1}{2} C_{D,L} \rho_0 U^2 A, \tag{1.20}$$

where $\rho_0$ is flow density, $U$ its velocity and $C_D$ the aerodynamical coefficient, named $C_D$ for pressure drag force and $C_L$ for lift forces. $A$ is the reference area (defined as the area of the orthographic projection for drag forces and the area facing the flow for lift forces).

Therefore, an appropriate parameter for characterizing this phenomenon are the aerodynamics coefficients $C_D$ and $C_L$. In this general introduction we will focus in spheres, where due to their symmetry, is assumed no lift force to act on them.

Therefore, we will only focus here on the drag coefficient $C_D$ for a sphere. Figure 1.5 shows how this curve varies with $Re_p$ for a fixed sphere. Deviations from this curve may occur and are related to instabilities and dynamical corrections to this law (these points will be discussed further below).

It becomes important in this context to model and quantify this parameter for the case of spheres. This has been extensively done in several studies, both numerical and experimental investigating the drag force acting on a steady static particle with an imposed flow around (see [19, 13] for a review). In this context, the drag force is usually written in the general form :

$$\vec{F_D} = \frac{\pi d_p \mu_f Re_p}{8} C_D(Re_p)(\vec{u} - \vec{v}), \tag{1.21}$$

where the drag coefficient $C_D$ is a function of the particulate Reynolds number:

$$Re_p = \frac{d_p \|\vec{u} - \vec{v}\|}{\nu}, \tag{1.22}$$

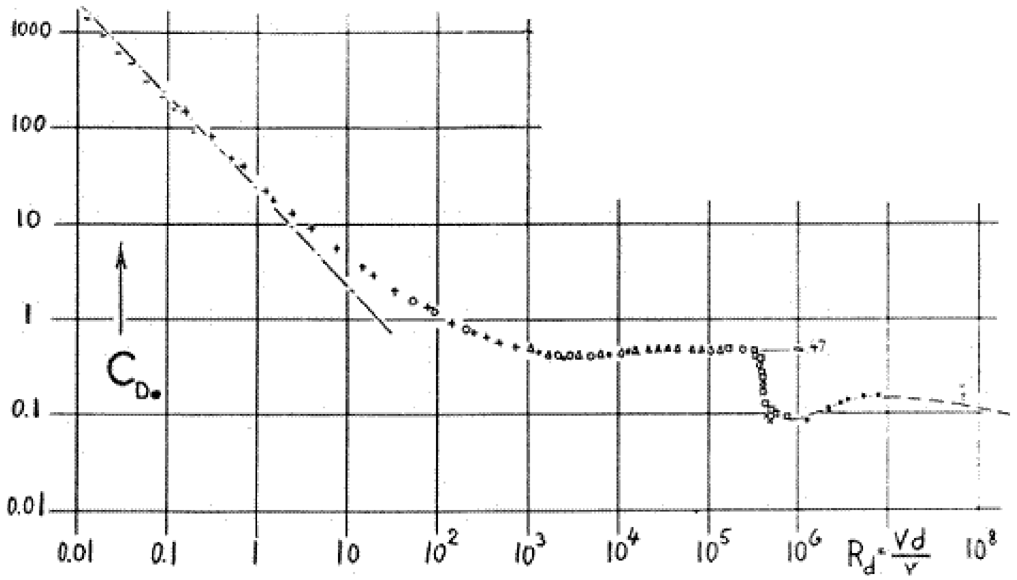

Figure 1.5: Drag coefficient of a sphere as a function of $Re_p$. Image taken from [41].

with $\nu = \mu_f/\rho_f$ the kinematic viscosity of the fluid (and for the steady particle case $\vec{v} = \vec{0}$).

In the limit $Re_p \to 0$ (point particle and/or slow relative slippage velocity), drag force reduces to the usual Stokes force acting on a sphere ($\vec{F}_D = 3\pi d_p \mu_f (\vec{u} - \vec{v})$), and the drag coefficient is simply $C_D = 24/Re_p$.

In case of finite particulate Reynolds number, this simple Stokes drag coefficient becomes invalid and has to be corrected. Known corrections are essentially empirical and have been obtained by an exhaustive investigation of the situation where the particle is fixed in a mean flow $\vec{u}$. By measuring the force acting on the particle (with a force gauge mounted on the particle support for instance) it is possible to calibrate $C_D$ as a function of $Re_p$.

Several empirical relations for particulate Reynolds number based drag coefficient exist [19] [65] ; the most effective one is probably the one given by Brown & Lawler [13]. In their review of drag and settling velocity of spherical particles, they have proposed an expression for the drag coefficient which satisfactorily fits the available experimental and numerical data for particles with Reynolds number up to $2 \times 10^5$:

$$C_D = \frac{24}{Re_p}(1 + 0.150 Re_p^{0.681}) + \frac{0.407}{1 + \frac{8.710}{Re_p}} \qquad \text{for} \quad Re_p < 2 \times 10^5 \qquad (1.23)$$

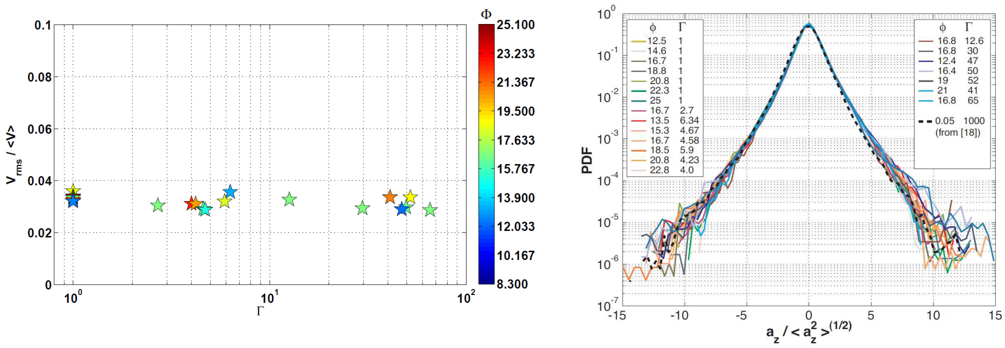

(a) (b)

Figure 1.6: (a) Velocity fluctuation level measured by [98] for inertial particles with various density ratios $\Gamma = \rho_p/\rho_f$ and diameters given by $\Phi = d_p/\eta$ (with $\eta$ the carrier flow dissipation scale). (b) Acceleration probability density functions for the same particle classes. A signature of the filtering due to the drag force is present neither in (a) nor in (b).

### 1.2.4 On the limits of Stokesian models for freely advected particles

As already mentioned, in the Stokesian models[1] the drag force is generally considered as *the* leading force acting on an inertial particle freely advected by a turbulent flow, though the actual range of validity of this approximation remains unclear. Recent experimental investigations have shown for instance that this assumption fails to predict simple dynamical features of finite size inertial particles [98]. For instance, while the dominant drag force assumption (1.15) predicts a filtering of velocity according to relations (1.18) and (1.19), measurements show that velocity fluctuation levels of inertial particles remain identical to that of the carrier flow, even when the particle inertia is large (see figure 1.6a); similarly, no trend of gaussianization of acceleration statistics have been observed experimentally for finite size particles with large inertia (see figure 1.6b). Recent numerical studies where particle size is fully resolved [35, 42, 26] also confirm the non-gaussianity of acceleration probability density function (PDF) for finite size inertial particles. This suggests that filtering mechanism due to the drag force and the particle viscous response time is not the main process ruling the turbulent dynamics of in-

---

[1] Rigorously, as Reynolds number corrections have been consider for obtaining $\tau_p$, the flow is no longer Stokesian and the term used is incorrect. Nevertheless, as in most studies $\tau_p$ is considered as a fixed value, the drag force is still lineal with slippage velocity. Therefore, during this thesis we will use the term Stokesian when referring to such models.

ertial finite size particles. A sampling scenario, where particles dynamics is mostly affected by a preferential sampling of the carrier flow as they preferentially explore, for instance, low vorticity regions (inertial particles tend to be centrifugally expelled from the core of turbulent vortices for instance) has been proposed in addition to the usual filtering mechanism. These observations question the exact role of the drag force in the equation of motion of freely advected particles. Though it is generally taken as a leading effect in theoretical and numerical approaches, very limited experimental evidence is available nowadays to fully support this assumption. When is the drag term really dominant? When can the particle dynamics indeed be related to that of the carrier flow by a simple filtering mechanism? What governs the possible competition between a filtering and a sampling scenario?

## 1.3 Inertial particles with constrained dynamics

The questions above have recently motivated one of the simplified experimental configurations investigated during this thesis to address the coupling between a turbulent flow and a transported sphere. The goal of these simplified experiments is to emphasize the role of filtering effects by forcing the drag force to somehow become indeed the leading forcing term. Therefore the idea of considering a semi-constrained particle with an imposed dominant motion relative to the surrounding fluid. Hence the idea of considering a towed sphere. We call this situation *semi-constrained*, because the longitudinal motion of the sphere is entirely constrained by the towing motion, while the transverse motion of the sphere is free, leaving to the particle two degrees of freedom. In the present study, this is achieved by considering a particle attached to a thin longitudinal thread in a windtunnel experiment (see figure 2.1 in the next section where the experimental setup is further detailed); as the particle is attached its streamwise motion is blocked which also imposes a strong slippage velocity ($u_z - v_z$) and therefore a dominant drag force (as shown in figure 1.7). In the same time as the particle cannot be advected with the flow, the sampling scenario is expected to be reduced as flow structures just pass by the blocked particle, in other words, the imposed constraint exacerbates the so called *crossing trajectories* effect (meaning that particle trajectory and fluid particles trajectory mostly crosses each other instead of being mostly advected together).

Beyond the fundamental interest of this simple experimental model, whose primary goal is here to explore fundamental features of the drag/filtering mechanism by imposing it as dominant, this investigation has also a relevant interest for different applications as towed systems are common for instance in acoustic streamers for submarine oil exploration.

More generally, the equation of motion of such semi-constrained particles can be written as :

$$\frac{d\vec{v}}{dt} = \beta \frac{D\vec{u}}{Dt} + \frac{1}{\tau_p}(\vec{u} - \vec{v}) + \vec{F}_p, \tag{1.24}$$

where the propulsion (towing) force $\vec{F}_p$ is assumed to have a dominant direction (let say $|F_{p,z}| >> |F_{p,x}|, |F_{p,y}|$) which imposes a dominant motion of the particle in this particular direction (note that propulsion force can include gravity, exclusively or not). At this point, the main simplification compared to the freely advected case is that it becomes legitimate to drop the history term in equation (1.13) as the particle never interacts with its own wake, which always stays behind it thanks to the dominant imposed propulsion. Moreover, when the density ratio of the particle compared to the fluid is sufficiently large ($\Gamma >> 1$), it is also legitimate to drop the added mass term (this point will be further discussed in chapter 6).

On the other hand other phenomena coupling the dynamics of the sphere to that of the fluid may appear. The dynamics of the sphere does not result only from the direct aerodynamic force (mainly the drag) from the fluid onto the particle, it is also related to the dynamics of the towing cable which itself interacts with the flow. Besides, imposing a dominant relative velocity between the sphere and the fluid results in non-trivial wakes downstream the sphere (as revealed for instance by the extensive litterature on free falling spheres [45, 29]).

Following this line, we have investigated during this thesis several configurations with increasing rate of complexity :

- Towed spheres in laminar flow with moderate towing velocity and particulate Reynolds number ($Re_p$) for which wake instabilities are observed from the direct coupling between the fluid and the sphere (chapter 4).

- Towed spheres at larger towing velocity in laminar conditions, for which aeroelastic instabilities between the towing cable and the fluid appear and affect the sphere dynamics (chapter 5).

- We then investigate the influence of turbulence on the dynamics of the towed sphere (chapter 6). We seek for the relevance of filtering mechanisms of turbulent fluctuations in this condition with an imposed dominant drag, compared to previous observations for fully freely advected particles.

As preamble to this work on towed spheres (with two degrees of freedom), we present in chapter 3 a preliminary study of the equilibrium and stability of a pendular disk (with one single angular degree of freedom) facing a mean flow. This example illustrates that a simple dynamical system with only one degree of freedom can exhibit non-trivial couplings with a flow, due to wake instabilities and turbulence.

Finally, it is important to remark an interesting point of this problem: if the imposed relative fluid-particle velocity is sufficiently large, the system becomes an hybrid Lagrangian-Eulerian. In a Taylor's hypothesis point of view, the particle describes a Lagrangian trajectory in the frozen Eulerian field of the surrounding turbulent background flow (at least for particles time evolutions faster than the Eulerian correlation time of the surrounding flow). This will have important consequences in our study as the temporal Lagrangian spectra of particles velocity $\vec{v}$ can then be related to the Eulerian spectra of the carrier flow $\vec{u}$ as discussed later.

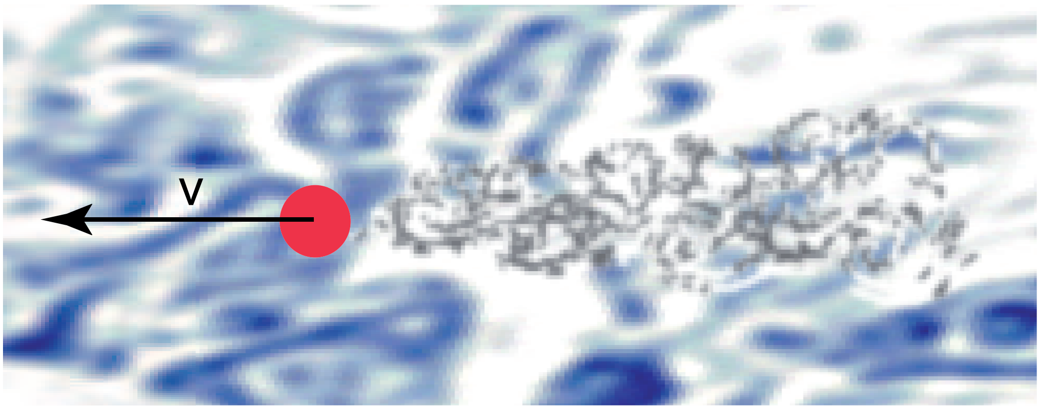

Figure 1.7: A particle with an imposed dominant motion will never interact with its own wake. Moreover, for time evolution faster than the Eulerian correlation time scale of the flow, it can be seen as traveling in a frozen Eulerian turbulence field.

## 1.4 Collective effects

Previous discussions focused on the aerodynamic interaction of a flow and one single particle with increasing degrees of freedom. We consider now the case of many freely advected particles (hence, each one with 3 translational degrees of freedom) interacting with a turbulent flow. A striking feature of such turbulent flows laden with inertial particles is the so-called preferential concentration or clustering that leads to very strong inhomogeneities in the concentration field at any scale. This has now been widely observed in many experimental and numerical configurations including homogeneous and isotropic turbulence (see [114, 31, 105]) and a robust result is that the concentration field is more intermittent for particles whose Stokes number are close to unity. Aliseda and co-workers [2] have suggested that the local enhancement of the concentration could be responsible for the measured enhancement of particle settling velocity in turbulent flows due to collective effects. It is therefore important to have a good quantification of the amount of clustering.

We mainly focus in this thesis on preferential concentration/clustering properties of heavy particles in turbulent flows. Most of the work dedicated to these studies consists of numerical simulations, in the limit of Stokesian point particle models, where back reaction of the particles on turbulence is not taken into account, and in experiments with mass and volume fraction loading that are small enough to neglect this back reaction. As a consequence the two-way coupling effects are supposed not to be relevant in these contexts and this section will only deal with the actions of the turbulent flows on the particles that enable their preferential accumulation. Several particle-turbulence interaction mechanisms have been proposed for explaining this phenomenon:

- *Response to flow structures:* also known as turbophoresis. The basic underlying mechanism is the following: due to their inertia, particles denser than the fluid tend to be ejected from vortical structures while they are easily trapped by convergent regions of the flow. The opposite behavior is expected for particles less dense than the carrier fluid. If these behaviors are easily seen and understood on simple steady flows, there is a wide gap to fill to directly apply them to homogeneous isotropic turbulent flows where, even if structures do exist, they do not necessarily live for long times. Results would imply that the effect of centrifuging usually invoked to explain clustering is not that relevant at moderately high Stokes numbers and thus there is a call for other physical mechanisms.

- *Sweep-stick mechanism:* Vassilicos and collaborators have elaborated along the last five years a new vision of particle clustering in homogeneous isotropic turbulence. In their pioneering work in 2D inverse cascading turbulence [38], they show visualizations that evidence very strong correlation in a wide range of scales between distributions of heavy inertial particles on the one hand and zero-acceleration points of the carrier turbulence on the other hand. Since then, they have extended their findings to 3D turbulence and put them on a more quantitative ground [15, 39, 20]. They explain the underlying mechanisms as follows: on the one hand, zero-acceleration points are swept by the fluid as they statistically move with the local velocity of the fluid. On the other hand, they show that a heavy particle that meets a zero-acceleration point moves with the fluid velocity, which is no longer true when the particle is at a point with nonzero acceleration. They refer to this as the sticky part of the mechanism.

Experimental investigations are still important to reach a better understanding of the underlying mechanisms, and many questions are still unsolved. Do clusters exist as a whole in these flows? How do they form? What is their structure and how does this structure evolve with time? Which effect do they have on the single particle dynamics? Here are some of the questions that still need to be answered.

The final chapters (7, 8 and 9) are dedicated to some of these questions. One of the goals (but not the only one) aimed by this study was to discriminate between the turbophoretic and the sweep-stick mechanisms as origin of preferential mechanism. As most existing studies on these mechanisms come from numerical studies, in the limit of point particles, we focus on the case of small sub-kolmogorov water droplets in a turbulent air-flow, produced in a wind-tunnel (chapter 9). However, our goals also involve characterizing as precisely as possible clustering properties, clusters geometry, Reynolds number dependencies, Stokes number dependencies, etc. Therefore, other configurations were also investigated: namely small air bubbles in a turbulent water channel (chapter 7) and solid particles in a turbulent von Kármán flow (chapter 8). At this point I would also like to point out that originally only the case of water droplets in the wind-tunnel was envisaged. However due to a technical breakdown, the wind tunnel stopped operating for 12 months. The water-channel and von Kármán configurations were then considered as an alternative, with finally the added value to extend the range of parameters explored.

## 1.5 A quick overview of this thesis

This thesis is organized in two main parts. After a brief discussion of the wind-tunnel (which is the main facility used for the experiments presented in this thesis) and some key experimental techniques (chapter 2), Part I (including chapters 3, 4, 5 and 6) is dedicated to the investigation of the interaction of single objects in turbulent and laminar flows :

- Chapter 3 investigates the equilibrium and stability of a simple pendulum (with one degree of freedom) with a laminar and turbulent incoming flow. Non-trivial multi-stability and hysteresis is exhibited, as well as turbulence drag enhancement.
- Chapter 4 investigates the stability and the dynamics of towed spheres in still water, where wake instabilities are shown to develop above a certain threshold of particles Reynolds number $Re_p$, imposing an helicoidal oscillating motion of the sphere.
- Chapter 5 investigates the stability and the dynamics of spheres towed by a long cable in a high speed laminar air flow. The towing configuration is artificially reproduced by considering a fixed cable in the wind-tunnel. Measurements are achieved by Lagrangian tracking of the towed sphere. Aeroelastic instabilities (of divergence and flutter type) resulting from the coupling of the cable with the fluid are evidenced and shown to impact the sphere dynamics. Possible reminiscence of the wake instability is discussed.
- Chapter 6 considers the same system as chapter 5, with the addition of a grid generating turbulence. This situation is compared on one hand to the towed sphere in laminar conditions in chapter 5 and on the other hand to the case of freely advected finite sized spheres investigated in previous studies and in the context of Stokesian filtering mechanisms. We show that turbulence tends to smear out wake and aeroelastic instabilities and that turbulent fluctuations are effectively filtered, in agreement with usual filtering arguments.

Part II of this thesis (including chapters 7, 8 and 9) is dedicated to the investigation of collective effects and preferential concentration :

- Chapter 7 investigates the concentration field of small air bubbles in a water channel, with simultaneous measurements of the carrier velocity field. Preferential concentration is investigated using Voronoï tessellation analysis. No clustering is observed (probably because of the low Stokes number of the bubbles) and no global impact of the bubbles on the carrier turbulence is measured.
- Chapter 8 investigates the concentration field of finite size solid particles in a turbulent von Kármán flow of water, with simultaneous measurement of the carrier velocity field. Clustering is observed and characterized and possible correlation with the background flow is discussed.

- Chapter 9 investigates the concentration field of small (sub-Kolmogorov) water droplets in wind-tunnel active-grid generated turbulence. Using the active grid allowed us to cover a wider range of Reynolds number compared to previous experimental studies. We evidence clustering and carefully characterize cluster geometry. Comparing our results to clustering properties of zero-acceleration points in DNS for single-phase homogeneous isotropic turbulence, we address the relevance of the sweep-stick scenario as a possible mechanism for the observed preferential concentration of particles in our experiment. Finally we propose a new approach to reconstruct large scale concentration fields using a Taylor hypothesis, which allows us to address new questions as the super-clustering phenomenon.

# Chapter 2

# Wind tunnel

The main equipment used during this work is the low turbulence wind tunnel SFT1, located in LEGI laboratory (figure 2.1). In this chapter a brief description of this equipment will be made. For any experiment in which other equipment has been used it will be detailed specifically in the corresponding chapter.

SFT1 is a closed-return type wind tunnel with guide vanes (figure 2.2), and a measurement section of 0.75m x 0.75m x 4m (a more detailed description of this wind tunnel may be found in [57]). A closed-return wind tunnel presents several advantages (principally it reduces the length of the equipment and the energy costs), but the flow passes by four corners that have to be carefully studied. The flow is generated by an helical two-steps fan. Each propeller is powered by a continuous current motor of 37 kilowatts (max) and is composed by 7 blades that counter-rotate in a way that the downstream propeller absorbs the rotation kinetic energy transmitted to the flow by the upstream propeller. The highest rotation regime is 1280 rpm, which corresponds to $\sim$ 45 m/s. For measurement feasibility matters, the highest velocity studied in this thesis is $\sim$ 20 m/s. For all the working conditions, the fluctuation level of the flow (without any grid added) stays below 0.5%.

Each corner is provided with directing blades, that are supposed to recover the flow direction downstream. It has also been checked that these blades do not generate any asymmetry in the flow and reduce the velocity fluctuations in a way that no honeycomb panels are needed. Upstream the measurement section, the flow passes by the settling chamber and the air filters. The last step before the measurement chamber is the convergence section. This last section is squared, as the measurement section has the same form, with a contraction coefficient of 12. The resulting dimensions of the whole equipment are 16.03 m long, 5.05 m high and 2.60 m width.

Three types of flow were studied using the wind tunnel: a laminar flow,

Figure 2.1: Wind tunnel SFT1.

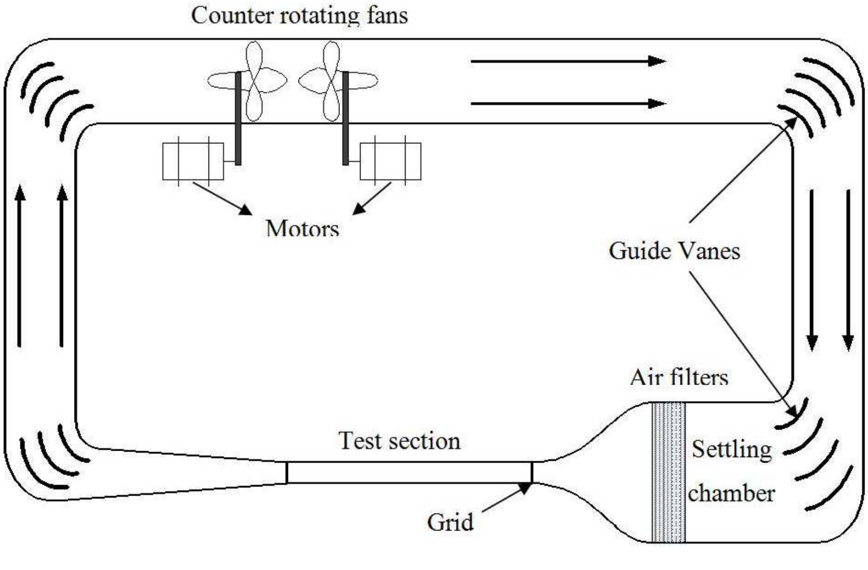

Figure 2.2: Schema of the wind tunnel $SFT1$.

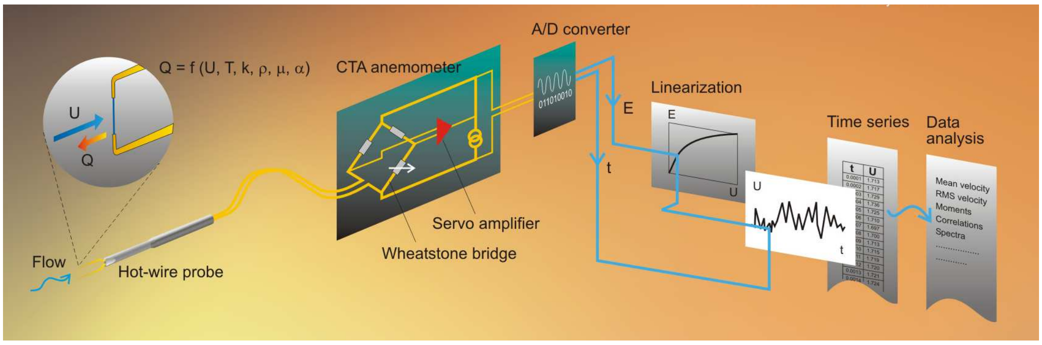

Figure 2.3: Schema of hot-wire anemometry. Image taken from [46].

a moderate turbulent flow generated with a passive grid and a highly turbulent flow generated with an active grid. Each flow has been characterised using hot-wire anemometry. In the following sections, this technique will be detailed and the properties of each flow will be explained.

## 2.1 Hot-wire anemometry

The hot-wire is still the most used system for studying turbulent flows. Its simplicity and excellent temporal resolution make it ideal for this kind of measurements. It is basically a temperature dependent resistance with a positive temperature coefficient. A schema of this technique is exhibited in figure 2.3.

The wire, with resistance $R_w$, is connected to one arm of a Wheatstone bridge and taken into the working temperature by Joule effect using constant current. The working temperature is slightly higher than that of the fluid, therefore this technique is based in the forced convection principle, with the fluid acting as a cooler. A servo amplifier keeps the bridge in balance by controlling the current to the sensor so that the resistance – and hence temperature – is kept constant, independently of the cooling imposed by the fluid. The energy transmitted by the wire to the fluid then growths with the velocity. Therefore, the voltage $V$ at the top of the bridge, proportional the the current $i$ is a function of the component of the flow velocity $U_\perp$ perpendicular to the wire. A semi-empirical relation has been obtained by King [50], which is known as King's Law:

$$V(T_e) = A^{HW}(T_e)U_\perp(T_e) + B^{HW}(T_e). \tag{2.1}$$

The constants $A^{HW}$ and $B^{HW}$ depend on the environmental temperature $T_e$ and on the properties of the wire, the flow, and the working parameters. As this parameters should also vary in time, for each series of measurements a calibration must be done. Assuring that $T_e$ remains constant during the measurements, this calibration is made using a direct velocity measurement (using a Pitot tube and a standard manometer). Using the mean value of the streamwise velocity measured and the mean value of voltage given by the hot-wire, the constants $A^{HW}$ and $B^{HW}$ are obtained.

King's Law has some limitations, as it only considers convective heat exchange between the flow and the wire, which is also considered infinitely long and perfectly cylindrical. For slow enough velocities this law is no longer valid, but in the range of velocities studied in this work the validity of King's Law has been corroborated.

The measurements are done using the same method and equipment described in [62]. A provision of attaching supports for hot-wire and pitot tube on the trolley made it possible to perform hot-wire anemometry and also allowed us to obtain the mean velocity flow fields and velocity fluctuations not only throughout the test section length but also on cross sections at different mesh distances from the grid. The anemometer used was $DISA55M01$ with a standard hot-wire with 6 $\mu m$ of diameter and 0.5 mm long.

For the laminar flow, it was corroborated that the fluctuation level, in the range from 4 to 18 m/s stays always below 0.5%, while the spectra do not exhibit any particular behavior (therefore no instabilities of the wind tunnel are observed in that range).

## 2.2 Passive grid

A passive grid consists in a set of static bars with an uniform mesh size M (figure 2.4a). It is known to produce almost ideal and isotropic turbulence between the production and the decaying regions, as shown in figure 2.5. The position of this region depends on the properties of the grid, the wind tunnel and the original flow. It is still the most used system for studying homogeneous turbulence [94], but it has the particularity that there is no turbulence production (only decaying turbulence is generated). The decaying law for passive grid turbulence is $\frac{<u^2>}{U^2} = A(\frac{x_0}{M} - \frac{x}{M})^{-n}$, where $< u^2 >$ is the variance of velocity fluctuations, $U$ is the mean flow velocity, $A$ and $n$ are the decay laws empirical constants, $x$ is the distance from the grid and $x_0$ is the virtual origin of turbulence. This last parameters depend on the streamwise velocity, so a different law is obtained for each $Re$. Besides, well developed turbulent conditions require a minimum work distance downstream the grid,

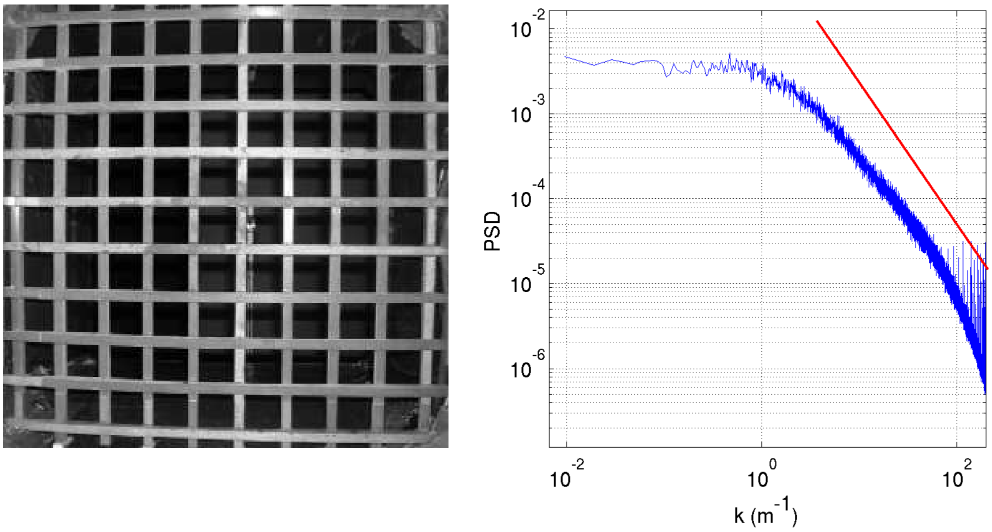

(a) (b)

Figure 2.4: (a) Photo of the passive grid used. (b) Typical spectrum obtained with it. The red solid line indicate a $k^{-5/3}$ power law.

empirically known to be of the order of $30M$. For avoiding this inconvenience, all the measurements were done in the same position, where fluctuations are almost constant and of the order of 3%.

The grid used in this work comprises of a set of 10 horizontal and 10 vertical square composite bars of 15 mm side, which were glued using epoxy resin adhesive. It resulted in a mesh size (M) of 60 mm. The solidity ratio; which is the ratio of the area occupied by the grid and the total cross section area, is 0.36. As it has already been mentioned, all the measurement were made at a fixed distance of $\sim$ 2.1 m of the grid (or $35M$). The isotropy and homogeneity of the turbulence generated at this position has been corroborated via hot-wire anemometry, while the turbulence parameters were obtained using the results in [62]. Figure 2.4b shows a typical power spectrum obtained for this grid at $U = 12.5$ m/s and $Re_\lambda = 165$, where the red line represents the five-thirds law. It is possible to observe that the inertial range of the spectrum agrees with this law (although the low value of $Re_\lambda$ results in a short inertial range). Figure 2.6 shows $Re_\lambda$ and $\eta$ as a function of velocity generated by this grid (as measured by Mazellier [62]), while the fluctuation level and the integral length scale (related to the grid mesh M) remains constant, being 3% and $L = 5.33$ cm respectively.

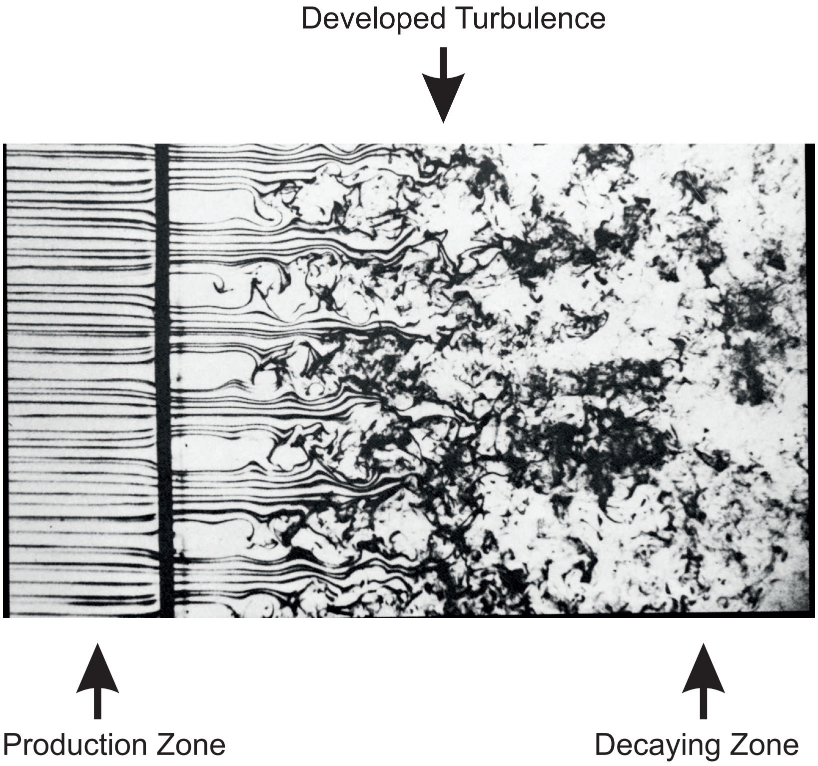

Figure 2.5: Turbulence generated downstream a passive grid (figure taken from [34]).

## 2.3 Active grid

Active grid consist in an array of moving flaps, that produce significantly higher turbulence levels than passive grids, and thus higher Reynolds number. This higher turbulence still conserves relatively good homogeneity and isotropy levels [59, 75, 93].

The grid used in this thesis is shown in figure 2.7a. It is made of 16 rotating axes (eight horizontal and eight vertical) mounted with square blades. Each axis is driven independently with a step motor whose rotation rate and direction can be changed dynamically. In the present work the active grid was driven in a triple random mode: each axis has a random rotation rate (within a prescribed range), with random rotation and both (rate and direction) may change randomly in time (within a prescribed time-lag range). In the experiments presented here, the range of prescribed rotation rate was typically between 0.5 Hz and 3 Hz and the time lag between random changes of direction and/or rate was typically between 1 and 3 seconds. Figure 2.7b shows

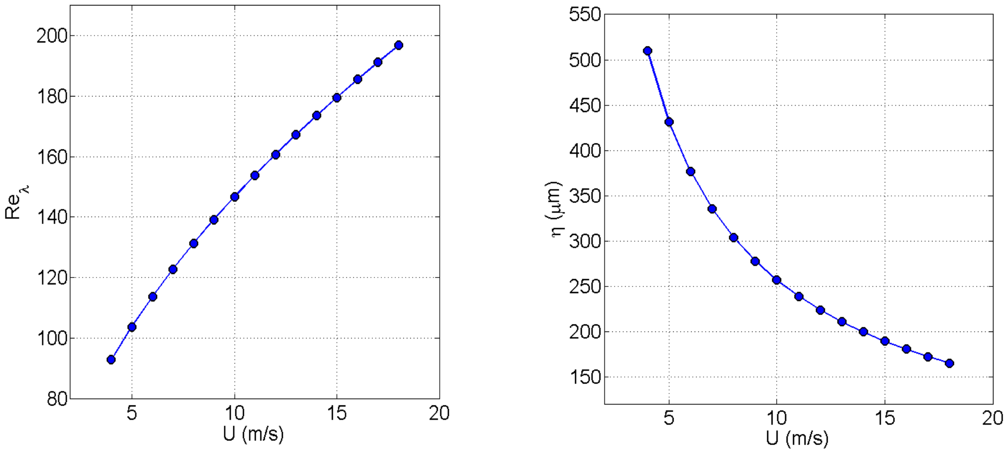

(a) (b)

Figure 2.6: Reynolds number based on the Taylor microscale (a) and Kolmogorov length scale (b) obtained for the passive grid for different streamwise velocities at $x = 2.1$ m.

a typical turbulent spectrum measured with hot-wire anemometry where a well developed inertial range can be identified, that spans for over more than two decades. A more detailed study of this device can be found in [82].

For the same reasons that have been explained before for the passive grid, all the measurements have been made in the same position ($x \sim 3$ m), where the fluctuation rate for all the $Re_\lambda$ studied remains almost constant and in the order of $\sim 20\%$. In this case, all the turbulence parameters have been obtained with hot-wire measurements.

As explained in chapter 1, the energy dissipation rate $\epsilon$ has been obtained using the second order spatial structure function $S_2(\rho)$, with $\rho$ the length scale. The spatial function is deduced from the temporal signal obtained with the hot-wire using the Taylor hypothesis. Then, $\epsilon$ is estimated as the value of the plateau of the compensated structure function: $\epsilon = (\frac{S_2}{C_2\rho_0^{2/3}})^{3/2}$, where $C_2 = 2.1$ is the Kolmogorov constant, universal for homogeneous isotropic turbulent flow [115].

Once $\epsilon$ is deduced, the usual relations are used (see [34, 94]). The Taylor length scale is $\lambda = \sqrt{15\nu < u^2 > /\epsilon}$, and therefore the Reynolds number based on the Taylor microscale is defined as $Re_\lambda = \frac{u_{rms}\lambda}{\nu}$. The Kolmogorov length scale results $\eta = (\frac{\nu^3}{\epsilon})^{\frac{1}{4}}$ while the temporal scale $\tau_\eta = \sqrt{\frac{\nu}{\epsilon}}$. Finally, the integral length scale is deduced via the spatial correlation function $R(\rho)$, resulting $\int_0^\infty R(\rho)d\rho$.

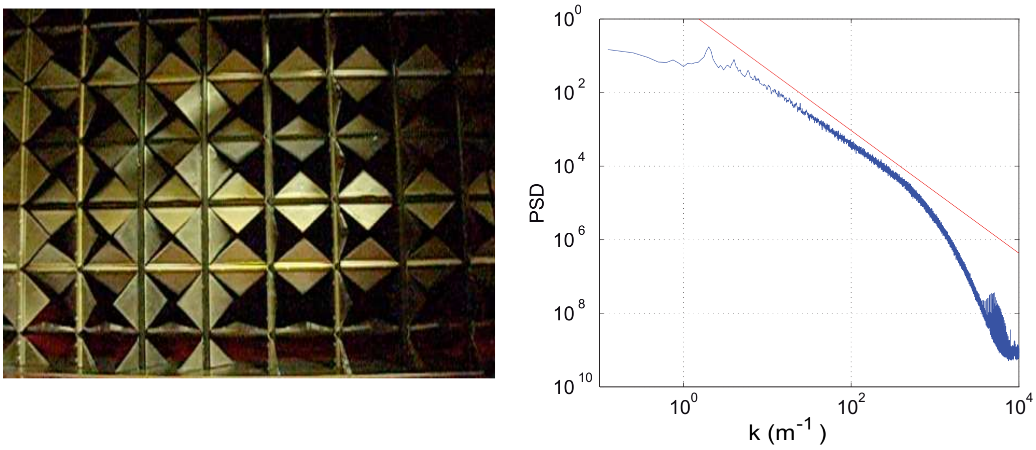

(a) (b)

Figure 2.7: (a) Photo of the active grid. (b) Typical velocity spectrum generated 3 m downstream the active grid. The red solid line indicate a $k^{-5/3}$ power law.

Figure 2.8a shows how the measured value of $Re_\lambda$ varies with the streamwise velocity. It is found to follow a power law $Re_\lambda = AU^n$, with $A = 95$ and $n = 0.71$. Figure, 2.8b represents the Kolmogorov length scale, that follows a similar law, with $A = 1 \times 10^{-3}$ and $n = -0.98$. For each other parameter a similar law was obtained and will be used to determine its values in the following chapters. As the passive grid folows the same kind of laws (figure 2.6), in table 2.1 all the power laws are shown.

| | $A_{Re\lambda}$ | $n_{Re\lambda}$ | $A_\lambda$ (m) | $n_\lambda$ | $A_\epsilon$ (m$^2$/s$^3$) | $n_\epsilon$ | $A_\eta$ (m) | $n_\eta$ | $A_{Lint}$ (m) | $n_{Lint}$ | $A_{\tau\eta}$ (s) | $n_{\tau\eta}$ |
|---|---|---|---|---|---|---|---|---|---|---|---|---|
| $PG$ | 46 | 0.50 | 0.017 | $-0.5$ | $8.0 \times 10^{-3}$ | 3.0 | $1.4 \times 10^{-3}$ | $-0.75$ | 0.053 | 0 | 0.14 | $-1.50$ |
| $AG$ | 95 | 0.71 | $9.2 \times 10^{-3}$ | $-0.38$ | 0.011 | 3.4 | $1.0 \times 10^{-3}$ | $-0.98$ | 0.070 | 0.49 | 0.057 | $-1.9$ |

Table 2.1: Fitting parameters for the principal turbulent parameters, considering a power law $AU^n$ for the passive grid ($PV$) and the active grid ($AV$).

## 2.4 Conclusion

In this section we have summarized the principal equipment used during this work and realized a brief description of hot-wire anemometry and the three types of flows studied. As this work consists of several different experiments

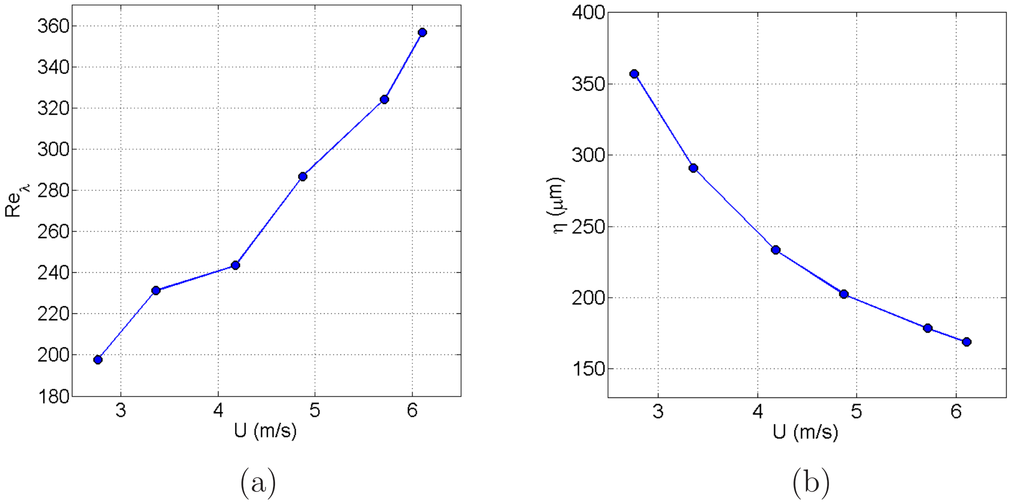

(a)

(b)

Figure 2.8: Reynolds number based on the Taylor microscale (a) and Kolmogorov length scale (b) obtained for the active grid for different streamwise velocities at $x = 3.0$ m.

performed in order to get further insight on the fluid-structure interaction, whenever the wind tunnel has been used a short description of the specific setup will be performed.

# Part I

# Single particle-flow interaction

# Chapter 3

# Pendulum in a flow

## 3.1 Introduction

The pendulum is a paradigm for many problems in physics (oscillators, resonances, instabilities, dissipative systems, etc.) which has been investigated for centuries and which remains one the most fundamental systems taught in academy. However, in spite of this popularity, the richness of this simple system is so that the topic is far from being exhausted. This is particularly the case when the coupling of the pendulum with its surrounding fluid is considered. This simple system has been chosen for starting this work because it is maybe the simplest setup possibly considered (after that of fixed objects in a flow), but at the same time it shows the complexity of fluid-particle interactions.

In a recent study, Neill *et al.* [78] have for instance investigated the role of added mass on a simple spherical pendulum, which offers an elegant framework to revisit the equivalence principle of inertial and gravitational masses. More recently, Bolster *et al.* [11] have evidenced additional *discrete* dissipative mechanisms arising on a spherical pendulum with large amplitude oscillations, due to vortex ring shedding.

These examples illustrate that non-trivial processes emerge when the pendulum is strongly coupled to fluid mechanics. In the present work we investigate further effects which appear when a pendulum faces a mean stream instead of being surrounded by still fluid. The mean flow results in additional aerodynamic forces whose first effect is to modify the equilibrium position of the pendulum as it is *dragged* and/or *lifted* by the flow. We focus here on the characterization of the equilibrium of a simple pendulum made of a circular flat plate facing a mean stream (see figure 3.1). Already in 1450, the italian mathematician Leon Battista Alberti imagined to use such a system as an anemometer, the inclination of the swing plate giving the wind velocity. Leonardo da Vinci and Robert Hooke recovered Battista's idea and built such a swing plate anemometer in 1500 and 1667 respectively. However, in spite of these early developments, although the case of fixed inclined disks and free falling plates, have received significant attention (see for instance the recent numerical studies by Auguste *et al.* [4] and by Chrust *et al.* [17] on instabilities of thin free falling disks), the study of the pendular plate configuration seems to have remained overlooked. We show in the present work that despite its apparent simplicity, this system reveals an unexpected richness including: (i) bi-stability and hysteretical behavior of the pendulum as the flow velocity is cycled up and down, (ii) influence of incident turbulence on the bi-stability and (iii) evidence of drag enhancement in highly turbulent conditions. Implications of these results are important, both from a fundamental point of view (in the context for instance of fluid-structure interactions and stochastic processes in bi-stable systems) and for practical fluid-structure interaction applications, as such swing plate systems are common elements in artificial heart valves and nuclear plant check valves among others.

## 3.2 Experimental setup

Our experiment runs in the wind tunnel described in the previous chapter (see figure 3.1). The three possible configurations of flow were investigated :

- *Laminar*, with no grid at the entrance, the velocity fluctuation rate, $\phi = \sigma_u/U$ (where $\sigma_u$ is the standard deviation of velocity fluctuations and $U$ is the average stream velocity) remains then below 0.5% ;
- *Moderately turbulent* ($\phi \simeq 3\%$) produced with the passive grid.
- *Highly turbulent* ($\phi \simeq 20\%$), with the active grid.

For each configuration, we monitor the equilibrium angle $\alpha_{eq}$ of the pendulum (using a high precision rotating angular sensor at the pendulum pivot) as a function of the mean wind velocity $U$. The pendulum is made of a thin aluminium disk (4 cm in diameter, 1 mm in thickness). The length $\overline{OD}$ between the pivot of the pendulum $O$ and the center of the disk $D$ is $\overline{OD} =$ 26 cm. The disk is connected to the pivot by a thin beveled rigid blade with negligible frontal area facing the flow. The center of mass $G$ of the system *blade+disk* is such that $\overline{OD} = 15.5$ cm. Finally we note that in the turbulent cases, the size of the disk remains smaller, but is of the order, of the energy injection scale of the flow $L_{int}$ ($L_{int} \simeq 5.3\ cm$ with the passive grid, and $L_{int} \simeq 15$ cm with the active grid).

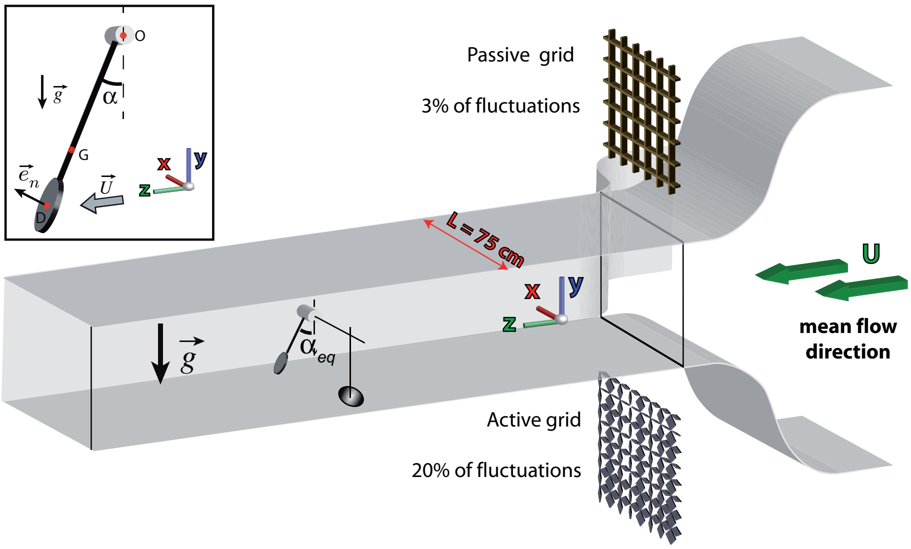

Figure 3.1: The experiment runs in the wind tunnel. Explored velocities range between 1 m/s and 20 m/s with a turbulent velocity fluctuation rate $\phi < 0.5\%$. A grid can be inserted at the entrance of the test section to increase the level of turbulence. The pendulum is located far downstream the entrance of the test section where the turbulence generated was verified to be well developed with good homogeneity and isotropy properties. The top left inset details the pendulum. It is made of a thin aluminum circular plate (4 cm in diameter, 1 mm in thickness) connected to the pivot axis $Ox$ by a thin beveled rigid blade with negligible frontal area facing the flow. $G$ denotes the center of mass of the system *disk + blade* and $D$ the center of the disk.

## 3.3 Results

### 3.3.1 Laminar case

Figure 3.2 shows the equilibrium angle of the pendulum in the laminar case (no grid in the wind tunnel) as a function of flow velocity, when the wind speed is cycled up and down. When the wind velocity is increased from rest, the equilibrium angle of the pendulum naturally increases as the plate is dragged by the flow (dark blue triangles pointing up, △). An abrupt transition from a low equilibrium branch to an upper equilibrium branch is observed for a critical velocity $U_{\uparrow}^{lam} \simeq 11.2$ m/s, where $\alpha_{eq}$ suddenly jumps from around 50° to around 65°. If we now start from a high speed configuration and the wind velocity is decreased starting from the upper branch (light blue triangles pointing down, ▽), a hysteretical behavior is observed: the reverse transition back towards the lower branch occurs for a lower critical velocity $U_{\downarrow}^{lam} \simeq 10$ m/s, where the equilibrium angle suddenly drops from around 60° to around 45°. As a result, the pendulum is found to be bi-stable for wind velocities in the range $10 - 11.2$ m/s, with an equilibrium position which depends on the history path of the system. We also observe a narrow band of forbidden angles which are never explored by the system.

### 3.3.2 Origin of the bi-stability

We will show that this peculiar behavior can be understood in aerodynamic terms, from the angular dependency of the normal drag coefficient $C_N$ of an inclined disk. $C_N$ is defined such that the aerodynamic force acting on the plate is $\vec{F}_{aero} = \frac{1}{2}\rho_{air} C_N S_D U^2 \vec{e}_N$, with $\rho_{air}$ the density of air, $S_D = \pi D^2/4$ the area of the disk and $\vec{e}_N$ the normal vector on the downstream face of the plate (see inset in figure 3.1). Figure 3.3a shows reference measurements of $C_N$ by Flachsbart [33] (note that in the present study as in [33] Reynolds number based on disk diameter $Re_D = UD/\nu$ exceeds $10^4$, hence aerodynamic coefficients are assumed not to depend on $Re_D$). Figure 3.3a shows that the angular dependency of $C_N$ exhibits a sharp discontinuity at a critical angle $\alpha^{stall} \simeq 51°$. This corresponds to the *stall* transition of the plate: when the *normal drag* coefficient is split into the *drag* ($C_D = C_N \cos(\alpha)$) and *lift* coefficients ($C_L = C_N \sin(\alpha)$), as shown in figure 3.3a, it becomes clear that for large inclinations $\alpha > \alpha_{stall}$ (*i.e.* for low angles of attack), *lift* dominates *drag* and *vice versa*. *Lift* is maximal for $\alpha \gtrsim \alpha^{stall}$, where the disk is somehow in a *flying* configuration. $C_L$ abruptly drops when $\alpha$ decreases below $\alpha^{stall}$ (until it vanishes when the plate is perpendicular to the flow at $\alpha = 0°$). For low inclinations (*i.e.* large angles of attack) *drag* dominates

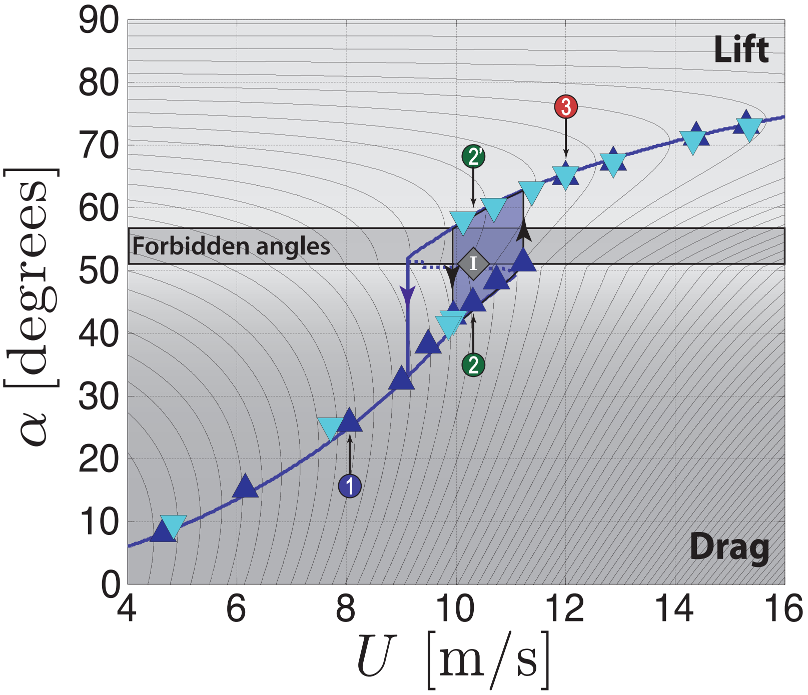

Figure 3.2: Equilibrium angle measured experimentally for increasing (dark blue △) and decreasing (light blue ▽) wind velocity. Lines in the background represent iso-contours of the total potential energy of the system (gravity + aerodynamic) as further illustrated in figure 3.3c. The blue solid line indicates the prediction of the stable equilibrium angle from the path of local minima of total potential energy. Labeled points corresponds to the equilibrium analysis discussed in figure 3.3. Dark gray bottom region indicates low inclination states (namely $\alpha < \alpha^{stall}$) where aerodynamic force is dominated by drag, while light gray upper region indicates high inclination states, where lift dominates.

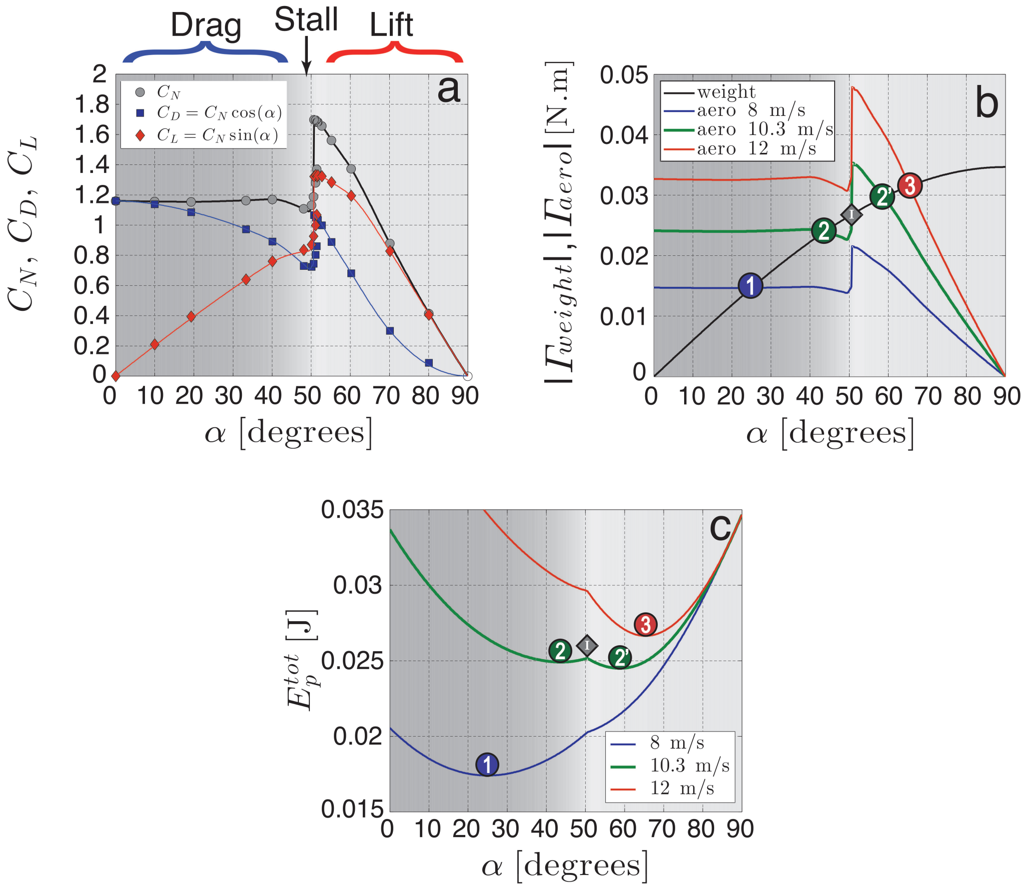

Figure 3.3: (a) Reference static measurements of *normal drag* coefficient $C_N$ for an inclined static circular cylinder as a function of inclination angle (gray circles) ; data is taken from [33]. Blue squares and red diamonds show the corresponding *drag* ($C_D$) and *lift* ($C_L$) coefficients. (b) Modulus of the moment of of gravity and of aerodynamic forces on the pendulum for three different wind velocities as a function of the inclination angle of the pendulum. Intersection points indicate equilibrium positions. (c) Total potential energy of the pendulum as a function of inclination angle.

*lift*.

In the sequel we shall therefore speak of *drag* dominated states when $\alpha < \alpha^{stall}$ and of *lift* dominated states when $\alpha > \alpha^{stall}$. Such a *stall* transition has been extensively studied in aeronautics as it is a major concern for airfoil design [41]. Its physical origin, which goes beyond the scope of this thesis, is a complex (though relatively well understood) fluid mechanics problem related to massive flow separation at the backside of the plate (or airfoil). We point however that, contrary to the case of certain aeronautic airfoils (see for instance [74, 67]), the *stall* transition for a flat circular plate does not exhibit any noticeable hysteresis when the inclination angle is cycled up and down at constant velocity. The hysteretical behavior observed here for the pendulum is therefore not related only to aerodynamics. It actually relies on the additional angular degree of freedom of the pendular system, whose equilibrium angle $\alpha_{eq}$ self adjusts to ensure the balance between the moment of aerodynamic force ($\vec{\Gamma}_{areo}$) and that of gravity ($\vec{\Gamma}_{weight}$):

$$\vec{\Gamma}_{areo} = \frac{1}{2}\rho_{air} S_d C_N(\alpha) U^2 \overline{OD} \cos\alpha \, \vec{e}_x, \tag{3.1}$$

$$\vec{\Gamma}_{weight} = -mg\overline{OG} \sin\alpha \, \vec{e}_x. \tag{3.2}$$

Figure 3.3b shows the modulus of the aerodynamic moment acting on the pendulum for three different wind velocities $U$ and that of gravity (which is independent of flow velocity), as a function of inclination $\alpha$. The quantitative estimation of the aerodynamic moment requires to know the actual angular dependency of the normal drag coefficient $C_N(\alpha)$: the reference measurements from Flachsbart [33] (shown in 3.3a) have been used for this purpose. Depending on the flow velocity, gravity and aerodynamic curves can have one or multiple intersection points meeting the equilibrium condition $|\Gamma_{aero}| = |\Gamma_{weight}|$. For low velocities, they intersect only once for $\alpha_{eq}^1 < \alpha_{stall}$ (point labeled " 1 " in the figure) and the equilibrium results mainly from a *drag vs gravity* balance. For large velocities, the intersection occurs for $\alpha_{eq}^3 > \alpha_{stall}$ (point labeled "3") and we have essentially a *lift vs gravity* equilibrium. For intermediate velocities, three intersection points exist: one at $\alpha_{eq}^2 \lesssim \alpha_{stall}$ (labeled " 2 "), one at $\alpha_{eq}^{2'} \gtrsim \alpha_{stall}$ (labeled " 2' ") and one at $\alpha_I \simeq \alpha_{stall}$ (labeled " I "). This situation corresponds to the range of bi-stability reported in figure 3.3a, where points " 2 " and " 2' " are two stable states (respectively on the *drag* and *lift* branches) and point " I " corresponds to an unstable equilibrium position of the pendulum close to the stall angle. This bi-stability scenario can be rewritten in terms of a two potential wells system, based on the total potential energy of the pendulum $E_p^{tot}(\alpha) = E_p^{weight}(\alpha) + E_p^{aero}(\alpha)$, where $E_p^{weight}(\alpha)$ is the gravity potential energy and $E_p^{aero}(\alpha)$ is the potential energy associated to aerodynamic force.

$$E_p^{weight}(\alpha) = mg\overline{OG}\sin\alpha, \tag{3.3}$$

$$E_p^{aero}(\alpha) = -\frac{1}{2}\rho_{air}S_dU^2\overline{OD}\int_{\alpha}^{\pi/2} C_N(\alpha')\mathrm{d}\alpha'. \tag{3.4}$$

Note that aerodynamic potential energy $E_p^{aero}(\alpha)$ is defined so to be zero when the pendulum is aligned with the mean stream (*i.e.* $\alpha = \pi/2$) which would be the natural equilibrium position in absence of gravity. Figure 3.3c shows the total potential energy $E_p^{tot}(\alpha)$, as a function of inclination $\alpha$, for the same three velocities for which balance of moments has been analyzed in figure 3.3b. It shows that for the lower velocity only one potential well defines the stable *drag* dominated angular position of the system and that for the higher velocity only one potential well defines the stable *lift* dominated angular position. For the intermediate velocity two stable potential wells coexist with an unstable equilibrium (local maximum of $E_p^{tot}$) in between. For a more complete analysis, we show in figure 3.2 the iso-contour lines of the total potential energy in the $\alpha - U$ parameter space. Experimental measurements of equilibrium angle are found to lie almost perfectly on the path of local potential minima (emphasized by the solid line). The range of bi-stability is also well predicted by the two potential wells description, although the predicted hysteretical cycle is broader than what is experimentally observed. In particular the experimental transition from the *lift* branch down to the *drag* branch (when velocity is decreased below $U_{\downarrow}^{lam}$) occurs sooner in the experiment compared to the theory. This sooner transition results in an intrinsic narrow band of *forbidden* angles between approximately 51° and 57°, which are never explored by the pendulum in the experiment. The reason of the anticipated *lift* to *drag* transition remains unexplained. First analysis of the pendulum fluctuations (see figure 3.10b), based on measurements of the standard deviation of the angular position of the pendulum, $\sigma_\alpha$, indicates that fluctuations in the laminar case are small ($\sigma_\alpha < 1$ degree in general and $\sigma_\alpha \simeq 0.1$ degree in the *lift* branch). It is therefore unlikely that fluctuations do activate here the anticipated departure from the *lift* branch. A possible explanation may be related to finite thickness effects (the thickness-over-diameter ratio of our plate is of the order of $4{\cdot}10^{-2}$) which may not be completely negligible when the edge of the plate faces the flow (as it is for the lifted case) and which may affect the stall transition compared to the reference measurements by Flachsbart [33] who considered a plate with aspect ratio below $10^{-2}$. Recent numerical studies by Auguste *et al.* [4] have shown for instance that such finite thickness effects still affect the free falling dynamics of flat disks with thickness-over-diameter ratios of the order of $10^{-1}$.

Further experiments with different plate thicknesses will be carried to explore such possible effects on the pendular system.

## 3.4 Numerical simulations

Computational Fluid Dynamics simulations, using ANSYS Fluent has been performed in order to get further insight on the system. As the experimental setup only allows us to define the aerodynamic forces normal to the pendulum, numerical simulations would permit us to better understand the behavior of the aerodynamic coefficients, the properties of the boundary layer and the flow affected by the disk. Note that we do not solve the dynamical motion of the pendulum, but simply characterize the aerodynamic forces and flow properties for the case of a steady inclined disk, where the angle of the plate and the velocity of the flow are adjusted to coincide to the equilibrium positions of the pendulum in the experiment.

For each angle, a coarsed DNS simulation has been made. Such simulations in a three-dimensional domain are extremely expensive, therefore only a laminar inflow has been considered.

Figure 3.4a shows the domain reproduced, where the domain has a length of 1 m and a squared section of $0.2 \times 0.2$ m$^2$ (the dimensions of the blob has been respected). The boundary condition at the blob and domain's lateral walls was no-slippage. The mesh cells number $N$ has been limited by the resources available in the workstation used, being $N \sim 4 \times 10^6$ cells (figure 3.4b). In a first step, in order to validate the model and the domain used, the well known problem of the circular plate perpendicular to the flow has been studied ($\alpha = 0$).

Figure 3.5 shows the velocity magnitude obtained for two different $Re$, where it can be seen that simulations are qualitatively well converged. Figure 3.5a shows the results for $Re = 0.1$, where the boundary layer appears to be well converged and is found to remain stationary and attached to the disk. Figure 3.5b shows the same magnitude for $Re = 1 \cdot 10^5$, where the boundary layer has clearly detached and the flow becomes unstationary and turbulent.

Figure 3.6 shows the drag coefficient resulting for 9 different $Re$ and the values compiled in reference [41]. Both curves are close, with some differences in the low $Re$ region, probably caused by boundary effects at low $Re$ (that can be clearly appreciated in figure 3.5a) at the walls. As all the experiments have been run for $Re > 1 \cdot 10^4$, where both curves present almost perfect agreement, we will consider that this simulations are properly resolved for our purposes.

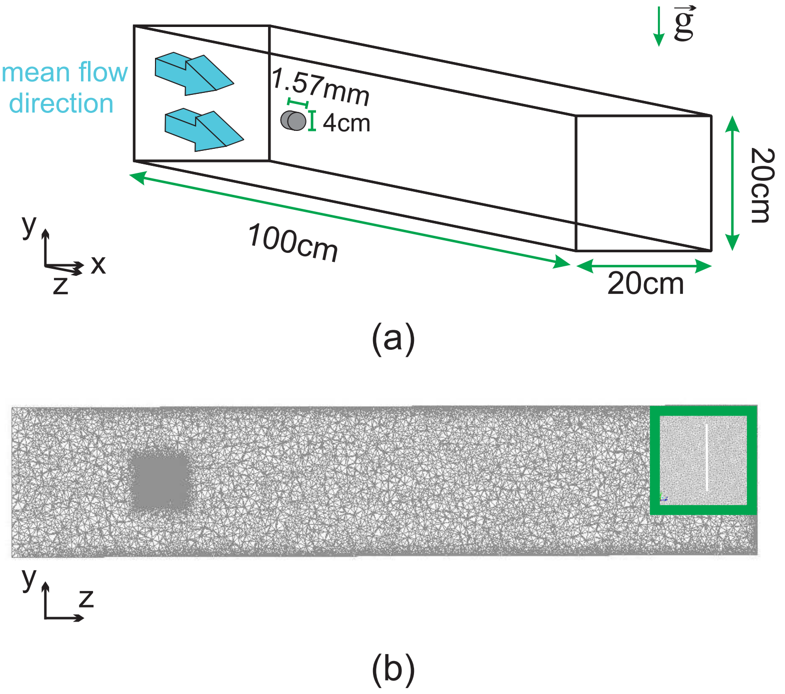

Figure 3.4: (a) Domain performed in Gambit for simulations. (b) Mesh in the $y0z$ plane, where a second cubic domain has been done for better resolving the zone adjacent to the pendulum (see inset of figure).

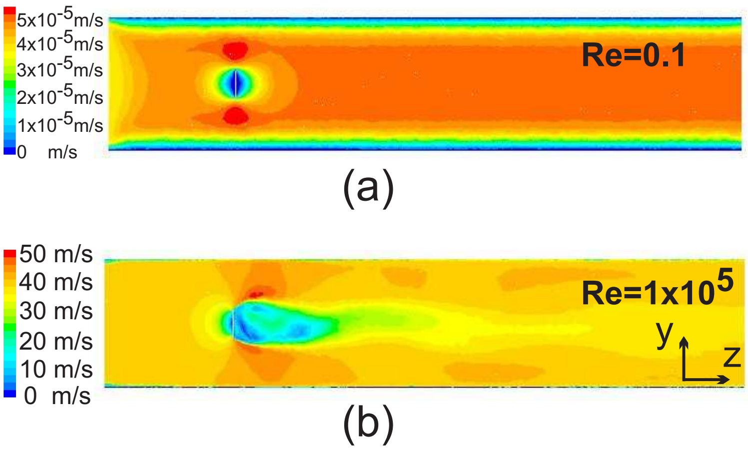

Figure 3.5: Velocity magnitude obtained for $Re = 0.1$ (a) and $Re = 1 \times 10^5$ (b).

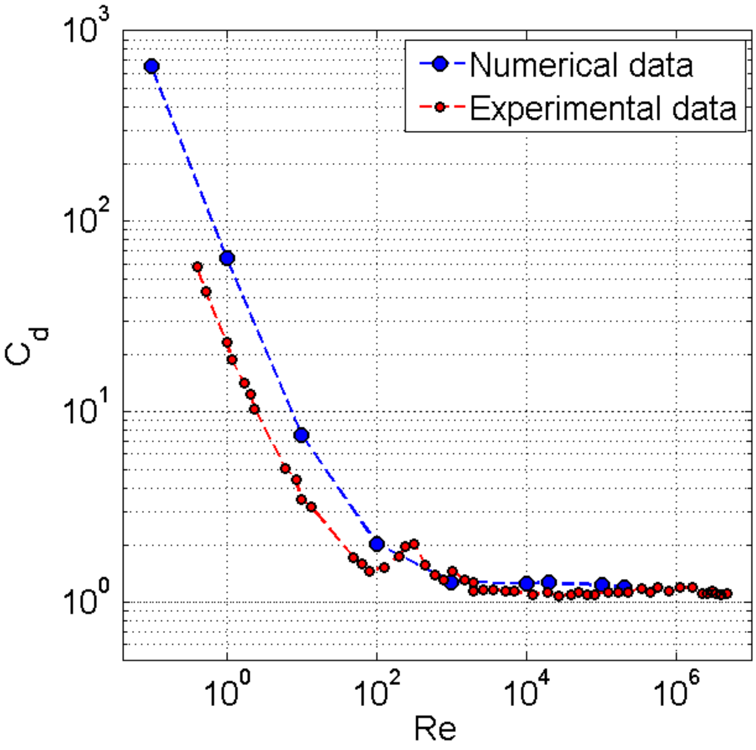

Figure 3.6: Drag force as a function of *Re*, for the results from ANSYS Fluent (blue line) and the experimental results compiled in [41] (red line).

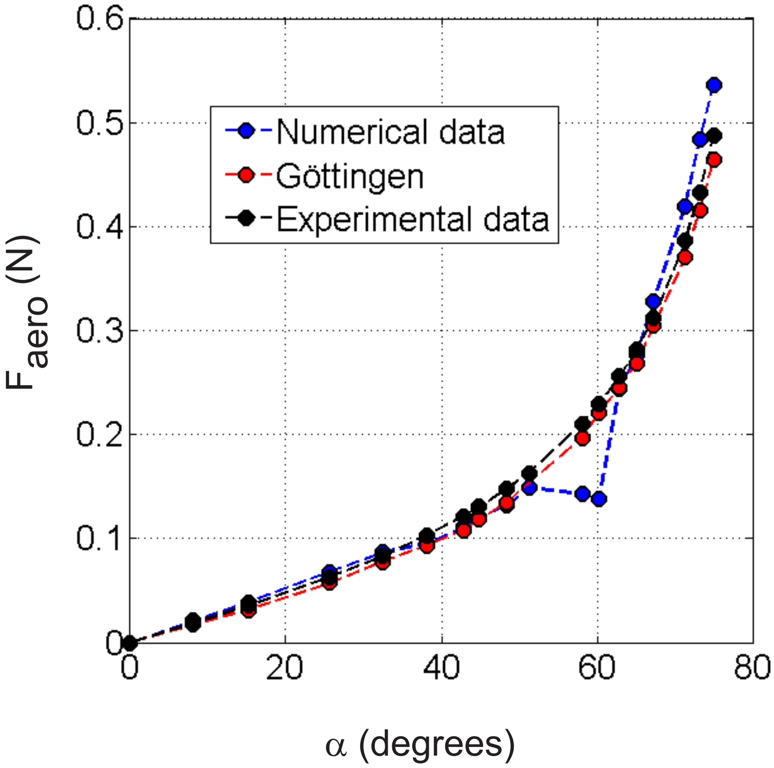

Figure 3.7: Comparison of the aerodynamical force obtained numerically (blue line), measured in reference [33] (red line) and obtained experimentally in this work (black line).

### 3.4.1 Inclined plate

Having well described the canonical problem of the disk facing the flow, the studied situation of the inclined angle has been simulated. The same parameters as in the previous section have been used, with the same number of mesh cells. Only a static situation has been reproduced, where the streamwise velocity and the angle are chosen according to the experimental results shown in figure 3.2. Therefore, the only parameter that can be compared is the force $F_{weight}$ (or equivalently $C_N$) of the experiments with $F_{aero}$ of the simulations. Figure 3.7 shows this force, where the blue line represents the simulations, the black line the experimental results and the blue one the results from reference [33] (interpolated for our working conditions). The numerical results are in a very good agreement, with the exception of two points, near $\alpha_{stall}$, which are clearly unresolved.

Better insight of the phenomenon can be obtained with the velocity pro-

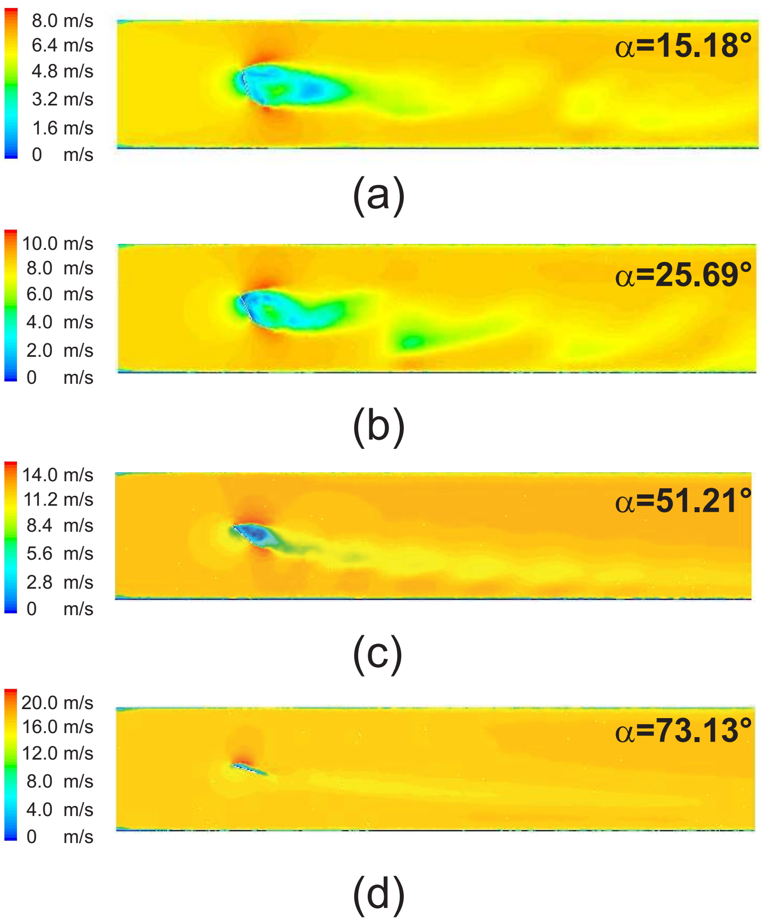

Figure 3.8: Velocity magnitude obtained for $\alpha = 15.18°$ (a), $\alpha = 25.69°$ (b), $\alpha = 51.21°$ (c) and $\alpha = 73.13°$

files. In figure 3.8 the velocity magnitude for different situations is exhibited. Figure 3.8a shows this parameter for $\alpha = 15.18°$, where the boundary layer is clearly defined, while some shedding is also observed. Figure 3.8b shows a similar scenario, with stronger vortices expelled from the disk. For 51.21° (figure3.8c), an angle at the limit of the drag–lift transition observed experimentally, we observe a strong vortex shedding, with a well characterized frequency (of the order of 90 Hz). This type of oscillations are well known in the drag–lift transition and other boundary layer detachment processes (for instance see [106]). Finally, for $\alpha = 73.13°$, no shedding is observed, while the boundary layer is clearly detached (although it does not seem to derive in a turbulent zone as in figure 3.8b).

The coefficients derived from the simulations are shown in figure 3.9. As expected, they agree with the results from Flachsbart [33], with desaveniencies in the detachment angles.

The numerical reconstruction of the flow around the plate therefore suggests that vortex shedding effects, which appear near the hystererical range, probably play an important role in the transitions between lift and drag branches. An interesting aspect to be investigated in the future is whether a resonance effect may occur when the frequency of the shedded structures approaches the natural frequency of the pendulum. We expect such resonances to have an important effect on the hysteresis cycle, as amplified resonant oscillations may promote the transition of the system between drag and lift potential wells.

Finally, it is interesting to note that simulations for the static plate are much harder to converge in the vicinity of stall. The complexity of the wake of the plate in this situation would very likely require simulations with much higher resolution.

## 3.5 Influence of turbulence intensity

We consider now the influence of enhanced free stream turbulence on the pendulum equilibrium in the experiment. Figure 3.10a shows that a few percent of turbulence level (achieved with the passive grid) already has a measurable effect : while the drag branch remains almost unchanged compared to the non turbulent case, the lift branch is slightly decreased to lower equilibrium angles, and the bi-stability range is significantly reduced. Figure 3.10c shows the corresponding angular dependency for the *normal drag* coefficient $C_N(\alpha)$, inferred from the measurements of $\alpha_{eq}(U)$ by writing the equilibrium condition $\vec{\Gamma}_{aero} = \vec{\Gamma}_{weight}$ (from eq. (3.1) and eq (3.2)) parametrized by $U$:

$$\begin{cases} \alpha = \alpha_{eq}(U), \\ C_N(\alpha) = \frac{2mg}{\rho_{air} S_d U^2} \frac{\overline{OG}}{\overline{OD}} \tan\alpha, \end{cases} \tag{3.5}$$

(the solid line in figure 3.10c recalls the reference measurements of $C_N(\alpha)$ by reference [33] previously discussed for the case of a *laminar* incident flow). At small inclinations ($\alpha < \alpha^{stall}$), a few percent of turbulence marginally affects the drag coefficient, consistently with previous results for plates normal to the flow (see for instance ([41]). At large inclinations on the contrary ($\alpha > \alpha^{stall}$) aerodynamic lift is reduced up to 8% compared to the *laminar* case. Regarding the hysteresis and bi-stability reduction, we find it to occur through an anticipated *drag* to *lift* branch transition compared to the

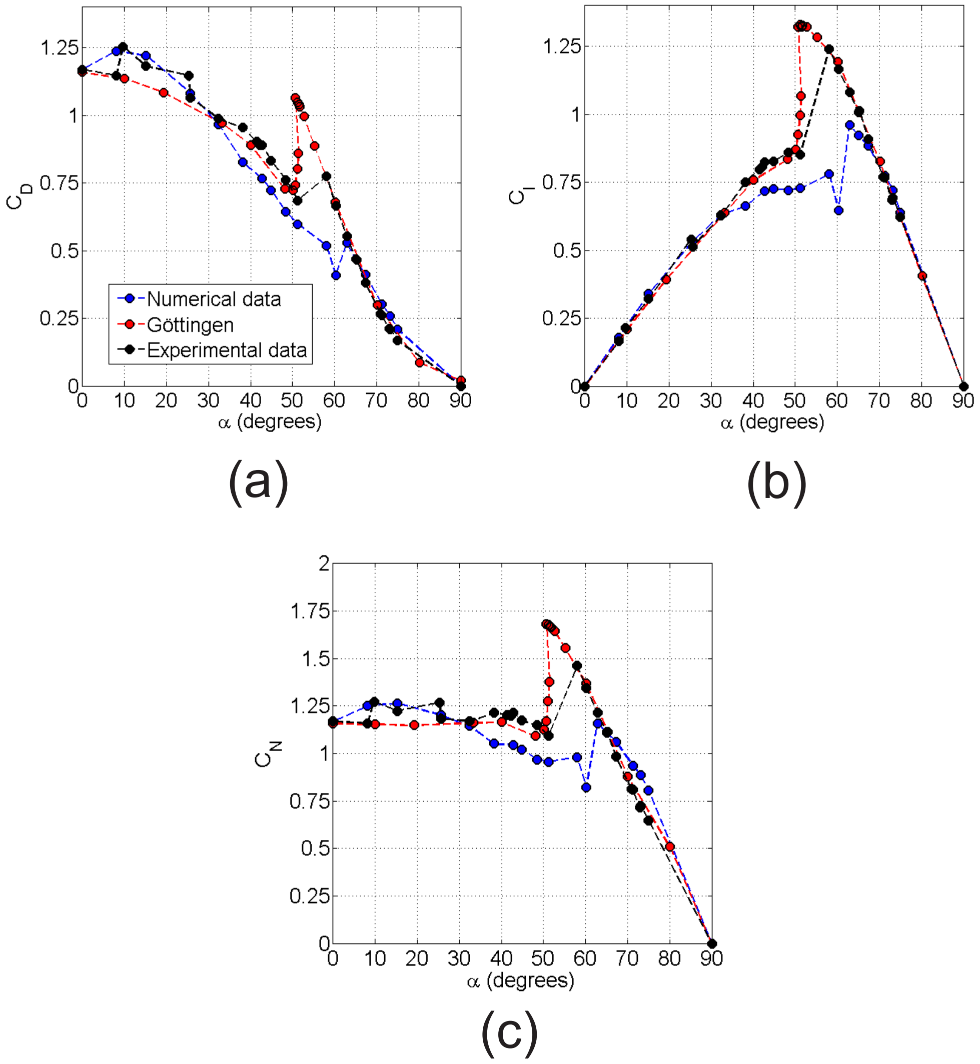

(a) (b)

(c)

Figure 3.9: Aerodynamical coefficients $C_D$ (a), $C_l$ (b) and $C_N$. In all the figures the blue line is for the results obtained with ANSYS Fluent while the red line are the experimental results from reference [33]

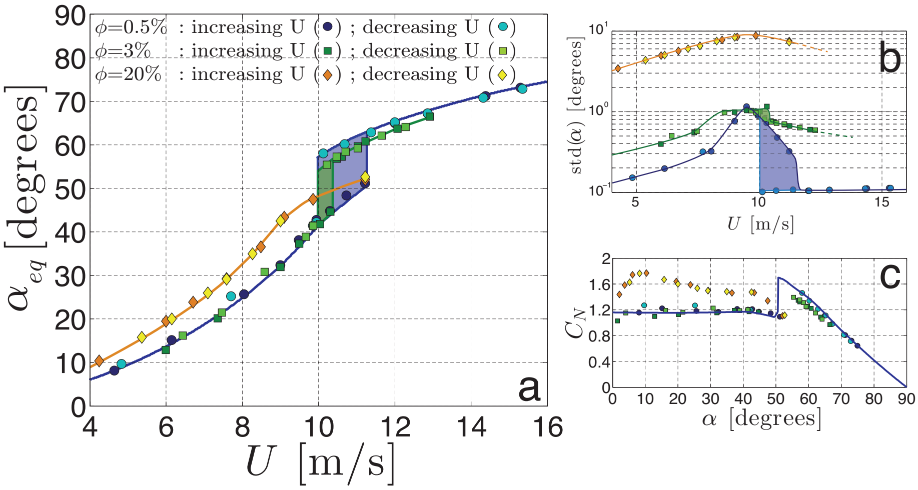

Figure 3.10: (a) Average angular equilibrium position of the pendulum as wind velocity is increased and decreased for the three different levels of turbulence ($\phi$) explored. Blue and green coloured surfaces emphasize the hysteretic cycle for the laminar and moderate turbulence cases respectively. (b) Corresponding standard deviation of the fluctuations of the angular position of the pendulum. (c) Angular dependency of normal drag coefficient of the plate estimated from the angular average position of the pendulum $\alpha_{eq}$. The blue solid line recalls the laminar static measurements of $C_N$ by Flachsbart [33] already shown in figure 3.3a.

laminar case ($U_{\uparrow}^{turb} < U_{\uparrow}^{lam}$), while the decreasing transition is unaffected by turbulence ($U_{\downarrow}^{turb} \simeq U_{\downarrow}^{lam}$). The anticipation of the *drag* to *lift* transition is very likely activated by the enhanced turbulent fluctuations of the pendulum. This should be discussed together with figure 3.10b and with the green curve in figure 3.3c which represents the laminar two potential wells landscape near $U_{\uparrow}^{turb} \simeq 10.3$ m/s. We assume as a first approximation that turbulence acts as an additive noise on this unmodified potential landscape (although strictly speaking, we know that the potential energy in the *lift* branch is slightly modified due to the reduction of the lift coefficient previously mentioned). It can be seen in figure 3.3c that the drag potential well is very shallow at 10.3 m/s, hence the escape from this well can be easily activated by enhanced fluctuations. Besides, the inspection of the standard deviation of the pendulum angular position (figure 3.10b) in the moderate turbulence case shows that at this same wind velocity, $\sigma_{\alpha}$ is about 50% larger than in the laminar case. Regarding the *lift* to *drag* transition, figure 3.10b shows that the fluctuation level in the turbulent *lift* branch is comparable to that of the laminar *drag* branch in the vicinity of the turbulent hysteretical cycle. Considering that, as shown in figure 3.3c, the *lift* potential well is deeper than the *drag* potential well at $U_{\uparrow}^{turb} \simeq 10.3$ m/s (this asymmetry has been checked to prevail even if the potential energy is estimated using the reduced lift coefficient), and that no escape from the *drag* potential well has been observed in the laminar case at this wind speed, it is reasonable that for a similar level of fluctuations the pendulum does not escape from the *lift* potential and hence $U_{\downarrow}^{turb} < U_{\uparrow}^{turb}$. It is however important to stress at this point that a more complete understanding of the role of fluctuations on the hysteretical behavior requires a more detailed statistical analysis, taking in consideration not only the standard deviation of fluctuations, but also higher moments, as the skewness (which characterize the asymmetry of the fluctuations) and the flatness (to investigate the possible occurrence of strong intermittent events) which may play a crucial role in transition processes between the two potential wells. Such a detailed investigation will be addressed in forthcoming studies.

When the turbulence level is further increased up to $\phi = 20\%$ (with the active grid) the scenario drastically changes. No clear transition between a *drag* branch and a *lift* branch is visible anymore and, bi-stability and hysteresis have disappeared. Due to mechanical power limitations, the wind speed could not be pushed above 11 m/s with the active grid operating. Therefore we cannot be conclusive regarding a possible transition toward a *lift* branch at higher wind velocities ; however this seems unlikely, considering that at 11 m/s the transition was already observed for $\phi = 3\%$. The high turbulence case also exhibits a significant increase of the equilibrium angle of the *drag* branch compared to lower turbulence cases. This corresponds to a significant increase of *normal drag* coefficient $C_N$, up to 50% as shown in the inset of figure 3.10. As for the moderate turbulence case, it is enlightening to consider the fluctuations of the pendulum, reported in figure 3.10b. It can be seen that the standard deviation of these fluctuations is now one order of magnitude larger. It attains values as large as 10 degrees. The amplitude of the fluctuations is therefore comparable to the angular extent of the hysteresis cycle reported in the laminar case, which is therefore completely smeared out. Further experiments are planned, where much longer time series will be recorded, in order to improve the statistical description of the pendulum fluctuations. An important aspect to be addressed concerns the question if the laminar bi-stability and hysteresis may remain reminiscent as a broad bi-modal distribution of the pendulum fluctuations or if on the contrary the dramatic change of the turbulent drag coefficient has killed all reminiscence of the laminar features.

### 3.5.1 Discussion

Our results are worth being briefly discussed in the context both of fundamental aspects of bi-stable systems and of practical implications for hydro and aerodynamic issues. Concerning the first aspect, our system offers a simple experimental model for the investigation of fundamental properties of bi-stable and hysteretical processes. In particular, it has the capability to simply address questions related to stochastic processes in bi-stable systems, what remains an active field of research and an archetype model for many problems in physics, chemistry, geophysics and biology ([124]). In the present work for instance turbulence plays the role of *noise*. In the moderate turbulence case ($\phi = 3\%$), velocity fluctuations mostly act as an additive noise on the aerodynamic force acting on the disk ($F_{aero} = 1/2\rho C_N S_d U^2$), as small velocity fluctuations can be linearized with respect to the perturbation $\phi << 1$. Turbulence can then be regarded as a heat bath where the reduction of hysteresis reported in figure 3.10 illustrates the thermal activation ([52, 124]) induced by additive noise which increases the escape probability from one potential well to the other. The case of high turbulence level is more complex and cannot be simply linearized as an additive noise. Multiplicative effects (resulting in fluctuations of the energy barrier itself between potential wells) are very likely involved, and require further investigations.

From the aero/hydro-dynamic point of view, learnings from this simple experiment are also rich. As already discussed from the inset of figure 3.10, the angle of equilibrium of the pendulum gives a direct measurement of the *normal drag* and hence of the *lift* and *drag* coefficients of the inclined plate. The impact of turbulence on such coefficients in general remains an open question with direct energetic and structural implications in aeronautics, civil engineering and turbulent transport phenomena. While evidence of lift reduction by turbulence is well documented in airfoil research literature, the impact of turbulence on drag remains debated. Numerical studies on the drag coefficient of a sphere are for instance controversial as Bagchi *et al.* [5] report that mean drag is not affected by turbulence intensity, while more recent studies by Homann *et al.* [43] report a significant enhancement of drag with increasing turbulence intensity. Though the quantitative values of lift reduction and drag enhancement by turbulence reported in the present study may change for other geometries than an inclined disk, our measurements reveal the necessity of a careful consideration of turbulent effects for instance in architectural design, spoiler conception and vehicle aerodynamic optimization. Besides, our results directly concern fluid-structure interaction (FSI) properties of flat pendular systems, which are common in many applications, including spoilers, industrial check valves and artificial heart valves. The fact that their equilibrium is bi-stable have important practical implications. For instance, pendular plate anemometers, as imagined by Alberti, da Vinci and Hooke, become intrinsically ineffective as in the bi-stable range, the angle of the pendulum is not univocally related to flow velocity. But beyond this, incorporating the bi-stability mechanism in FSI analysis may significantly improve the understanding and predictability of such systems. This is particularly important for the design of tilting disk and swing check valves, which are crucial elements of nuclear plant security systems ([58, 63]), but also of prosthetic heart valves ([40, 112]). Bi-stability implies an intrinsic limitation of *static* FSI models, and the requirement of a dynamic modeling, to properly account for the history of the system, as the flow rate in the valve cycles up and down. With this respect, the pendular system investigated here, also gives a simple and quantitative benchmark to test the accuracy of FSI models. Alternatively, the two-well potential approach gives a possible strategy to replace complex and computationally expensive dynamical FSI simulations by an empirical model based on static macroscopic data of the angular dependency of hydro/aerodynamic coefficients, which may be relevant to investigate valve dynamics and stability. Finally our results also show how design strategies may include possible effects of fluctuations which can help reducing hysteresis or improving the opening of the valve at low flow rates as a result of turbulent drag enhancement.

Numerical simulations in Fluent supports the scenario described, with a leading role of wake structures near stall, adding some interesting relation with boundary layer shedding and bistability.

## 3.6 Conclusion

To summarize, we have evidenced the bi-stability and hysteresis of a flat pendulum facing a flow. We have given a quantitative interpretation of the phenomenon (for the case of a laminar incident flow) where the complex hydrodynamical interaction of the plate with the fluid is reduced to a simple two potential wells model mainly defined by the plate normal drag coefficient. The academic attractiveness of the pendulum paradigm makes this configuration ideal for pedagogical purposes as well as for fundamental researches on stochastic processes in bi-stable systems. Present work has focused only on the quasi-steady equilibrium of the pendulum, but much remains to be done regarding to dynamical features and fluctuations. We will for instance carry further experiments (with very long temporal recordings), to monitor the dynamics of the *noisy* pendulum in the vicinity of the bi-stable range, in order to better quantify the actual impact of fluctuations on the transition between branches and to extract escape time statistics. This question, known as Kramers problem ([52]), remains a classical problem of stochastic multi-stable systems. An interesting point to be addressed in our particular configuration concerns the influence of specific properties of the forcing *noise*. In the laminar case resonant effects between periodic structures shedded downstream the plate and natural oscillations of the pendulum, may for instance be important. In the turbulent case, we expect transitions between the two stable states to be also affected by time-correlation properties of turbulence (which define the *color* of the imposed noise, but also by spatial-correlation effects (related for instance to the ratio between the integral scale of the surrounding turbulence and the size of the pendulum) as well as by intermittency effects. Beyond the present configuration where additive noise is introduced by moderate turbulence, the versatility of our system allows to investigate the influence of several parameters, such as amplitude and color of noise (which can be simply introduced by a controlled random mechanical forcing of the pendulum), but also of the shape of the potential well itself (which can be tailored by adding a torsional spring or a magnetic force for instance). The ability of the bi-stable pendulum to undergo stochastic resonance will also be investigated.

# Chapter 4

# Instabilities on a sphere towed at constant speed

## 4.1 Introduction

In the previous chapter the study of the stability of a pendulum strongly coupled with the surrounding fluid was made. It was already an extremely rich and complex problem that indeed would need further study that exceeds the scope of this work. The next step for studying the nature of fluid-particle interactions would be to analyze a dynamical case. We investigate here the case of a spherical particle towed at constant speed.

The dynamics of towed objects in a fluid environment is of interest for many practical situations. For instance acoustic streamers, where a sonar array is towed at the tip of a long cable attached to a ship or a submarine are commonly used to detect and analyze sonic signals in the ocean [25]. Aerial systems towed by aircrafts have also been used for express mail delivery in the first half of the twentieth century, and applications are still considered for precision payload delivery or snatch pick-up [47, 110, 134], aerial refuelling (see figure 4.1) and low-altitude atmospheric research [97, 111] among others.

In the context of these applications, it is of crucial importance to warrant the stability of the trajectory of the towed object (at the tip of the cable), which turns to be an interesting and complex fluid dynamics problem. The dynamics of the towed object results indeed from several contributions: (i) the aero/hydro-dynamic forces exerted by the surrounding fluid (including primarily drag and lift but possibly also added mass effects and pressure gradients when the environment is turbulent, etc.) directly on the object itself, (ii) the tension of the towing cable (which is itself submitted to aero/hydro-dynamic forces) and (iii) gravity. As a consequence the towed object is cou-

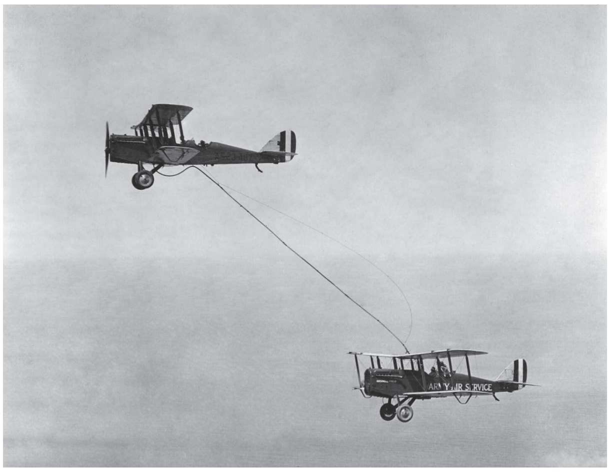

Figure 4.1: Aerial refuelling is an example of a towed cable system for which stability issues are crucial for connecting manoeuvres. The picture shows the first aerial refuelling, on 27 June 1923. (Source: U.S. Air Force).

pled to the fluid both directly and also indirectly via the cable. The study of the coupling between the cable and the fluid is therefore also of crucial importance. In this chapter we will study the instabilities that can appear in the particle wake, while in the following chapter we will focus on the influence of the towing cable in the development of instabilities. In chapter 6 we then investigate the influence of a surrounding turbulence.

We note that the results presented in this chapter concern a preliminary work, carried during a one week visit in the Turbulent Flow Group (Institute for Hydromechanics) at the Karlsruhe Institute of Technology, in collaboration with Pr. Markus Uhlmann. In spite of their simplicity, the results of the experiment carried out during this short visit, appear to give interesting complementary insight regarding the onset of wake instabilities, as previously reported for instance for the case of free falling spheres. The situation of a sphere towed at constant velocity can indeed be related to the case of a sphere freely falling at its terminal velocity. This problem has already been considered by Newton [79] while he was studying the drag of spheres in falling liquids. With the DNS at higher Reynolds number and high speed imaging techniques, over the last 15 years this problem received renewed attention [125, 19, 44, 45, 23]. A big variety of motions has been reported for such a system. A review on this subject may be found in [29].

The physical causes of path instability can be separated in two classes. The first class is related to the way the hydrodynamical forces and torques evolve when a disturbance is applied to the body degrees of freedom. The second class involves the wake instability that occurs beyond a critical Reynolds number even if the body is translating with constant speed and orientation. This is caused by two subsequent bifurcations (the second being a Hopf bifurcation), that occur for the free falling case at $Re^1_{pc} = 212$ and $Re^2_{pc} = 273$ respectively (where $Re_p$ is defined as $Re_p = d_p U_s/\nu$, where $U_s$ is the settling velocity of the sphere, $d_p$ its diameter and $\nu$ the kinematic viscosity of the flow). The first bifurcation leads to a stationary state that is no longer axisymmetric. The second bifurcation is related to a periodic state. The lift force associated with this mode oscillates in magnitude about a non-zero mean. Both trajectories conserve a planar reflectational symmetry with respect to a longitudinal plane passing through the sphere center (with an arbitrary angular orientation).

Three basic parameters will be considered for studying this problem. The particle Reynolds number $Re_p$, the density ratio $\Gamma = \rho_p/\rho_0$, where $\rho_p$ and $\rho_0$ are particle and fluid's density respectively and the Galileo number, defined as $Ga = \sqrt{\frac{g d_p^3 \rho_0(\rho_p - \rho_0)}{\mu^2}}$, where $g$ is gravity acceleration and $\mu$ the kinematic viscosity of fluid. Dimensional analysis shows that the system is governed by two parameters (in this introduction we consider $Re_p$ and $\Gamma$ accordingly to [29], while in [45], $Ga$ and $\Gamma$ are considered). From the situations investigated in the literature, three different regimes of oscillatory motion for a sphere can be identified:

- *Regime A* ($Re_{pc} \sim 260$, $\Gamma_c > 0.36$): this regime is characterized by small-amplitude, possibly irregular or even chaotic movements of the body.
- *Regime B* ($Re_{pc} \sim 260$, $\Gamma_c < 0.36$): the sphere follows regular harmonic oscillations with significant amplitudes. Wake vortices control the dynamics of path instability, and their evolution is intimately related to the changes in the translational and rotational velocities of the body.
- *Regime C* ($Re_p >> Re_c$, $\Gamma_c < 0.36$): this regime occurs at $Re_p$ much larger than the threshold of wake instability, when higher-order harmonics become important. Various oscillating paths are reported, more or less regular and possibly chaotic but with still-significant amplitudes. This paths develop in conjunction with complex wake structures.

An appropriate parameter for characterizing this phenomenon is the drag coefficient $C_D$. Figure 4.2a shows how this curve varies with $Re_p$ for a static case (already shown and detailed in chapter 1). Deviations from this law would be related to instabilities and dynamical corrections to this law.

In the DNS in [45, 24], spheres with $Re_p < 550$ and density ratios in the range $0.5 < \Gamma < 10$ or $\Gamma = 0$ (no intermediate values have been con-

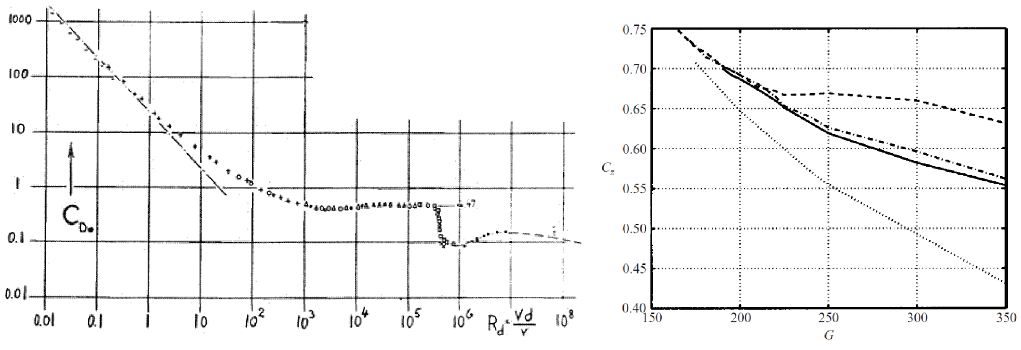

(a) (b)

Figure 4.2: (a) Drag coefficient of a sphere as a function of $Re_p$. Image taken from [41]. (b) Mean drag coefficient (defined as $C_z = 4/(3U_z^2)$) as a function of $Ga$ for reduced densities, $\Gamma = 0$ (dashed line), $\Gamma = 0.5$ (dash–dotted line) and $\Gamma = 5$ (solid line). The dotted line plots the drag coefficient of the axisymmetric wake (image taken from [45]).

sidered) were studied. Figure 4.2 shows their result of how the usual drag law varies with $\Gamma$. The drag coefficient of spheres corresponding to density ratios $\Gamma_c > 0.5$ follows the standard drag law throughout the entire range of $Re_p$ investigated. In contrast, for $\Gamma_c = 0$, $C_D$ almost stops decreasing for $Re_p > 300$ and keeps a value close to 0.65. A similar behavior was found In the experimental work of [125] at higher $Re_p$ numbers ($900 < Re_p < 2000$), but with a critical value $\Gamma_c = 0.3$. In [44], another experimental study, a much broader range of $Re_p$ is covered ($100 < Re_p < 15000$), whilst results are qualitatively similar.

These works give a consistent picture of this phenomenon, that always occurs after a critical particle Reynolds number $Re_{pc}$. Beyond a critical density ratio $\Gamma_c$, the drag coefficient barely deviates from its standard curve, probably signature of an $A$ regime. In contrast, path oscillations are much larger for $\rho < \Gamma_c$, corresponding to a $B$ or $C$ regime (depending in the distance $Re_p - Re_{pc}$), and they result in a marked increase in $C_D$, which is typically twice as large as the fixed–sphere value for $Re_p > 10^3$.

Vibration first occurs at $Re_{pc} \sim 260$, slightly less than the critical Reynolds number marking the onset of vortex shedding for a fixed sphere, $Re_{ps} \sim 275$ ([104, 76]). Over the range $Re_p = 260 - 1550$, the critical density ratio $\Gamma_c$ has a value just below 0.4. At $Re_p = 1550$, it jumps to $\Gamma_c \sim 0.6$, where it remains at least until $Re_p \sim 15000$, the upper limit of $Re_p$ considered in available experiments. The amplitude of the oscillations has a typical value of $0.75d_p$.

The case studied in this chapter, where the particle is towed at a constant speed $U_y$ (being always $U_y = 2.24$ cm/s, hence orders of magnitude lower than the settling velocities, as can be deduced from table 4.1) is an intermediate case with the fixed sphere and the free falling case. When the results for the last case can be applied remains unclear. While in the free fall case the settling velocity is controlled by $\rho$ and $Ga$ (via $d_p$), in our case this velocity is kept constant, and these parameters varied independently. This situation is a new scenario in which this two parameter can be combined in new ways, never explored before in a systematic way. Nevertheless, as has been pointed in [29], for the case of a sphere the wake instability is the only candidate to generate oscillations. Therefore, some analogue instabilities should appear in the towed case, although it is not evident how the tension of the towing cable would affect this motion.

The purpose of this chapter is to study such a towed system and to try to identify the critical values $Re_{pc}$ and $\Gamma_c$. Any differences with the free falling situations would be essential for the cited applications. For this purpose we investigate the stability of the trajectory of different classes of particles, with various density ratios and Reynolds numbers.

## 4.2 Experimental setup

The experiment has been run in a water tank located at Karlsruhe Institute of Technology (figure 4.3). The cross-section dimensions are $50 \times 35$ cm$^2$ (in the $x0z$ plane), while the height is 133 cm. More information about this experimental system can be found in [53, 133]. A moving platform, with a constant speed $U_y$ of 2.24 cm/s is located in front of the tank, facing the particle. A light source and a camera are placed and fixed on the platform. As can be appreciated in figure 2.2, the towing cable is positioned in such a way that particle's displacement has the same direction than the platform. This fact allowed us to record the particle at an almost fixed height during all particle's displacement (in the moving frame), making it possible to record much longer trajectories compared with a free falling case. Note that for technical reasons related to the towing system the velocity of the sphere could not be varied in the present study. It will be interesting in future experiments to vary this parameter as well.

A white panel has been placed on the back of the tank, in order to be capable to track both particle and particle's shadow. In section 4.4.4 we will show that this setup allowed us to perform three-dimensional tracking of the spheres with one single camera.

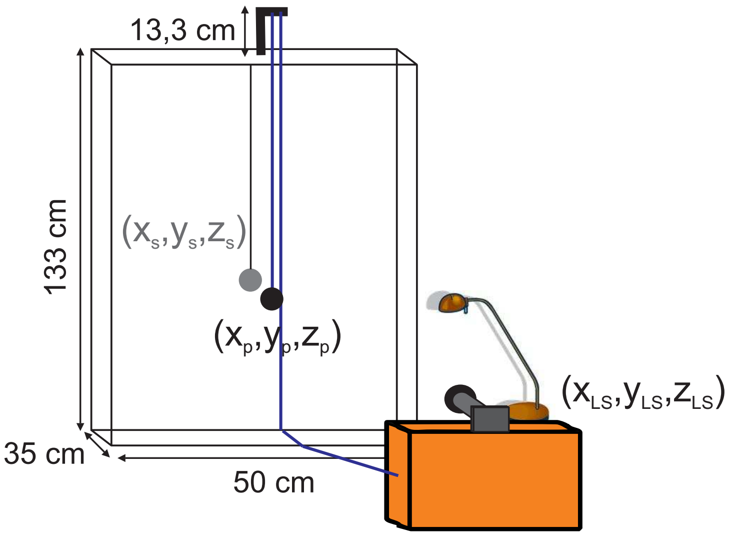

Figure 4.3: Experimental setup.

Eight different types of particles were analyzed, trying to explore the widest possible range of $Ga$, $Re_p$ (here defined with the towing velocity $U_y$) and $\Gamma$. The wire used to tow the spheres is a simple cotton fiber, with a linear density of less than 30 mg/m, hence with a density and mass orders of magnitude lower than the spheres. The properties of the particles can be found in table 4.1. The column labelled as $Ga^*$ shows a Galileo number based on the Archimedes force and the wire tension (see section 4.3). For deducing this parameter it is important to note that the standard Galileo number can be written as $Ga = \sqrt{Fd_p^3/m_p}/\nu$, $m_p$ being particle's mass and F the "traction" force (therefore the Archimedes force for the free falling case). In our situation the Archimedes force has to be replaced by the wire's tension (that we will consider equal to the drag force as expected in the stable case $T_z = F_D = \frac{1}{2}\rho_0\pi(d_p/2)^2U^2C_D$), obtaining then $Ga^* = \sqrt{F_D/m_p}/\nu = Re_p\sqrt{3C_D/4}$.

Particle's trajectories were recorded using a standard web cam, in RGB colour, with a resolution of 640 × 380 pixels and an acquisition frequency of 24 Hz. Considering the towing speed and the dimensions of the recipient, $\sim$ 40 s of trajectory were recorded, resulting in $\sim$ 900 frames. In order to have statistical convergence for each class of sphere, 10 films were recorded for each sample. Image 4.4a shows a raw image obtained with the web cam, where using standard tracking techniques and a calibration mask, the trajectory in the $xOy$ plane is easily obtained (figure 4.4b). As the towing cable

| $N$ | $\phi(mm)$ | $m(g)$ | $\rho(kg/m^3)$ | $Ga$ | $Ga^*$ | $Re_p$ |
|---|---|---|---|---|---|---|
| 1 | 10.0 | 0.60 | 1150 | 1200 | 169 | 224 |
| 2 | 10.1 | 1.35 | 2510 | 3900 | 170 | 226 |
| 3 | 15.1 | 2.03 | 1140 | 2140 | 235 | 337 |
| 4 | 18.0 | 3.46 | 1130 | 2710 | 273 | 404 |
| 5 | 22.4 | 14.63 | 2500 | 12820 | 326 | 501 |
| 6 | 24.1 | 8.21 | 1130 | 4170 | 347 | 539 |
| 7 | 25.46 | 9.1 | 1053 | 2930 | 364 | 570 |
| 8 | 39.6 | 35.1 | 1080 | 7060 | 530 | 886 |

Table 4.1: Particles considered. The density ratio $\Gamma$ is trivially deduced considering that $\rho_0 = 1000$ kg/m$^3$.

is made of cotton fiber, it suffers a small elongation during the trajectory caused by its elasticity. This fact can be observed in the small variation in the vertical component of the trajectory, typically in the order of a few millimeters for a trajectory of $\sim 1m$. Considering the deliberate simplicity of the system (trajectories measured with a web camera, a standard filament lamp as illumination, etc), the resulting trajectories are noisy, but with enough quality for simple stability analysis purposes.

The method for tracking the trajectories is, conceptually, very simple:

- Starting with the raw image (figure 4.5a), and considering that the vertical coordinate of the particle is almost constant (in the frame moving with the camera), a smaller region (in which the particle is always inside) is extracted.

- The image is then bandpass filtered to eliminate any spurious defect with size significantly different from particle's, and morphologically closed using a disk as a structuring element (figure 4.5b).

- The image is made binary considering an intensity threshold and the image is morphologically opened in order to remove small remaining objects. Finally, the center is detected by searching the eccentricity of all the objects in the binary image. The disk is then represented by the object with eccentricity closest to 1 (figure 4.5c).

- Then, picture by picture, the position of the sphere is saved, obtaining at the end the Lagrangian trajectory of the particle, as it can be seen in image 4.5d.

No particular post-filtering has been applied at this point. However, the remaining noise (visible on figure 4.5d) is not harmful for the stability analysis

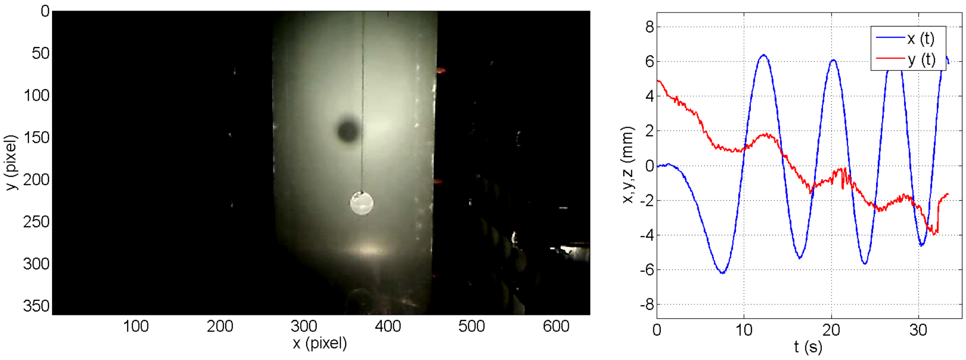

(a) (b)

Figure 4.4: (a) Raw image of the seventh particle in table 4.1. (b) Cartesian components of the particle as a function of time.

performed here.

For the dark particles and shadows the same process has been performed, but with the complement of the image. Once the Lagrangian trajectories are obtained, it is possible to perform a systematical analysis of such trajectories.

## 4.3 Equation of movement

Before showing the experimental results on the stability of the towed sphere, let us briefly discuss the equation of motion of the sphere as if it was simply a pendulum, with varying length, considering usual drag dissipation, but without including any subtle effect related to symmetry breaking of the wake. This will serve as a reference to discriminate real fluid-structure instabilities to just pendular oscillations of the system.

We consider only Archimedes, added mass and drag forces are present. Drag force is considered as in chapter 1, as been obtained in a static case (therefore neglecting any dynamical effects) and no history force or pressure gradients are assumed. The drag in the wire is also neglected, as the wire surface remains always at least one order of magnitude lower than the spheres studied. The equation for particle's velocity $\vec{v}$ obtained for the $x0y$ plane results:

$$\frac{d\vec{v}}{dt} = \frac{1}{\tau_p}(\vec{u}-\vec{v}) + C_{AM}\frac{d(\vec{u}-\vec{v})}{dt} + (1-\frac{\rho_0}{\rho_p})\vec{g} + \vec{T}, \tag{4.1}$$

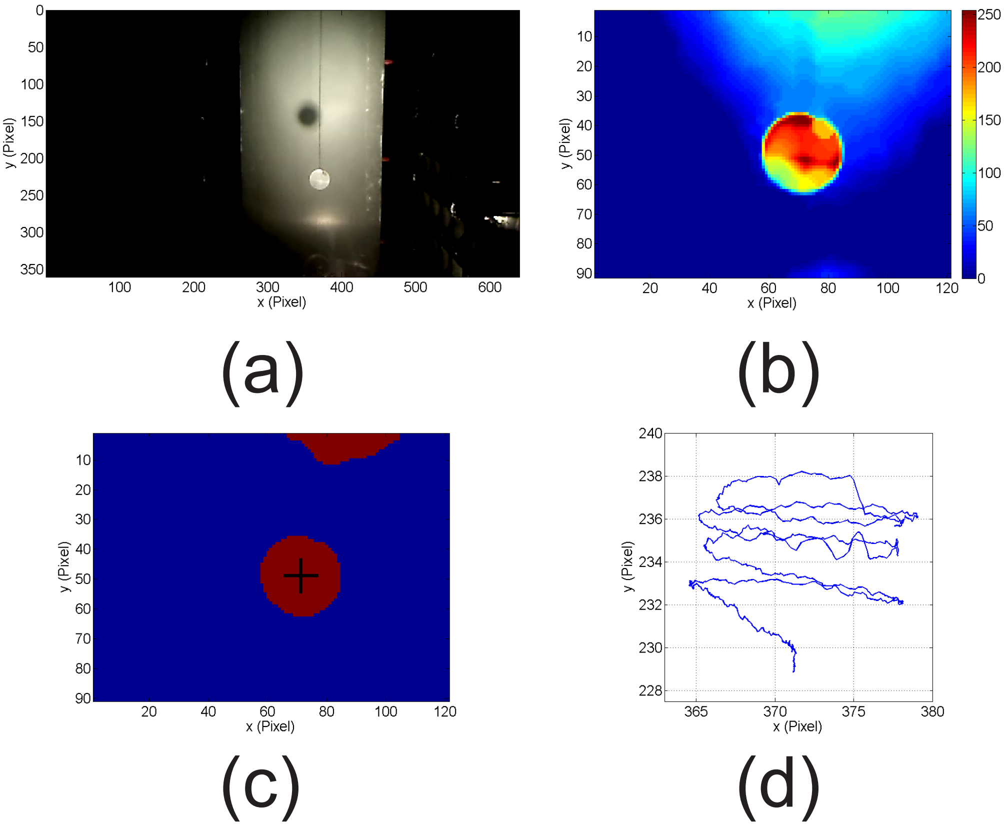

Figure 4.5: All the steps performed for tracking particle's trajectory. Starting with the raw image of the seventh particle in table 4.1 (a), a smaller region near the particle is extracted, then bandpass filtered and closed (b). The image is made binary with a threshold, opened and the center is detected by searching the object with eccentricity closest to 1 (c). Finally, each step is recorded and the Lagrangian trajectory reconstituted (d).

with $C_{AM}$ the added mass constant, being 0.5 for the case of a sphere. $\vec{u}$ is the flow velocity interpolated at the center of the particle.

Drag force is represented by particle's viscous response time $\frac{1}{\tau_p} = \frac{\pi d_p \mu_0 Re_p C_D(Re_p)}{8m_p}$, where $m_p$ is the mass of the particle, $V$ its volume and $C_D$ the drag coefficient, considered according to figure 4.2a. Therefore, in the range of $Re_p$ explored this coefficient depends on $Re_p$ accordingly to the empirical adjustment proposed by [13]: $C_D(Re_p) = \frac{24}{Re_p}(1 + 0.150Re_p^{0.681}) + \frac{0.407}{1+8.710/Re_p}$.

Considering that the flow velocity is constant in the vertical direction ($\vec{u} = (0, U_y, 0)$), from the $y$ component it is possible to deduce an expression for the cable tension:

$$T = \frac{m_p U_y}{\tau_p \cos\theta} + g(m_p - m_f)/\cos\theta, \tag{4.2}$$

where $m_f$ is the mass of a fluid occupying the volume of the sphere. Considering small perturbations, we can consider $\cos\theta \sim 1$ and $\sin\theta \sim \frac{x}{l(t)}$, while $l$ is the length of the cable (that varies in time following to the equation $l(t) = l_0 - U_y t$, where $U_y$ is the towing velocity). Finally, using (4.2) the equation of movement in the horizontal coordinate is obtained:

$$\left(1 + \frac{1}{2}\frac{\rho_0}{\rho_p}\right)\frac{d^2x}{dt^2} + \frac{1}{\tau_p}\frac{dx}{dt} + \left(\frac{U_y}{\tau_p l(t)} + g/l(t)(1 - m_f/m_p)\right)x = \frac{U_y}{\tau_p}. \tag{4.3}$$

It is trivial to obtain an equivalent equation of motion for the $y0z$ plane. This equation has been solved numerically in order to compare the results with the experimental trajectories. Figure 4.6a shows the trajectory obtained for particle 5. As will be seen in the next section, this is a particle that resulted to be stable, but a small perturbation was applied just to excite a pendulum-like oscillation. It can be observed a good similarity between the solution to (4.3) and the measured perturbed particle. The slow discrepancies can be attributed to the fact that the perturbation has been applied to the wire and not the particle, inducing also a dynamics for the wire more rich than that described by equation (4.3).

This equation is an interesting case in which stationarity is not achieved as, always considering a pendulum analogy, the frequency depends on wire's length $l$ and varies as the sphere is towed. Therefore, the appropriate basis for analyzing frequencies in equation (4.3) is to obtain the instantaneous frequency of the particle via Hilbert transform. Hilbert transform is a useful tool when dealing with non-stationary systems and is capable to determine an instantaneous amplitude and frequency at each time step of the trajectory.

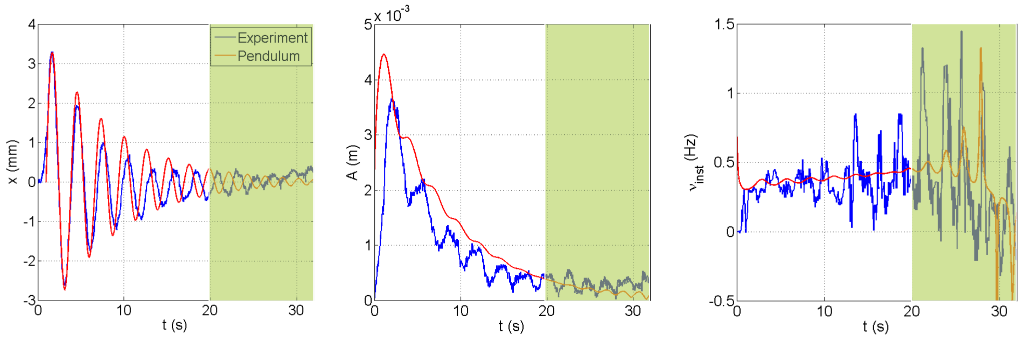

(a) (b) (c)

Figure 4.6: (a) Comparison of the experimental $x$ coordinate considering the parameters of the fifth particle (blue line) and the solution obtained for equation (4.3) for a particle with the same properties. Same comparison but for the instantaneous amplitudes (b) and frequencies (c) obtained via Hilbert transforms. The highlighted zones are those were damping is important and noise becomes large, probably affecting the estimation of Hilbert transforms.

Figures 4.6b&c show the results from the amplitude and frequency after the Hilbert transform. These appear very noisy for the experiment (blue line in figures), particularly when the amplitude becomes small. However the observed tendencies are sufficient to simply compare the order of magnitude and the tendencies of experimental signals and a theoretical pendular motion (red line in figures). It is also possible to observe that after $t \sim 20$ s (highlighted zones in figure 4.6), the instantaneous frequency shows an erratic behavior, probably due to the fact that damping becomes big and noise extremely relevant, affecting the results of the Hilbert transforms. A better estimate of instantaneous amplitudes and frequencies could for instance be achieved using parametric techniques as the maximum of likelihood Approximation (MLA), proposed in [73].

## 4.4 Results

### 4.4.1 Instability diagnoses

The main objective of this experiment is to study possible instabilities of a sphere towed at constant speed in the water tank. Figure 4.7 shows all the trajectories obtained. This figure shows that for some particles a qualitative visual inspection is sufficient to diagnose a possible instability. For instance, particle 5 clearly appears (figure 4.7e) as stable. This is further confirmed when the particle is perturbed (figure 4.7f) and rapidly damped oscillations are excited (which has been discussed in previous section). Particle 7 on the contrary is a clear case of instability (figure 4.7h), where without any external perturbation, an oscillating motion grows spontaneously. We propose in the sequel a more quantitative diagnosis of the instability growth.

Moving through a more quantitatively analysis, instantaneous amplitudes obtained via Hilbert transforms are shown for all trajectories in figure 4.8. A stable particle, as particle 5 in figure 4.7e has an amplitude that tends to zero when time grows (even after being perturbed as can be appreciated in figure 4.7f). On the other hand, an unstable particle (like particle 7 in figure 4.7h) maintains a finite amplitude for all times.

Therefore, the stability of a particle has been determined using two criteria. The first is a qualitative inspection of particle's trajectories and the second an analysis of the instantaneous amplitudes obtained using Hilbert transforms. Results are that particles 6, 7 and 8 are unstable, while the others remain stable. Particles 3 and 4 seem to have stable trajectories, but in figure 4.8c&d they show a particular behavior, different of the stable particles but not converging exactly to zero. These two ambiguous cases will be further studied in section 4.4.3.

Figure 4.9a relates $Re_p$ with the stability of particles (the value 0 is assigned for the stable $Re_p$ whilst 1 for unstable regimes). The threshold for the oscillatory motion results in the range $501 < Re_{pc} < 539$, thus higher than the free falling situation. It is also interesting that oscillatory instabilities occur with values of $\Gamma$ much higher than the observed in other studies. Figure 4.9b relates the stability with the modified Galileo number ($Ga^*$). A similar behavior than the other curve is observed, with a critical value of $326 < Ga_c^* < 346$ (while no particular trend is observed for the standard $Ga$).

### 4.4.2 Discussion

Once that unstable particles have been identified, we will analyze the nature of the instabilities. The unstable particles exhibit big amplitude oscillatory motions, compatible with a regime B as reported for the free falling case. Considering the experimental set-up, this regime is the most easily observed, as a consequence of the restitution and almost harmonic force generated by the wire. A regime C, as the maximum $Re_p$ is 886, would be strange to observe, considering that it is usually reported (for the free falling case) for $Re_p$ significantly above threshold.

Figures 4.7e and 4.7f are interesting because they show the robustness of

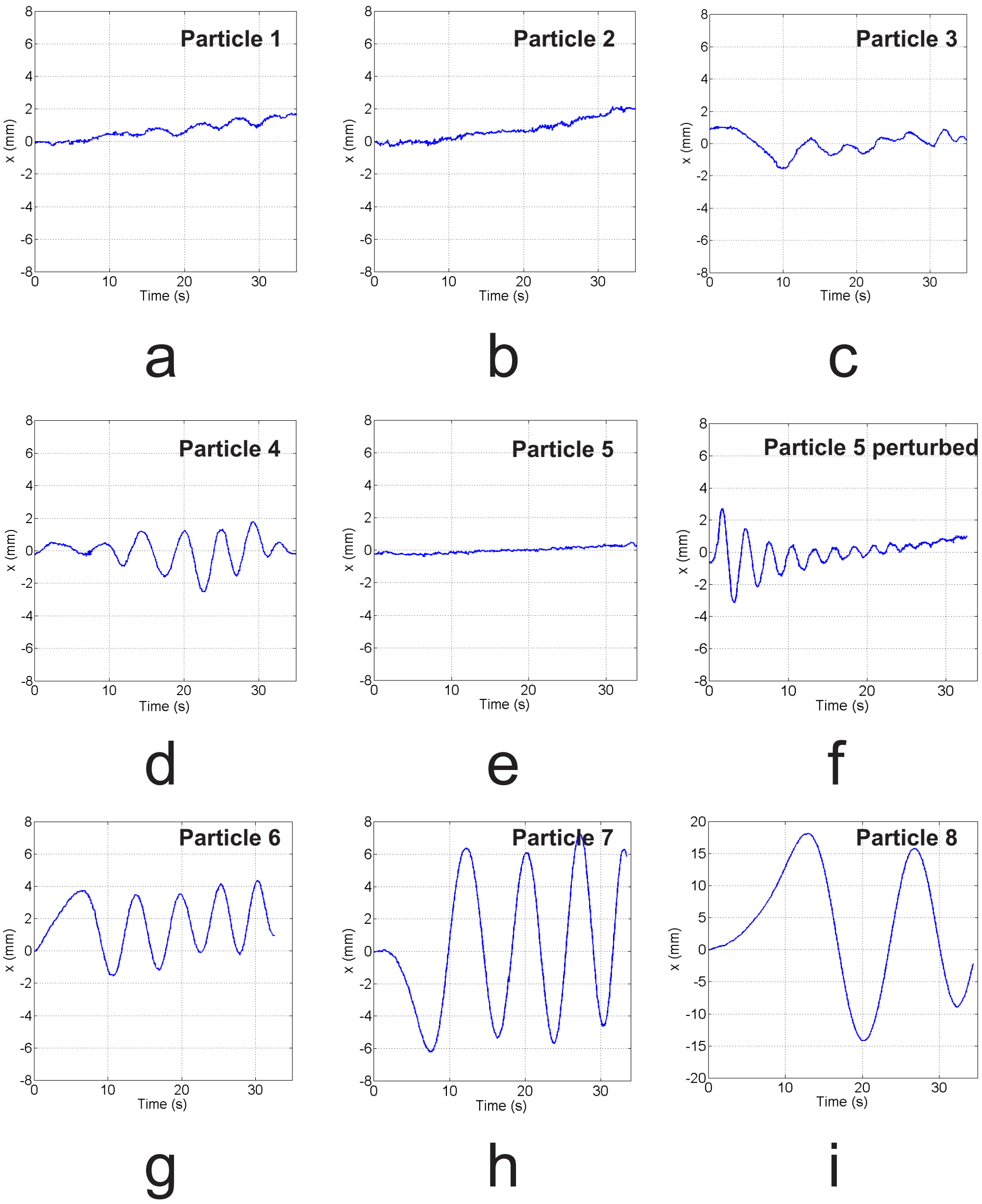

Figure 4.7: Trajectory obtained for all the particles shown in table 4.1. For particle 5 we also show the trajectory of the particle after being perturbed for generating a pendulum-like motion.

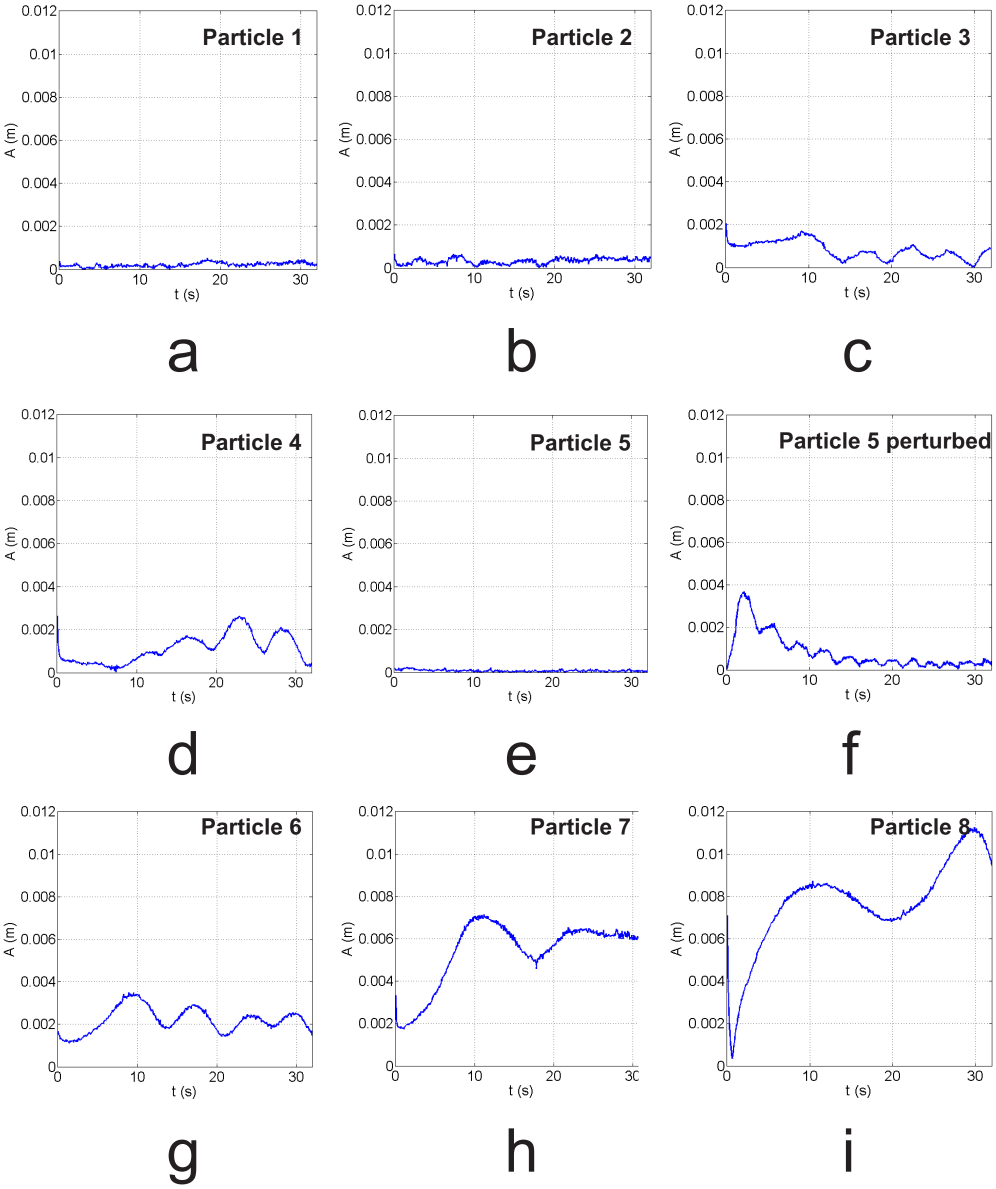

Figure 4.8: Instant amplitudes obtained for all the particles shown in table 4.1 via Hilbert transform. For particle 5 is also shown the instant amplitude of the particle after being perturbed for generating a pendulum-like motion.

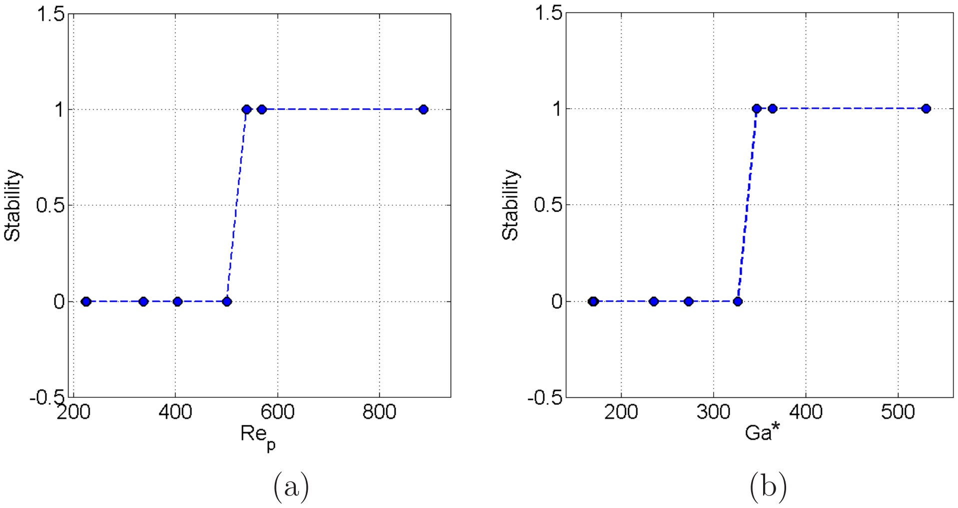

Figure 4.9: Stability of particles depending on $Re_p$ (a) or $Ga^*$ (b). In both curves a value of 1 corresponds to an unstable path while 0 for a stable one.

particle's stability in this case. A perturbation generates damped oscillations that disappear rapidly leaving the particle in stable conditions again.

In order to compare the unstable trajectories observed with a pendular case, figure 4.10a shows an unstable trajectory (particle 7), but compared with what would be expected for a damped pendulum (as deduced in section 4.3). The different character of both trajectories becomes evident, these trajectories having different frequencies and different damping (furthermore, the experimental trajectory does not seem to be damped at all).

Let us now compare the initial frequency of the experimental oscillations (estimated from the first two peaks) to that expected for a simple pendular motion. Table 4.2 shows this frequency compared to that resulting from equation (4.3) using the same criterion (the particular case of particles 3 and 4 will be discussed in section 4.4.3). Figure 4.10b shows how this frequency varies with $Re_p$. The first row is the perturbed but stable particle, that as expected gives the closest frequency to the pendulum-like system. Particles 7 & 8 are clearly different from the pendular case and hence can be declared as actually unstable by this simple criterion, particle 6 is ambiguous as visual inspection of figure 4.7g suggests instability, but the growing frequency is close to that of the pendulum. We therefore push further the analysis by investigating the instantaneous evolution of amplitude and frequency of the Hilbert transformed particle trajectories.

Figure 4.11 shows instantaneous amplitudes and frequencies for the un-

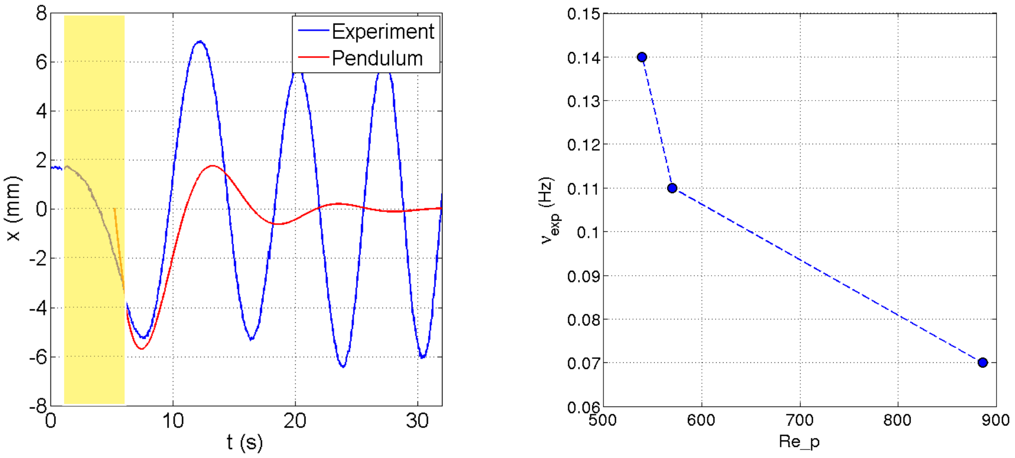

(a) (b)

Figure 4.10: (a) Horizontal displacement of the seventh particle (blue line) compared with the pendulum-like motion for a particle with the same properties (red line). The different nature of each trajectory is visible. The yellow region corresponds to the development of the instability and is properly fitted by the power law $x(t) = Ae^{\frac{t-t_0}{\tau_{ins}}}$. (b) Experimental frequencies observed for the unstable trajectories as a function of $Re_p$.

| $N$ | $Re_p$ | $Ga^*$ | $\nu_0^{exp}$ (Hz) | $\nu_0^{pend}$ (Hz) | $\nu_0^{exp}/\nu_0^{pend}$ | $A_{max}(mm)$ | $A_{max}/\phi$ | $\tau_{ins}(ms)$ |
|---|---|---|---|---|---|---|---|---|
| 5 | 501 | 326 | 0.34 | 0.35 | 0.98 | – | – | – |
| 6 | 539 | 347 | 0.14 | 0.14 | 0.96 | 8.1 | 0.34 | 190 |
| 7 | 570 | 364 | 0.11 | 0.090 | 1.30 | 11.9 | 0.47 | 48 |
| 8 | 886 | 530 | 0.070 | 0.12 | 0.57 | 36.0 | 0.90 | 0.018 |

Table 4.2: Experimental parameters obtained for unstable spheres. The natural frequency of a pendulum-like motion is shown to compare with experimental results.

stable particles. For comparison, the theoretical value expected for a simple pendulum is shown in red. Its value depends on the initial conditions, that were chosen in order to obtain initial amplitudes similar to that of the experiment. This figure shows that even when the measured frequency is similar to that of the pendulum (4.11a), the behavior of the instantaneous amplitude is different (and not only considering the differences in damping). As has been already analyzed previously, more clear results may be obtained from the instant amplitudes, which should tend to zero for stable or pendulum-like cases. In figure 4.11 it is observed that the unstable trajectories conserve non-zero amplitudes for all the trajectory, giving a determinant support to a non pendular instability scenario.

For the stable trajectories the instant frequency is extremely noisy and shows no clear pattern at all. Figure 4.12 shows the amplitude of two stable trajectories. Both of them are again different from a pendulum-like one (which only means that no strong perturbation has been applied to the particle) and tends to a zero value, which is expectable in a stable damped system. The fact that none of the trajectories goes exactly to zero is caused probably by the noise present in trajectories' tracking.

Table 4.2 also shows the maximal amplitude observed for each unstable case and its ratio with particle's diameter. These ratios are always different from the value of 0.75 observed in [29] for free falling particles, as could be expected considering the restitution force applied by the wire. It is therefore remarkable that particle 8 has a maximal amplitude in the same order of its diameter. The ratio of these amplitudes with particle's diameter grows when the distance $|Re_p - Re_{pc}|$ increases. On the other hand, the instability frequencies $\nu_{ins}$ tends to drop when $|Re_p - Re_{pc}|$ grows. Finally, the last column of the table shows a characteristic growth time of the instability $\tau_{ins}$, that is obtained fitting the beginning of the motion of the spheres (as the region marked in yellow in figure 4.10) with the power law $x(t) = Ae^{(\frac{t-t_0}{\tau_{ins}})}$. As expected, the growth rate $\tau_{ins}^{-1}$ increases with $Re_p$ (or $Ga^*$) above threshold. Unfortunately the lack of points for these parameters does not allow us to

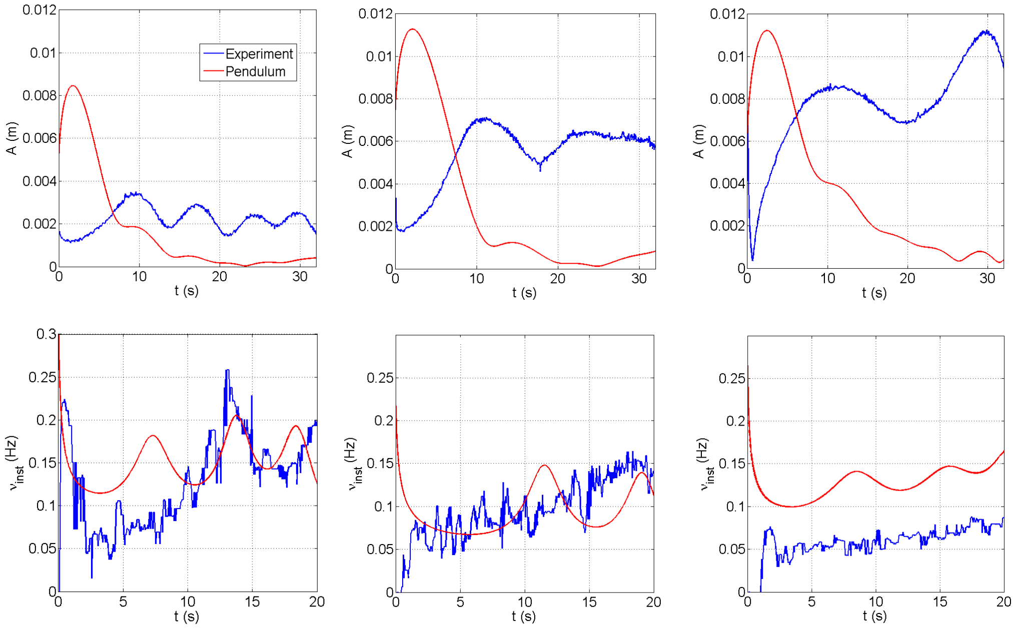

(a) (b) (c)

Figure 4.11: Up: Measured instant amplitudes (blue line) obtained compared with theoretical ones (red line) for particles 6 (a), 7 (b) and 8 (c). Down: Measured instantaneous frequencies (blue line) obtained compared with theoretical ones (red line) for the same particles. The instantaneous frequencies are exhibited for $t < 20$ s because then they become erratic.

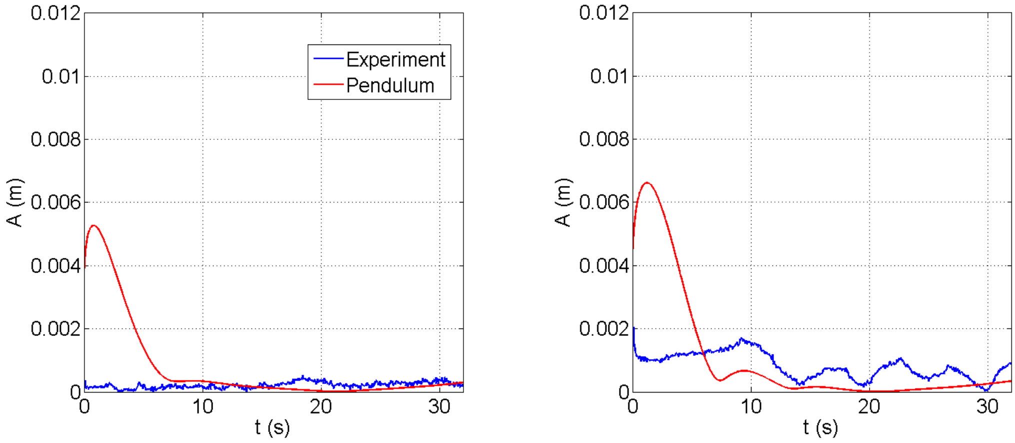

(a) (b)

Figure 4.12: Measured instant amplitudes (blue line) obtained compared with theoretical ones (red line) for the stable particles 1 (a) and 3 (b).

perform a more systematic study.

### 4.4.3 Traces of a chaotic regime?

Particles 3 and 4, that have been considered as stable in the previous section, show some intermittent non-pendular oscillations that could be considered as a signature of an instability. Figure 4.13 shows both trajectories. Whether this is a trace of an $A$ regime or a transition to a $B$ or $C$ regime ($Re_p$ of both particles is in the range of the second bifurcation for spheres) still remains unclear.

### 4.4.4 3D tracking

In this section we propose an attempt of reconstruction of the 3D trajectory of the towed sphere. An important aspect to be addressed is the exact geometry of the sphere motion: is the instability of zig-zag type (planar oscillations) or is it helicoidal? Three dimensional tracking of the particle is possible with the present setup. It is only necessary to accurately measure the position of the particle, its shadow and that of the light source. Particle and shadow trajectories are easily obtained via standard tracking techniques while light source position has been obtained indirectly, assuming that this light source is virtual and with the point source approximation. As the light

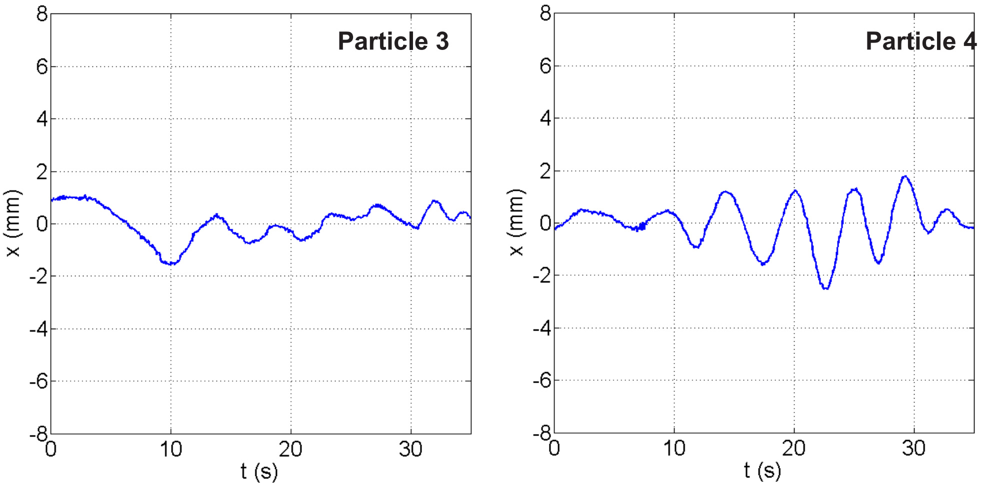

(a)

(b)

Figure 4.13: Experimental trajectories for particles 3 and 4.

passes an air-plastic-water interface, this point source approximation will only remain if the angle explored by the particle (with respect to particle's initial position) is small enough. Therefore, in a first step the position of the light source is obtained. According to figure 4.3, the light source is in position $(x_{LS}, y_{LS}, z_{LS})$, the particle in position $(x_P, y_P, z_P)$ and its shadow in $(x_S, y_S, z_S)$. As these three points are aligned, they follow the equation:

$$\begin{pmatrix} x_P \\ y_P \\ z_P \end{pmatrix} = \begin{pmatrix} x_S \\ y_S \\ z_S \end{pmatrix} + p \begin{pmatrix} x_{LS} - x_S \\ y_{LS} - y_S \\ z_{LS} - z_S \end{pmatrix} \tag{4.4}$$

Provided that the only measured coordinates are $x_P$, $y_P$,$x_S$, $y_S$ and $z_S$ (the shadow is projected onto a plane at constant $z$), it is necessary to add more equations to solve the system. For that purpose, it is enough to consider the positions in the instant $t = 0$ s, when the sphere is still static and placed in the exact middle of the tank:

$$\begin{pmatrix} x_{LS} \\ y_{LS} \\ z_{LS} \end{pmatrix} = \begin{pmatrix} x_S^0 \\ y_S^0 \\ z_S^0 \end{pmatrix} + p_1 \begin{pmatrix} x_P^0 - x_S^0 \\ y_P^0 - y_S^0 \\ z_P^0 - z_S^0 \end{pmatrix} \tag{4.5}$$

where now the three components of the initial position of the particle and its shadow are known. This system is finally composed by six equations and six parameters ($z_P$,$p$,$p_1$,$x_{LS}$,$y_{LS}$ and $z_{LS}$) and should have a unique solution.

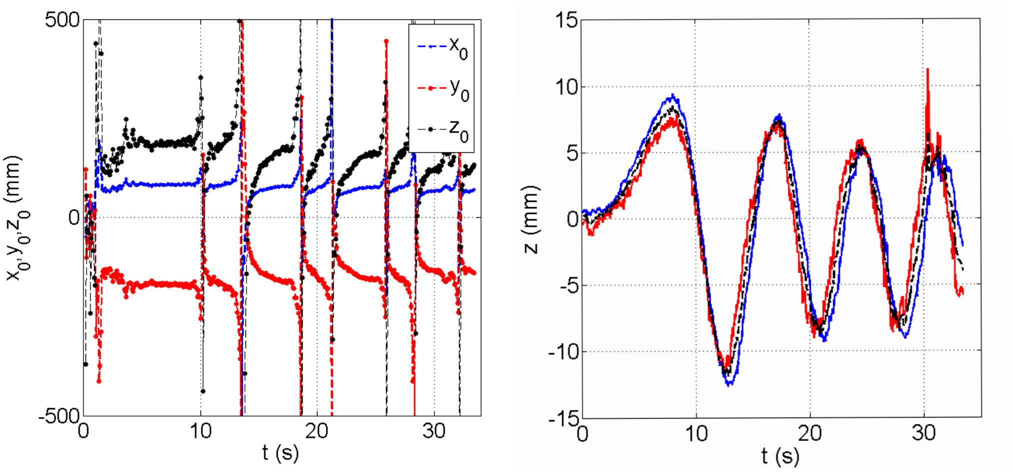

(a) (b)

Figure 4.14: (a) Webcam position obtained solving equation for the seventh particle. (b) $z$ coordinate of the particle solving equation system (4.4) (blue and red). Black dashed line represents the mean value of previous curves.

The problem resides now in that these three points are aligned in physical space, but the points obtained by tracking, even assuming sub-pixel accuracy, are not exactly aligned (taking into account measurement errors). As the equation system to solve is complex and has many variables, this results in a very noisy estimation of the $z$ component of the particle.

In order to solve this problem we proceed iteratively. In a first iteration, we focus on deducing only the position of the light source. Figure 4.14a shows the position of the light source obtained for each time step for the seventh particle. It can be appreciated that, although the results are noisy, a clear mean value emerges, which will be considered as the position of the punctual light source. The maximal diverging deviations from this value occur when the particle returns to its initial position, and $\vec{x_p} \sim \vec{x_p^0}$, and the system composed by equations (4.4) and (4.5) becomes under-constrained. With this position and the maximal amplitude obtained in table 4.2, it is possible to verify that the angle explored by the particles is lower than $1^o$, being legitimate to neglect the departure from a point source approximation due to refraction in the interfaces. Nevertheless, the approximation of the finite lamp by a punctual source is always needed.

Once the lamp position is known, the system can be decomposed in two linear systems with two equations each, the first only considering $x$ and $z$ coordinate and another considering $y$ and $z$ coordinates. Hence, two solutions

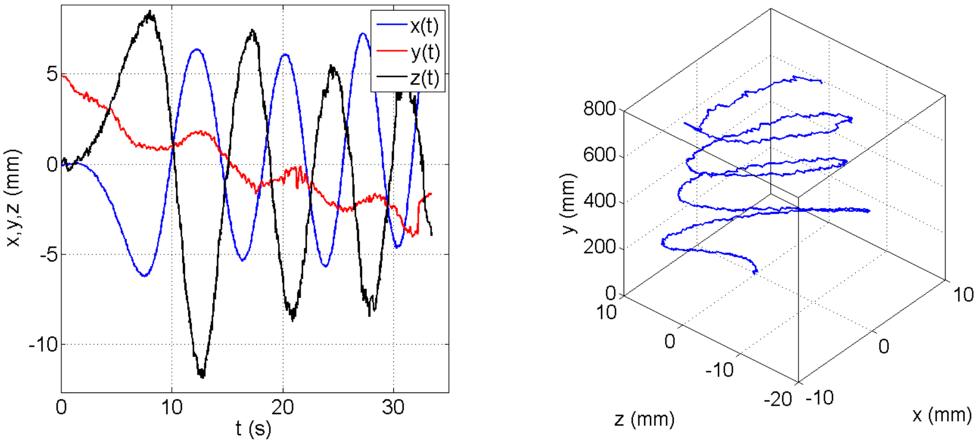

(a) (b)

Figure 4.15: (a) Three Cartesian components of the particle as a function of time. (b) Three dimensional trajectory of the particle.

for the $z$ component of the particle are obtained as shown in figure 4.14b. This allows us to verify the consistency of the system, as both solutions are similar, and to define finally the $z$ component of the particle as the mean value of this solutions. Figure 4.15a shows the three components of the position of the particle in time domain, while figure 4.15b shows the resulting particle tracking in the real space. The trajectory shows a helical trajectory, consistent with a regime B instability.

For concluding this section, it is important to emphasize the simplicity of this method. It is only necessary to assume a small perturbation regime and a point-like light source. It is always possible to add more cameras, that will expand the number of linear equations allowing us to better determine, in a first step, the position of the light source. In a second step, each camera will provide two different solutions for 3D particle position (as in figure 4.15b), giving more solutions to average and increase the tracking precision. Other solution would be to add more light sources obtaining new shadows to track. The method exposed in this section could be seen as a first iteration, as it could be repeated indefinitely: once that the $z$ coordinate is obtained, it can be used in the equation system for obtaining a new position for the light source and so on in order to improve at each iteration the estimation of the third dimension.

## 4.5 Conclusions

We studied in this chapter spheres towed at constant velocity varying $\rho_p$ and $d_p$. The threshold for the oscillatory motion was found in the range $501 < Re_{pc} < 539$, or $326 < Ga_c^* < 346$. This is comparable but slightly larger than for the free falling case. Interestingly, the ratio $\Gamma = \rho_p/\rho_0$ in our study is larger than the largest critical value reported in the literature for the case of free falling spheres. Therefore although all the spheres investigated are expected to have a stable and rectilinear settling motion regardless of their $Re_p$, we have shown that their trajectory can become unstable when they are towed. Whenever unstable trajectories were observed, three-dimensional tracking showed helical trajectories.

Although the case of a towed sphere is of interest for many applications, it is not clear whether this case can be related to the free falling case. The main difference between both cases is that $U$ (the towing velocity in our case, the settling velocity for the free falling case) does not depend on $\rho_p$ for the system exposed in this chapter. Nevertheless, the thresholds measured are similar in both cases, but not equal. This may be caused by the influence of the towing cable in the dynamics, affecting the wake of the sphere or generating a coupling of the unstable motion with a pendular one. We have not found the relation that rules the frequency of the oscillation, although it was shown not to be simply the frequency of a pendulum with the experimental parameters for each case.

Considering the simplicity of the experimental setup, a next step would be to perform simultaneous measurements of the spheres and the properties of its wake, also talking advantage of the versatility of the water tank in KIT. An important extension of this preliminary study would also consist in exploring systematically the effect of varying the towing velocity. Another effect to be studied is how turbulence would affect the wake of the spheres and the instabilities reported in this work.

# Chapter 5

# Equilibrium and stability of long towed cable systems. Part I: instabilities under a laminar flow

## 5.1 Introduction

In this chapter a towed system, similar to that investigated in the previous chapter is exposed. In this case, the experiment has been run in the wind tunnel, which allows us to the reach much higher $Re_p$ and to vary the streamwise velocity.

Despite the similarities between both experiments, this setup allows us to study different phenomena. The higher streamwise velocity results in the development of aeroelastic instabilities in the towing cable, which finally govern the dynamics of the particle. Moreover, the particle being towed horizontally in the windtunnel (while it was towed vertically in the previous chapter), the action of gravity on the towed sphere must be more carefully addressed. Therefore, this chapter shows the enormous diversity of fluid-structure interactions and the importance of correctly understand even the simplest configurations.

Existing investigations of aeroelastic effects on such towed systems are essentially numerical and investigate the stability of the system using lumped mass models for the cable [16, 48, 134], but few systematic experimental investigations are available [116, 121]. The problem is also closely related to that of cylinders or elongated filaments in axial flows which has been extensively investigated theoretically, numerically and experimentally [87, 84, 88, 80, 25, 108, 22, 10]. Most studies concern however cylinders with moderate length-to-diameter ratio, for which it is now well established that in axial flows, the free end of the cylinder becomes unstable above a certain threshold of wind velocity. Several types of instability have been reported, including mainly divergence (which corresponds to a non-oscillatory motion with growing amplitude) and flutter (oscillatory motion) [87, 90]. Recently, Schouveiler *et al.* have also reported a flutter instability for a cylinder inclined in a flow. In both cases (short cylinder in axial or inclined flow), the instability is relatively well predicted numerically from the coupling between the fluid and the cylinder (via inviscid terms and friction) [109]. A more detailed review on the dynamics of flexible cylinders in flows can be found in [89].

The case of very long cylinders is of particular interest because most of the mentioned practical applications of towed systems do use long cables where the length-to-diameter ratio is large (cables towing acoustic streamers in the ocean can be kilometers long for a few centimeters in diameter). However, the study of the stability of such long cylinders in a flow remains an open field of theoretical and numerical research. The problem of long cylinders is particularly difficult to tackle theoretically and numerically due to the important scale separation related to the large length to diameter ratio and also to small scale deformations induced by bending stiffness effects. A detailed discussion on this subject may be found in [22]. Using a string model, which neglects flexural rigidity, Triantafyllou & Chryssostomidis [122] found that a cable will always remain stable above a certain finite length-to-diameter ratio. Dowling [25] developped a different analysis, based on asymptotic expansion, and including flexural rigidity when necessary, but also concluded that long cylinders in axial flows should remain always stable. More recently de Langre [22] performed a finite element numerical resolution of the governing equation for long cables in axial flow, including effects of bending stiffness. Their results suggest that both *divergence* and *flutter* instability are possible for long cylinders. *Flutter* is found to develop as a secondary instability following *divergence* and its appearance is found to depend on the base drag at the free end of the cable. On the experimental side, characterization of the dynamics of long cylinders remains scarce, probably due to the difficulty of achieving appropriate conditions in laboratory facilities. The main works available are those realized by Ni & Hansen [80] and by Sudarsan [116] (with a length to diameter ratio of the cable of 500 and 150 respectively) for cylinders submerged in water. Both studies report *divergence* and *flutter* of the cylinders.

In the present chapter we consider a towed system where the length-to-diameter ratio of the cable is of $5 \cdot 10^4$, hence several orders of magnitude higher than previous studies. The focus is put on the analysis of the Lagrangian dynamics of the tip of the cable. The towing configuration is artificially obtained by considering a steady cable (with one fix end and a free tip end to which a sphere is eventually attached) in a horizontal low turbulence wind-tunnel (see figure 5.1). This reproduces the situation of an object towed horizontally at constant speed (therefore we will indifferently use the terminology *wind velocity* or *towing velocity* in the subsequent). We consider three different configurations of cable tip: (i) just the free end by itself (without any sphere attached); (ii) a light millimetric sphere made of expanded polystyrene and (iii) a denser millimetric towed sphere made of lead. For each situation a systematic study of the influence of the towing velocity on the equilibrium and stability of the cable extremity is performed.

This chapter is organized as follows: the first section describes the experimental setup (wind tunnel, cable characteristics, towed particles, and Lagrangian tracking technique); the second section focuses on the investigation of the equilibrium position of the cable tip for the three cases (free end, polystyrene sphere and lead sphere); in the third section we investigate fluctuations of the cable tip and address the problem of the stability of its dynamics. Finally a brief discussion of the observed behaviors is proposed.

## 5.2 Experimental setup

The experiment has been run in the SFT1 wind tunnel (see chapter 2). The mean wind velocity, $U$, was varied in the range $[4-15]$ m$\cdot$s$^{-1}$, in which the tunnel operates in stable conditions with a fluctuation level below 5‰.

The towing cable is a thin Polyamide-Nylon fiber, with a lineal density of order 17 mg/m, made of three stranded filaments with a diameter of 25$\mu$m each. The resulting equivalent diameter for the stranded cable is of the order of $a_c = \sqrt{3} \cdot 25\mu\text{m} \simeq 43\mu\text{m}$. Table 5.1 summarizes the main physical properties of the cable. One extremity of the cable is fixed at the entrance of the test section at the center of the tunnel, while the other end is free to move. The fixed extremity of the cable is attached at the middle of a transverse horizontal *support* cable tensed across the tunnel at mid-height and located at the entrance of the test section (see figure 5.1). The support cable must be as thin as possible in order to minimize perturbations of the flow; we use the same fiber with 43 $\mu$m of equivalent diameter and we have checked that no measurable increase of the natural fluctuation level of the flow in the wind tunnel was detected downstream due to the presence of the *support* cable. The fixed point is nearly at the center of the test section.

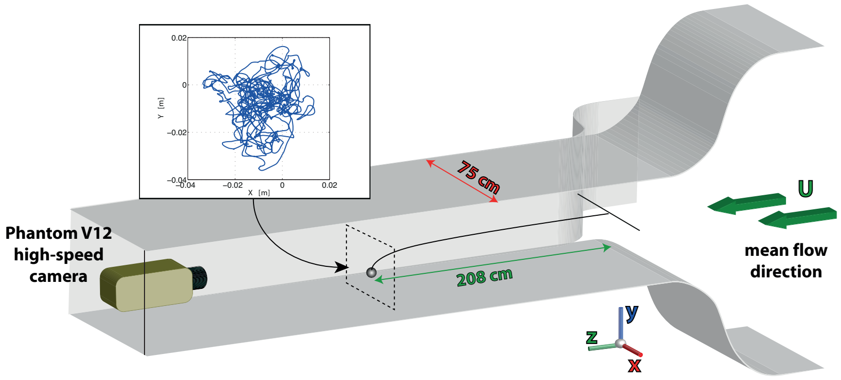

Figure 5.1: Sketch of the experimental setup. The inset shows an example of fluctuating trajectory of the tip of the cable, recorded using a high speed camera. The amplitude of the transverse motion is of a few centimeters at most, and remains small compared to the length of the cable (2.08 m), so that the tip moves practically in a transverse plane ($xOy$), located around 2.1 m downstream the entrance of the wind tunnel measurement section.

| Material | Length (L) [m] | Lineal density [mg/m] | Elastic tension* ($E_t$) [GPa] | Elastic flexion ($E_f$) [GPa] | Flexural rigidity ($EI$) [Nm$^2$] | Poisson coeff. ($\nu$) | Friction coeff. |
|---|---|---|---|---|---|---|---|
| Polyamide Nylon 6,6 | 2.08 | 1.7 | 3.3 | 2.8 | $4.9{\cdot}10^{-10}$ | 0.41 | 0.2 – 0.3 |

Table 5.1: Main physical properties of the towed cable investigated. (*) The corresponding global elastic stiffness for the considered cable, made of 3 filaments of $d = 25\mu$m in diameter and length $L = 2.08$m long, is $k = 3E_t(\pi d^2/4)/L \simeq 2.3$.

The length of the towing cable is $L = 2.08$ m, which places the free tip nearly at mid-distance between the entrance and the exit of the 4 m long test section. Considering this length, which is significantly longer than the maximum transverse displacement of the tip (which does not exceed a few centimeters), the motion of the moving extremity of the cable is essentially two-dimensional, in a transverse $xOy$ plane.

Three configurations were investigated for the moving end of the cable: free end, expanded polystyrene sphere and lead sphere. For the case of the free end, a small single knot (with effective diameter $d_k \simeq 2a_c$), colored with red varnish, was made at the tip of the cable to improve its visualization. Note that in the following we shall generically use the terminology *cable tip* or *cable end* though for the cases where a sphere is towed, this should

| Material | Diameter (mm) | Density (kg/m$^3$) | $Re_p$ [min,max] |
|---|---|---|---|
| Free end (Nylon) | $\sim$ 0.09 | 1140 | $\sim$ [10,45] |
| Expanded Polystyrene | 6.3 | 13.35 | [1680,6300] |
| Lead | 1.7 | 9130 | [450,1700] |

Table 5.2: Characteristics of the towed spheres investigated.

be understood as *the sphere at the cable tip*. The parameters of the towed spheres are shown in table 5.2. We define the particle Reynolds number as $Re_p = Ud_p/\nu$, with $d_p$ the sphere diameter and $\nu$ the kinematic viscosity of air (for the free end case, $Re_p$ is estimated based on the cable equivalent diameter of 43 $\mu$m). The table also gives the range of $Re_p$ spanned in each case as the wind velocity is varied from 4 m/s to 15 m/s. We note at this point that due to the very small diameter of the cable (which is required to achieve the large aimed length-to-density ratio) the Reynolds number based on the cable diameter is order of magnitudes below that of most previous works and below that of applications mentioned in the introduction. The main impact of this results in the necessity to consider non trivial Reynolds number dependencies of the several drag coefficients involved in modeling the cable-fluid interaction. This point will be further discussed in section 5.3.1.

The motion of the moving extremity of the cable is recorded using a high speed camera Phantom V12 from Vision Research Inc. (New Jersey, USA). The spatial resolution used was of 768 × 600 pixels, with a repetition rate of 1000 fps. We recorded sequences of 18500 images (corresponding to 18.5 s of continuous recording after which the 8Gb on-board memory of the camera was full). To improve statistical accuracy 40 such acquisitions were taken for each mean velocity and each of the three towed systems investigated.

### 5.2.1 Lagrangian tracking

All the analysis was realized using standard imaging techniques which allows to obtain the trajectories of the spheres in the $(x, y)$ plane from the videos recorded with the camera. The first challenge is to determine with the highest possible accuracy the center of the ball on each picture. Images were recorded in a non compressed 8 bits gray format so that each picture is directly represented as a pixel intensity matrix. The method for tracking the trajectories is, conceptually, very similar to that used in chapter 4. Nevertheless, some differences are present, considering that in this case the particles are smaller (some pixels in the case of the free end) and the displacement bigger than the case of the previous chapter :

- Previous to the data acquisition, a reference image was taken (but without covering the camera lens, as it is usually done to determine a black reference image). The idea is to have a reference of the view without the sphere but with all the remaining static elements, which we then subtract from the acquisition images in order to better isolate the particle.
- The image is then bandpass filtered to eliminate any spurious defect with size significantly different from particle's, and finally the center of the particle is determined as the center of mass of the most intense remaining filtered blob (image 5.2).
- Then, picture by picture the position of the sphere is saved, obtaining at the end the Lagrangian trajectory of the ball, as it can be seen in the inset of image 5.1. The conversion from pixels to length units was made using a known printed patron (mask) which allows to determine the projective transformation between pixels and real world units.

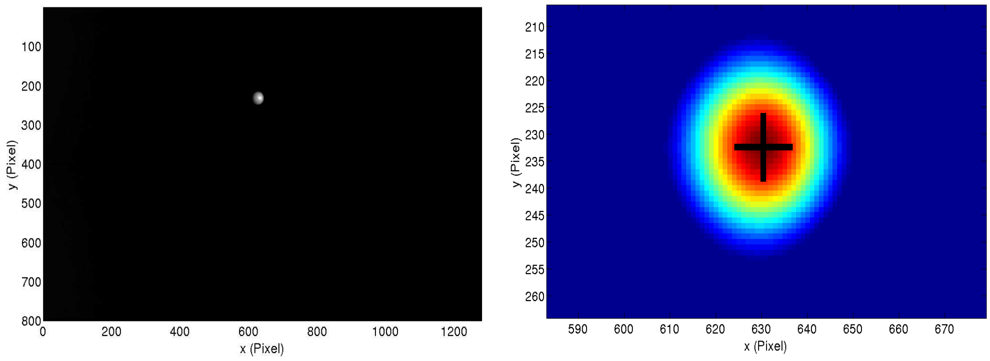

(a) (b)

Figure 5.2: Image captured by the camera in grey scale (a) and the same image in color scale with the center identified with a cross (b).

Velocity and acceleration are then estimated at first order by differentiation (with a simple finite differences scheme). Then, the statistical parameters of trajectories, such as spectra, standard deviations (of position, velocity and acceleration), probability density functions (PDFs), etc. are easily obtained.

For a more accurate estimation of fluctuation properties, filtering of trajectories is generally required. This was achieved following an original scheme described in chapter 6 (paragraph 6.3.3) and which we call E-LES (Empirical-LES, by analogy to small scale modeling in Large Eddy Simulations). Standard deviations of displacement and velocity presented in this chapter follow this estimator.

## 5.3 Results

### 5.3.1 Mean height

We first investigate the average equilibrium position of the cable tip as a function of the wind velocity for each configuration (free end, light towed sphere and heavy towed sphere). The picture is qualitatively trivial: at zero velocity the tip lies on the floor of the tunnel test section; the tip *takes off* when the aerodynamic forces on the cable and towed object are sufficient to produce a vertical component overpassing the weight of the system; then as the velocity is increased, the cable tends to align with the main stream.

Figure 5.4a shows the height $y$ of the cable tip as a function of the wind speed $U$ for the three configurations ($y = 0$ m corresponds to the particle being on the floor of the tunnel). As we will see in the next subsection, for large wind velocities the dynamics of the cable end may become highly fluctuating. In this section we investigate the average vertical position of the cable tip. For the free end and for the light polystyrene particle, it can be seen that, as the velocity increases, the average height reaches an asymptotic value corresponding to the height of the fixed end of the cable ($y_0 \simeq 0.4$ m) which is then aligned with the horizontal mean stream. For this *light* towed objects, the tip of the cable has already *taken off* even for the lowest wind velocities investigated. The heavy lead particle on the contrary, is found to *take off* only when the wind velocity exceeds a threshold of the order of 6 m/s. We also note that for this heavy towed particle, the highest velocity investigated is not sufficient to reach the asymptotic horizontal cable limit.

As already mentioned, the *take off* of the towed objects results from mainly two contributions: (i) the aeordynamic drag acting on the cable, which tends to rise globally the cable and the object at its tip and (ii) the aerodynamic drag acting on the towed sphere (when present), whose reaction on the cable tends to enhance the horizontal component of the tension at the tip and hence to flatten the cable horizontally. Dowling [25] has derived the system of equations governing the average cable position, based on the tension average amplitude $\overline{T}(l)$ and on its local average angle $\overline{\theta}(l)$ (defined with respect to the mean stream) along the cable length. By considering the

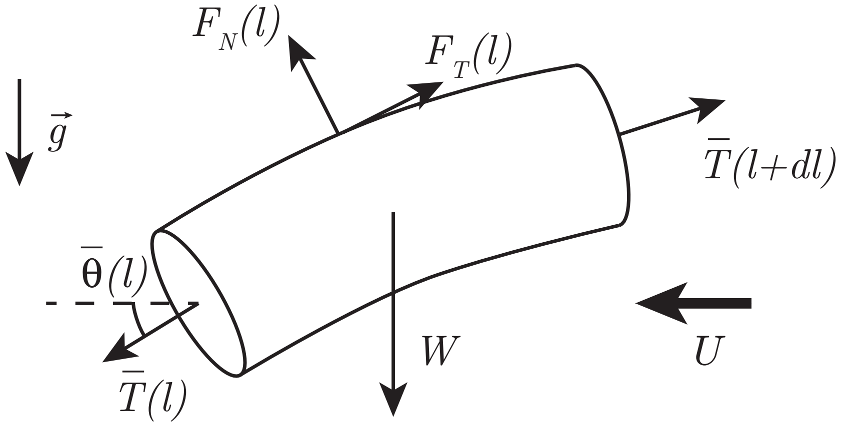

Figure 5.3: Schematic of the forces acting on an elementary element of cable of length $dl$. $\overline{T}(l)$ is the tension along the cable ; $F_N(l) = 1/2\rho_0 a_c U^2(C_D \sin^2\overline{\theta}(l) + \pi C_N \sin\overline{\theta}(l))$ is the normal lineal aerodynamic force (frictional + pressure drag) [25] ; $F_T(l) = 1/2\rho_0 \pi a_c U^2 C_T \cos\overline{\theta}(l)$ is the tangential lineal aerodynamic force (frictional drag) [25]; $\vec{W} = \rho_0(\sigma-1)\pi/4\, a_c^2\vec{g}$ is the lineal net weight of the element. Note that for the stationary equilibrium analysis, where no acceleration of the cable relative with the fluid is considered, added mass effects are not included.

tangential and perpendicular equation of motion of an elementary element of cable (see figure 5.3 for a schematic of the forces acting on the cable at equilibrium), the following system of equations can be obtained for the equilibrium tension and local angle (details of the derivation of these equations can be found in [25]):

$$\begin{cases} \frac{\partial\overline{T}}{\partial l} = -\rho_0(\sigma-1)\pi a_c^2 g\sin(\overline{\theta}) - \rho_0 U^2\pi a_c C_T\cos(\overline{\theta}) \\ \overline{T}\frac{\partial\overline{\theta}}{\partial l} = -\rho_0(\sigma-1)\pi a_c^2 g\cos(\overline{\theta}) + \rho_0 U^2 a_c(C_D\sin(\overline{\theta}) + \pi C_N)\sin(\overline{\theta}) \end{cases} \tag{5.1}$$

where $l$ denotes de curvilinear coordinate along the cable ($l = 0$ corresponds to the fixed end, $l = L$ to the cable tip), $\rho_0$ is the density of air, $\sigma$ is the specific density of the cable, $a_c$ is the equivalent cable diameter (here taken as $a_c = 43.3\mu$m), $C_T$ is the tangential frictional drag coefficient, $C_N$ the normal frictional drag coefficient and $C_D$ the pressure drag coefficient [41].

This system of equations has then to be completed with an appropriate set of boundary conditions to be applied at the extremity of the cable. When the cable is towed by itself (with no object trailed at its end), this condition is simply $\overline{T}_{tip} = 0$ (as the tension vanishes then at the free end of the cable).

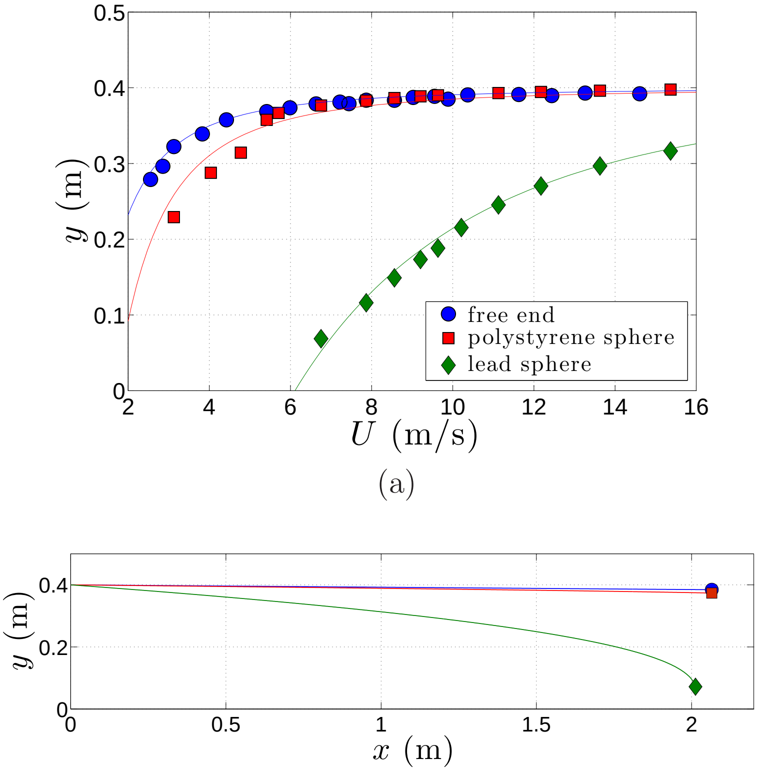

(a)

(b)

Figure 5.4: (a) Mean height for the wire cable tip measured for the three configurations of towed object. The solid lines correspond to the best simultaneous adjustment of the drag coefficients $C_D$, $C_N$ and $C_T$ acting on the cable in equations (5.1). (b) Global shape of the cable calculated from the resolution of equations 5.1 for a towing velocity of $U = 7$ m/s.

It can be shown in this case that the shape of the cable is a straight line, with the angle $\overline{\theta}(l)$ remaining constant along the cable length ($\frac{\partial\overline{\theta}}{\partial l} = 0$) at a critical value $\theta_c$ [92, 25]. Then the critical angle can be simply obtained from the boundary condition $\overline{T}_{tip} = 0$, applied to the transverse equation in system (5.1), as the root of the equation

$$-\rho_0(\sigma-1)\pi a_c^2 g\cos(\overline{\theta}_c)+\rho_0 U^2 a_c(C_D\sin(\overline{\theta}_c)+\pi C_N)\sin(\overline{\theta}_c)=0. \tag{5.2}$$

When the cable does tow an object at its end, the appropriate boundary condition is given by the balance of the forces acting on the towed particle at the tip (this boundary condition accounts for the contributions coming from the aerodynamic forces acting on the particle):

$$\left\{\begin{array}{l}\overline{T}_{tip}\cos\overline{\theta}_{tip}=\frac{\pi}{8}d_p^2C_pU^2\\ \overline{T}_{tip}\sin\overline{\theta}_{tip}=\quad m_pg\end{array}\right. \tag{5.3}$$

with $d_p$ the diameter of the towed particle, $m_p$ its mass and $C_p$ its drag coefficient.

We have solved the system of equations (5.1) with the appropriate boundary conditions for the three towing configurations, for mean wind velocities $U$ varying within the accessible experimental range. The height of the cable is then derived from the resulting calculated profile of the cable shape. Note that solving these equations requires the knowledge of several parameters, in particular the drag coefficients of the particle $C_p$ and of the cable, $C_T$, $C_N$ and $C_D$. The drag coefficient for spherical particles is well tabulated (see for instance [41, 13]), so we have used the commonly accepted values according to the particulate Reynolds number of our particles. In the range of velocities explored, this coefficient is essentially constant and equal to $C_p \simeq 0.5$ ; however for each velocity and particle diameter, we estimate the drag coefficient precisely according to well established empirical formulae [13]. Concerning the cable coefficients, it should be noted that the Reynolds number based on the equivalent diameter of the cable varies in the range $10 < Re_c = a_cU/\nu < 45$ when the mean wind velocity $U$ is varied between 4 m/s and 15 m/s. In this relatively low Reynolds number regime, the drag coefficients of the cable have a non-trivial dependency on Reynolds number [41]. The behavior of $C_T$ and $C_D$ is relatively well documented for cylinders, cables and wires [41, 123]. In the present range of interest the Reynolds number dependence of $C_T$ and $C_D$ is well approximated by power laws :

$$C_{T,D} \simeq A_{T,D}Re_p^{\alpha_{T,D}} \tag{5.4}$$

where we have determined $A_T = 10$, $\alpha_T = -0.76$, $A_D = 7.6$ and $\alpha_D = -0.43$, based on the data in [123]. Values for $C_N$ are much less documented, though it is generally accepted that $0 < C_N < C_T$ [25, 118]. Therefore $C_N$ is used as a fitting parameter to adjust the theoretically calculated height to the experimental measurements. More precisely, a power law dependence $C_N = A_NRe_p^{\alpha_N}$ is also assumed and we use the two fitting parameters $A_N$ and $\alpha_N$. We stress that these two parameters are simultaneously fitted, at once from the experimental data shown in figure 5.4a for the three configurations (free end, polystyrene sphere and lead sphere). The solid lines represented in figure 5.4a show the corresponding best fit, which is obtained for $A_N = 0.8$ and $\alpha_N = -0.12$. We find a very good agreement between the simple theoretical approach and our measurements. Besides, we note that being able to simultaneously fit the three configurations with a single set of fitting parameters is particularly satisfactory with regard to the relevance of the model and of the estimation of the various parameters involved (in particular $C_p$, $C_T$ and $C_D$).

As an example, figure 5.4b illustrates the corresponding shape of the cable calculated from the solution of equations (5.1) using these best fitting parameters for a towing velocity $U$ =7m/s. Although we do not have at present the possibility to accurately measure in our experiment the global shape of the cable, the calculated profiles shown in figure 5.4b are qualitatively consistent with the visual inspection of the cable. In particular, the cable is observed to be nearly straight for the case with no sphere at the end and when the light polystyrene sphere is towed, while it is clearly curved for the heavy sphere case.

### 5.3.2 Dynamical fluctuations and stability

In this section we report on statistics of velocity fluctuations of the towed bodies. We first describe the dependence on experimental parameters of velocity standard deviation of the cable tip motion before discussing its spectral properties.

#### Velocity fluctuations

Figure 5.5 shows the standard deviations of the cable tip velocity for each towing configuration. Figure 5.5a corresponds to the free end case, figure 5.5b to the light polystyrene particle and figure 5.5c to the heavy lead particle. For each configuration the plot shows the dependency of the standard deviations of horizontal and vertical velocity components ($\sigma_{v_x}$ and $\sigma_{v_y}$) on the towing velocity $U$. For comparison purposes, the range of the vertical axis has been kept identical for the three plots.

**Free end case.** We first analyze the results of the velocity of the tip of the cable alone, without any sphere attached. Interestingly, the level of fluctuations remains almost null below a threshold of wind velocity of the order of $U^* \simeq 6 - 7$ m/s. Above this threshold the tip of the cable becomes unstable and fluctuations of velocity are observed to grow as the mean wind speed is increased. It can be argued, based on the data reported on this plot, that the instability threshold might be slightly lower for the vertical component than for the horizontal one. Moreover, fluctuations of velocity exhibit a small (but measurable) anisotropy with higher fluctuations in the horizontal component far above threshold. It is also enlightening to compare

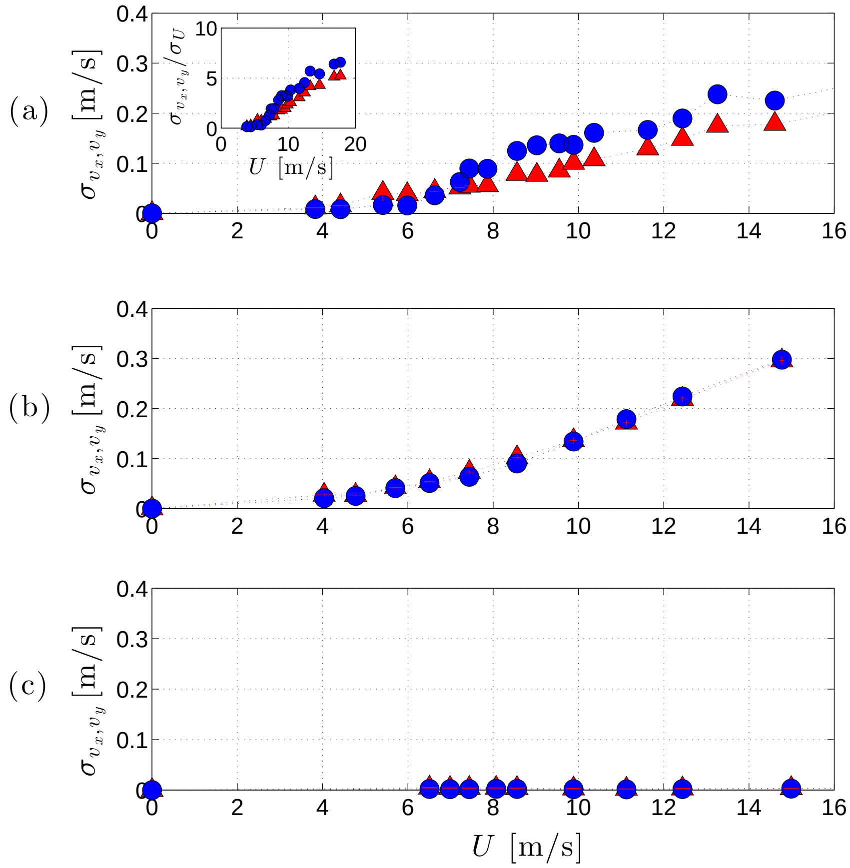

Figure 5.5: Experimental values of the standard deviations of the horizontal (blue circles) and vertical (red triangles) components of the cable tip for the three configurations: (a) free end; (b) polystyrene sphere and (c) lead sphere. The inset in figure (a) shows the same data as the main graph, with the velocity standard deviations of the cable tip normalized by that of the carrier flow itself.

the level of fluctuation of the cable tip to the natural small fluctuations of the flow itself. This is shown in the inset plot in figure 5.5a which represents the ratio of standard deviation of the cable tip velocity to that of the streamwise velocity of the flow itself $\sigma_{v_x,v_y}/\sigma_U$. As it can be seen in this graph, the level of fluctuations of the cable tip velocity is about 6 times larger than the ambient fluctuations of the flow at the highest mean velocities investigated. This indicates that the instability of the tip dynamics is not related to possible reminiscent fluctuations of the flow (we recall that the turbulence level of our tunnel is very small and of the order of a few per thousands only).

**Polystyrene sphere.** The light sphere exhibits a similar dynamical behavior compared to the free end case just described: the fluctuation level is low as soon as the mean wind velocity remains below 5-6 m/s and increases above that threshold. The typical amplitude of velocity fluctuations is slightly larger than that of the free end, but remains of the same order of magnitude. A clear difference concerns the almost perfect isotropy of the fluctuations of the sphere compared to the free end.

**Heavy sphere.** The dynamical behavior of the heavy sphere is clearly different than the previous cases. The fluctuation level is about two orders of magnitude lower than that of the polystyrene sphere or the free end. It is also one order of magnitude below the natural fluctuation level of the flow. It is therefore concluded that the heavy sphere is always towed in stable conditions.

### Spectral analysis

Further insight can be obtained on the dynamics of the towed system by exploring the Lagrangian power spectral density (PSD) of the velocity as a function of the frequency component $f$ for each configuration.

**Free end case.** Figure 5.6a shows the PSDs of horizontal velocity for the free end case at the different mean wind velocities investigated (vertical component exhibit almost identical spectral features). All the spectra naturally vanish at zero frequency which reflects the absence of any mean drift velocity of the tip of the cable which simply wiggles around its average position. The low frequency regime shows a clear $f^2$ law, consistent with a flat spectra for the long-term uncorrelated random displacement of the tip (note that the PSD of the displacement $x$ is simply related to that of velocity $v_x$ by a factor $1/(2\pi f)^2$). A remarkable feature in figure 5.6a is the trend of the spectra to exhibit a clear maximum as the wind velocity $U$ increases. The amplitude and the peak frequency $f_{pk}$ increases with $U$. It can be observed that the first hint of emergence of the spectral peak appears for a mean wind velocity between 6 m/s and 7 m/s, what is comparable to the threshold velocity $U^*$ for which the standard deviation of velocity for the free end was previously noted to start growing. The low frequency $f^2$ regime holds all the way below

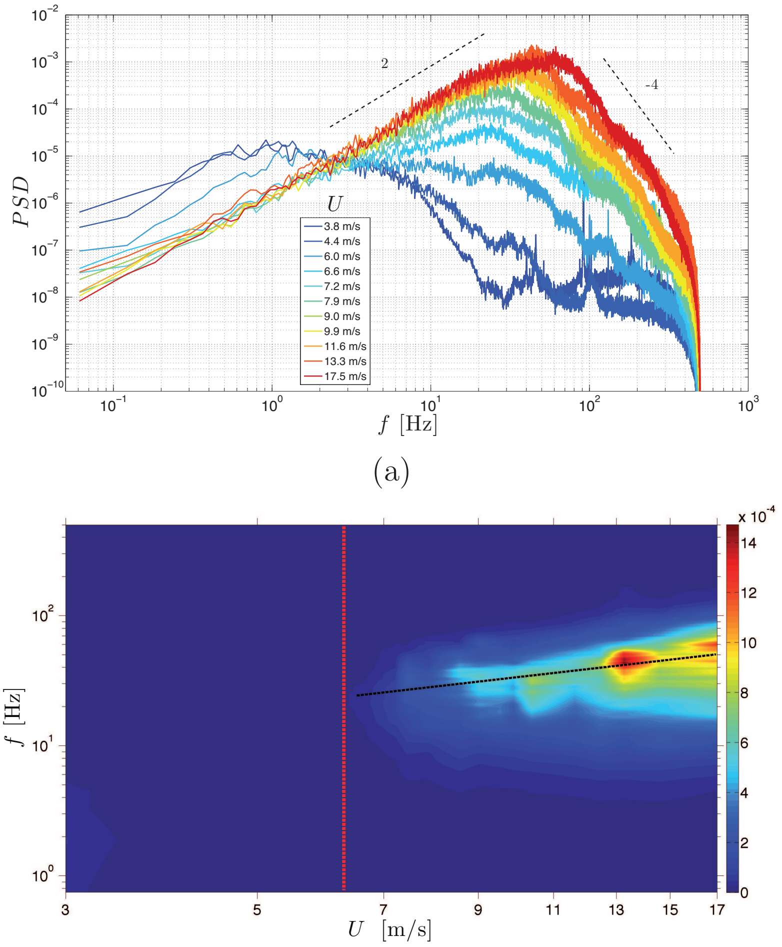

(a)

(b)

Figure 5.6: (a) Power Spectral Density of the velocity fluctuations measured for cable tip with no towed sphere (only the horizontal component is showed). The color codes the mean wind velocity, with the lowest in blue and the highest in red. (b) Interpolated representation of the previous PSDs in the velocity - frequency ($U - f$) plane. The color codes the amplitude of the spectra in logarithmic scale.

the maximum ($f < f_{pk}$). Above the peak ($f > f_{pk}$), the spectral power density decreases rapidly as $f^{-4}$, indicating an efficient dissipative mechanisms of high frequency fluctuations (very likely due to internal viscoelasticity [132] which is known to be important in polymer filaments). We stress that this broad spectral peak does not correspond to an oscillatory mode of the cable tip. Indeed, the corresponding spectra for the particle displacement remains flat for ($f < f_{pk}$) and is damped as $f^{-6}$ for ($f > f_{pk}$). Hence at the instability onset, the cable tip simply wiggles randomly with no characteristic frequency and the peak frequency $f_{pk}$ is simply related to the high-frequency dissipative cut-off.

The onset of the instability of the cable tip is better observed in figure 5.6b where we show a 2D interpolation of the spectra in figure 5.6a in the $(U - f)$ plane (20 measurements for different values of the mean wind speed, between 4 m/s and 15 m/s were used to obtain this interpolation). This representation clearly shows that the tip of the cable becomes unstable for $U \gtrsim 7\ m/s$, with a dominant frequency $f_{pk}$ which increases with $U$ as qualitatively illustrated by the dashed line in figure 5.6b.

**Polystyrene sphere.** The same spectral analysis for the velocity of the light towed sphere shows some similarities but also clear distinctions compared the free end case. Figure 5.7a shows the PSDs for the light sphere towed at different mean velocities. Similarly as for the free end, at low frequencies, the velocity PSDs follow a $f^2$ regime, again consistent with a fully uncorrelated long term dynamics of the sphere displacement. At high frequencies, a steep $f^{-4}$ damping regime is also observed for the highest towing velocities $U$ (though the damping is slightly less steep for the lowest towing velocities). As for the free end case, we observe the growth of a clear peak above a threshold mean wind velocity of the order of 5-6 m/s.

However, the peak is much sharper and clearly defines a resonant frequency $f_{pk}$. The first hint of such a resonant peak, identifiable by the appearance of an inflexion point prior to the spectral maximum, occurs for a wind velocity around $U^* \simeq 5.7$ m/s. This threshold is consistent with the growth of velocity standard deviation previously reported. We also note that above this threshold the amplitude of the resonant peak starts to exceeds the maximum amplitude of the low velocity spectrum. The sharpness of the resonant peak can be quantified by its quality factor $Q = f_{pk}/\delta f$, where $\delta f$ is the 3dB bandwidth. This is shown in the inset of figure 5.7a, which shows that $Q$ exceeds one and grows sharply above $U^*$ until it saturates around $Q \simeq 3.5$ for the highest velocities explored. These observations indicate that the instability of the towed sphere operates via an oscillatory mode. The amplitude and the frequency of the unstable mode increase with the mean velocity $U$. We also note that above threshold, the spectral signature of the dynamics of the sphere for frequencies slightly below the resonant peak is much richer than that of the free end case. The resonance is indeed preceded by a plateau of random velocity fluctuations and the $f^2$ regime is only recovered at the very lowest frequencies (typically for slow fluctuations below 1 Hz). Finally, we note that like for the free end case, the growth of the sphere instability is well illustrated from the interpolated data in the $(U - f)$ plane, shown in figure 5.7b.

**Heavy sphere.** The spectral analysis of the velocity of the heavy sphere reveals a completely different landscape. Figures 5.8a shows the spectra of the horizontal dynamics for the heavy towed sphere (again, vertical component exhibits similar behavior). This dynamics is clearly dominated by slow fluctuations with a resonant frequency peak $f_{pk}$ around 1 Hz, which increases with the mean towing velocity $U$. At low frequencies the spectra follows a $f^2$ regime, though our measurements barely resolve the slowest fluctuations in this case (this is limited by the onboard memory of the camera which limits the total length of the recorded trajectories to slightly less than 20 s). The high frequency damping seems less steep than for the free end and light sphere case and roughly follows a $f^{-3}$ regime. Several narrow peaks are also observed for frequencies above $f_{pk}$ which are probably to be related to spurious noise (we point that for consistency reasons, we used the same optical magnification for imaging the three configurations ; hence the lesser amplitude of fluctuations of the heavy particle inevitably reduces the signal to noise ratio).

To finish the spectral analysis description, we show in figure 5.9a the power spectral densities at a given towing velocity (here $U \simeq 11$ m/s) for the three configurations. This graph is instructive in comparing the dynamics of the three situations:

- Though the standard deviations of the velocity of the free end and the light particle were found to be of the same order of magnitude in figure 5.5, the PSDs in figure 5.9 show that these results from a spurious compensation effect: slow fluctuations are order of magnitude larger for the light sphere, while rapid fluctuations are stronger for the free end. For the towed light sphere case, more thant 50% of the fluctuating energy comes from the narrow 3dB bandwidth around the resonant peak (which corresponds to a band $\delta f \in [22; 29]$ Hz for the data shown in figure 5.9).

- The global amplitude of PSD is order of magnitude lower for the heaviest sphere, which was already illustrated by the standard deviations of velocity, $\sigma_v$ previously discussed (we recall that the variance $\sigma_v^2$ of the velocity is simply given by the integral of the PSD) ;

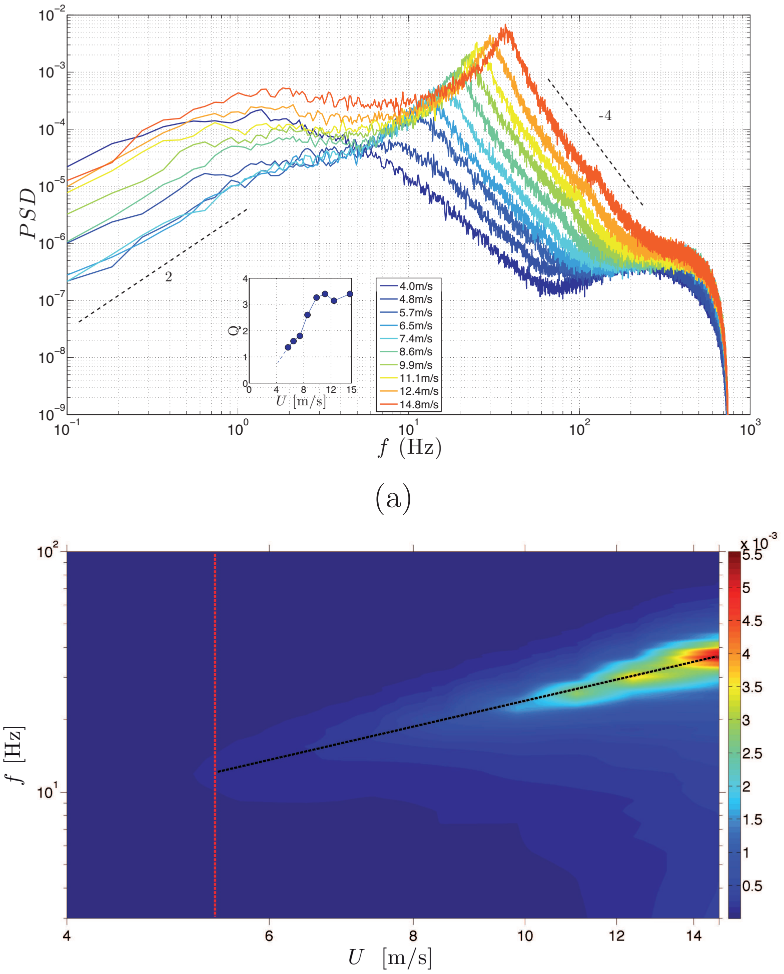

(a)

(b)

Figure 5.7: (a) Power Spectral Density measured for the velocity fluctuations for the towed polystyrene sphere at different towing speeds (only the horizontal component is showed). The color codes the mean wind velocity, with the lowest in blue and the highest in red. Inset shows the quality factor $Q$ of the resonant peak above the threshold instability. (b) Interpolated representation of the previous PSDs in the velocity - frequency ($U - f$) plane. The color codes the amplitude of the spectra.

- The peak frequency of the heavy particle is much lower than that of the free end and the light sphere.

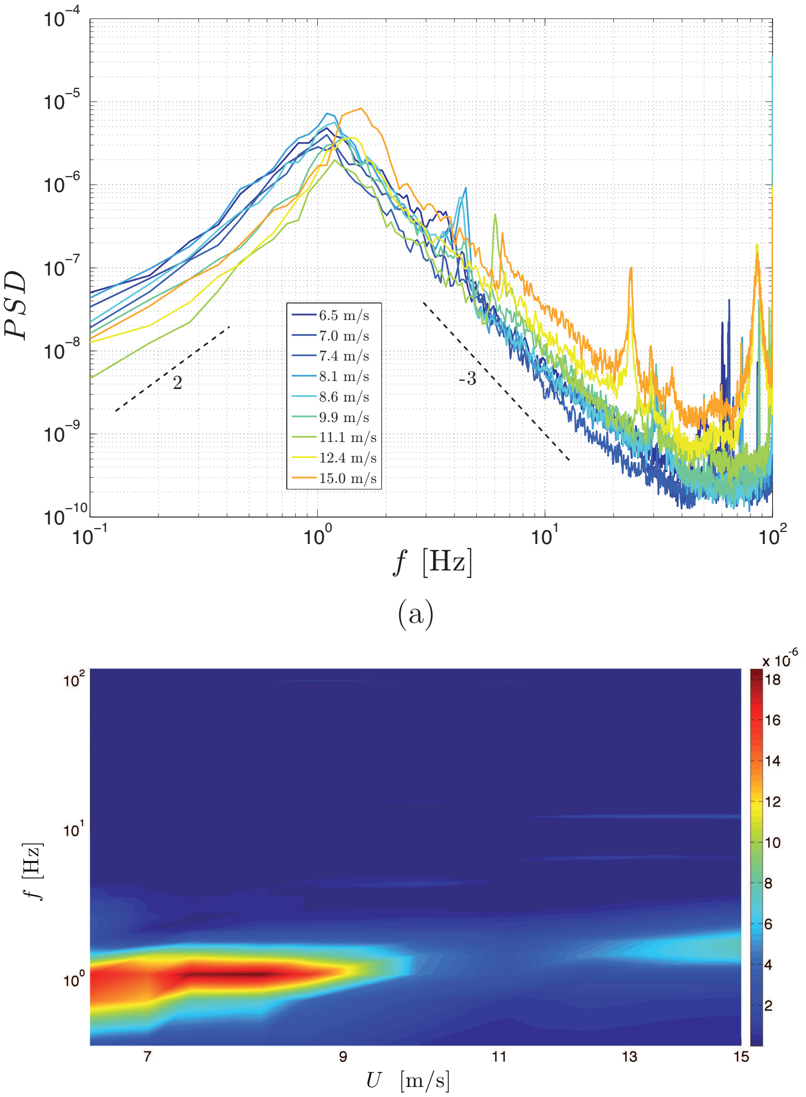

(a)

(b)

Figure 5.8: (a) Power Spectral Density of the velocity fluctuations for the heavy sphere at different towing speeds (only the horizontal component is showed). (b) Interpolated representation of the previous PSDs in the velocity - frequency ($U - f$) plane. The color codes the amplitude of the spectra.

Finally, figure 5.9b shows the dependency of the frequency peaks on the towing velocity $U$ for each case. The free end case and the heavy particle case are well described by a linear law where $f_{pk} \propto U$ whereas the resonant

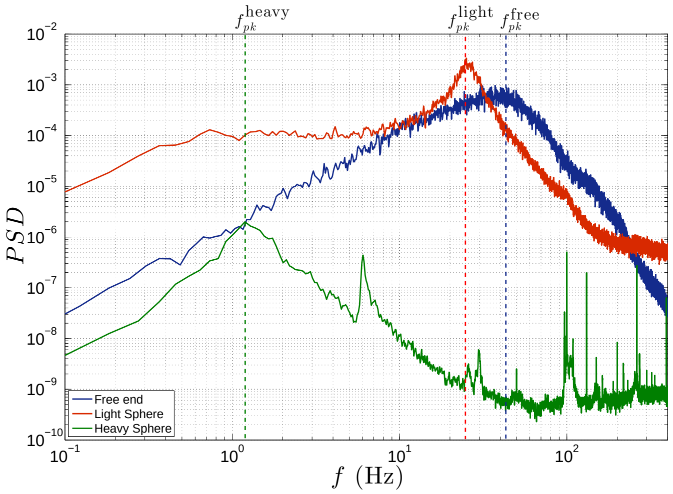

(a)

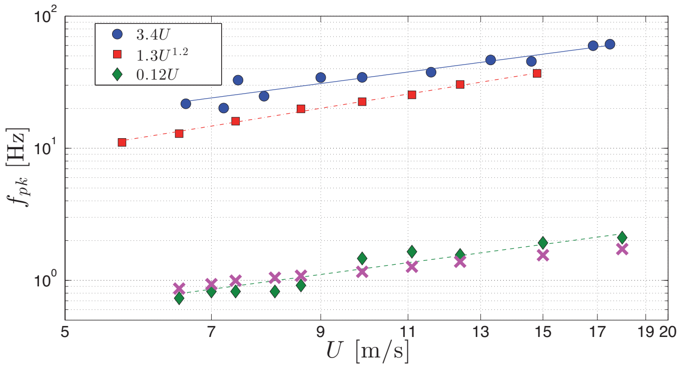

(b)

Figure 5.9: (a) Comparison of the spectral densities for the three towed configurations (free end, light particle and heavy particle) at a given towing velocity $U \simeq 11$ m/s. (b) Dependency of the peak frequency on mean towing velocity $U$ for the three configurations : free end (blue circles), polystyrene sphere (red squares) and lead sphere (green diamond). The lines indicate the best power law fit, whose parameters are given in the legend (note that linear fit indeed correspond to a power law fit for which the best fitting exponent was found to be almost 1). Magenta crosses indicate the estimation of the peak frequency for the heavy lead particle based on a simple pendular model discussed in section 5.3.4.

frequency for the polystyrene particle increases slightly faster and is better described by a power law $f_{pk} \propto U^{1.2}$.

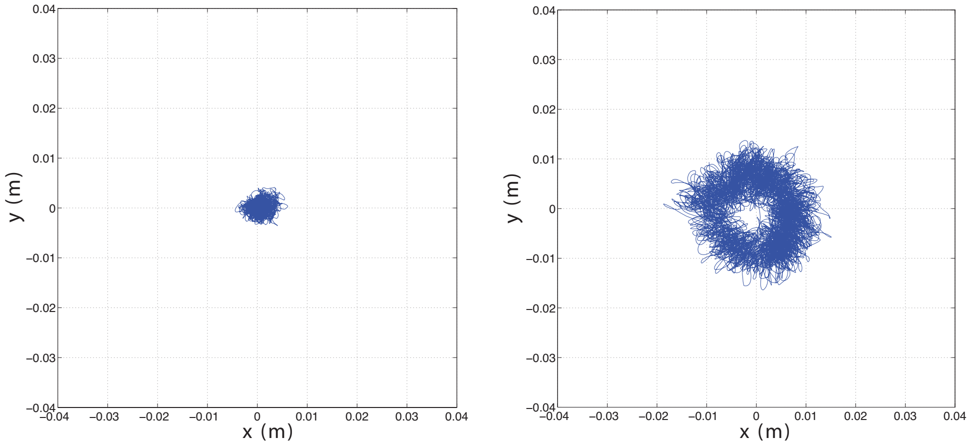

(a) (b)

Figure 5.10: Trajectory in the real space for the light particle for $Re_p = 3.2 \cdot 10^3$ (a) and for $Re_p = 5.2 \cdot 10^3$ (b). The $z$ coordinate is simply $U \cdot t$, with $U$ the streamwise velocity and $t$ the time. The trajectory projected to each plane is also represented (where the base plane is the $xOy$ plane, directly reconstructed by tracking).

### 5.3.3 A second instability towards toroidal trajectories.

Toroidal trajectories (figure 5.10a&b) have been observed for the light particle at high velocities. The nature of this transition to a toroidal regime is not well understood yet, but is an interesting case of this system. Figure 5.11 shows the trajectory for the light sphere at different $Re_p$. It can be clearly seen that at the higher $Re_p$ a different type of motion emerges.

Whereas instabilities described in the previous sections of this chapter are very likely to be connected to the aeroelastic coupling of the cable with the surrounding flow, this toroidal instability is reminiscent of the helicoidal trajectories reported in chapter 4. We would therefore tend to attribute it to a wake instability associated to the sphere itself. In figure 5.12a the square of the polar angle as a function of time for this trajectory. The averaged value shows a quadratic regime at small times (characteristic of a ballistic regime) and a transition to a Brownian regime at bigger times (although more statistics should be needed for be conclusive about this last assumption). Figure 5.12b shows for instance that the typical timescale for the sphere to achieve one loop is of the order of 7 s, hence much slower than the aeroelastic effects, and more comparable to frequencies of the instabilities reported in

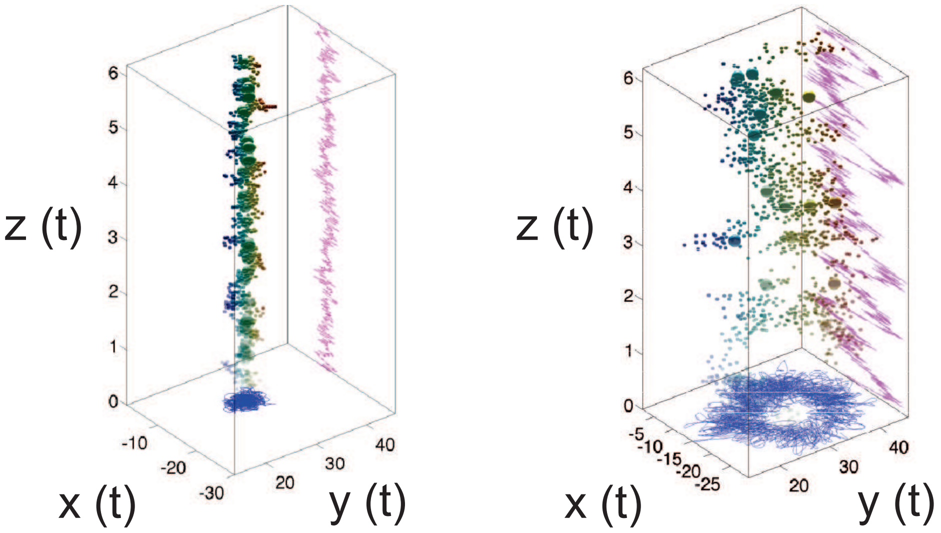

(a) (b)

Figure 5.11: Trajectory in the real space for the light particle for $Re_p = 3.2 \cdot 10^3$ (a) and a high velocity $Re_p = 5.2 \cdot 10^3$ (b).

chapter 4 at lower $Re_p$. Other aspects of this particular trajectories will be studied in the following chapter, where they are going to be compared with the results for a turbulent flow.

### 5.3.4 Discussion

The previous observations show that the dynamics of the free end and that of the light towed sphere becomes unstable above a certain threshold (which is comparable for both situations and of the order of 6 m/s). However, while the simple analysis of velocity standard deviations may have suggested similar dynamics for both cases, the spectral analysis has revealed clear different dynamical landscapes. The heavy particle is on the contrary found to be always towed in stable conditions. In the following paragraphs, we briefly discuss some of these observations.

**Pendular motion of the heavy sphere case.**

Let first discuss the case of the heavy particle. During the experiment, a pendular motion of the sphere, with a relatively short effective pendulum length (compared to the cable length) can be visually observed in the tip

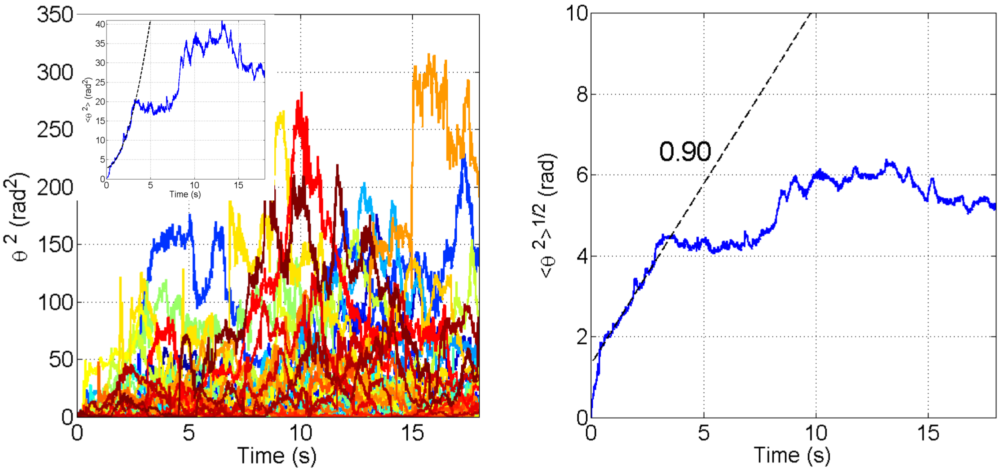

(a)
(b)

Figure 5.12: (a) Square of polar angle of all trajectories recorded at $Re_p = 5.2 \cdot 10^3$ as a function of time (the mechanism for obtaining the polar coordinates is described in the next chapter in paragraph 6.6). The inset shows the averaged curve, that at low time shows a quadratic behavior. (b) Square root of $< \theta^2 >$ and the corresponding linear regime observed at small time. The slope of the line gives a characteristic frequency $\nu = \frac{0.90 s^{-1}}{2\pi} = 0.14$ Hz (that corresponds to a typical timescale of 7 s).

region of the cable. We argue here that the peak observed in the spectrum of the heavy particle is reminiscent of this slow pendulum-like motion. The order of magnitude of the pendular oscillation frequency can be estimated based on a very crude model illustrated in figure 5.13. The profile of the cable is qualitatively approximated by two linear pieces obtained from the tangents at the fixed point and at the tip of the cable, estimated from the calculated equilibrium profile (as shown for instance in figure 5.4b). As shown in figure 5.13, in this crude approximation, the effective length $l_{eff}$ of the pendular motion of the sphere at the tip of the cable represents a fraction of $(y_0 - y_s)$, where $y_s$ is the height of the sphere and $y_0 \simeq 0.4$ m is the vertical ordinate of the cable fixed end. For the sake of simplicity in estimating the order of magnitude of the oscillation frequency, we approximate $l_{eff} \simeq (y_0 - y_s)/2$. The expected frequency for the pendular motion at the tip of the cable can then be estimated as

$$f_0 = \frac{1}{2\pi}\sqrt{\frac{g}{l_{eff}}} \simeq \frac{1}{2\pi}\sqrt{\frac{2g}{y_0 - y_s}} \qquad (5.5)$$

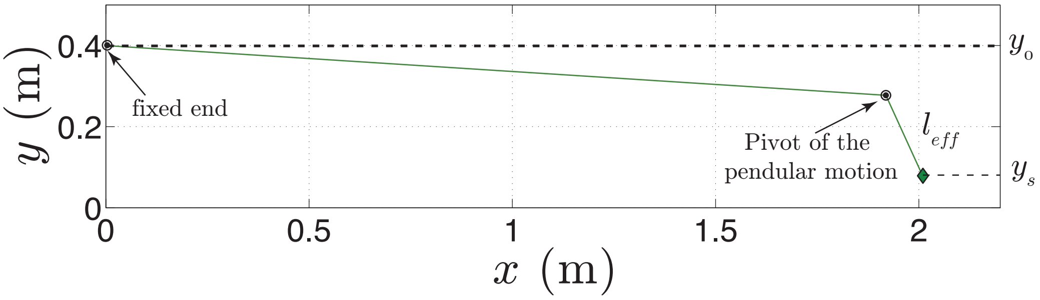

Figure 5.13: Simple pendulum model for the heavy particle, where the profile shown in figure 5.4b is crudely approximated by the two tangent (at the fixed end and at the tip of the cable). The pivot of the pendular motion at the tip of the cable is taken at the intersection of this two lines.

with $g$ the gravity acceleration. The magenta crosses in Figure 5.9b present the corresponding estimate based on the actual measurement of the sphere height $y_s$ shown in Figure 5.4a. In spite of the crudeness of the model a very good agreement is found. The model can certainly be improved by a better piecewise decomposition of the cable, but this simple analysis seems to confirm the pendular origin of the observed spectral peak.

We point however, that except for this pendular motion, the dynamics of the heavy particle remains stable with a level of fluctuation much lower than the free end and polystyrene sphere cases, as shown in figure 5.4a. The stabilizing effect of a heavy mass on the dynamics of towed cables is a well known property in the underwater community. Adding a weight depressor in two-part towing system has become a common strategy to reduce the instability of under-water towed systems [55].

**Divergence instability of the towed cable.**

Concerning the free end case, where the cable is towed by itself, our results are worth to be discussed in comparison with recent numerical simulations of long cylinders in axial flow by de Langre & Païdoussis [22] which we briefly summarize first. Their simulations are the first to show, that contrary to previous predictions [122, 25], long cylinders may become unstable. The existence of the instability for such long cylinders requires bending stiffness effects to be correctly included in the model. It is indeed directly related to the presence of a *neutral point* in the cable at which base drag, axial compressive forces and tangential friction balance. Upstream the *neutral point*, the cable is in tension due to the frictional drag along its length which plays a stabilizing role. Downstream the *neutral point*, the cable is in compression, and no stiffness exists other than flexural rigidity which then needs to be correctly modeled. The position of the *neutral point* along the cable is $x_c = L - L_c$, with [25, 22]

$$L_c = \frac{a_c}{2C_T}(\pi - 2C_b), \tag{5.6}$$

where $C_b$ is the base drag coefficient at the tip of the cable (defined such that $F_{BD} = 1/2\rho D^2 U^2 C_b$ is the base drag force). A necessary condition for the instability to appear is that $x_c < L$ (so that the *neutral point* is actually *in* the cable), which requires $C_b < \pi/2$ (*i.e.* the cable tip must be sufficiently streamlined). More precisely, de Langre & Païdoussis have shown that the instability diagram (see for instance figure 6 in [22]) depends mainly on two parameters: (i) the shape of the downstream end of the cable (characterized by a parameter $f \in [0;1]$ related to base drag and lift coefficients at the tip of the cable (de Langre & Païdoussis use the *ad hoc* empirical relation $f = 1 - 4C_b/\pi$) ; it is such that $f = 0$ for blunt cylinder tips and $f = 1$ for perfectly streamlined tips) and (ii) the ratio $C_N/C_T$ (the range of $C_N/C_T$ investigated by de Langre & Païdoussis is [0.5 ; 1.5]). They find that long blunt cables ($f \to 0$) remain always stable. Above a certain threshold of $f$ (which depends on $C_N/C_T$, but which is typically of the order of $f \sim 0.5$), *i.e.* for sufficiently well streamlined cable tips, a *divergence* instability appears. The typical predicted velocity threshold $U_d^*$ for *divergence* is of the order of some meters per second in the range of parameters they investigated. If $f$ is further increased (the tip becoming even more streamlined) a secondary bifurcation may develop, from *divergence* to *flutter* (the motion of the cable then becomes oscillatory). Results by de Langre & Païdoussis also show that for long cylinders stability analysis becomes independent of the cable length, and only a short portion at the downstream end of the cable is concerned. The length of the unstable portion is given by $L_c$.

A direct quantitative comparison of these numerical results with our experiments is difficult due to the impossibility to exactly match the parameters of the simulation to that of the experiment. The ratio $C_N/C_T$ in the experiment can be estimated from the fitted Reynolds number dependency for $C_N$ and $C_T$ discussed in section 5.3.1. We find it to vary from 0.2 to 1.1 as the flow velocity increases from 4 m/s to 20 m/s typically. It is therefore in a comparable range to that explored by de Langre & Païdoussis. Estimation of parameters $f$ and $C_b$ (characteristic of the tip shape of the cable) in the experiment are more subtle and will be discussed below. It is first interesting to note that several results by de Langre & Païdoussis are in good qualitative agreement with our experiment:

(i) We do observe in the experiment a transition toward a *divergence*, non-oscillatory, instability. The instability appears above a velocity threshold of the order of 6-7 m/s.

(ii) Visual inspection of the cable shows that only a short portion (a few centimeters long) at the downstream end of the cable is destabilized.

(iii) We have carried a few extra experiments, identical to what was presented above but increasing the length of the cable up to 3.5 m. These measurements confirm that the dynamics of the cable tip is independent on the cable length. In particular, instability threshold and PSDs of the cable tip motion are undistinguishable for the 2 lengths.

A more quantitative discussion requires to estimate the base drag coefficient $C_b$ (which controls the position of the *neutral point* on the cable). The presence of the small knot used to visualize the cable tip makes this estimation non trivial. When examined under a magnification lens, the knot appears as a deformed sphere with diameter of the order of $d_k \simeq 2a_c$. The base drag coefficient $C_b$ can be related to the knot drag coefficient $C_k$ by $C_b = \pi/4(d_k/a_c)^2 C_k$ (approximating the projected area of the knot as $\pi d_k^2/4$). Considering the low value of the Reynolds number $Re_k = Ud_k/\nu$, and approximating $C_k$ by the drag coefficient of a sphere of diameter $d_k$, we can estimate $C_k \simeq 24/Re_k$. Hence, base drag coefficient can be estimated as: $C_b \simeq \frac{6\pi\nu}{Ud_k}\left(d_k/a_c\right)^2$. The condition $C_b < \pi/2$ for the neutral point to be in the cable then requires:

$$U > U^* = \frac{12\nu}{a_c^2} d_k. \tag{5.7}$$

Using the values $a_c = 43\mu$m and $d_k = 2a_c$, leads to $U^* \simeq 8$ m/s. Considering the several approximations (in particular regarding the spherical shape of the knot and the estimation of $C_k$) this value is in good agreement with the measured threshold (6-7 m/s). It suggests that the appearance of *divergence* in our experiment is concomitant to the appearance of a neutral point in the vicinity of the downstream end of the cable.

Finally, we note that we do not observe in our experiment any secondary bifurcation toward *flutter* when the cable is towed without any sphere attached. A possible explanation for that may be also related to the small knot at the tip of the cable. This tends to make the tip of the cable not very well streamlined and hence not suitable for *flutter* according to de Langre & Païdoussis results.

**Oscillatory instability of the light towed sphere.**

An oscillatory instability is however found when a light sphere is towed at the tip of the cable. The frequency of the observed oscillations increases from 10 Hz to about 40 Hz in the range of wind velocities explored above the instability threshold (from 5 to 15 m/s). It is enlightening to note that this range of frequencies is inconsistent with simple mechanisms such as vortex shedding, pendular motion of the sphere, vibrating eigenfrequencies or elastic oscillations:

- *Vortex shedding:* in the range of Reynolds number considered for the sphere ($Re_p = d_pU/\nu > 2000$, above the instability threshold), its Strouhal number can be considered as constant and of the order of $St \simeq 0.2$. The vortex shedding frequency $f_p^{shed} = StU/d_p$ should therefore exceed 120 Hz for wind velocities above 4 m/s. Such high frequencies are in the damped region of the spectra of the particle motion (see figure 5.7a), and have not been detected in the experiment. Note that vortex shedding has also been shown to be inconsistent with instabilities observed in under-water systems [6]

- *Pendulum oscillations:* when it is aligned with the main stream, a pendulum motion of the sphere can be expected to appear with a characteristic frequency $f_p^{pend} = 1/2\pi\sqrt{T_{tip}/m_pL}$, where $T_{tip} = \pi/8d^2C_pU^2$ is the aerodynamic drag exerted on the sphere and $m_p \simeq 1.8$ mg is the mass of the sphere. In the range of particle Reynolds number considered here, drag coefficient $C_p$ is almost constant and of the order of 0.7. Hence $f_p^{pend}$ can be estimated to increase almost linearly from 2 Hz to about 4 Hz, when the wind speed is increased from 5 m/s to 15 m/s. Such a low frequency peak is not visible in the spectra in figure 5.7a. Besides, the frequency peak would be expected to be modified when the cable length is changed. The few experiments we carried with the longer cable, show that the spectral peak reported in previous section is not affected by the length of the cable.

- *Vibrating string frequencies:* one may also expect frequencies resulting from vibration modes of the tensed cable to appear. In the present case, where the cable has one fixed end and one free end, vibrating modes would have wavelengths $\lambda_n = 4L/(2n+1)$ (with $n \geq 0$). The corresponding eigenfrequencies are $f_p^n = (2n+1)/4L\sqrt{T_{tip}/\mu}$, where $\mu = 1.7$ mg/m is the lineal density of the cable and $T_{tip}$ is the main tensioning force due to aerodynamic drag on the sphere. We note that the given expression for $f_p^n$ assumes the tension to be constant along the cable and of the order of $T_{tip}$. This is not exactly the case, as frictional drag imposes a linear increase of the tension from the fixed upstream end of the cable to the downstream end (where tension is maximal and equal to $T_{tip}$). Hence the estimation given here should be taken as an upper bound of the eigenfrequencies. Let consider the case $U = 10$ m/s as an example for discussion. Using $C_p \simeq 0.7$, we estimate $T_{tip}^{10\ \mathrm{m/s}} \simeq 1.3 \cdot 10^{-3}$ N. The first ten vibrating eigenfrequencies are therefore expected to be $f_p^{n=0\to 9}[0.11; 0.32; 0.53; 0.74; 0.94; 1.2; 1.5; 1.6; 1.8; 2.0]$ Hz, and are much lower than the resonant peak observed in figure 5.7a. Figure 5.9b shows that the experimental resonant peak for $U = 10$ m/s appears at a frequency $f_{pk} \gtrsim 20\ Hz$. In the vibrating string scenario, this would correspond to a high order mode ($f_p^{100} \simeq 21$ Hz). Besides, in such a scenario, a whole set of eigenfrequencies should be visible in the spectra, what is not the case here. Finally, in this scenario, a length dependency would also be expected.

- *Elastic oscillation of the cable:* another simple possible oscillatory mechanism would result from the elasticity of the cable. This would generate a natural oscillating frequency $f_p^{elast} = 1/2\pi\sqrt{k/m_p}$, where $k$ is the elastic constant of the cable. The constant $k$ can be estimated from the elastic properties of Nylon 6,6 given in table 5.1 ; it is of the order of $k = 2.3$ N/m. The elastic frequency is therefore expected to be of the order of 5 Hz. It is again much lower than the observed resonant peak. Besides, the elastic frequency is expected to remain independent of wind velocity, while figure 5.9a shows a clear increase of the resonant frequency $f_{pk}$ as $U$ increases. However, the order of magnitude of the elastic frequency may be consistent with the low frequency plateau observed in figure 5.7a and which seems to be independent of $U$.

- *Wake instabilities:* in a more general case than a simple vortex shedding scenario, the instabilities studied in chapter 4 may be also responsible for the motion of the light sphere. The frequencies observed in chapter 4 (as shown in figure 4.10b) are in the order of 0.1 Hz, hence much slower than those reported here. Furthermore, in the previous chapter the frequencies tend to decrease with $Re_p$, while the frequencies of the light particle in this chapter grow with $Re_p$. Nevertheless, the wake instability may be responsible of toroidal trajectories reported in paragraph 5.3.3.

As a consequence, none of these simple mechanisms can explain the observed spectral peak. Our interpretation is that these oscillations are related to a *flutter* instability of the cable tip. This is also supported by the visual inspection that only a short section, a few centimeters long, in the vicinity of the downstream end of the cable is unstable. At first sight, *flutter* may appear contradictory to the qualitative conclusions by de Langre & Païdoussis concerning the requirement of a very well streamlined tip. However, results from de Langre & Païdoussis cannot be directly extrapolated to the present case as the characteristic physical parameters differ by orders of magnitude. The base drag coefficient $C_b$, estimated from the aerodynamic drag on the sphere as $C_b = \pi/4(d_p/D)^2 C_p$ exceeds for instance $10^4$ in the experiment while it is of order one at most in simulations by de Langre & Païdoussis. We also note that in our experiment no *divergence* is observed prior to the oscillatory instability of the towed sphere.

## 5.4 Conclusion

In this chapter we have reported the experimental investigation of the equilibrium and stability of a cable hanging in a uniform flow of air with one fixed end and three configurations for the free extremity : free cable, light polystyrene sphere and heavy lead sphere. The system mimics the situation of a long towed cable at constant velocity in a steady environment. An important aspect of this work is the length to diameter ratio considered for the cable which to our knowledge is the highest ever reported in experimental studies.

The average equilibrium position of the system is found to be consistently described by equations for the local average tension and angle of the cable given by [25] and estimates of drag coefficients for cables [123] and spheres [13] in the literature.

The stability analysis turned out to be an interesting fluid/structure coupling problem. Depending on the situation we observed that the system could remain always stable (heavy towed particle) or could become unstable with either a *divergence* instability (when the cable is towed alone) or an oscillatory motion (when a light sphere is towed).

For the heavy particle, only small oscillations consistent with a pendular motion, are observed. We note however that we could not reach velocities high enough for the cable to even approach an axial flow condition and the question of a possible instability at higher velocities is not excluded.

The case of the cable alone, is found to be qualitatively consistent with recent simulations of long cylinders in axial flows by de Langre & Païdoussis [22]. The threshold of the instability is found to coincide with the appearance of a neutral point at the downstream end of the cable. No secondary instability toward *flutter* was observed.

The instability for the light sphere exhibits oscillations with a clear resonant frequency which is inconsistent with simple mechanisms as vortex shedding, pendular motion, string vibrations, elastic oscillations or wake instabilities (as reported in chapter 4). We therefore interpret it as a *fllutter* instability. This should be confirmed by further simulations of the cable stability, accounting for the particular boundary conditions associated to the presence of the sphere at the downstream tip.

From a practical point of view, our results may also be relevant for strategies of stabilization of towed systems, as the use of weight depressors. Our experiment shows indeed that depending on the size and/or density of the added weight, the system can be stabilized or on the contrary oscillations can be promoted.

Although much remains to be done to obtain a complete and reliable description of such long towed systems, we hope that the present work will offer valuable experimental data to be confronted to future theoretical and numerical models.

It is striking how by changing the $Re_p$ of the system a totally different physics emerged when comparing to chapter 4. Instabilities in the system in chapter 4 were clearly dominated by wake effects of the towed object with negligible effects of the towing cable. In the present chapter (where much higher towing velocities were considered) aeroelastic instabilities of the cable become dominant, while the towed object essentially influences these aeroelastic phenomena as a boundary condition effect. Wake effects seem marginal and may be responsible of a slow helicoidal motion observed for the polystyrene towed sphere. In the next chapter it will be shown that when changing the streamwise laminar flow for a turbulent one, new exciting physics emerges again.

# Chapter 6

# Equilibrium and stability of long towed cable systems. Part II: the role of turbulence

## 6.1 Introduction

In chapter 5 a towed system in laminar conditions has been studied. In this chapter we will study how environmental turbulence affects previous results. A particle towed at constant speed by a turbulent flow is also of great interest as it constitutes an intermediate case between the static and the freely advected particle.

Turbulent transport of material inclusions plays an important role in many natural and industrial situations. From a quantitative point of view, no general and reliable model to describe and accurately predict the statistical properties of inclusions advected by a turbulent flow has emerged yet. As it has already been detailed in chapter 1, even writing an appropriate equation of motion for a particle transported by a turbulent flow remains a theoretical challenge, which has mostly been approached in some limit cases, assuming generally point like particles, as the celebrated Maxey-Riley-Gatignol equation [61, 36] which assumes point particles as it neglects non-uniformities of the flow field around the particles. In most theoretical and numerical studies, this equation is further simplified and inertial effects are dominantly modeled by the Stokes drag force resulting from the finite response time $\tau_p$ of the particle. In such models, dynamics of the particle is simply coupled to that of the carrier flow by a Stokesian equation of motion :

$$\frac{\mathrm{d}\vec{v}}{\mathrm{d}t} = \frac{1}{\tau_p}(\vec{u} - \vec{v}), \tag{6.1}$$

where $\tau_p$ is the particle's viscous response time, $\vec{v}$ is the particle's velocity and $\vec{u}$ is the fluid's velocity at the position of the particle. The actual range of validity of this approximation remains unclear. Recent experimental and numerical investigations have shown that this assumption fails to predict simple dynamical features of small though finite size inertial particles [98]. For instance, while the dominant drag force assumption predicts a low-pass filtering effect of particle velocity fluctuations with increasing inertia, measurements show that the fluctuation level of inertial particle velocity remains identical to that of the carrier flow, even when the particle inertia is large (as has been already shown figure 1.6a in chapter 1). Similarly, Stokesian models predict a gaussianization of particle acceleration statistics as inertia is increased [9], while no such trend is observed experimentally for finite size inertial particles [98, 42], (figure 1.6b in chapter 1). These observations raise the question of the exact role of the drag force in the equation of motion of advected particles. When is the drag term really dominant? When can the particle dynamics indeed be related to that of the carrier flow by a simple filtering mechanism?

Besides the interest from the point of view of towed systems in turbulent conditions, the study presented in this chapter has also been motivated by these questions. The towing configuration appears indeed as potentially interesting to emphasize the role of drag and of filtering effects in particle-turbulence interaction processes. The strong mean relative velocity $(\vec{u} - \vec{v})$ imposed between the fluid and the particle in this configuration, forces the drag to become indeed an unambiguous leading term of the forcing from the fluid onto the particle. The towing system considered is identical of the one described in the previous chapter. Spheres are towed using a thin and long cable. From the particle-turbulence interaction point of view, the towed sphere can therefore be considered as a a semi-constrained inclusion (its motion is constrained to remain in the $xOy$ plane) interacting with a carrier turbulent flow where the role of drag can be expected to play a role. From the point of view of towed systems, the role of the cable and its instabilities is also to be considered.

## 6.2 Experimental setup

The experiment has been run in the wind tunnel SFT1 (chapter 2), were the turbulence was generated by the passive grid (figure 6.1). The active grid was also used, but the particle trajectories were so fluctuating that they crashed onto the walls, making any systematic study impossible. Therefore,

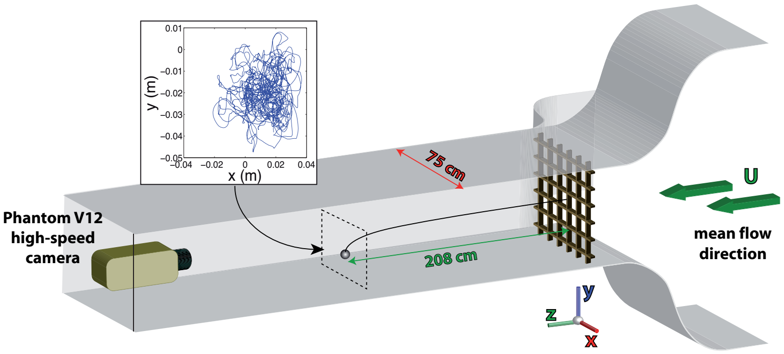

Figure 6.1: The measurement plane is located 2.08$m$ downstream the grid, in a region where the turbulence is fully developed, homogeneous and isotropic.

we considered three different mean streamwise velocities with the passive grid for the experiments: $U_{z1} = (7.33 \pm 0.11)m/s$, $U_{z2} = (9.89 \pm 0.08)m/s$ and $U_{z3} = (12.44 \pm 0.07)m/s$ (mean velocity $U_z$ is adjusted using a Pitot anemometer). In the following we will refer to the streamwise velocity as $u_z = U_z + \tilde{u}_z$ with $U_z$ as the mean streamwise velocity and $\tilde{u}_z$ its fluctuating part. In the considered wind tunnel, the turbulence intensity $\tau_\epsilon = \tilde{u}_z/U_z$ is known to be constant and of the order of 3%.

The turbulence parameters induced in the tunnel for these velocities are shown in the table 6.1 (these values have been calculated using the results from previous studies on the same wind tunnel [62]).

| | $U_{z1}$ | $U_{z2}$ | $U_{z3}$ |
|---|---|---|---|
| $\eta$ (m) | 3.22x$10^{-4}$ | 2.57x$10^{-4}$ | 2.16x$10^{-4}$ |
| $Re_\lambda$ | 125.7 | 146.0 | 163.7 |
| $\lambda$ (m) | 0.0064 | 0.0055 | 0.0049 |
| $\epsilon$ (W/kg) | 0.3148 | 0.7718 | 1.5376 |
| $\tau_\eta(s)$ | 0.0069 | 0.0044 | 0.0031 |
| $T_e(s)$ | 0.1800 | 0.1335 | 0.1061 |

Table 6.1: Turbulence parameters for the velocities used. The parameter $\eta$ is the Kolmogorov length scale and $\tau_\eta$ its time scale associated, $Re_\lambda$ the Reynolds number, $\lambda$ the correlation length of turbulence, $\epsilon$ is the rate of energy dissipation and $T_e$ is the Eulerian correlation time.

Seven different spheres were used in the experiment and they were all measured with the three different velocities. The parameters of the spheres are shown in table table 6.2, while table 6.3 contains the values of particle Reynolds numbers and the particle viscous response times, estimated according to equation 1.16.

| Sphere | Weight (mg) | Diameter (mm) | Density (kg/m$^3$) | $\delta_{density}$ (kg/m$^3$) |
|---|---|---|---|---|
| 1 | 0.96 | 4.3 | 23.06 | 0.40 |
| 2 | 1.83 | 6.29 | 14.04 | 0.14 |
| 3 | 0.44 | 3.05 | 29.62 | 0.96 |
| 4 | 0.31 | 2.08 | 65.8 | 3.1 |
| 5 | 17.39 | 3.11 | 1104 | 11 |
| 6 | 14.29 | 1.79 | 4758 | 83 |
| 7 | 24.03 | 1.69 | 9510 | 173 |

Table 6.2: Weight, diameter and density of the spheres used in this work.

| Sphere | $Re_p(Re_1)$ | $Re_p(Re_2)$ | $Re_p(Re_3)$ | $\tau_p(Re_1)(s)$ | $\tau_p(Re_2)(s)$ | $\tau_p(Re_3)(s)$ |
|---|---|---|---|---|---|---|
| 1 | 2101 | 2835 | 3566 | 0.039 | 0.030 | 0.024 |
| 2 | 3074 | 4147 | 5217 | 0.036 | 0.027 | 0.021 |
| 3 | 1490 | 2011 | 2530 | 0.033 | 0.026 | 0.021 |
| 4 | 1016 | 1371 | 1725 | 0.046 | 0.036 | 0.030 |
| 5 | 1520 | 2051 | 2579 | 1.248 | 0.966 | 0.782 |
| 6 | 875 | 1180 | 1485 | 2.738 | 2.178 | 1.804 |
| 7 | 826 | 1114 | 1402 | 5.087 | 4.057 | 3.366 |

Table 6.3: Particle Reynolds number and particle viscous time for each sphere and flow Reynolds number.

Particle transverse trajectories were recorded with a high speed camera Phantom V12 from Vision Research Inc. (New Jersey, U.SA.), at a frame rate of 3000 fps (see inset in figure 6.1). Available onboard memory allows to recordings as long as 6.15 s, corresponding to about $\sim 50$ integral time scales of the carrier flow. For each class of particles, we record typically 40 such long trajectories (so that statistics are accumulated over more than 2000 integral time scales of the carrier flow) which are then post-processed to determine Lagrangian velocity and acceleration statistics. The camera is located inside the tunnel, at least 1 m downstream from the particle in order not to perturb its motion.

## 6.3 Post-processing

### 6.3.1 Trajectories

As the particles are large, their position is efficiently determined frame by frame with sub-pixel accuracy with a simple center of mass analysis (following the same scheme as in the previous chapter). As only one particle is present in the field of view, tracking and trajectory reconstruction is trivial, leading for each recording to particle tracks as represented in the inset in figure 6.1.

### 6.3.2 Spectral analysis

Spectral analysis will be a key ingredient in the present work for the characterization of particle trajectories. We present indeed in the following an original approach based on spectral analysis which allows us to accurately estimate statistical quantities (variances of velocity and acceleration), minimizing biases from noise and avoiding data filtering with arbitrary parameters, which is a recurrent issue when it comes to analyze Lagrangian data using for instance Gaussian kernels [70] or local parabolic fits [131]. We also consider spectral analysis to access the energy transfer function $H^2 = \frac{\|\widehat{v}\|^2}{\|\widehat{u}\|^2}$ between the dynamics of the particle and the carrier flow in the spirit of the seminal analysis by Tchen and Hinze for freely advected particles, and we seek for possible filtering mechanisms coupling the dynamics of the particle and the carrier turbulence (as explained in chapter 1).

For a given experimental configuration Lagrangian spectra of position, velocity and acceleration components are first estimated for each individual trajectory. At this point, velocity and acceleration are simply calculated as time differences of the position, without any filtering procedure. This is intentionally done so, in order to keep a maximum of spectral information, including information on noise level (which is very sensitive to differentiation), usually withdrawn by filtering the position. We then average all the individual spectra to obtain an estimation of the Lagrangian spectra of each class of particle. Figure 6.2a shows such typical spectra for particle position, velocity and acceleration. We also note that velocity and acceleration spectra can be consistently estimated from position's spectrum by simply multiplying it by $(2\pi f)^2$ and $(2\pi f)^4$ respectively (from now on $f$ is the frequency variable in Hz in Fourier space). Physical results from these spectra will be discussed in the following sections, but for post-processing purposes we note here a common feature observed on the spectra for all the trajectories recorded in the present study: it has been observed in all the spectra that at high frequency they follow a power law energy dissipation cut-off, as represented by the dashed line in figure 6.2a. Deviation at high frequencies from this power law appears when noise level is reached.

The following section describes a new estimator of Lagrangian variances (of position, velocity and acceleration) from the spectral properties of the trajectories.

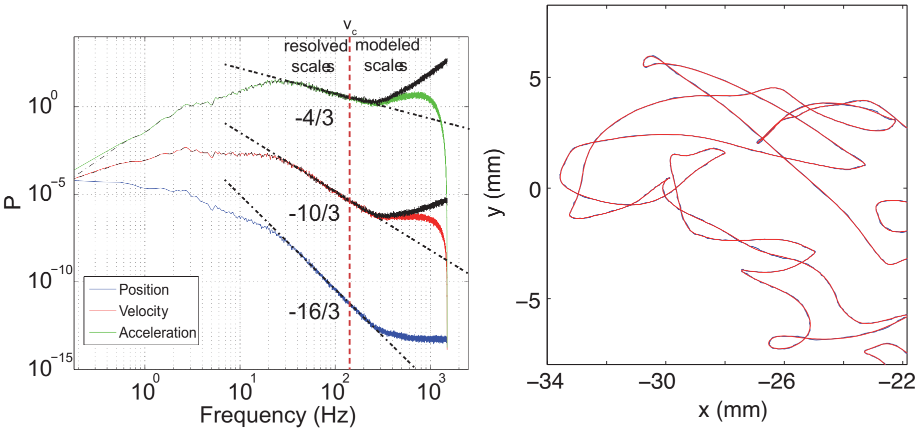

(a) (b)

Figure 6.2: (a) Spectra for particle with $St = 4.8$. The blue line is the position spectrum, the red and green lines are the velocity and acceleration spectra, respectively. The black line represents the velocity and accelerations spectra calculated from the position one multiplied by $(2\pi f)^2$ for the velocity and by $(2\pi f)^4$ for the acceleration. Dashed-lines represent power-law behaviors at high frequency before noise level is reached (exponent is 5.3 for position, 3.3 for velocity and 1.3 for acceleration) ; $f_c$ is the cut-off frequency above which the signal is modeled for the E-LES estimation of variances. (b) Raw trajectory (blue line) and trajectory low-pass filtered representing only the *resolved* dynamics below $f_c$ (red line).

### 6.3.3 "Empirical Large Eddy Simulation" (E-LES): a new estimator of variances and correlation functions

Classically, noise of the reconstructed trajectories in Lagrangian turbulence research is removed by low-pass filtering the signal at an *optimal* frequency cut-off $f_n$ which *preserves most of the signal and eliminates most of the noise* (criteria in italic in the previous sentence are generally mostly qualitative and subjective, rather than quantitative and objective). An usual way is to filter the signal using a gaussian kernel (derivatives of gaussian kernels are used to filter and differentiate the signal simultaneously), where the kernel width is spanned and the optimal value is chosen based on the estimation of the variance of the filtered acceleration [70] (in the present data, such *optimal* filtering frequency would lie somewhere between 200 Hz and 300 Hz). In spite of the optimization of the choice of this cut-off frequency, the filtering

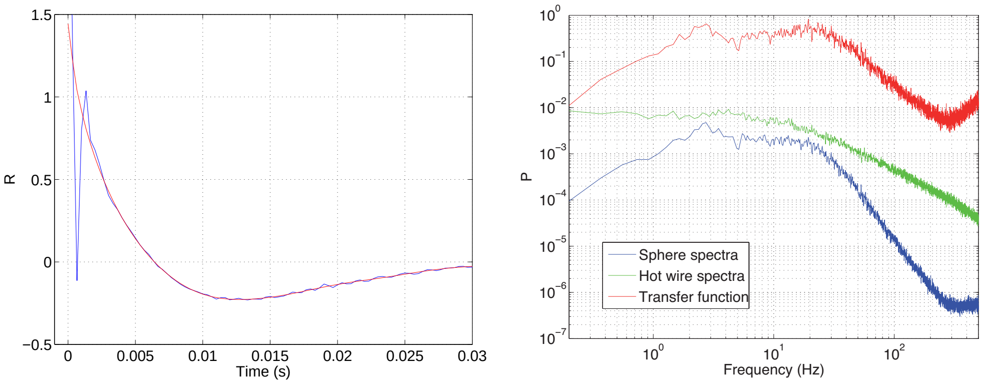

(a) (b)

Figure 6.3: (a) Correlation function obtained with the non-filtered spectra (blue line) and with the filtered one (red line). (b) Typical velocity spectrum of a particle (blue line), flow spectrum from hot-wire anemometry (green line) and energy transfer function (red line) obtained as the ratio of the previous values.

process necessarily results in an underestimation of fluctuation level, as energy at high frequency is removed simultaneously with the noise. Though this is generally negligible for position or velocity fluctuations which are essentially large scale quantities (with a sharply decreasing spectrum at small scales), it can become a significant bias for the estimation of acceleration variance requiring empirical compensations. For instance, the *rule of the thumb* to estimate the variance of Lagrangian acceleration of tracers from particle tracking measurements is to take 80% of the value of the linear extrapolation to zero of the trend with kernel width of the variance of filtered acceleration. Such empirical procedures for the estimation of Lagrangian variances are a recurrent problem in the community.

Here we propose a new estimation of variances of position, velocity and acceleration, based on the analysis of the signal spectrum. We first recall that the variance of a given quantity $q$ can be estimated from its spectrum as $\sigma_q^2 = \int \|\widehat{q}^2(f)\| \mathrm{d}f$. Therefore, instead of simply filtering arbitrarily the signal which drastically eliminates the high frequency contribution to the total variance, we propose to model the high frequency behavior of the spectra using the best available empirical trend, based for instance on the measured spectrum at high frequency but before the onset of noise. This approach is similar to LES (*Large Eddy Simulation*), we call it Empirical-LES (E-LES): we consider the scales above the experimental noise level as being *resolved* and we choose to model the *unresolved* small scales. In practice the actual cut-off frequency $f_c$ defining the resolved and modeled scales will be chosen for scales slightly larger than the noise limit, as illustrated in figure 6.2a. In the present study, the small scale model for unresolved scales is empirically chosen based on the power-law behavior observed for the smallest resolved scales. Compared to simple classical filtering approach, the benefit here is that, though we cannot completely warrant the extent of validity of the small scale model, we do not simply withdraw high frequency contributions but we model them with an empirical and non arbitrary correction. This approach is also convenient as the estimation of variances for velocity and acceleration can be mostly obtained from information on position only, as the spectra of velocity and acceleration are trivially obtained from that of position, thus reducing errors from signal differentiation.

In the end, the variance of position, velocity and acceleration is estimated as the contribution of the resolved scales (which can be equivalently obtained either as the integral of the spectrum up to $f_c$, if the slow dynamics is resolved for sufficiently low frequencies, or as the variance of the *resolved* temporal signal low-pass filtered below $f_c$ – see figure 6.2b –) to which we add the contribution of the small scales estimated as the integral above $f_c$ of the model for the high frequency unresolved spectrum. When the high frequency model for the position spectrum is a power law $Af^\alpha$, the standard deviations can be calculated using the following formulas :

$$\sigma_x = \sqrt{< x_f^2 > + \frac{A}{\alpha+1}\left[\left(\frac{f_s}{2}\right)^{\alpha+1} - f_c^{\alpha+1}\right] - < x >^2}, \tag{6.2}$$

$$\sigma_{vx} = \sqrt{< v_{xf}^2 > + \frac{A}{\alpha+3}\left[\left(\frac{f_s}{2}\right)^{\alpha+3} - f_c^{\alpha+3}\right] - < v_x >^2}, \tag{6.3}$$

$$\sigma_{ax} = \sqrt{< a_{xf}^2 > + \frac{A}{\alpha+5}\left[\left(\frac{f_s}{2}\right)^{\alpha+5} - f_c^{\alpha+5}\right] - < a_x >^2}, \tag{6.4}$$

where the subindex $f$ is used to indicate the *resolved* low-pass filtered signal and $f_s$ is the sampling frequency of the acquisitions. The values $A$ and $\alpha$ are obtained fitting high frequency behavior of the spectrum of position modeled as $\|\widehat{x}\|^2(f) = Af^\alpha$. We assume here that noise has zero mean, so that mean quantities $< x >$, $< v >$ and $< a >$ are directly estimated from the raw signal.

Finally, we point that the same E-LES approach also gives an appropriate way to obtain *clean* estimations of Lagrangian correlation functions, in particular for acceleration. Such estimation is indeed generally polluted by the small scale noise, which produces spurious oscillations at short time lags (see figure 6.3a showing the correlation function of acceleration for the raw signal, corresponding to the acceleration spectrum in figure 6.2). Removing such oscillations is usually achieved by filtering the signal in order to eliminate the noise, which generally also results in a widening of the correlation peak which may bias the estimation of the correlation time of acceleration. In the E-LES approach, we can estimate the correlation function as the inverse Fourier transform of the corrected spectrum built as the actual resolved spectrum for frequencies below $f_c$ and extrapolated based on the adopted model for frequencies above $f_c$. The resulting correlation function, shown in figure 6.3a does not exhibit the spurious oscillations any more and preserves the characteristic correlation time scales.

### 6.3.4 Transfer functions

As already mentioned, the present study is highly motivated by the fact that the effect of particle inertia is usually described as a simple filtering effect, where the dynamics of the particle only experiences turbulent solicitations from the carrier flow at time scales typically slower than the viscous response time of the particle $\tau_p$. This is for instance a direct theoretical result of the Tchen-Hinze theory [119], where the Stokesian dynamics of inertial particles freely advected by a turbulent velocity field $\vec{u}$, modeled by equation (6.1) directly acts as a first-order low-pass filter where particle energy spectrum is related to the fluid via an energy transfer function $H_{TH}^2 = \frac{\|\widehat{v}\|^2}{\|\widehat{u}\|^2} \propto 1/(1+f^2\tau_p^2)$ with a low-pass cut-off frequency $f_{lp} = \tau_p^{-1}$. In a more general context, the transfer function approach gives an interesting insight in the coupling between particle and carrier flow dynamics [65].

In the coming sections, we will therefore discuss the experimental energy transfer function

$$H^2 = \frac{\|\widehat{v}\|^2}{\|\widehat{u}\|^2}, \tag{6.5}$$

where $\|\widehat{v}\|^2$ is the particle Lagrangian velocity spectrum and $\|\widehat{u}\|^2$ is temporal spectrum of the background flow measured with classical hot-wire anemometry in the plane of motion of the particle. We note that hot-wire signal directly gives the Eulerian spectrum in terms of the time frequency variable $f$ so that it is not necessary to apply back and forth a frequency/wave number transformation. Figure 6.3b shows an example of experimentally estimated

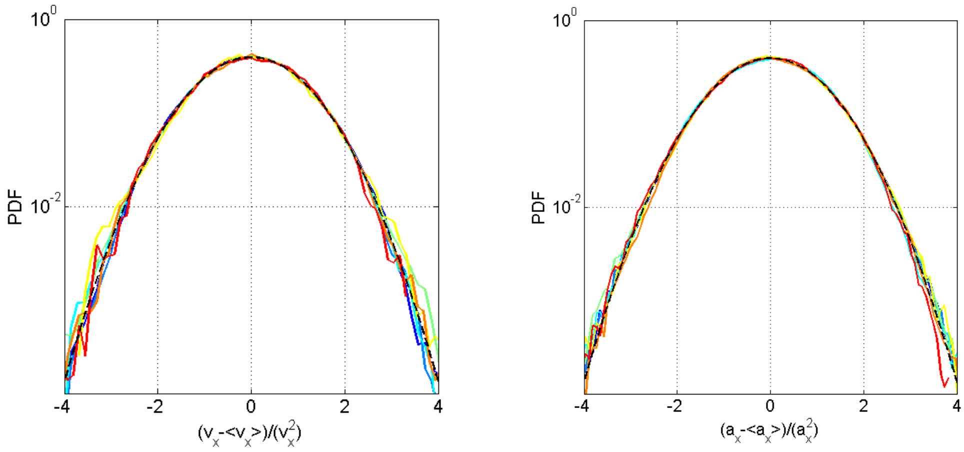

(a) (b)

Figure 6.4: Probability density functions (centered and normalized to variance one) of the horizontal velocity (a) and acceleration (b) for all the particles investigated. The black dashed line, in the figures, is a Gaussian with variance 1. Vertical components (not shown) have identical PDFs.

transfer function for the particle with $St = 4.8$.

## 6.4 Results on the turbulent dynamics of towed spheres

### 6.4.1 Statistical Analysis

Figures 6.4a&b represent velocity and acceleration probability density functions (PDFs) centered and normalized to variance one for all the particles and velocities investigated. Remarkably, all the PDFs collapse onto a single curve which is found to be well fitted by a Gaussian distribution. While gaussianity of velocity statistics was already observed for freely advected particles, gaussianization of acceleration is an interesting finding. Recent investigations made for freely advected finite size particles [98, 136] have shown that the acceleration PDFs remains in that case highly non-Gaussian even for particles with large inertia. This observation has been noted as being in contrast with the prediction from Stokesian models (with a dominant drag force due to particle/fluid relative motion) of the turbulent dynamics of particles which predict a gaussianization of acceleration PDFs for highly inertial particles [9]. Our present measurements show that such gaussianization is indeed observed when a strong dominant slippage velocity and hence a dominant drag force is exerted on the particle, therefore in qualitative agreement with Stokesian models.

As a result of their gaussianity, velocity and acceleration fluctuations are therefore simply characterized by their standard deviations $\sigma_v$ and $\sigma_a$ which we estimate with the E-LES method previously described. Figure 6.5a&b represents the velocity turbulent fluctuations rate for the horizontal and vertical components of the velocity $\tau_{v_{x,y}} = \sigma_{v_{x,y}}/U$ as a function of particle Stokes number (note that, as in the previous chapter, a small anisotropy in particle's dynamics is evidenced by bigger fluctuations in vertical coordinate). Interestingly, we observe that the turbulence fluctuation level $\tau_{v_{x,y}}$ decreases with increasing inertia. This is in contrast with measurements for freely advected particles [98] where the turbulence fluctuation level has been measured not to depend on particles inertia. Moreover the decrease of turbulence level is in qualitative agreement with a low-pass filtering effect due to particle inertia as predicted with drag dominated models in the spirit of the Tchen-Hinze model [119]. We note that acceleration variance is also observed to decrease with increasing inertia (figure 6.5c&d), though this was also observed for freely advected particles. It is significant that, when normalized according to Heisenberg-Yaglom scaling, no trend is observed for acceleration fluctuations when varying $Re_\lambda$, where almost the same curve is reproduced. This suggests that the main forcing on the particle is indeed from the turbulence and not from instabilities in the towing cable as reported in previous chapter.

### 6.4.2 Transfer functions analysis

In order to probe further the filtering scenario, we investigate the power spectra of particle velocity as well as the transfer functions between particle's and carrier flow's energy. Figure 6.6 shows the spectra for all the 7 different particle classes and the three streamwise velocities investigated in the present work. The first remark is that, as for the standard deviations study, the three $Re_\lambda$ show a similar trend, only with a different background. We also observe that, at low frequencies, the spectra are not significantly dependent on particle inertia while on the contrary high frequency cut-off occurs earlier as particles Stokes number increases, consistently with a filtering scenario due to an increased particle response time. For very large inertia, the spectra becomes relatively peaked with a dominant frequency, corresponding to a pendulum mode for the heaviest towed particles, reminiscent of oscillatory modes already reported in laminar conditions.

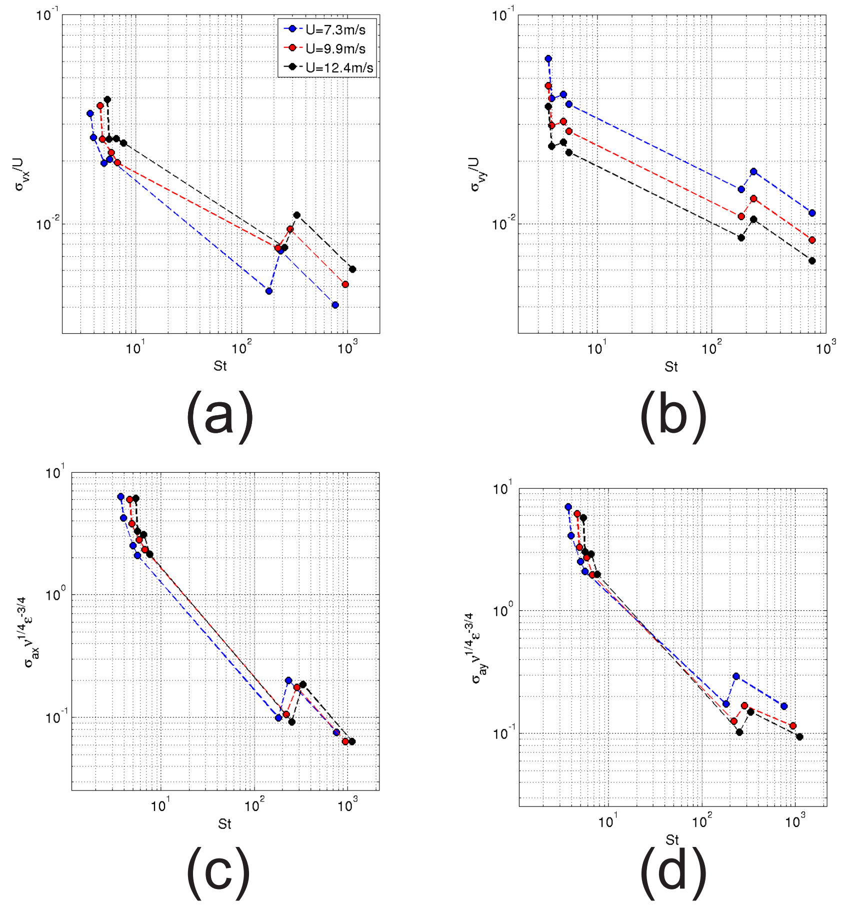

(a) (b)

(c) (d)

Figure 6.5: Fluctuations of horizontal (a) and vertical components of velocity (b). Standard deviations of acceleration normalized with Heisenberg-Yaglom parameters for the horizontal (c) and vertical component (d).

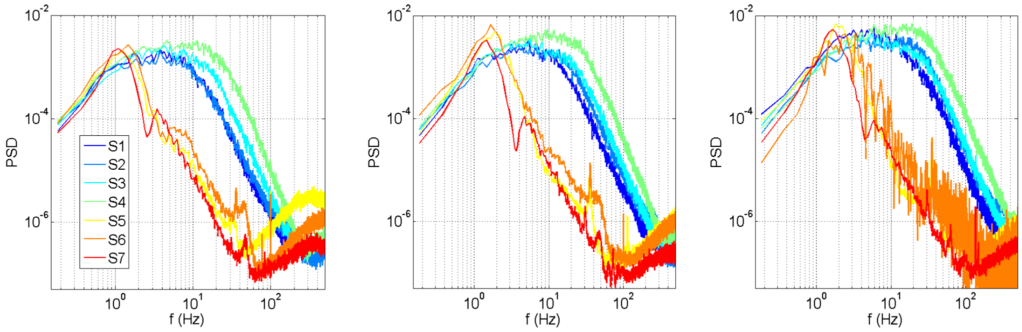

(a) (b) (c)

Figure 6.6: (a) Velocity spectral density for all the particles investigated for $U_z = 7.3$ m/s(a), $U_z = 9.9$ m/s (b) and $U_z = 12.4$ m/s(c).

As in this case again the qualitative behavior is the same for all the velocities studied, from now on we will focus our analysis on just one streamwise velocity, $U_z = 9.9 m/s$. It has been checked that the other $Re_\lambda$ present equivalent properties.

Figures 6.7a&b show two typical energy transfer functions $H^2 = \|\widehat{v}_x\|^2 / \|\widehat{u}_x\|^2$, one for low inertia particles the other for large inertia. The global shape of this transfer function is relatively well approximated as a second order band-pass filter :

$$H^2 = \frac{A}{1 + Q^2 \left( \frac{f}{f_0} - \frac{f_0}{f} \right)^2}, \tag{6.6}$$

with $A$ the gain factor, $Q$ the quality factor and $f_0$ the central frequency. The second order filter can be seen as a combination of a first order high-pass and a first order low-pass filter and can be equivalently characterized by the corresponding low-pass and high-pass cut-off frequencies, $f_{lp}$ and $f_{hp}$ such as $f_0 = \sqrt{f_{hp} f_{lp}}$ and $Q = f_0/(f_{lp} - f_{hp})$.

The fact that we observe a second-order band-pass behavior rather than just a first order low-pass behavior (as in classical Stokesian models for freely advected particles) is related to the fact that in the present configuration the motion of the particles is constrained by the cable. As already discussed in the laminar case, the high pass part (corresponding to low frequencies) follows a $f^2$ regime and is to be related to the interaction of the particle with the towing cable which constrains the motion to be bounded and imposes the average velocity of the particle (and hence the density of energy at vanishing frequency $f \to 0$) to be null. On the other hand, the low-pass part of the

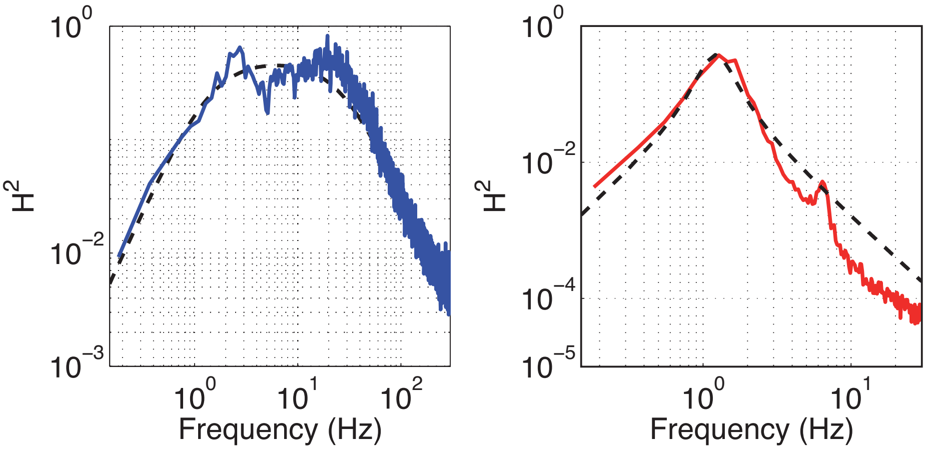

(a) (b)

Figure 6.7: Energy transfer function for particle with $St = 4.8$ (a). Energy transfer function for particle with $St = 950$ (b).

transfer function (related to the high frequency behavior) is expected to be related to particle inertia and to its coupling with turbulence.

This is supported by figure 6.8 which shows the trend with Stokes number of the high-pass and low-pass cut-off frequencies determined from the fit of the measured transfer function with a 2nd order band-pass filter model as defined by equation 6.6. We can observe that the high-pass frequency is independent of particle inertia, while the low-pass frequency does decrease with increasing particle inertia.

## 6.5 Advected sphere in turbulence: the role of filtering effects.

### 6.5.1 Dynamical model for the attached particles motion

As already discussed, Stokesian models cannot be directly applied to the present system as the constraints imposed by the cable must be taken into account. We propose here a simple implementation of Stokesian models to include the role of the cable tension as already briefly presented in equation (6.1). In this first study we assume the cable to be straight, which is indeed the case for the lightest particles (which are also the largest and the ones with the larger Stokes number) and we neglect aeroelastic instabilities of the

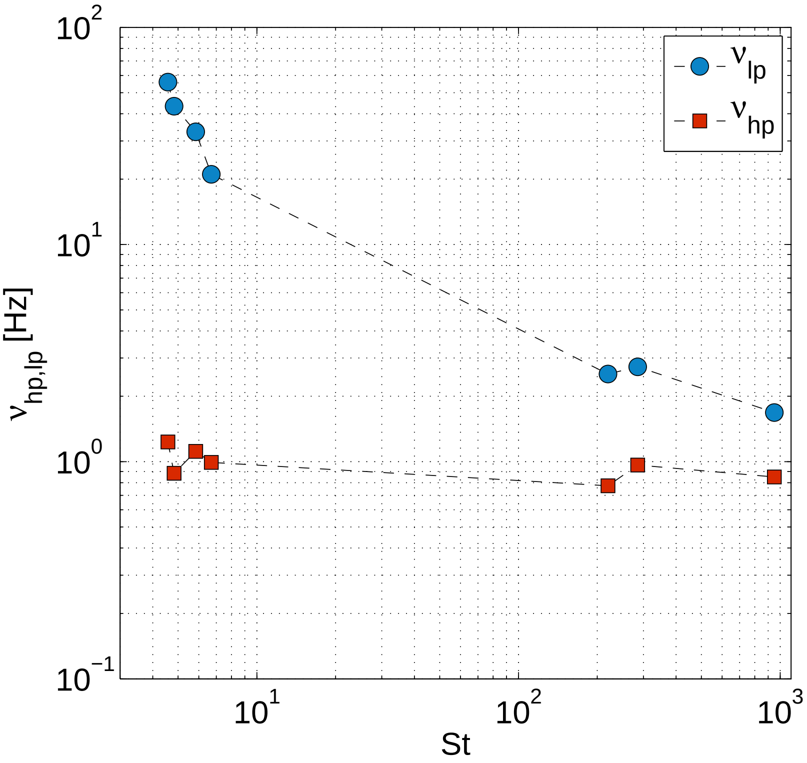

Figure 6.8: High-pass and low-pass frequencies obtained from the 2nd order band-pass model (equation (6.6)) fit of the energy transfer function for all particles investigated, plotted as a function of Stokes number.

cable. The forces acting to the system are shown in figure 6.9[1]. For the system proposed, the equation (6.1) can be written as:

$$\frac{d\vec{v}}{dt} = \frac{1}{\tau_p}(\vec{u} - \vec{v}) + \frac{1}{m_p}\vec{T} + \vec{g}, \tag{6.7}$$

where the added mass term has been neglected. To neglect the added mass term, it is sufficient for instance that $\beta a_c \ll \frac{1}{\tau_p} u_c$, where $a_c$ and $u_c$ are characteristic particle acceleration and fluid velocity respectively and $\beta = 3\rho_{air}/(\rho_{air} + 2\rho_p)$. Considering that the $rms$ values are the characteristic ones, and using the Heisenberg-Yaglom expression ($a_{rms}^2 = a_0 \epsilon^{3/2} f^{-1/2}$ with $a_0 = \mathcal{O}(1)$), this condition can be written as $\beta St \ll U_z \tau_\epsilon / (\epsilon f)^{1/4}$, with

---

[1] A more complex model, considering a catenary shape of the cable is currently being developed.

$St = \tau_p/\tau_\eta$. This condition is satisfied in all cases, and the added force term will not be considered in this model.

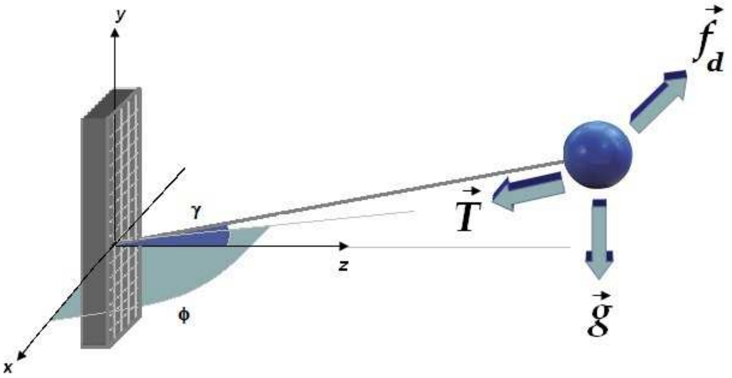

Figure 6.9: Forces acting in the particle: drag force, gravity and tension of the wire.

By projecting this equation of motion on $\widehat{x}$, $\widehat{y}$ and $\widehat{z}$ axis we get :

- $\widehat{z}$)

$$0 = \frac{1}{\tau_p} u_z + \frac{1}{m_p} T \cos\phi \cos\gamma \tag{6.8}$$

where $\gamma$ and $\phi$ are the angular displacements of the wire holding the particle (figure 6.9). Maximal measured displacements of the particle do not exceed 10 cm to be compared to the total length of the wire ($L = 208$ cm). We therefore assume angular oscillations to be small (*i.e.* $\cos\gamma \sim \cos\phi \sim 1$ and $\sin\phi \sim x/L$ and $\sin\gamma \sim y/L$). Moreover, considering that $u_z = U_z + \tilde{u}_z$ with the turbulence level $\tilde{u}_z/U_z \sim 0.03$, the amplitude $T$ of the tension will be approximated as,

$$T = -\frac{m_p}{\tau_p} U_z. \tag{6.9}$$

Thus, we obtain:

- $\widehat{x}$)

$$\frac{dv_x}{dt} = \frac{1}{\tau_p}(u_x - v_x) + \frac{1}{m_p} T \sin\phi \cos\gamma$$

$$\Rightarrow \frac{dv_x}{dt} + \frac{1}{\tau_p} v_x + \frac{U_z}{\tau_p L} x = \frac{1}{\tau_p} u_x \tag{6.10}$$

- $\widehat{y}$)

$$\frac{dv_y}{dt} = \frac{1}{\tau_p}(u_y - v_y) + \frac{1}{m_p} T \cos\phi \sin\gamma$$
$$\Rightarrow \frac{dv_y}{dt} + \frac{1}{\tau_p} v_y + \frac{U_z}{\tau_p L} y - g = \frac{1}{\tau_p} u_y \tag{6.11}$$

Equations 6.10 and 6.11 in the $x0y$ plane are those of a damped oscillator with "noise" (turbulent fields $u_x$ and $u_y$ can be considered as a noise exciting the oscillator).

In the context of oscillators theory, it is relevant to consider the Fourier transform of those equations (from now on just the $x$ coordinate will be studied as the problem in the $y$ axis has the same solution, adding the constant term $g$, which gives a Dirac contribution at zero frequency in Fourier space):

$$-i\omega \widehat{v_x} + \frac{1}{\tau_p} \widehat{v_x} + i \frac{U_z}{\omega \tau_p L} \widehat{v_x} = \frac{1}{\tau_p} \widehat{u_x}, \tag{6.12}$$

$\omega$ being the angular frequency: $\omega = 2\pi f$. The equation can be rewritten as,

$$\widehat{v_x} = \frac{1}{1 + iQ(\frac{\omega}{\omega_0} - \frac{\omega_0}{\omega})} \widehat{u_x}, \tag{6.13}$$

where,

$$\omega_0 = \sqrt{\frac{U_z}{L\tau_p}} \text{ and } Q = \omega_0 \tau_p = 2\pi f_0 \tau_p. \tag{6.14}$$

$\omega_0$ and $Q$ are the filter frequency and the quality factor respectively. This equation is reminiscent of Tchen's filtering equation (as shown in chapter 1) except that the transfer function,

$$H = \frac{1}{1 + iQ(\frac{f}{f_0} - \frac{f_0}{f})}, \tag{6.15}$$

is now a band pass, second order filter instead of a first order low-pass filter (note that in the high frequency limit both are equivalent with a 20dB attenuation rate per decade). This is in qualitative agreement with the results obtained in the previous section.

Furthermore, from the fit of the experimental transfer function we can extract the experimental values of the filter frequency $f_0$ and quality factor $Q$. Image 6.10 shows the theoretical values obtained for $f_0$ and $Q$ as a

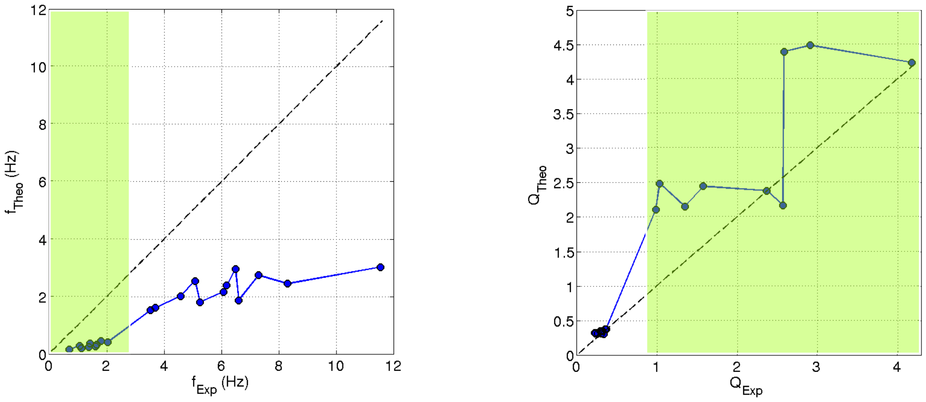

(a) (b)

Figure 6.10: (a) Relation between the theoretical and the experimental values of the frequency (remember that $f_0$ is the frequency in Hz). (b) Relation between the theoretical and the experimental values of the quality factor. In both cases the black dashed line is a line with slope 1 (that represents perfect agreement between theory and experiments). In both figures, the regions highlighted correspond to the four heavier particles, where the cable was not tensed and the hypothesis of the model developed in this section are no longer valid.

function of the experimental ones, where the black dashed lines represents a slope 1 line (therefore, the perfect agreement between theory and experiments). The agreement is far from being quantitatively perfect. Although the order of magnitudes are correct, the theoretical quality factor generally overestimated the experimental one, while the theoretical central frequency underestimates the experimental one. A possible reason for these discrepancies can be the difficulty to correctly estimate the particle response time $\tau_p$, which is a recurrent issue in the community, in particular when finite size and finite Reynolds number corrections are to be considered.

In the context of the filter model introduced previously, $f_0$ and $Q$ appear to be the natural parameters governing particle dynamics (instead of just particle size or density for instance). Therefore we have represented the measured standard deviations as a function of those parameters. Figure 6.11 represents the turbulent fluctuation rate ($\tau_{x,y} = \sigma_{x,y}/U_z$) of particles as a function of the experimental values of those parameters. In spite of some scatter it can be seen that velocity fluctuations tend to increase with $f_0$ whereas it decreases with $Q$. Remembering that $f_0$ is a decreasing function of particle response time $\tau_p$ and $Q$ and increasing function of $\tau_p$ (see definitions 6.14), these trends are in qualitative agreement with the filtering prediction that fluctuations are suppressed when particle response time increases. This result is particularly interesting as no modification of fluctuations has been measured in the case of freely advected particles.

This observation is therefore also a good indicator that filtering effect has indeed been enhanced in the present experiment while it remains marginal in the freely advected situation.

### 6.5.2 Inhibition of intermittency

We continue here the comparison between the case of freely advected inertial particles and the present configuration of a towed inertial particle. We have just noted that the filtering scenario results in a reduction of velocity fluctuations with increasing inertia, which was shown experimentally irrelevant for finite size freely advected inertial particles but becomes relevant for the towed particle. Another important prediction of the Stokesian models is the Gaussianization of acceleration PDFs. Such a progressive inhibition of Lagrangian intermittency as particle Stokes number is increased was also shown in experiments not to be relevant for freely advected finite size particles, which show persistent non-gaussian acceleration PDFs regardless of particle Stokes number. On the contrary, the results for the semi-constrained particle present a remarkable gaussianity. This comparison can be seen in figure 6.12. The presence of wider tails when comparing with a Gaussian distribution is one

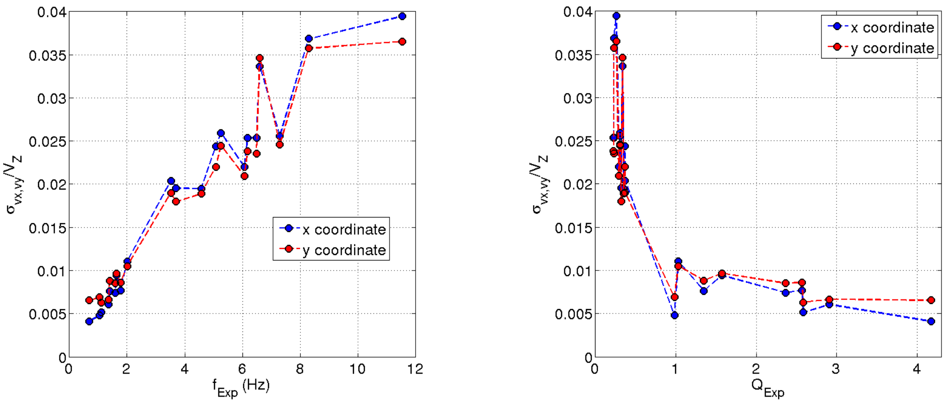

(a) (b)

Figure 6.11: Fluctuations rate for both components ($\sigma_{vx,vy}/U_z$) as a function of the experimental values of $f_0$ (a) and $Q$ (b).

of the characteristic trends of Lagrangian intermittency. Interestingly, the dynamics of the towed particle has lost all evidence of intermittency of the surrounding turbulence. This is consistent with predictions from Stokesian models, where particles with high inertia, and hence with large relative velocities ($\vec{u}-\vec{v}$) are found to have Gaussian acceleration statistics. In the present work the relative velocity is imposed to be important, avoiding the possibility to explore intermediate situations and to investigate the progressive gaussianization process (all the cases we investigated are exactly Gaussian). It would be interesting in the future to investigate situations with less relative velocity. If we want to keep a reasonable turbulence level, this cannot be done by simply decreasing the mean wind velocity. A possible approach may consist in gradually release the longitudinal motion of the towed particle, in order to span all situations from purely towed to freely advected particle. An interesting aspect of such a study will be to address the role of relative velocity, independently of that of the response time of the particle, regarding to intermittency.

### 6.5.3 Turbulent versus laminar towing

To finish this chapter and the first part of this thesis, dealing with single particle-fluid interactions, a comparison of the dynamics of towed spheres in the laminar case (detailed in chapter 5) and in the turbulent situation of this chapter will be made. The discussion proposed in this section is related to the following question: is the particle trajectory more predictable in turbulent or

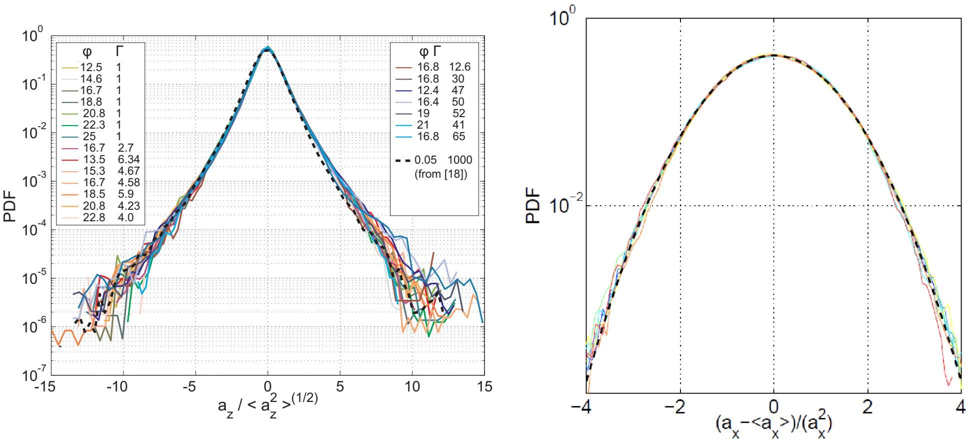

(a)

(b)

Figure 6.12: (a) Acceleration PDFs for freely advected particles measured by Qureshi and collaborators [98]. (b) Acceleration PDFs for semi-constrained particles.

in laminar conditions? On one hand one can argue that the erratic behavior of turbulence may impose randomness to the dynamics of the particle, making its motion more complex, richer and less predictable. On the other hand, if we consider homogeneous and isotropic turbulent conditions, some of the known generic laws of turbulence (as the Gaussianity of velocity fluctuations, the Kolmogorov $-5/3$ energy spectra [51], the large scale Brownian like turbulent diffusion properties, etc.) may be transferred to the particle dynamics. The fluctuations of its motion may then acquire some well characterized universal properties, which may in turn wipe out any subtle effect eventually imparted to the particle by the instabilities reported in laminar conditions, which have been shown to depend significantly on particle class. As a consequence, the dynamics of the particle may then be expected to be less complex and less rich in the turbulent case, but simply obey to some generic statistical properties. In this section we address the question of how universal properties of turbulence influence the dynamics of spheres. To this end, we compare our experimental results of the dynamics of a towed sphere in a fluid under laminar and turbulent conditions. This discussion was motivated by the participation to a workshop dedicated to the physics of sports [18], where we proposed to explore the possible role of turbulence on ball games.

On behalf of a realistic approach, the system consists on a sphere attached to a long cable in a wind tunnel facility. This towed sphere configuration reproduces the situation of a ball traveling across the fluid, with an imposed mean relative velocity. The cable holding the particle helps mimicking subtle effects which would be eventually imparted to the ball by a player. In our system these effects result from the instabilities (both aeroelastic as discussed in chapter 5, or from wake effects as discussed in chapter 4) of the cable-sphere system triggered by the aerodynamic coupling [81] with the surrounding flow. These give rise to a non trivial motion of the sphere under laminar conditions. We investigate how this non-trivial trajectory is affected by the presence of surrounding turbulence.

We will use the results obtained in this chapter for a turbulent flow and in the previous chapter for a laminar one. Considering the present chapter, the first four particles of table 6.2 and 6.3, all of them made of expanded polystyrene have been studied. Then, $Re_p$ varies from 1000 to 6000 depending on particle diameter and flow velocity. Considering the results of the previous chapter, we started the investigation with the largest particle (#2 of table 6.2), for which a systematic comparison of particle trajectory under laminar and turbulent conditions was performed. As discussed below this motivated to extend the investigation in the turbulent case to the other classes of particles.

## 6.6 Results

Figure 6.13a shows examples of trajectories recorded for particle 3 in the case of laminar flow, for two towing velocities. At low velocities the trajectory remains relatively localized and well aligned with the mean velocity. At higher velocities the shape of the trajectory becomes non-trivial and shows the helicoidal behavior already reported in chapter 5, and possibly reminiscent of wake instability reported in chapter 4. In particular, it exhibits a forbidden region in the alignment of the mean velocity, which is statistically almost never explored by the particle. Such toroidal trajectories are systematically observed at sufficiently high velocities in the case of laminar flow. In the context of ball dynamics in sports this peculiar behavior may mimic for instance the trajectory of a ball, with an *easy to catch* case at low velocities and a less predictable kick at higher velocities. This shares similarities for instance with the well known knuckleball [77], that talented pitchers and soccer players are capable to produce and which is feared by batters and goalkeepers.

Figure 6.13b shows the trajectories for the same sphere, at the same velocities, when 3% of turbulence intensity is introduced by the grid at the entrance of the test section. It can be qualitatively seen that trajectories fluctuations are now larger but all the subtle effects present in laminar conditions seem to have disappeared. In particular no transition toward a toroidal

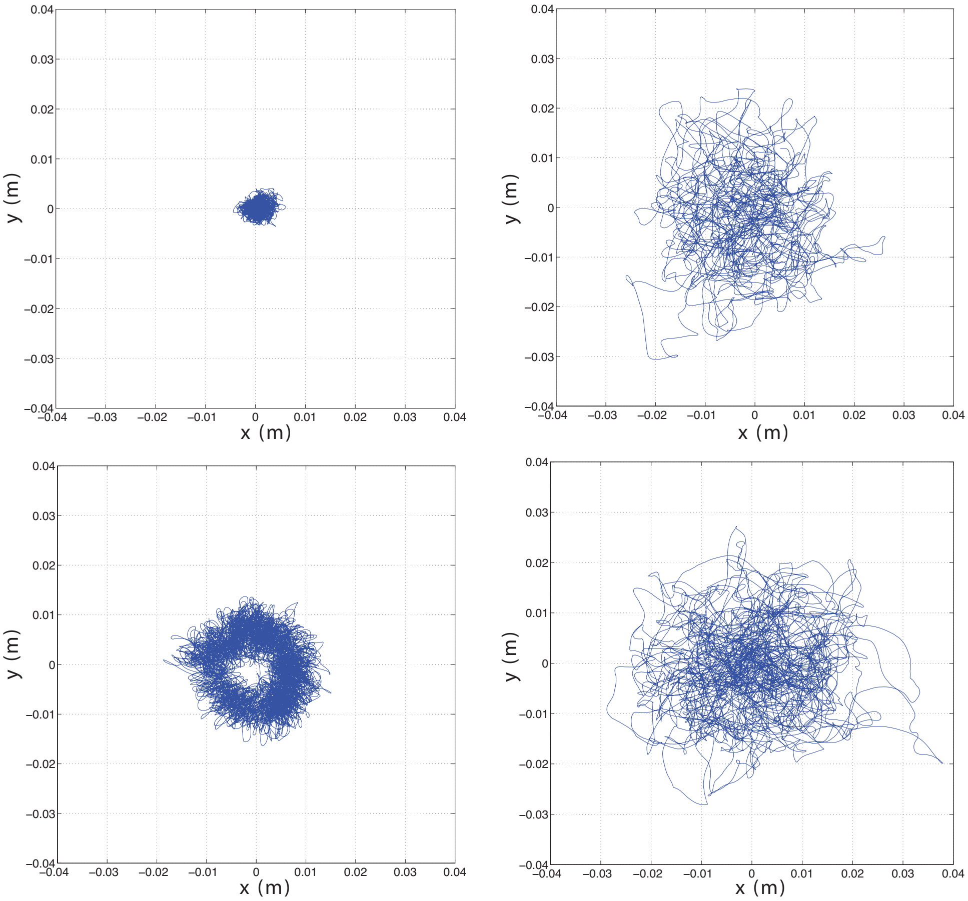

(a) (b)

Figure 6.13: Trajectory in the real space for the third particle in the laminar flux for in laminar (a) and turbulent conditions (b). For each case a low (upper in figures) velocity (with $Re_P = 3.2 \cdot 10^3$ for both cases) and a high velocity (lower figures, with $Re_P = 5.2 \cdot 10^3$ for the first and $Re_P = 6.2 \cdot 10^3$ for the second case) are represented.

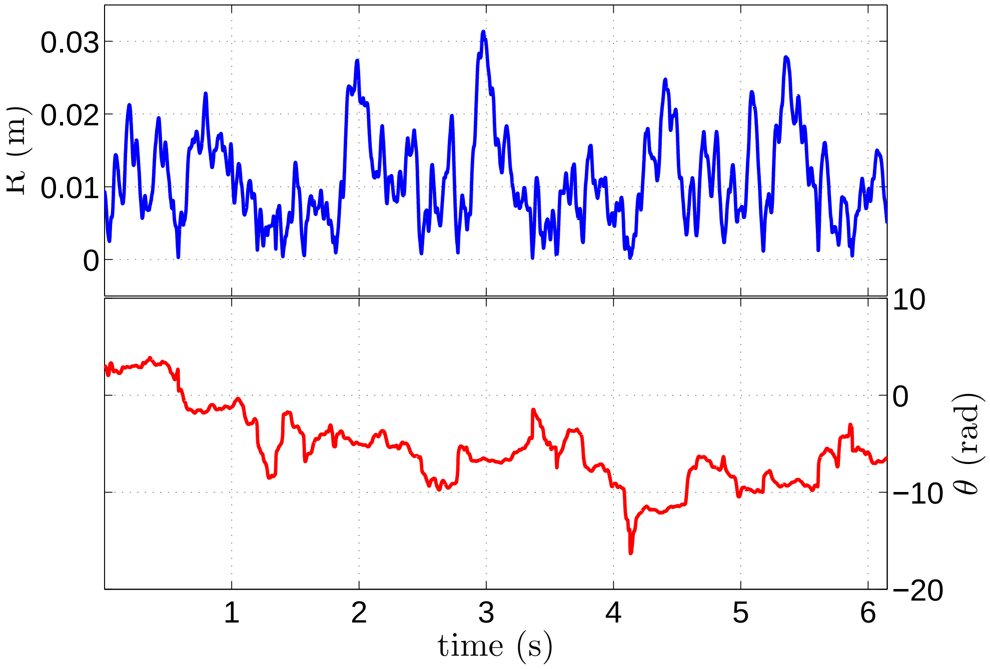

Figure 6.14: Time evolution of the particle polar coordinates. The example shown here corresponds to the laminar case at $Re_p = 4.1510^3$.

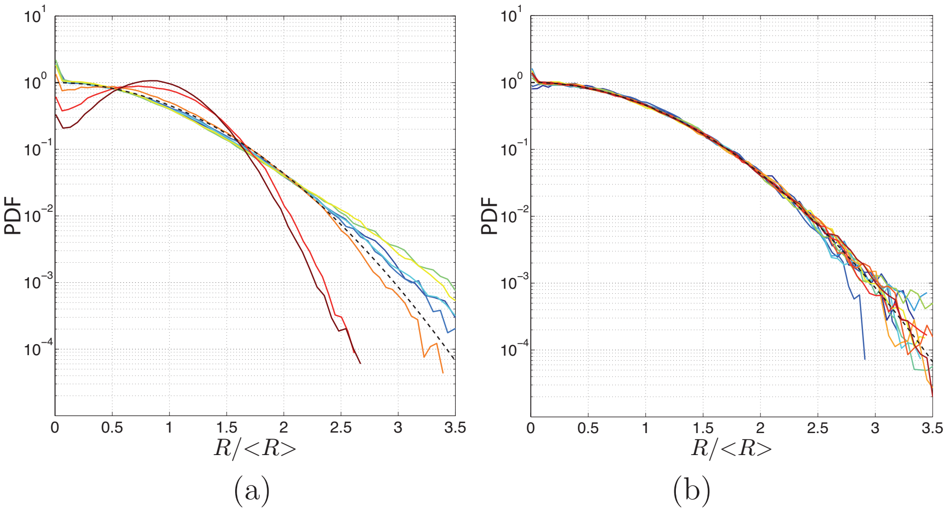

Figure 6.15: Probability density function for the radial component of the position for the laminar (a) and turbulent case (b).

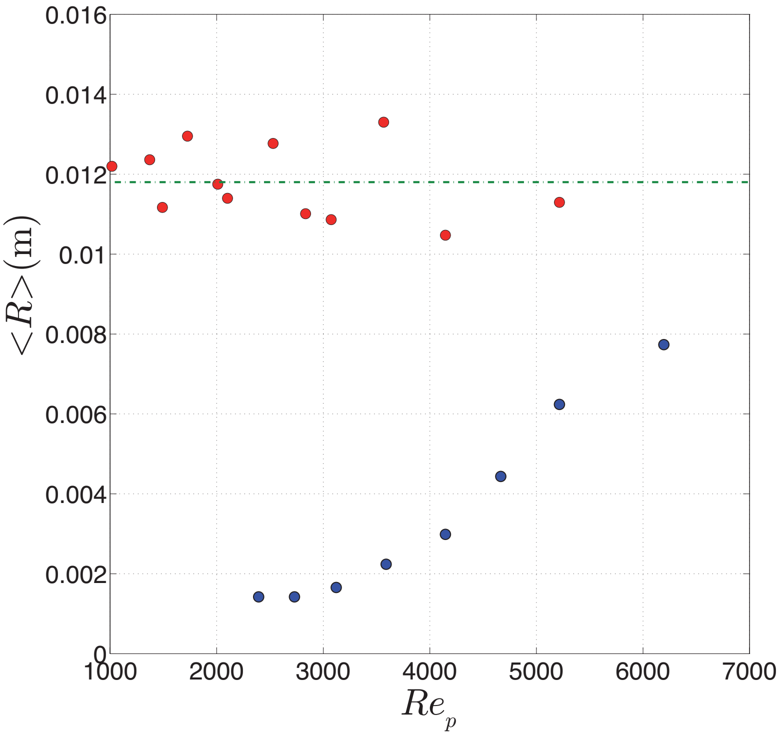

Figure 6.16: Mean value for the radial component of the position for the laminar case (blue) and the turbulent case (red), were the green line represent the average of these points ($R = 1.18$ cm).

trajectory is visible anymore.

A more quantitative inspection of the statistical properties of particle trajectories is given by the analysis and comparison of the radial probability density function of the position of the sphere in the different situations. To achieve this, we first transform the cartesian coordinates $(x, y)$ of the particle position to polar coordinate $(r, \theta)$, where the origin of the polar coordinates is taken at the average position of the particle. A typical time evolution of the radial $(r)$ and angular $(\theta)$ coordinate is shown in figure 6.14 (note that angular coordinate has been unwrapped). PDFs of the angle $\theta$ (not shown here) do not show any specific pattern, which simply reflects the isotropy of the particle motion, with no preferential angular position neither in the laminar, nor in the turbulent case. On the contrary PDFs of the radial coordinate exhibit a more interesting scenario. Figure 6.15a&b show the PDFs of $r$ for the laminar and turbulent cases respectively. Measurements for several particles and velocities explored are superimposed: for the laminar case, this corresponds to particle #3 at several velocities, while for the turbulent case, several particle classes at several velocities are considered (note that PDFs have been normalized by the average trajectory radius for each case). The transition toward a toroidal like position probability is clearly seen for the laminar case (figure 6.15a). At low velocities the radial distribution is Gaussian, with a maximum of probability at the center of the trajectory ($r_{max} = 0$). For the highest velocities, the maximum of radial probability moves toward a non-zero value, while the probability at $r = 0$ is significantly reduced (which corresponds to toroidal trajectories). This statistical richness completely disappears in the turbulent case, where all the PDFs collapses onto a single Gaussian distribution.

PDFs shown in figure 6.15a&b have been normalized by the average radius, so they are only informative regarding the qualitative shape of the radial distribution, but not regarding its quantitative extent. For this reason, figure 6.16 shows the average radial position of the sphere as a function of the particulate Reynolds number $Re_p$. It can be seen, that for the laminar case, the radial position is very sensitive to variations of $Re_p$ (corresponding here to variations of velocity). On the contrary, for the turbulent case, the mean radius of the particle trajectory is essentially independent of $Re_p$ (within the explored range), regardless of how it is varied (changing the particle size or its velocity). The typical radius of the trajectory in the turbulent case is of the order of 1.2 cm, regardless of the velocity and of the particle diameter. This in the order of integral scale, $L_0$, of the surrounding turbulence. $L_0$ is also known not to vary significantly with the mean wind velocity, which suggests that the extent of the turbulent trajectory of the towed sphere is related to the energy injection scale of the carrier turbulence. On the contrary, in the laminar case, the growth of the trajectory radius is to be related to the growth of an instability (as already discussed).

Finally, dynamical aspects of the motion of the sphere can be analyzed from the Lagrangian power spectral density (PSD) of the particle trajectory. Figure 6.17a,b,c&d show the Lagrangian PSD for the radial and angular position both in laminar and turbulent cases. Spectra for all available configurations (depending on particle class and velocity) have been superimposed. It can be observed that in the laminar case qualitative and quantitative trends are observed depending on experimental details. For instance the appearance of spectral peaks can be seen for the highest sphere velocities (we have shown in the previous chapter that such peaks may be related to an aero-elastic instability, similar to *flutter* [81]). This dynamical richness is lost in the turbulent case, where the spectra have all the same shape regardless of the considered configuration. In the turbulent case, spectra are mostly dominated by a flat PSD at low frequencies (characteristic of the uncorrelated large-scale fluctuations) followed by a rapid cut-off for frequencies above 10 Hz. We also note that the level of large-scale fluctuations (at low frequencies) does not significantly change with experimental conditions. This explains why the average radial position in turbulent conditions was mainly independent on experimental details. On the contrary, the level of low-frequency plateau of uncorrelated fluctuations, clearly increases with increasing velocity in the laminar case. This corresponds to the increase of uncorrelated radial fluctuations (and hence of the average radius of the sphere trajectory) with increasing $Re_p$ previously reported.

Our results in turbulent conditions show that even a low level of fluctuation rate of the surrounding environment (our grid generates a flow with 3% of velocity fluctuations) suffices to smear out all the subtleness of the coupling between the moving sphere and the surrounding fluid. The variety of effects and of dynamical signatures visible in laminar conditions has completely disappeared in the turbulent case. Although fluctuations of the sphere are quantitatively larger in the turbulent case, from a qualitative point of view they are essentially featureless, in the sense that their statistical properties remain generic and independent of experimental details (such as towing velocity or particle diameter).

## 6.7 Physics of sports

These last observations have an interesting application to physics of sports. The aerodynamics of sport balls is a subject which has always captivated the attention of physicists. It is only by the end of the nineteenth century that the first relevant equation of motion for balls in sports has been derived after Rayleigh's work [101]. The dynamics of such a system is rather complex: several terms such as drag, lift, gravity and Magnus force need to be simultaneously taken into account. The balance of these forces depend on many factors, such as the characteristics of the ball (size, density, shape, surface texture, etc.) and the initial conditions given to it [64]. This is the origin of the variety and richness of sports played with balls and of the many effects talented players are capable to induce to the motion of the ball, as for instance lifted kicks, chaotic knuckleballs [77] or spinning ball spirals [27].

However, the influence of turbulence present in the environment surrounding the ball as it moves has never been carefully investigated yet in the context of sports.

Our study shows that in laminar conditions this "towed ball" configuration reproduces subtle and non-trivial dynamics of the sphere (related to various aero-elastic and wake instabilities), mimicking effects of balls in sports.

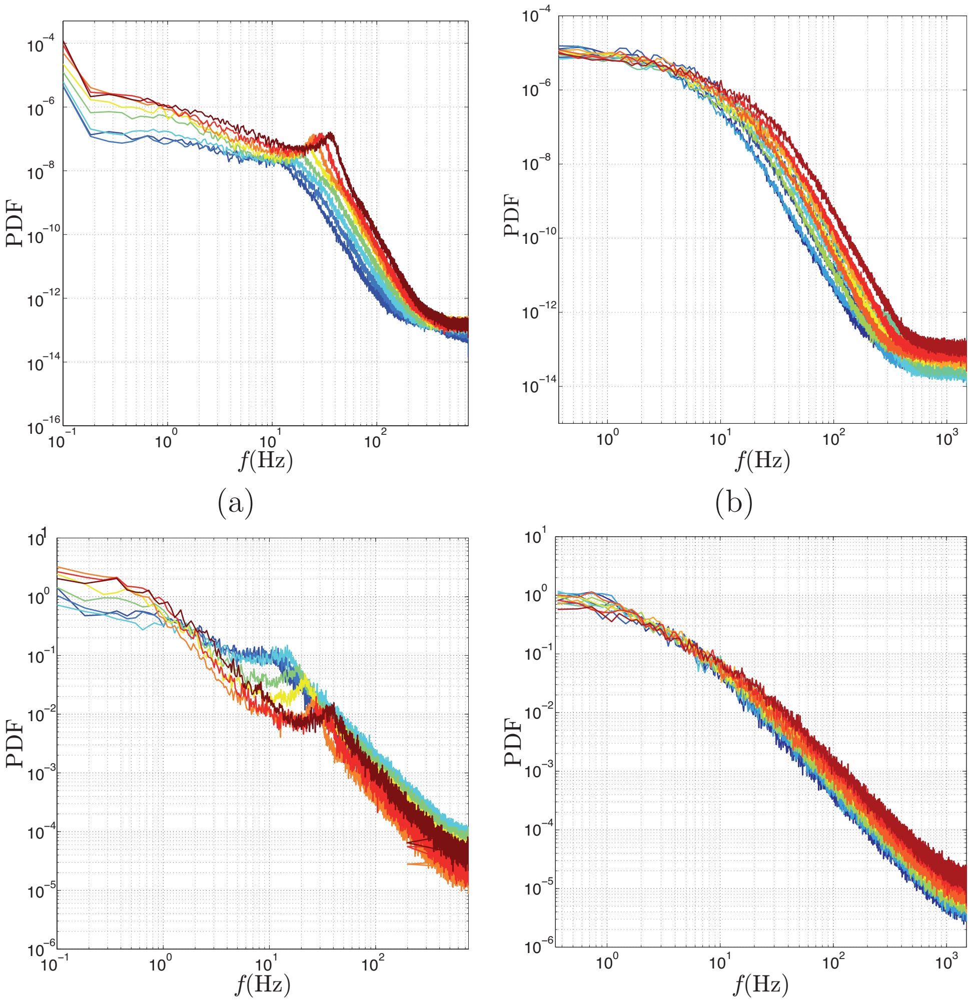

(a) (b)

(c) (d)

Figure 6.17: Power spectral density of the radial evolution of the sphere position for the laminar (a) and turbulent case (b). Power spectral density of the angular evolution of the sphere position for the laminar (c) and turbulent case (d)
.

In particular, non-trivial statistics of the radial position of the particle, similar to knuckleball effects in sports is well reproduced. We have shown that the radial position of the particle is very sensitive to experimental conditions (as for instance changes of the sphere velocity) which mimic here different initial conditions eventually imposed in the field by a player pitching or kicking a ball. We have shown that the dynamics of the particle also exhibits non-trivial trends with experimental conditions. These observations support the fact that in laminar conditions, the coupling between the particle and the surrounding flow is very sensitive to experimental details (and hence to initial conditions in the field of sports). For instance although the transition toward a toroidal trajectory is not fully understood at the moment, it is very likely to be related to small asymmetries in the system (either intrinsic to geometrical imperfections, or inherent to aerodynamic effects, as the appearance of an asymmetric wake, as observed under certain conditions for settling spheres for instance [45]). Similarly, the appearance of a dominant peak in the power spectral density of particle trajectories is believed to be related to subtle aeroelastic instabilities of the system *sphere+cable* [81]. Although effects actually involved for balls in real sports are different in details, they rely on similar fluid-structure interactions. It is the richness of such mechanisms that produces the broad variety of possible kicks and pitches and that makes the beauty of ball sports; and it is the capacity to control them (by imparting appropriate initial conditions to the ball) that makes the talent of a player. All this richness disappears in the turbulent case.

To conclude, let us note that although more work is still needed for a clear understanding of the precise role of turbulence in ball sports, our results show that this influence is eventually important and not always in agreement with our common sense. At present, it seems that the main effect we can expect from turbulence in ball games is to transform the qualitative richness of the whole ensemble of possible trajectories, which may be differently explored according to the talent, the creativity and the will of the payer, into a purely random process with well determined statistical laws, independent of the talent, the creativity and the will of the player. Therefore, it somehow turns a game of skill into gambling, but these are games to be played in different fields.

## 6.8 Conclusions

This chapter aimed at investigating fundamental features of aerodynamic forces acting on a towed particle in a turbulent environment, with the particular goal to emphasize the filtering mechanism due to particles inertia, whose role has not been clearly identified for the case of freely advected particles. This has been accomplished by considering a semi-constrained particle dynamics, where the particle cannot follow flow structures and where a dominant drag is imposed by a strong particle-fluid slippage velocity. At the same time, this arrangement is particularly interesting in the context of towed systems, which are of primary importance for instance in aeronautics or acoustic streamers in the ocean.

As far as we know, our results give the first clear experimental observation of a filtering effect on the Lagrangian dynamics of finite size particles in turbulent flow induced by their inertia, consistent with usual Stokesian models. However, at this point the agreement is only qualitative. The fact that the cable itself is also submitted to turbulent fluctuations further complicates the problem, taking into account its complex dynamics shown in chapter 5. These interaction with the towing cable (which can for instance, on one hand enhance dissipation due to the cable stiffness, and on the other hand enhance fluctuations as it transmits to the particle part of its own fluctuating energy) may explain for instance that at high frequencies the energy transfer function is not perfectly fitted by a first order low-pass filter and that the low-pass cut-off frequency represented in figure 6.8 does not simply scale as the inverse of particles response time $\tau_p^{-1}$ – or equivalently as $St^{-1}$ – as it would be expected for a simple Stokes drag. It has also been shown that this towed configuration inhibits the intermittent behavior of the particle (present in the freely-advected case). The main difference with the freely advected case is the larger slippage velocity in the towed configuration. Therefore, experiments where the slippage velocity is reduced by gradually releasing the longitudinal motion of the towed particle in order to span all situations from purely towed to freely advected particle, are being prepared. This experiment would be interesting for better studying the role of relative velocity in intermittency (independently of that of the response time of the particle) and the progressive gaussianization of acceleration PDFs.

On the other hand the influence of turbulence on the dynamics of towed systems has been studied. In this chapter we have seen that the wake and aeroelastic instabilities reported in the previous chapter disappear with only 3% of fluctuations, and the system recovers relatively universal statistical properties of turbulence.

# Part II

# Collective effects

# Chapter 7

# Air bubbles in a water tunnel

## 7.1 Introduction

Turbulent flows laden with particles occur very often in natural and industrial situations: dispersion of pollutants in the atmosphere, sedimentation in rivers, rain formation in warm clouds, plankton dispersion in the ocean, optimization of chemical reactors and in various industrial processes including combustion of liquid fuel among others. In these examples, particles consist of dust/sand in air or water, liquid droplets or solid particles (such as coal, catalyst...) in gas and are then denser than the carrying fluid. Thus, their dynamics is not strictly following the fluid velocity field but is instead lagging behind it. This is a specific case of inertial particles immersed in turbulent flows that also refer to situations when particles are less dense than the fluid or when particle size is much greater than the smallest turbulent scale, namely the Kolmogorov length. The common occurrence of this class of flows deserves thorough fundamental studies since no proper or practical modeling is yet available. As already discussed, the equations governing inertial particle dynamics have been obtained under strong assumptions in very limited situations ([61, 36]) and most of the recent numerical works use even simpler models.

A striking feature of turbulent flows laden with inertial particles is the so-called preferential concentration or clustering that leads to very strong inhomogeneities in the concentration field at any scale. This has now been widely observed in many experimental and numerical configurations including homogeneous and isotropic turbulence (see [114, 31, 105]). Particles interacting with a turbulent flow are then commonly characterized by their Stokes number, that is, the ratio between the particle viscous relaxation time $\tau_p$ and a typical time scale of the flow (as it has been detailed in chapter 1).

When dealing with finite-size particles, we use the same definition as in references [107, 135], using the eddy-turnover time at the scale of the particle, $\tau_d$, as the time scale of the flow, and a corrective factor $f_\phi$ based on the Reynolds number at particle scale:

$$St = \tau_p/\tau_d = f_\phi \phi^{4/3}(1 + 2\Gamma)/36, \tag{7.1}$$

where $\Gamma = \rho_p/\rho_0$ is the particle to fluid density ratio and $\phi = d_p/\eta$ is the particle diameter normalized by the dissipation scale. This dimensionless number is often used as the key parameter to characterize particle dynamics in turbulence, using simple Stokesian models where the dominant force acting on the particle is taken as the drag due to the difference between the particle velocity and that of the fluid. These models predict preferential concentration of particles with nonvanishing Stokes number, with a maximal segregation for $St$ around unity [8, 20]. This behavior is confirmed, at least qualitatively, in experiments with small and heavy particles [68]. In [32] finite-size particles, both neutrally buoyant and heavier than the fluid have been investigated, finding preferential concentration for heavy particles and nothing in the neutrally buoyant case. This latter work suggests that Stokes number by itself cannot be taken as sufficient to characterize clustering. The validity of this parameter is then an open and active field of research and it is important to explore particles with different sizes and densities in different types of flow. This questioning regarding the relevance of $St$ to characterize clustering is of course concomitant of the previously discussed questioning regarding the validity of point-particle Stokesian models. Finally, Aliseda and co-workers [2] have suggested that the local enhancement of the concentration could be responsible for the measured enhancement of particle settling velocity in turbulent flows due to collective effects. It is therefore important to have a good quantification of the amount of clustering, of its physical origin and of its collective consequences.

An important motivation of this work is related to the investigation of the relevance of the sweep-stick mechanism as the origin of clustering (see chapter 1). In this mechanism, zero-acceleration points are swept by the fluid as they statistically move with the local velocity of the fluid. On the other hand, numerical simulations using Stokesian models [20] show that a heavy particle that meets a zero-acceleration point moves with the fluid velocity (which is no longer true when the particle is at a point with nonzero acceleration). They refer to this as the sticky part of the mechanism. Other models, such as turbophoresis could be also involved in this phenomena and will be considered.

Originally, the goal of this thesis was to investigate preferential concentration of small and heavy particles in turbulence by considering a fog of water droplets in the active grid generated turbulence in the SFT1 wind-tunnel. However during the development of this thesis, the wind tunnel SFT1 was out of service during 12 months. This technical problem motivated the study of collective effects in different systems. In the end three complementary systems have been studied:

- Air bubbles in a water tunnel: Kolmogorov-size air bubbles in a water tunnel have been studied with $Re_\lambda = 100$ and $St = 0.06$. This system is studied in the present chapter.

- Finite size particles in a water french washing machine: particles with $d_p >> \eta$ and moderate particle-flow density ratio in an inhomogeneous turbulent flow with $Re_\lambda$ from 340 to 810 are explored. Corresponding $St$ ranges from 0.8 to 4 (chapter 8).

- Heavy sub-Kolmogorov particles in grid turbulence: small water droplets ($d_p << \eta$) have been investigated in the active grid generated turbulence with $Re_\lambda$ in the range 230–400. The corresponding $St$ number ranges from 2 to 10. This study (presented in chapter 9) corresponds to the original project and is the most extensively investigated configuration.

In this chapter we will study the properties of air bubbles in the LEGI water channel. This experiment has been made in collaboration with Pr. Nicolas Mordant (LEGI). Simultaneous PIV measurements allows us to study the preferential concentration of the bubbles and the flow properties at the same time. In the present and in the next chapter we will study if the flow tends to concentrate in particular regions of the flow and if the particles affect the flow properties.

## 7.2 Experimental setup.

The experiment has been run in a water channel (figure 7.1) with a measurement section of 0.1 m x 0.1 m x 1.7 m. It is manufactured in plexiglas, that allows an easy flow visualization in order to perform optical measurements such as particle image velocimetry (PIV), particle tracking velocimetry (PTV), etc..

In this chapter the results for a flow rate of $Q = 185.3$ cm$^3$/s are shown. They correspond to mean stream velocity $U_z = 1.85$ m/s (this is a flow measurement in the 10 cm$^2$ section that only considers water flow, no air contribution, therefore the real flow velocity might be slightly higher depending on the air/water proportion). The inertial particles are air bubbles artificially generated by adding soap to the liquid while small tracers (10 $\mu$m

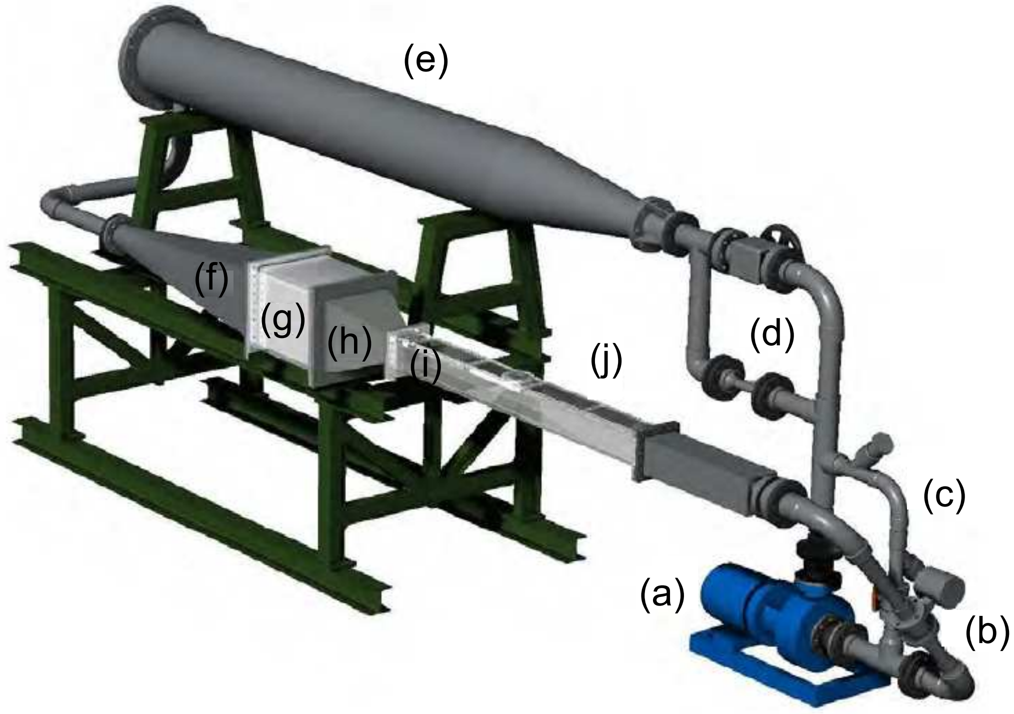

Figure 7.1: Water channel used in the experiments. It consists on a pump (a), a flowmeter (b), a bypass (c), the valves (d), a degasifier (e), the divergence section (f) and a relaxation chamber (g). Then, the flow passes over a convergence section, where downstream the grid is placed and finally the flow gets to the measurement section.

red fluorescent PS microspheres from Magsphere Ltd.) are added to the water in order to perform simultaneous PIV measurements of the flow and of the concentration field of bubbles.

The grid used to produce the turbulence is composed of six horizontal and six vertical bars (figure 7.2a). Downstream of the grid is placed a SprayTec equipment that allows us to simultaneously measure the granulometry of the bubble population seeding the flow (figure 7.2b). Then, the flow passes by a laser sheet (inclined 45° with respect to the measurement section walls), where two high-speed cameras Phantom-Miro M310 are placed (as shown in figure 7.2b): one vertically placed (camera 1), in order to record the backscattered light from air bubbles, and the other placed horizontally (camera 2) to record the scattered light from the fluorescent tracers for PIV purposes. For the latter an orange filter has been placed in order to only obtain the fluo-

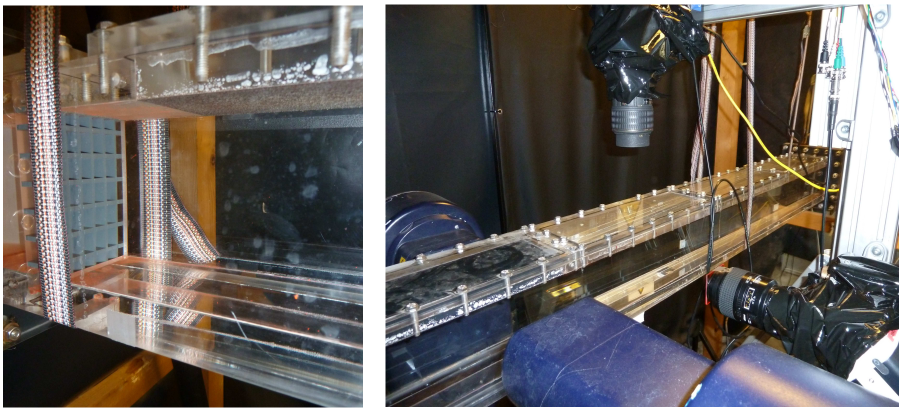

(a) (b)

Figure 7.2: (a) Grid used for generating turbulence. (b) Measurement section where the SprayTec and the cameras are placed.

rescence from the rodamine particles. The laser produces a continuous beam with a wavelength of 532 nm working at 5.2 W. Both cameras are connected to a Scheimpflug dispositive in order to have a proper focus on the inclined measurement section.

10 films are obtained with a sample rate of 1000 fps at a resolution of $1280 \times 800$ at 12 bits (which considering camera's available internal memory gives 8309 images per film, or $\sim 8.3$ s). Therefore, $\sim 83$ s are recorded for granting proper statistical accuracy. Considering that the integral length scale is in the order of the grid mesh ($L_0 \sim 1.6cm$) and a velocity fluctuation rate in the order of 3%, it is possible to have a good estimation of the energy dissipation rate: $\epsilon = U_{yRMS}^3/L_0 \sim 0.014\ \mathrm{m}^2/\mathrm{s}^3$. Finally, the Kolmogorov time scale (*i.e.* the smallest time scale of the flux, defined as $\tau_\eta = \sqrt{\nu/\epsilon}$) can be approximated as $\tau_\eta \sim 10$ ms and the Kolmogorov length can be approximated as $\eta = {\frac{\nu^3}{\epsilon}}^{1/4} = 90\ \mu\mathrm{m}$ (in section 7.3 these parameters will be calculated with PIV measurements and these approximations will be corroborated). Therefore, an acquisition rate of 1000 fps is enough for properly resolving the smallest temporal scales of turbulence.

The size of the window measured in the real world is $\sim 4 \times 2$ cm. A calibration mask is used for performing this transformation from pixels to

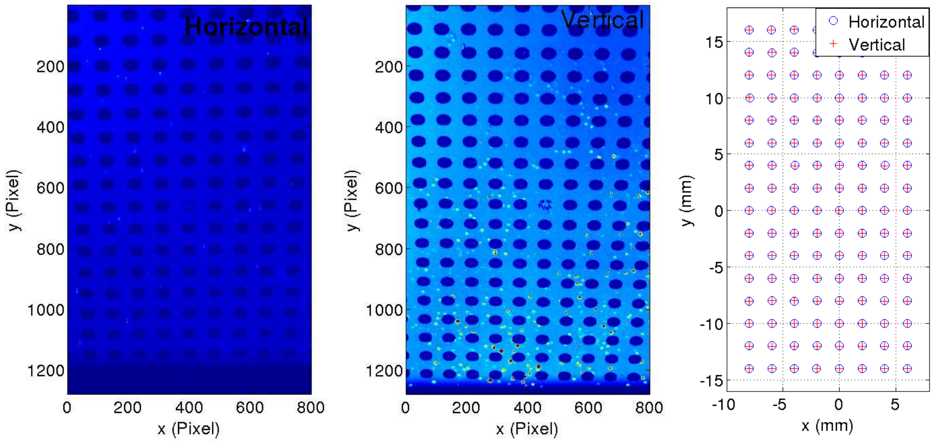

Figure 7.3: (a) Raw image of the calibration mask for the horizontal camera. (b) Raw image of the calibration mask for the vertical camera. (c) Match of centers of both images in the real world.

millimeters, which was the same for both cameras (the mask is a transparent sheet with black dots). Each camera has then a transformation matrix, where we have checked that both transformations are compatible (in the sense that we can define an absolute position in real space for tracers and bubbles). In figure 7.3c it can be seen that both images match extremely well, with an average error of 12.5 $\mu$m. If the comparison is made converting just one of the masks to real world and then the resulting image into the space of the other mask, the mean error obtained is of 0.68 pixels. In section 7.4.3 this latter results will allow us to superpose the bubble concentration fields (taken with camera 1) to the flow velocity fields (taken with camera 2).

### 7.2.1 SprayTec

During the data acquisition, the distribution of bubble size is measured taken using the Spraytec from Malvern Instruments Ltd. Considering that the whole experiment requires several hours, only 3 series of 5 min were taken with the Spraytec (the first during the first film, the second during the fifth

| | Film 1 | Film 5 | Film 10 |
|---|---|---|---|
| D[3][2] | 140 $\mu$m | 145 $\mu$m | 160 $\mu$m |

Table 7.1: Bubble mean diameter for different measurements.

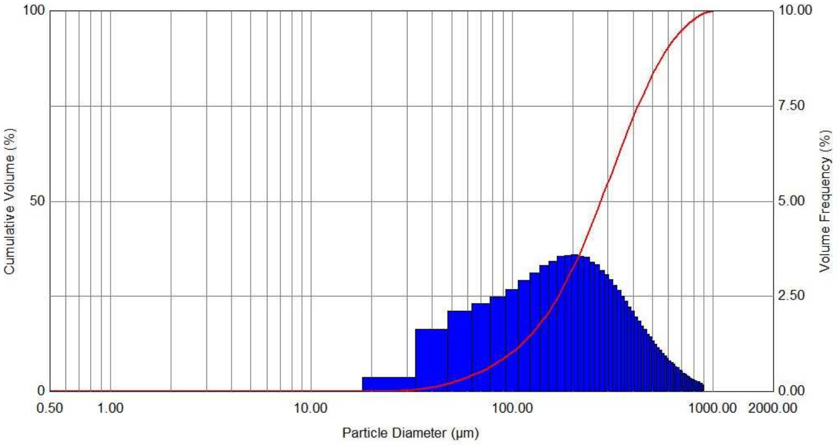

Figure 7.4: Histogram of particle's diameter obtained with spraytec.

film and the third for the last one). Figure 7.4 shows a typical distribution of particle diameter obtained (averaged during a whole series). The parameter chosen as representative of bubble diameter is $D[3][2]$, which is related to the ratio between the mean volume and the mean surface. Table 7.2.1 shows this value for the three measurements, that slowly grows with time, but remains almost constant during the acquisition. The diameter obtained as an average of the three measurements is $d_p = 150\ \mu$m.

## 7.3 PIV

The PIV analysis is realized using the commercial LaVision Davis software. More information about this technique may be found in reference [1]. The best resolution achievable for the rodamine particles concentration is $32 \times 32$ pixels (and the biggest possible window, useful for deducing mean values is $256 \times 256$ pixels). In real world coordinates this resolution corresponds to $720 \times 720\ \mu\text{m}^2$ (hence, larger than Kolmogorov length). Figure 7.5 shows a typical velocity field.

The velocity fields for all the films were calculated. The statistical values obtained are shown in table 7.2. A good isotropy is observed, and the flatness in both coordinates is almost 3, revealing the gaussianity of velocity fluctuations. The fluctuations in the flow are thus in the order of 3% (were the maximal std has been used). We can also deduce, considering the water flow obtained with the flow meter in the channel and the velocity obtained with PIV, that the volume fraction of air in the flow is $\sim 8.5\%$.

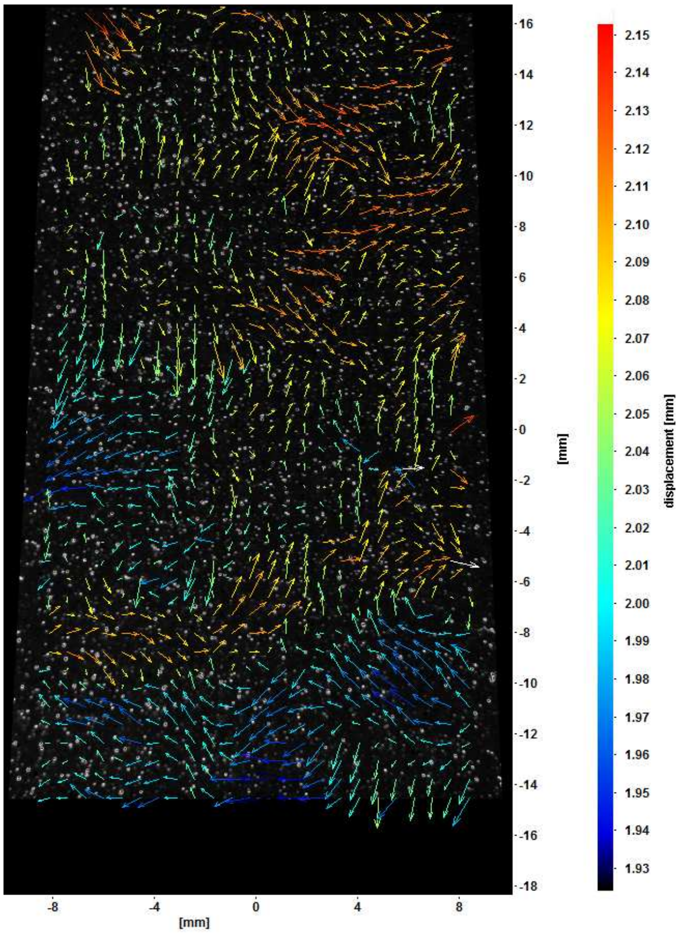

Figure 7.5: PIV image obtained with Davis software. For this case the displacement is equivalent to the velocity in $m/s$

To obtain the turbulence parameters, we estimate the energy dissipation $\epsilon$ from the peak of the longitudinal second order structure function, considering that the Taylor hypothesis is satisfied. The longitudinal second order structure function verifies $S_2(l) = C(l\epsilon)^{2/3}$, with $C$ an universal constant: $C = 2.1$ [94]. The transversal structure function follows a similar law but with a different coefficient $C' = 4/3C$ for homogeneous isotropic turbulence. Figure 7.6 shows the longitudinal and transversal second order structure functions, normalized as $(S_2(l)/(2.1l^{2/3}))^{3/2}$. From the maximum in figure 7.6 (which is not really a plateau due to the relatively low Reynolds number of the flow) we estimate $\epsilon = 0.0174$ $\mathrm{m^2/s^3}$. It is also possible to verify that $C'/C = 1.26$, a value close to the theoretical one, confirming the homogeneity and isotropy

|  | Mean | std | Skewness | Flatness |
|---|---|---|---|---|
| $U_z$ | 2.0245 m/s | 0.0444 m/s | 0.0451 | 3.1024 |
| $U_x$ | 0.0014 m/s | 0.0593 m/s | 0.0672 | 2.9949 |
| $\|U\|$ | 2.03 m/s | 0.048 m/s | -3.5$\times$ $10^{-3}$ | 2.97 |
| $w$ | -1.5 1/s | 46 1/s | 1.8$\times$ $10^{-3}$ | 3.86 |
| $\|a\|$ | 0.076 m/s$^2$ | 0.16 m/s$^2$ | 16 | 290 |
| $a_z$ | 0.0015 m/s$^2$ | 0.16 m/s$^2$ | 0.15 | 300 |
| $a_x$ | 6.6$\times 10^{-4}$ m/s$^2$ | 0.0703 m/s$^2$ | 1$\times 10^{-4}$ | 3.82 |

Table 7.2: table
Statistical parameters obtained with PIV for velocity components, norm of velocity, vorticity, norm of acceleration and its components.

of the flow. We note that the departure at large scales between the two curves in figure 7.6 (which should go asymptotically to $l^{-1}$) is related to the limited extent of the measurement volume (in particular in the transverse direction for which the measurement volume is about one third of the integral scale, estimated above).

Now it is possible to obtain the characteristics of the flow according to the relationships presented in chapter 2.
The Kolmogorov scale is:

$$\eta = \left(\frac{\nu^3}{\epsilon}\right)^{\frac{1}{4}} = 103.54\ \mu m. \tag{7.2}$$

The Kolmogorov time:

$$\tau_\eta = \sqrt{\nu/\epsilon} = 24\ ms. \tag{7.3}$$

The Taylor microscale, based on $U_y^{RMS}$:

$$\lambda = \sqrt{15\nu U_{yRMS}^2/\epsilon} = 1.7\ mm. \tag{7.4}$$

The Taylor scale based Reynolds number:

$$Re_\lambda = \frac{\lambda U_{yRMS}}{\nu} = 100.81. \tag{7.5}$$

Finally, the integral length scale:

$$L_0 = \frac{Re_\lambda^2 \nu}{15 U_{yRMS}} = 1.14\ cm. \tag{7.6}$$

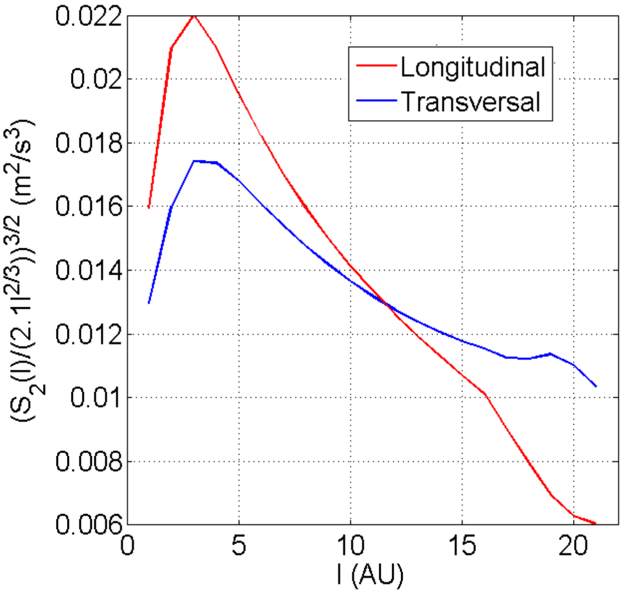

Figure 7.6: Compensated second order structure function.

Finally, the Power spectral density of $U_y$ for the flow is shown in figure 7.7. It averages all the films for an arbitrary point of the PIV measurements. The spectra shows a reasonable $-5/3$ inertial range (actually the slope is slightly lower than $-5/3$, as it is expectable for low Reynolds number HIT [3]). We remark that the dissipation scale is not resolved, which limits the estimation of gradients of velocity.

Now that we have obtained all the parameters, we are able to estimate the Stokes number of the bubbles in the flow:

$$St = \frac{\tau_v}{\tau_\eta} = \left(\frac{d_p}{\eta}\right)^2 \frac{1+2\Gamma}{36} = 0.060. \tag{7.7}$$

An estimation of Stokes number considering finite size and finite particulate Reynolds number corrections [135], following equation (7.1), leads to

$$St^* = \frac{\tau_v}{\tau_\eta} = 0.028. \tag{7.8}$$

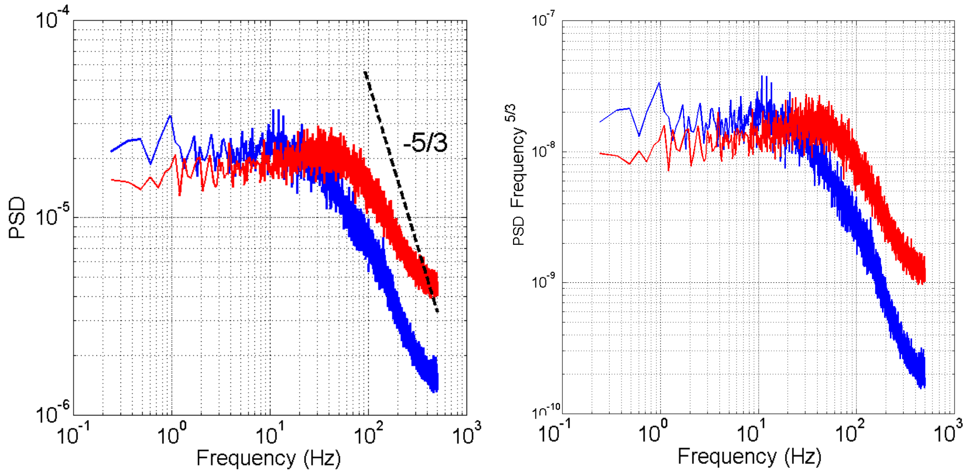

(a) (b)

Figure 7.7: (a) Power spectral density for a given point in the vertical axis for the horizontal (blue line) and the vertical (red line) coordinate. (b) Same spectra where the vertical coordinate has been normalized as $\nu^{5/3}$. Therefore, a plateau indicates the inertial range.

## 7.4 Preferential concentration analysis

### 7.4.1 Post-processing to quantify clustering

In the past few years, the group at LEGI specialized in a particular technique, that consists in analyzing the preferential concentration via Voronoï tesselations. This technique recently introduced for the investigation of preferential concentration of small water droplets in a turbulent airflow [68] was shown to be particularly efficient and robust to diagnose and quantify clustering phenomena. It has been used since then by other groups to characterize for instance clustering properties of bubbles in a water channel [96] and clustering properties of dense finite size particles in channel flow simulations [35, 49].

The Voronoï diagrams give a tessellation of a two-dimensional space (it can be extended to 3D) where each cell of the tessellation is linked to a detected particle, with all points of one cell closer to its associated particle than to any other particle. An example taken from [68] is exhibited in figure 7.8. Thus, the area of each Voronoï cell is the inverse of the local concentration of particles, *i.e.*, Voronoï area fields are a measure of the local concentration fields at interparticle length scale.

Whatever the measurement and data analysis technique used, when one

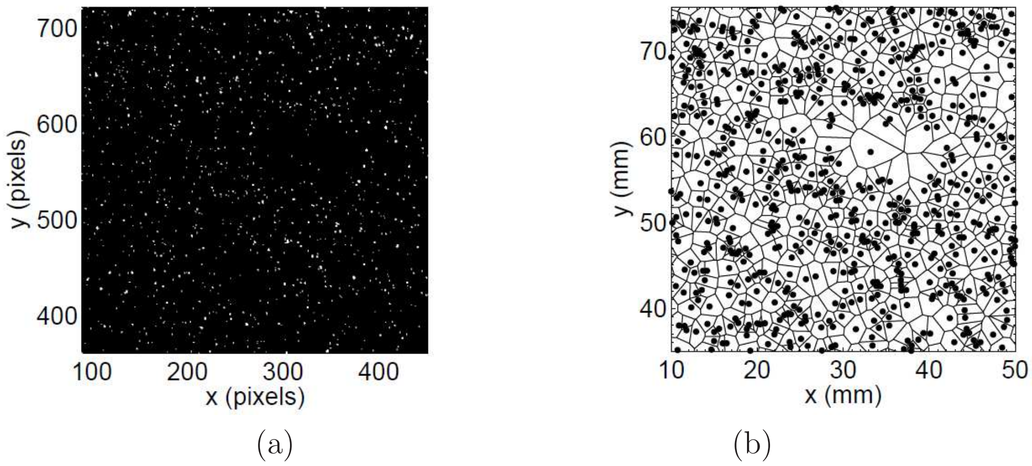

Figure 7.8: (a) Raw image of particles taken with the camera. (b) Voronoï tessellation of the previous image in the real world (images taken from [68]).

refers to preferential concentration, it is implicitly assumed that one deals with statistical preferential concentration compared to the case where particles would be spatially distributed as a random Poisson process (RPP). In order to quantify preferential concentration, we therefore compare for each experiment the PDF of the measured Voronoï areas to that expected for a RPP. Main known properties of Voronoï diagrams associated to RPP can be found in a short review by Ferenc and collaborators [30] and references herein. The first moment of Voronoï areas PDF has nothing to do with the spatial organization of the particles since the average Voronoï area, $\bar{A}$, is always identical to the mean particle concentration. Therefore, in the sequel we will generally focus on the distribution of the normalized Voronoï area $\mathcal{V} = A/\bar{A}$ which is of unit mean. The only known exact result for RPP Voronoï areas statistics concerns the second order moment in the 2D case which is equal to $< \mathcal{V}^2 >_{RPP} = 1.280$, corresponding to a standard deviation $\sigma_{\mathcal{V}}^{RPP} = \sqrt{< \mathcal{V}^2 >_{RPP} - 1} = 0.53$. Regarding the shape of the PDF of Voronoï areas statistics for a RPP, no analytical solution is known (most of the authors fit them with Gamma distributions). Ferenc and collaborators propose a compact analytical expression involving the space dimension as a single parameter:

$$f_{2D}(\mathcal{V}) = \frac{343}{15}\sqrt{\frac{7}{2\pi}}\mathcal{V}^{5/2}e^{-\frac{7}{2}\mathcal{V}}. \tag{7.9}$$

We use this analytical expression as a RPP reference.

### 7.4.2 Voronoï analysis of bubble concentration field

In this section we present the statistical analysis of Voronoï areas for the air bubbles. Figure 7.9a shows a typical image obtained with the vertical camera of the bubbles in the system. The post-processing of the images has been made as follows: first of all, the pixels whose intensity level is below a threshold (in this case 2500, as it can be appreciated in figure 7.9b) are set to zero. The histogram in figure 7.9b is made computing the intensity histogram of each raw image and then averaging. It can be seen that the histogram has a peak for low intensities and it follows a power law for high intensities. An exhaustive analysis varying the intensity threshold showed that the power law is related to the scattered light from bubbles while the peak is probably related to light scattered by tracers. This method has been shown to be extremely effective for separating tracers and bubbles scattered light. Then the image is band pass filtered, to conserve only the structures between 3 and 10 pixels long (which is observed visually to be the relevant range for the size of bubble images). Finally, the centers are found using a weighted center of mass method. Figure 7.9c shows the centers detected on the first image, while in figure 7.9d the intensity is now in a logarithmic scale. It can be seen that the centers obtained are in good agreement with the location of the centers of the bubbles in the image.

Finally, we have checked that the concentration of bubbles seems to be very stable in time, as shown in figure 7.10, where, for the mentioned set of parameters we obtain: $N_{centers} = 296 \pm 20$.

Considering this post-processing analysis, the Voronoï diagrams can be easily obtained. Figure 7.11 shows the Voronoï area $\mathcal{V}$ probability density function (PDF, blue line) and the equivalent distribution of a random Poisson process (red line), obtained according to equation (7.9). The two curves match almost perfectly. The matching is also quantifiable by the standard deviation ($\sigma_{\mathcal{V}}$) of the distribution, which should be $\sigma_{\mathcal{V}} = 0.53$ for a RPP, while the experiment gives $\sigma_{\mathcal{V}} = 0.54$. Therefore, we can conclude that the bubbles in the system studied do not form clusters at all. We have checked the robustness of this results by changing the threshold of particles detection.

### 7.4.3 Conditioned statistics

Although no preferential clustering is found for the bubbles, we still propose a conditional analysis of particles position and local turbulence properties from PIV. Such conditioning would be of course more interesting if clustering would have been observed as it allows for instance to investigate if particles cluster preferentially in specific regions of the turbulent field, in the

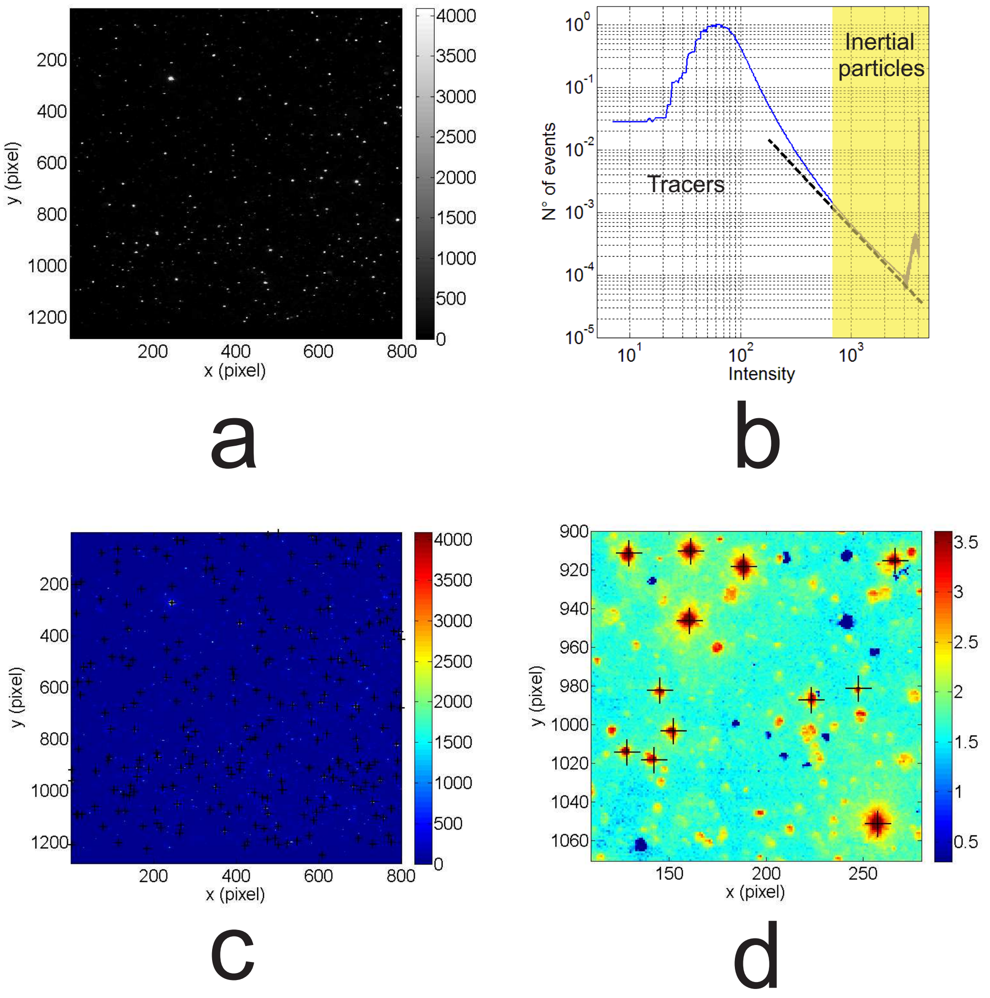

Figure 7.9: (a) Raw image obtained with the camera. (b) Intensity histogram for the previous image. (c) Raw image from the camera with the centers obtained. (d) The same image, but amplified and with logarithmic scale for the intensities

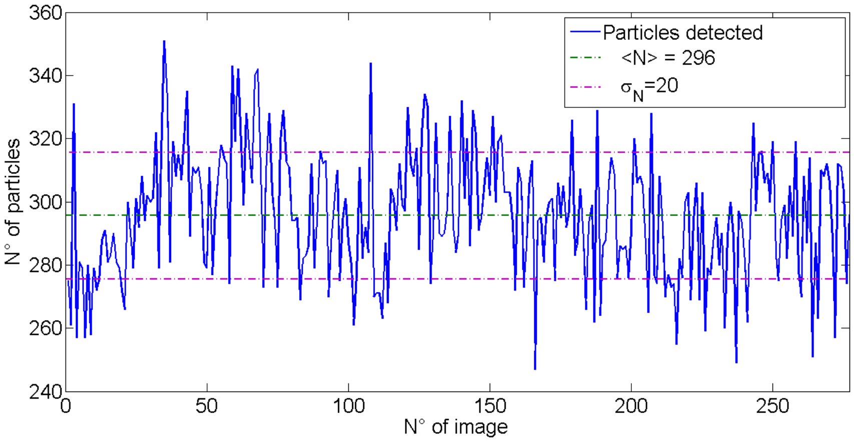

Figure 7.10: Number of bubbles found for a given film.

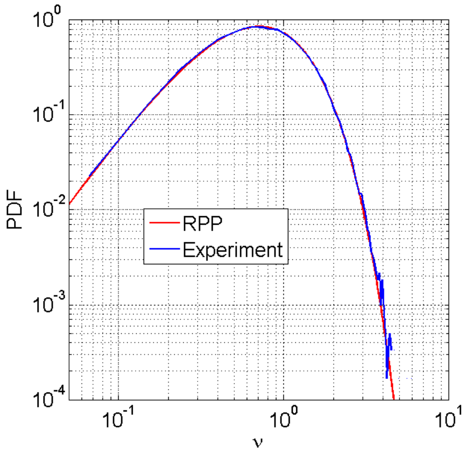

Figure 7.11: Probability density function of the Voronoï areas for the bubbles (blue line) and for a random Poisson process (red, obtained according to equation (7.9)).

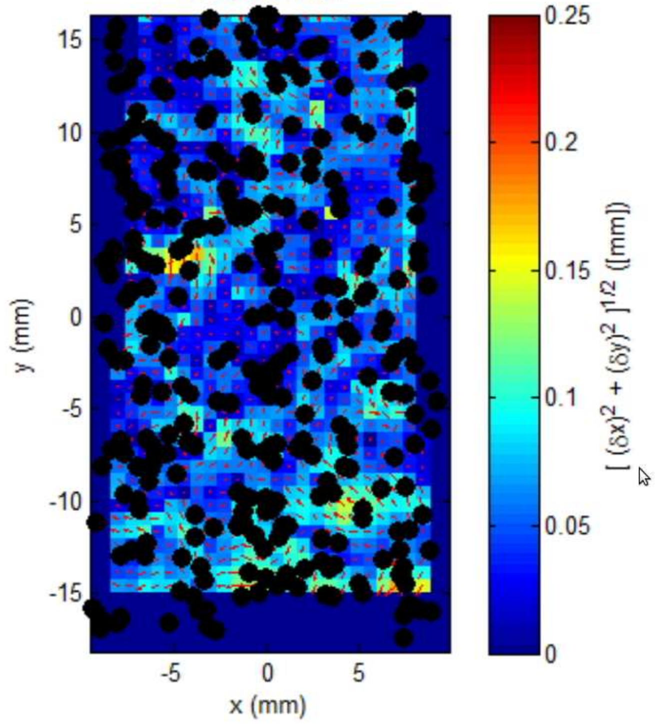

Figure 7.12: Flow velocity field obtained with PIV and inertial particles recorded with the other camera.

spirit of turbophoretic or sweep-stick mechanisms. In the present case we do not expect such effects, but this analysis gives the basis of such conditional analysis, which will be also performed in the next chapter. It is also interesting for future studies for instance with larger bubbles, which may be expected to cluster. Besides, the same analysis also allows to investigate if local properties of the flow are massively affected or not by the presence of the bubbles.

Having assured that PIV and bubble positions are defined in almost the same coordinate system, the flow properties evaluated at the position of the bubbles can be obtained (figure 7.12). Once these values are obtained, the same analysis done in the PIV section may be done, conditioned to the neighborhoods of bubbles in order to investigate any particular correlation between particle position and local turbulence field.

Two approaches have been performed: the first considering the statistics for the PIV cell corresponding to each center of bubble, and the other one considering a mean value of that cell and its first neighbors. Considering

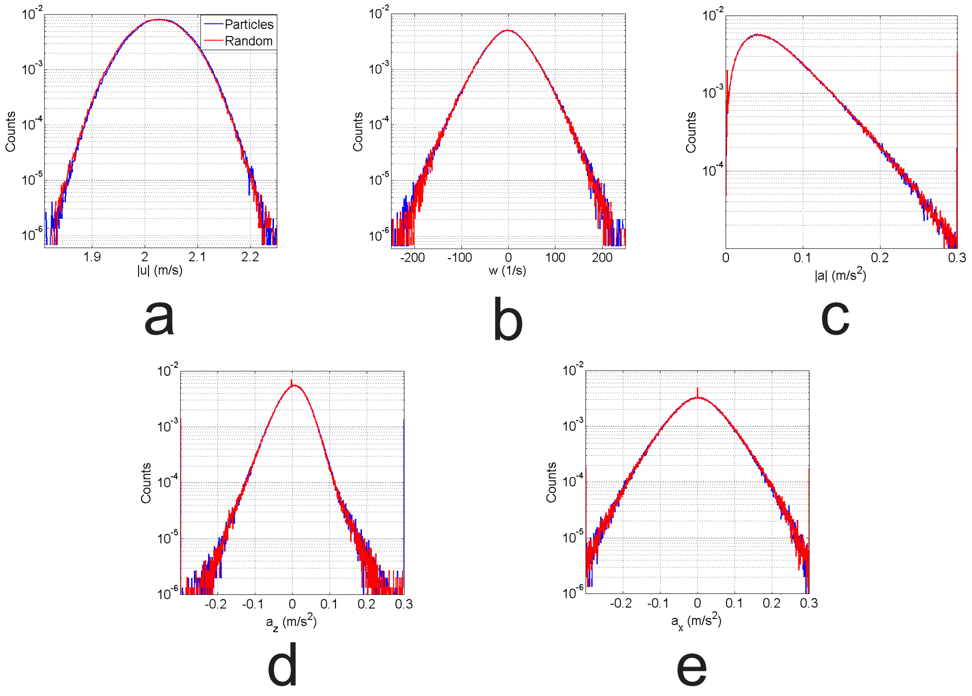

Figure 7.13: Histograms for velocity modulus (a), vorticity (b), Lagrangian acceleration modulus (c), its $z$ component (d) and its $x$ component (e). Blue line is for flow parameters evaluated at the position of inertial particles while the red line is for random positions.

an average of the order of 300 particles for image and that almost 83000 images were obtained, conditioned statistics are evaluated over an ensemble of almost $\sim 25 \times 10^6$ points, giving an excellent statistical accuracy. We have checked all the parameters of table 7.2 conditioned on bubble position. No differences are found between this conditioned velocity statistics and those obtained from the whole $PIV$ field presented in section 7.3.

In a second step, an exhaustive analysis of the histograms of several quantities (velocity, vorticity and acceleration) has been made. Note that the vorticity and acceleration require spatial gradients of the PIV field to be estimated. These estimations are limited by the actual resolution of the PIV correlation windows, which in the present case marginally resolve the dissipation scale of the carrier flow as previously discussed. Figure 7.13 shows the histograms for velocity modulus, vorticity, Lagrangian acceleration modulus and its components. The histograms compare the flow properties evaluated at the position of particles and in random positions (in order to compare the

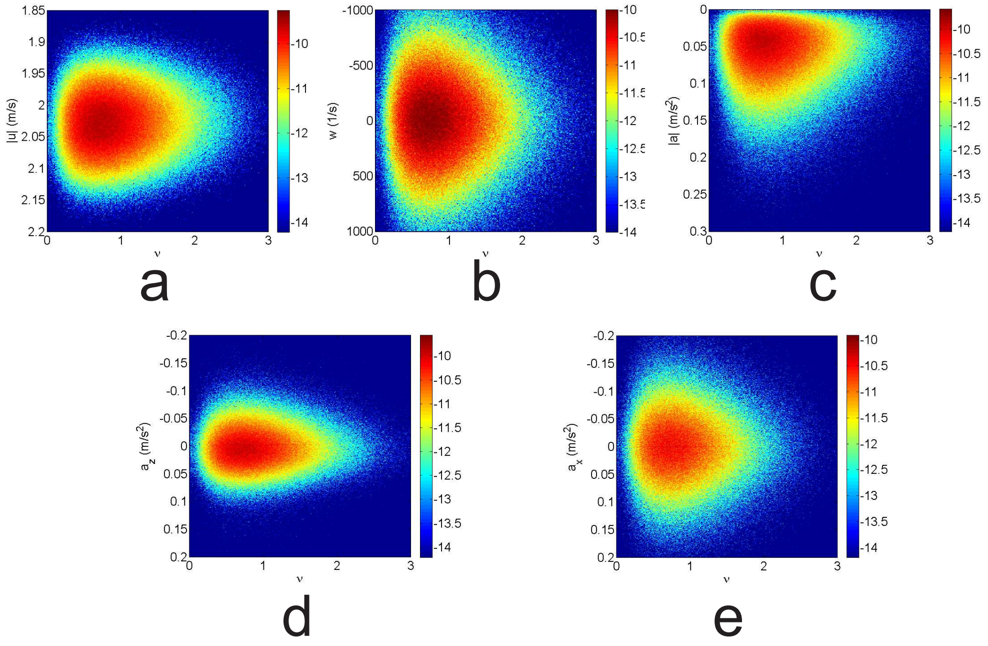

Figure 7.14: Joint histograms of Voronoï areas and local turbulent fields. The horizontal coordinate represents the Voronoï area $\mathcal{V}$ while the vertical is, depending on the figure: the velocity modulus (a), vorticity (b), Lagrangian acceleration modulus (c), $z$ component of acceleration (d) and $x$ component of acceleration (e).

same number of events). No appreciable differences are observed between both curves in any case.

In a further analysis, we analyze joint statistics of Voronoï areas $\mathcal{V}$ and turbulent properties (velocity, vorticity or acceleration). This is particularly interesting when clustering is observed to identify if small Voronoï areas (hence dense regions) are related for instance to low vorticity regions (in a turbophoretic scenario) or to low acceleration regions (in a sweep-stick scenario). In the present case we do not expect any particular trend, but we present this analysis because of its relevance for future works (including study presented in chapter 8). The joint histograms are shown in figure 7.14a-e.

We have compared again the flow properties evaluated at the position of the particles and in random positions (where the random positions simulate particles with the same $\mathcal{V}$ distribution). An example of this comparison is given in figure 7.15 for vorticity. In order to do a proper comparison, the same color scale is used and the histograms are normalized by the total number of events. Again, no significative differences are observed. This analysis has

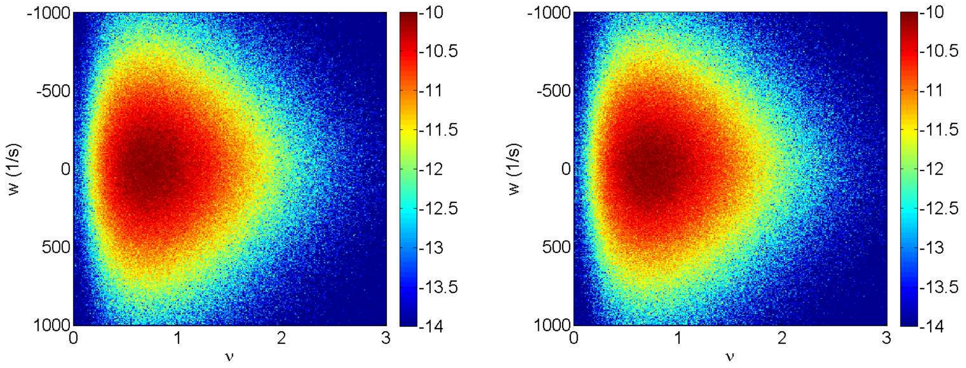

(a) (b)

Figure 7.15: Joint histogram for random positions (a) and particle centers (b). The horizontal coordinate represents Voronoï areas $\mathcal{V}$ while the vertical the vorticity.

been repeated for all the other parameters of figure 7.14 with similar results.

Therefore, in this case where no clustering has been observed, the particles do not seem to sample any preferential region of the flow.

## 7.5 Conclusions

To conclude, we have run an experiment for bubbles with a typical size of 150 $\mu$m in a turbulent flow with $Re_\lambda = 100$ and $\eta = 103$ $\mu$m (what results in $St = 0.060$, $\frac{d_p}{\eta} = 1.5$ and $\Gamma = 0.001$). Therefore, Kolmogorov scale light particles have been studied, and have not shown preferential concentration.

A similar work, by Prakash and collaborators [96], studies the Lagrangian statistics of air bubbles in a vertical water tunnel with nearly homogeneous and isotropic turbulence generated by an active grid. The Reynolds number $Re_\lambda$ is varied from 145 to 230, $d_p/\eta$ ranges from 7 to 13 and Stokes numbers from 1.5 to 4.4 are reached (hence much higher than in this work). They find that the dynamics of bubbles deviates from that of tracers, as the variances of both the horizontal and vertical acceleration components are about $5 \pm 2$ times larger than those measured in the same flow for fluid tracers. In a further study [117] the properties of clustering are analyzed.

An interesting result of this chapter is that, considering the optimal experimental circumstances achieved, a simultaneous PIV has been performed during the inertial particles study. Although no clustering is observed, these particles could always affect the global properties of the fluid (considering a gas fraction of almost 10% in the water) or tend to concentrate in particular regions of the fluid (regions which do not tend to agglomerate though). Nevertheless, we have shown that the statistical properties of the fluid evaluated at the position of the bubbles are almost exactly the same as those observed for the global fluid and that joint statistics of Voronoï areas of bubbles with different turbulent fields do not exhibit any difference compared to an artificially built distribution of particles. This shows on one side that Kolmogorov scale bubbles do not explore any particular region of the flow and on the other side that the local properties of the flow in the neighborhood of the bubbles is not affected by the presence of the inclusion.

The next step would be to achieve an experimental setup that allows us to reproduce this experiment but achieving preferential concentration. For that purpose, a setup with significantly higher $Re_\lambda$ and the possibility of varying the properties of particles will be studied in the following chapter.

# Chapter 8

# Preferential concentration of finite solid particles in a swirling von Kármán flow of water

## 8.1 Introduction

In this chapter we will perform a similar study of preferential concentration with Voronoï diagrams and a simultaneous PIV study as shown in the previous chapter. This experiment is made in collaboration with Pr. Romain Volk (ENS-Lyon) and Pr. Nicolas Mordant (LEGI). The main difference is that in this case we study finite size solid particles in a von Kármán flow. This flow is an interesting case of strongly inhomogeneous turbulence with high $Re_\lambda$.

We investigate preferential concentration of PMMA particles with density $\rho_p = 1400$ kg/m$^3$ and diameter $2.8 < d_p/\eta < 6.3$ for $340 < Re_\lambda < 810$. Therefore, with high $Re_\lambda$ and heavy particles in the limit between point particles and finite-size particles (Fiabane and collaborators [32] suggest a limit $d_p/\eta = 5\eta$).

## 8.2 Experimental setup.

The flow is a turbulent von Kármán swirling flow, described in references [128, 130]. Water fills a cylindrical container of internal diameter $D = 15$ cm and a length of 25 cm. It is driven by two disks of diameter 14 cm, fitted with blades. Three different rotation rates were studied: 2.8 5.6 and 8.3 Hz (figure 8.1a).

The distance between the disks is 20 cm while the rotation frequency is imposed by two calibrated constant current engines. The angular velocity is measured with two dynamos with a precision in the order of 2% and is adjusted in a way that the disks have the same velocity but opposite direction (figure 8.1b). This setup allows us to obtain developed turbulence with $Re_\lambda$ up to $\sim$ 800 in a compact region of space. This type of flow has been extensively used for studying the properties of turbulence, Lagrangian ([54, 72, 131]) or Eulerian ([137]).

In chapter 2 we detailed the properties of grid turbulence, and its homogeneity and isotropy. This contrasts with the von Kármán flow, which has a large scale non-homogeneous, non-isotropic 3D mean structure (figure 8.1b). As the disks counter-rotate, the mean flow has a strong azimuthal velocity component (in the order of $\pi D\Omega$ close to the disks) and vanishes in the middle plane of the cylinder. Furthermore, the impeller disks work as centrifugal pomps ejecting the flow in the radial direction near the disks, creating a poloidal re-circulation with a stagnation point at the center of the cylinder. Therefore, the turbulence generated is locally homogeneous in the center of the cylinder but conserves the anisotropy for big and small scales ([131]). In the limit $Re_\lambda >> 1$ the usual local isotropy hypothesis is generally assumed for the small scales of the flow (although the validity of this assumption has been recently questioned [86]).

For the measurements reported here, the Taylor-based Reynolds number reaches values up to 810 and the dissipation rate $\epsilon$ values up to 25W/kg (table 8.1). We study PMMA particles with density ratio 1.4 and two different radii: 80 and 100 $\mu$m. The same tracers used in chapter 7 have been used for PIV analysis: 10 $\mu$m rodamine spheres from Magsphere Ltd. (red fluorescent PS microspheres). The water temperature was maintained constant during all measurements at $T = 30°C$. As the flow is anisotropic, the Reynolds number based in the Taylor scale is estimated as $Re_\lambda = \sqrt{\frac{15u^4}{\epsilon\nu}}$, where $u = \sqrt{\frac{2u_x^2+u_z^2}{3}}$, is obtained using the $rms$ value of velocity fluctuations .

The measurement system is similar to that used in chapter 7. The cylindrical container is equipped with three windows that allow a proper visualization of the flow. The flow passes through a laser sheet (inclined 45°, as shown in figure 8.1c), where two high-speed cameras Phantom-Miro M310 were placed in the horizontal directions but on opposite sides of the vessel. The camera labeled 1 in figure 8.1c catches the backscattered light from PMMA particles, and the other (camera 2) placed for taking the forward scattered light of rodamine tracers. Camera labeled 2 is mounted with an orange filter and only records the motion of the rodamine particles. This

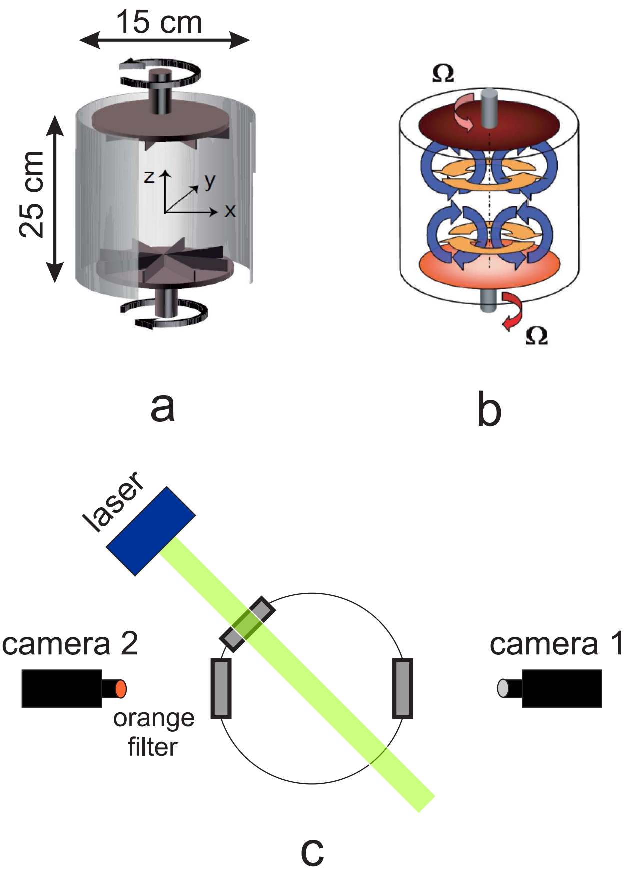

Figure 8.1: (a) Schema of the experimental setup. (b) Inhomogeneous flow generated in the container. (c) Schema of the imaging system: a laser sheet illuminates the flow. The camera on the right films inertial particles while the camera on the left (with an orange filter) films tracers in order to perform PIV measurements.

camera is used to provide the PIV. Note that camera 1 does not have any filter, so it is also a priori sensitive to fluorescence of rodamine particles (as well as to direct green light scattered by those same particles). However, as the rodamine particles are at least one order of magnitude smaller than the PMMA particles the light they scatter is significantly less intense and a simple thresholding allows to simply ignore it. The laser produces a continuous beam with a wavelength of 532 nm working at 5.2 W. Both cameras are connected to a Scheimpflug system in order to have a proper focus of the measurement section.

| $\Omega$ (Hz) | $u_x$ (m/s) | $u_z$ (m/s) | $\eta$ ($\mu$m) | $\tau_\eta$ (ms) | $\epsilon$ (Wkg$^{-1}$) | $Re_\lambda$ |
|---|---|---|---|---|---|---|
| 2.8 | 0.38 | 0.19 | 28.5 | 3.55 | 3.1 | 340 |
| 5.6 | 0.76 | 0.41 | 21.2 | 7.11 | 7.2 | 570 |
| 8.3 | 1.14 | 0.62 | 16.4 | 20.7 | 20.7 | 810 |

Table 8.1: Turbulent parameters of the flow for the three velocities studied. The values are obtained using the results in [130].

| *Particle* | $d_p$ ($\mu$m) | $St_{\Omega 1}$ | $St_{\Omega 2}$ | $St_{\Omega 3}$ |
|---|---|---|---|---|
| 1 | 80 | 0.83 | 1.50 | 2.50 |
| 2 | 100 | 1.30 | 2.30 | 4.0 |

Table 8.2: Particles considered and their Stokes number for each velocity.

10 films are recorded for each configuration (*i.e.* for each given particle class and rotation rate of the impellers) with a sample rate of 3200 fps at a resolution of 1280 × 800 at 12 bits (which considering camera's available internal memory gives 8309 images per film, being $\sim$ 2.60 s). Therefore, $\sim$ 26 s were recorded for granting proper statistical accuracy. The real size of the window measured in the real world is $\sim 4\times2$ cm$^2$. A calibration mask was used for performing pixel to real world transformation, which was the same for both cameras (the mask is a transparent sheet with black dots, pasted between two identical PVC frames). This warrants that both cameras are correctly calibrated with respect to each other, allowing to match positions on one camera onto the other. As in previous chapter, this is particularly intended for superimposing PIV fields obtained from one camera and particle positions obtained from the other.

The image processing performed is shown in figure 8.2. Starting from the raw image (figure 8.2a), in order to avoid differences in illumination (caused

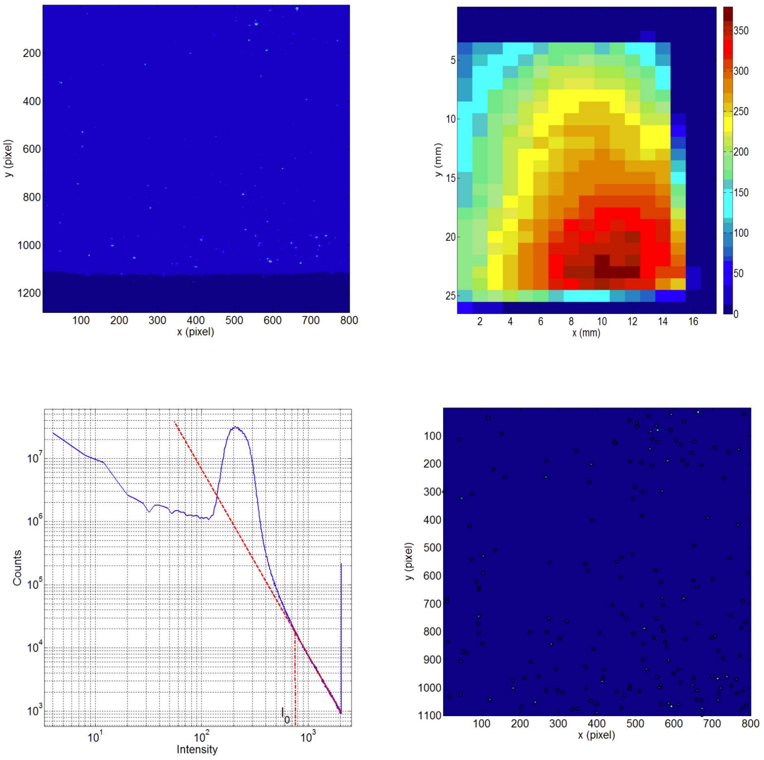

Figure 8.2: (a) Raw image obtained for camera 1. (b) 2-D histogram of intensity of all the raw images of a series after a 2-D adaptive noise-removal filtering. (c) 1-D histogram of intensity of all the raw images for a series. (d) Resulting images with the centers detected in black circles.

by laser attenuation) a 2-D adaptive noise-removal filtering is applied. The resulting 2D histogram is shown in 8.2b. Illumination conditions seem relatively uniform after the correction, although not perfect. It has been tested that the results shown in this chapter are robust for a wide range of filtering parameters. The one dimensional histogram of intensity from camera 1 is computed in order to determine the threshold of intensity that differenciates noise and tracers light from PMMA particles (as performed in the previous chapter), as shown in figure 8.2c. Finally, the corrected image is obtained and the centers identified (figure 8.2d), where only a pixels-real world correction need to be performed (that can be observed below in 8.6).

PIV measurements have been performed in the same way as in chapter 7. Tracers are 10 $\mu$m rodamine particles and the processing is made using commercial software Davis 8.0 from LaVision. The PIV correlation window

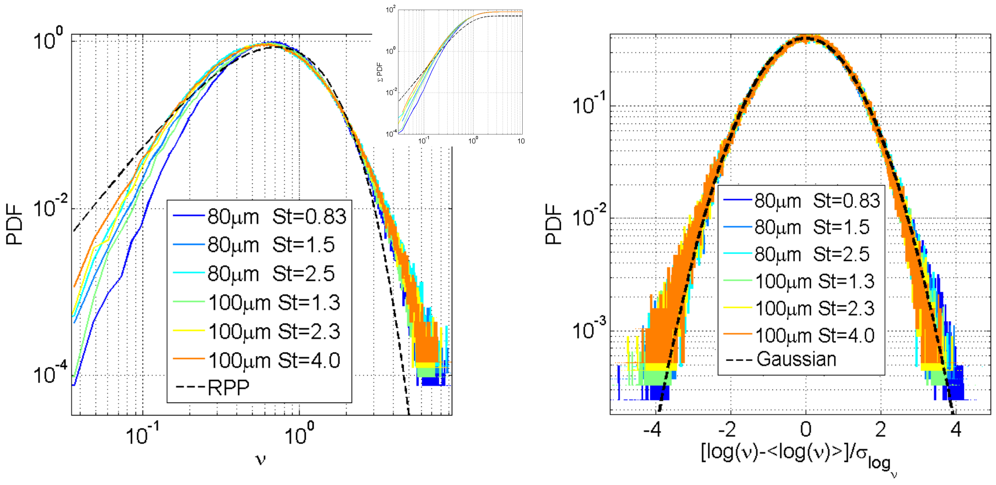

(a) (b)

Figure 8.3: (a) Probability distribution of normalized Voronoï area $\mathcal{V}$ for experiments at different Reynolds number and Stokes number. (b) Probability distribution function, centered and reduced, of $\log(\mathcal{V})$.

is $32 \times 32$ pixels (that corresponds to $290 \times 290$ $\mu\mathrm{m}^2$, hence bigger than particles studied here). PIV is only measured for the smallest Reynolds investigated, $Re_\lambda = 340$. This is due to the fact that we use the continuous 3200 fps acquisition rate in the camera. No specific PIV equipment (pulsed laser or double frame camera, which would allow to reduce the inter-frame time lag below the repetition rate) was available at the time we performed the experiment. The laser sheet has a thickness of $\sim 0.25$ mm. Taking into account the values of velocity of fluctuations in table 8.1, only for $\Omega_1$ we have assured that a particle will remain for two consecutive images in the laser sheet (while for the other cases all the high frequency dynamics will be filtered for this spurious effect). Also a measurement without any particle was performed in order to check that the particles were not changing the properties of the flow (allowing also to verify that no two-way coupling occurred in the flow).

## 8.3 Results

The Voronoï diagrams have been obtained with the same technique as in the previous chapter. Figure 8.3 shows the PDFs of $\mathcal{V}$ and of $\log(\mathcal{V})$ centered and reduced.

It can be clearly seen that the measured distributions are not that of a uniform random process (figure 8.3a). Large Voronoï areas are significantly over-represented compared to the RPP case, indicating the existence of large depleted regions. Similarly, normalized areas between a few tenth (depending on the particle class) and about $\mathcal{V} \sim 0.5$ are over-represented in the experiment compared to a RPP, indicating the preferential concentration phenomenon. Besides, the most probable value for the normalized Voronoï area is smaller for the particles than for a RPP, which indicates the predominance of over-concentrated areas. Much smaller areas are on the contrary under-represented. However, the log-log representation misleadingly exacerbates this under-representation. As shown in the inset in figure 8.3a, showing the cumulative PDF, normalized areas above $0.15 - 0.3$ are already cumulatively more represented with the inertial particles compared to a RPP. The origin of the under-representation of very small normalized Voronoï areas remains unclear. It can be related to a statistical bias, due to the limited seeding density which reduces the probability to find very nearby particles. But it can also be physical and indicate some sort of ordering of the particles at small scales. This aspect requires further investigations, for instance varying the seeding density of the flow, which will be addressed in future works and will not be discussed in this manuscript.

Big Voronoï areas (or depleted regions) are robust when changing particle and flow parameters, but small areas (or concentrated regions) are affected by these changes. This has been already observed in the previous study by Monchaux and collaborators [68] at moderate Reynolds number. In that work it was also observed that the Voronoï area PDFs for inertial particles in turbulence were well approximated by a lognormal distribution. This is confirmed as a robust characteristic also preserved in the higher Reynolds number regime explored in the present study, as it can be seen in figure 8.3b: the PDF of $\log(\mathcal{V})$ is approximately Gaussian, at least within the range $\pm 3\sigma_{\log(\mathcal{V})}$. Deviation from lognormality is only observed for small values of $\log(\mathcal{V})$ which are slightly over-estimated. Therefore, the overall statistical distribution of Voronoï areas is almost characterized entirely by one single parameter, which we choose to be the standard deviation $\sigma_{\mathcal{V}}$ and whose dependency with experimental parameters can be used to quantify the evolution of particles clustering.

Figure 8.4 shows the standard deviation of normalized Voronoï areas $\sigma_{\mathcal{V}}$ as a function of Stokes number. It can be observed that it is clearly larger than $\sigma_{\mathcal{V}} = 0.53$, that corresponds to a RPP. This is a strong evidence of the formation of clusters and voids in our system, while the amount of clustering tends to grow when $St$ is increased with possibly a saturation or even a reduction for the largest explored Stokes number. This may suggest a maximum

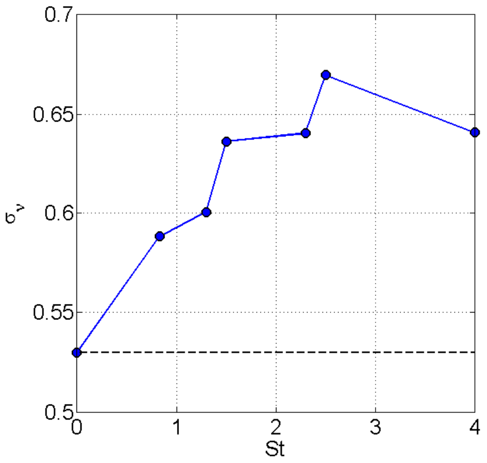

Figure 8.4: Standard deviation of normalized Voronoï areas $\sigma_{\mathcal{V}}$ as a function of Stokes number. The point for $St = 0$ has been artificially added while the black dashed line represents the value $\sigma_{\mathcal{V}} = 0.53$, that correspond to a RPP phenomenon.

of clustering for $St \sim 3-4$, as also observed by Monchaux *et al.*, although the available data here does not allow to be conclusive on this point.

### 8.3.1 Clusters

In the present section, we will focus on the identification and characterization of clusters and voids formed by the particles. One important aspect concerns the analysis of the geometry of the clusters. Do they have a fractal structure? Do they have a characteristic size?

To define a cluster and a void, we follow the idea proposed by Monchaux *et al.* [68, 69]. Clusters and voids are easily identified by choosing an appropriate threshold for particles local concentration (defined as the inverse of Voronoï cell area) as can be seen in figure 8.6 (where the distribution for higher $St$ of figure 8.3 is shown). The two intersections of the experimental PDF with the RPP closer to the maximum of the distribution are used as thresholds. The values that satisfy $\mathcal{V} < \mathcal{V}_{\mathcal{C}}$ are defined as clusters while the values where $\mathcal{V} > \mathcal{V}_{\mathcal{V}}$ as voids. The values in between are not considered clusters nor voids. The referred work shows the validity of $\mathcal{V}_{\mathcal{C}}$ and $\mathcal{V}_{\mathcal{V}}$ as such thresholds. These two parameters are robust when varying $St$ and $Re_{\lambda}$, as it can be observed in figure 8.3a. The resulting process for obtaining clusters and voids from the centers in real world is shown in figure 8.6.

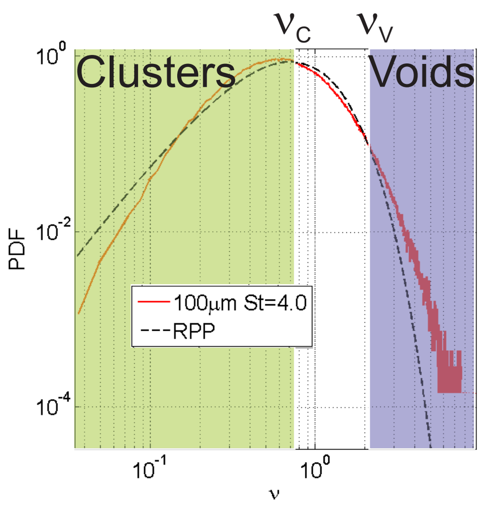

Figure 8.5: Schema of clusters and voids detection. Starting from a Voronoï cells area PDF, the two intersections closer to the maximun of the distribution are used. Small resulting areas corresponds to clusters (concentrated regions) while big areas are for voids (depleted regions). The intermediate values are considered as intermediate and no computed as clusters or voids.

Once clusters and voids have been identified, their geometry can be analyzed. We start by investigating the statistics of the area of clusters while voids will be analyzed in the following section. Figure 8.7a shows clusters area PDFs, normalized by the mean area value. Surprisingly, all curves collapse and show a clear peak at $\frac{A_V^{max}}{<A_C>} \sim 0.15$. This is a strong experimental evidence of a system with a typical cluster area. We also observe a power law behavior of area PDF for large events, with an exponent of the order of $-1.5$, slightly less steep than the $-2$ exponent reported by Monchaux *et al.* Figure 8.7b shows how the mean value of clusters area varies with $St$. This value tends to grow with $St$, and it seems to reach an asymptotic value of the order of 3.5 mm$^2$ (corresponding to $\sim 100\eta^2$) for $St \sim 4$, although more values would be required to confirm this asymptotic trend.

Aliseda and collaborators [2], working with grid turbulence in a wind tunnel with $Re_\lambda = 75$, using qualitative inspection found that poly-dispersed water droplets form clusters with a typical area of $10\eta$. In order to compare results, figure 8.8a shows $\sqrt{< A_C >}/\eta$ as a function of $Re_\lambda$ and $St$. Figure 8.8b shows the same relationship but considering the most probable cluster area $A_C^{max}$ instead of the average area $< A_C >$ (*i.e.* the peak of the PDFs of areas in figure 8.7a). The fact that the PDF of cluster area collapses,

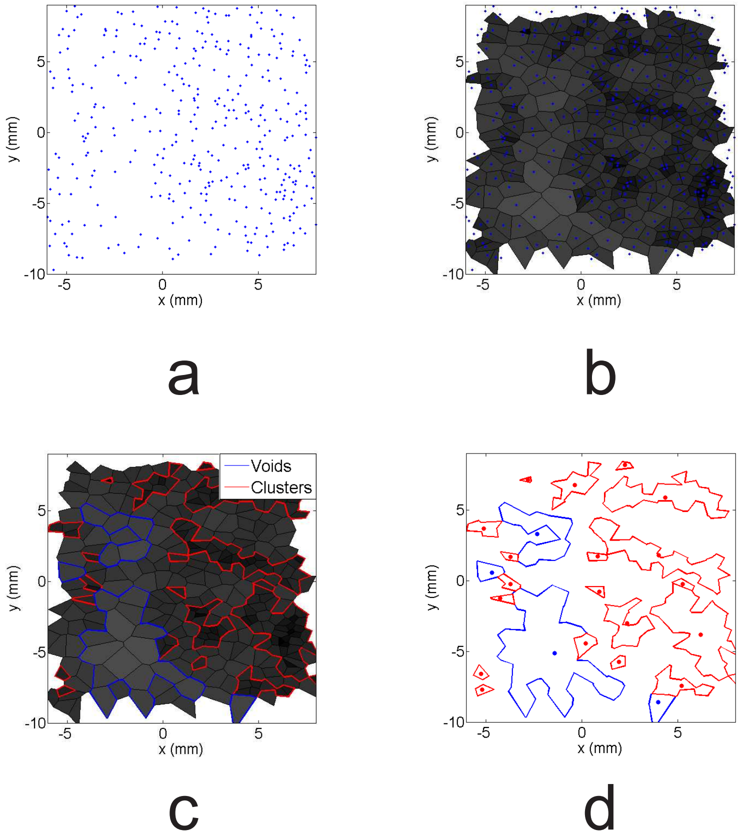

Figure 8.6: Schema of clusters and voids detection. Starting from particle's centers in real space (a), the Voronoï diagrams are obtained (b). With the method explained above, clusters and voids are identified (c). In a final step, centers of mass of clusters and voids are calculated (d).

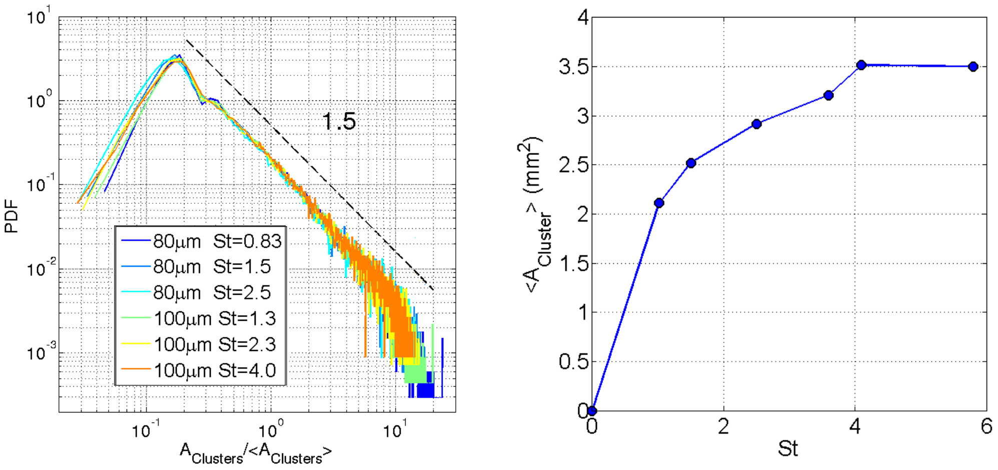

(a) (b)

Figure 8.7: (a) Clusters area PDFs, normalized by the mean area value. (b) Mean value of clusters area as a function of Stokes number.

means that the mean area and the most probable area are simply related by a proportionality relation: $A_C^{max} = C < A_C >$ with $C = 0.15$ for clusters. Therefore, both curves in figure 8.8 show a similar trend.

Interestingly, the characteristic areas reported here are always bigger than the results reported in [2], the minimum value reaches $\sqrt{A_C^{max}}/\eta = 20$, while the maximum goes up to $50\eta$ (figure 8.8c). This may suggest that different mechanisms may be responsible for the preferential concentration observed in both experiments. This may be due either to differences of the flows (hit open turbulence in Aliseda, anisotropic closed turbulence in von Kármán flow) or to differences in particle classes or it may indicate a strong Reynolds number dependency (in particular at small $Re_\lambda$, in the experiment by Aliseda *et al.*). Indeed, although the range of $St$ explored is similar in both experiments, this range was obtained differently: Aliseda had sub-Kolmogorov and very dense particles, while here we consider large particles (around Kolmogorov scale) but not as dense.

### 8.3.2 Voids

The same analysis has been performed with the voids detected. Figure 8.9a&b represent the void area PDFs (normalized by the mean area value) and their mean value as a function of the Stokes number. The first figure is extremely similar for the cluster case, but with a maximum for $\frac{A_V^{Max}}{<A_V>} \sim 0.3$.

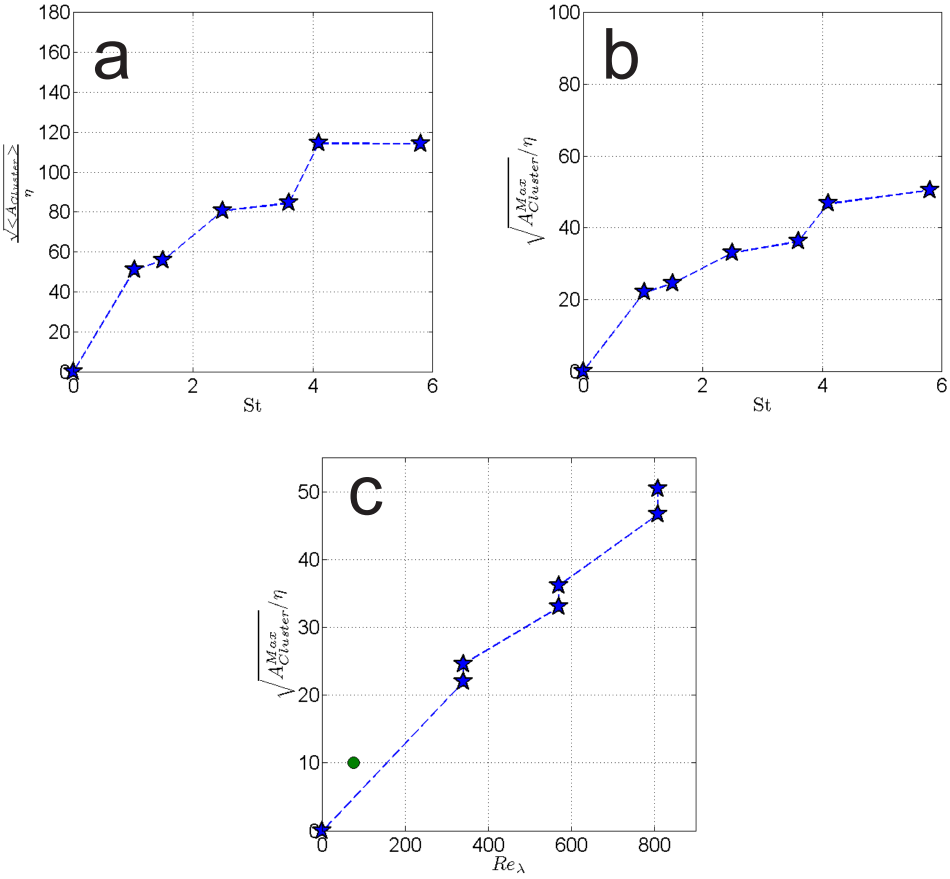

Figure 8.8: (a) Square root of the mean value of clusters area, normalized with the Kolmogorov length scale $\eta$ as a function of Stokes number. (b) Same figure as before but for the peak of cluster area distribution. (c) Value of the peak of cluster area distribution as a function of $Re_\lambda$. The green point corresponds to the measurements by Aliseda an collaborators [2].

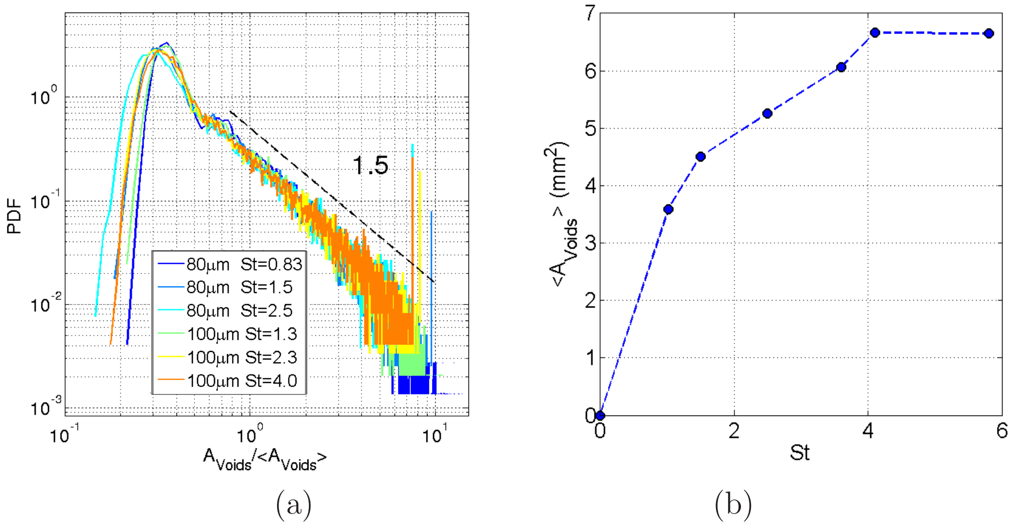

(a) (b)

Figure 8.9: (a) Voids area PDFs, normalized by the mean area value. (b) Mean value of voids area as a function of Stokes number.

Figure 8.9b shows again a similar trend to that observed for clusters, with higher values of $< A_V >$ reached. In fact, when comparing figures 8.7a and 8.9a voids seem larger than clusters globally by a factor 2.

Figure 8.10a shows the square root of the mean value of void area, normalized with the Kolmogorov length scale $\eta$ as a function of Stokes number, while figure 8.10b shows the same relationship but considering the most probable area. Again the same behavior as clusters is observed but with larger values (always in the order of a factor 2). In this case the mean area and the most probable area are simply related by a proportionality relation: $A_V^{Max} = C < A_V >$ with $C = 0.3$ (8.10b).

Therefore, voids and clusters show extremely similar properties for all the parameters explored. Although the resulting values for $< A_{C,V} >$ and $A_{C,V}^{Max}$ are different for clusters and voids, the trends are similar for all the cases studied.

### 8.3.3 Fractal structure of clusters and voids

Figure 8.11a shows cluster perimeters as a function of the square root of its area. The figure shows many different tendencies but the fractional behavior of the exponent evidences the fractal nature of clusters with the presence of several different populations. Moreover, the almost continuum range for this exponent (ranging from $\sim 1.4$ to $\sim 3.1$) and the differences with previous

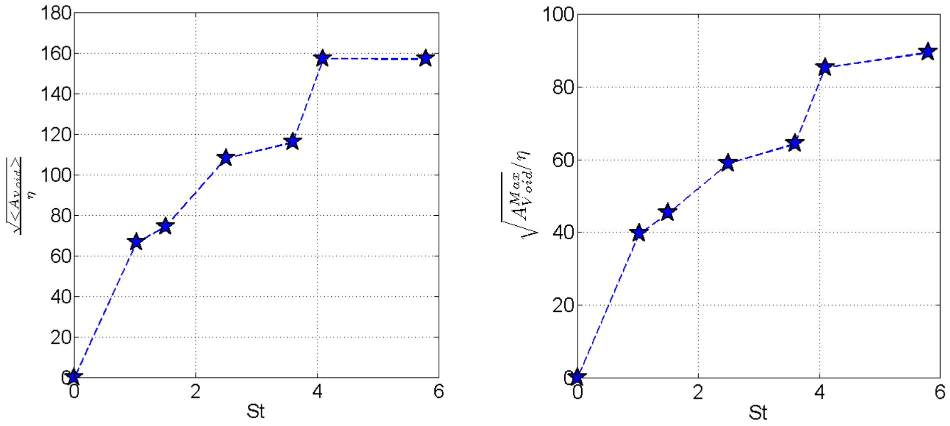

(a)

(b)

Figure 8.10: (a) Square root of the mean value of voids area, normalized with the Kolmogorov length scale $\eta$ as a function of Stokes number. (b) Same figure as before but for the maximal value of voids area.

works evidence the extreme complexity of these structures, and the necessity of further studies for better understanding this phenomenon. The fractal populations for voids (figure 8.11b) are similar to that observed for clusters, with similar trends.

## 8.4 PIV

As it has been mentioned above, the PIV analysis has been performed only for $Re_\lambda = 340$ and a resolution of $290 \times 290$ $\mu$m$^2$. This marginally resolves the dissipation scales of the flow (of the order of 25 $\mu$m). Besides, such PIV window is capable to resolve clusters and voids whose typical area was shown in previous section to be above a few millimeters squared. Figure 8.12 shows the temporal spectrum for $Re_\lambda = 340$ and $St = 0.83$. It can be appreciated that part of the inertial range is captured for approximately one decade, although it is affected at $f > 100Hz$ by noise.

The main results of the PIV are shown in 8.3. These results are in good agreement with the values obtained by Volk *et al.* [130] with the same apparatus used as reference in table 8.1. Therefore, main statistical properties of the velocity field are properly recovered for the PIV performed for this particular $Re_\lambda$. We note that the average value of velocity is not exactly zero, which probably reflects the fact that the measurement volume was not

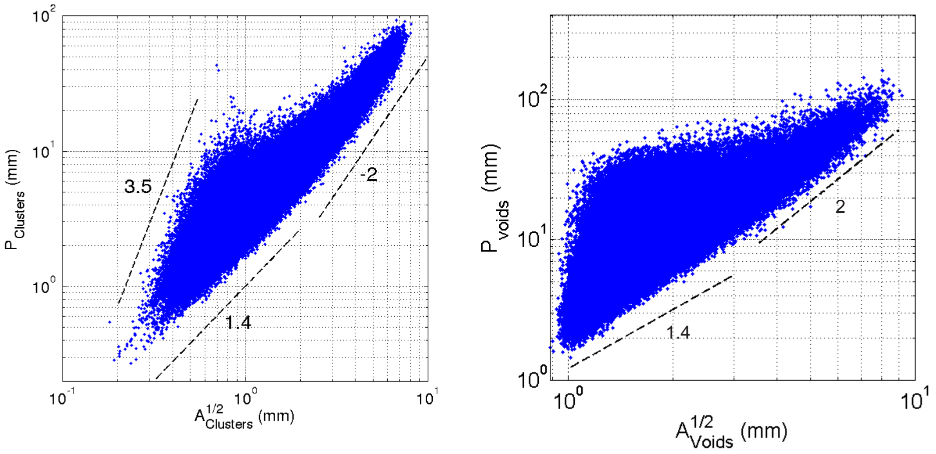

(a) (b)

Figure 8.11: (a) Clusters perimeters as a function of the squared root of its area. (b) Same figure as before considering voids.

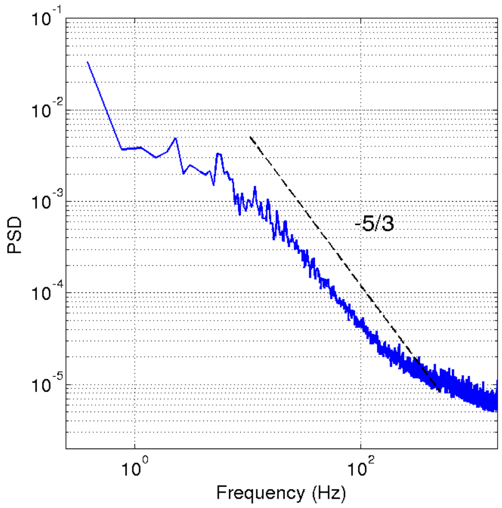

Figure 8.12: Temporal spectrum obtained with PIV for $Re_\lambda = 340$ and $St = 0.83$. The black dashed line has a slope $-\frac{5}{3}$. It can be seen that at least one part of the inertial regime is correctly resolved in the spectrum.

|  | Mean | std | Skewness | Flatness |
|---|---|---|---|---|
| $U_x$ | 0.13 m/s | 0.40 m/s | -0.06 | 3.06 |
| $U_z$ | -0.03 m/s | 0.20 m/s | 0.06 | 3.9 |
| $\|U\|$ | 0.41 m/s | 0.22 m/s | 0.41 | 3.05 |
| $w$ | 2.43 1/s | 404 1/s | 0.0034 | 4.90 |
| $\|a\|$ | 0.12 m/s$^2$ | 0.13 m/s$^2$ | 2.4 | 12 |
| $a_z$ | 0.0013 m/s$^2$ | 0.10 m/s$^2$ | 0.01 | 10.37 |
| $a_x$ | -0.022 m/s$^2$ | 0.14 m/s$^2$ | 0.01 | 9.90 |

Table 8.3: Statistical parameters obtained with PIV for velocity components, velocity modulus, vorticity, acceleration modulus and its components.

exactly centered and located at the statistical stagnation point expected at center of the apparatus.

The same analysis as in the previous chapter has been performed, where the conditioned statistics of the points of the flow at which inertial particles were placed were calculated. As in the previous chapter, no differences have been noticed between the global PIV of the flow and this conditioned statistics. Figure 8.13 shows the histograms for velocity modulus, vorticity and Lagrangian acceleration modulus. The results shown are for particles with $d_p = 80$ $\mu$m, while the particles with $d_p = 100$ $\mu$m show the same trend. The flow statistics evaluated at the position of particles and in random positions (in order to compare the same number of events). No appreciable differences are observed between both curves in any case.

In a second step, the same analysis have been performed but conditioning flow statistics to clusters and voids centers of mass (as shown in figure 8.6d). Again, no differences were observed, where all the parameters in table 8.3 have been compared.

In a further analysis, joint histograms have been studied, shown in figure 8.14 (always for particles with $d_p = 80$ $\mu$m). The horizontal coordinate represents Voronoï areas $\mathcal{V}$ while the vertical is the modulus of velocity, vorticity, the modulus of Lagrangian acceleration or the acceleration Cartesian components respectively. All the parameters have similar shapes to those observed in the previous chapter. Each figure is in the same color scale when comparing particles and random positions and are normalized with the mean value of parameters. As in chapter 7, the random positions simulates particles with the same $\mathcal{V}$ distribution.

No strong effect can be seen although the joint PDFs for the real particles seem slightly more peaked (the maximum is more intense) than for the ran-

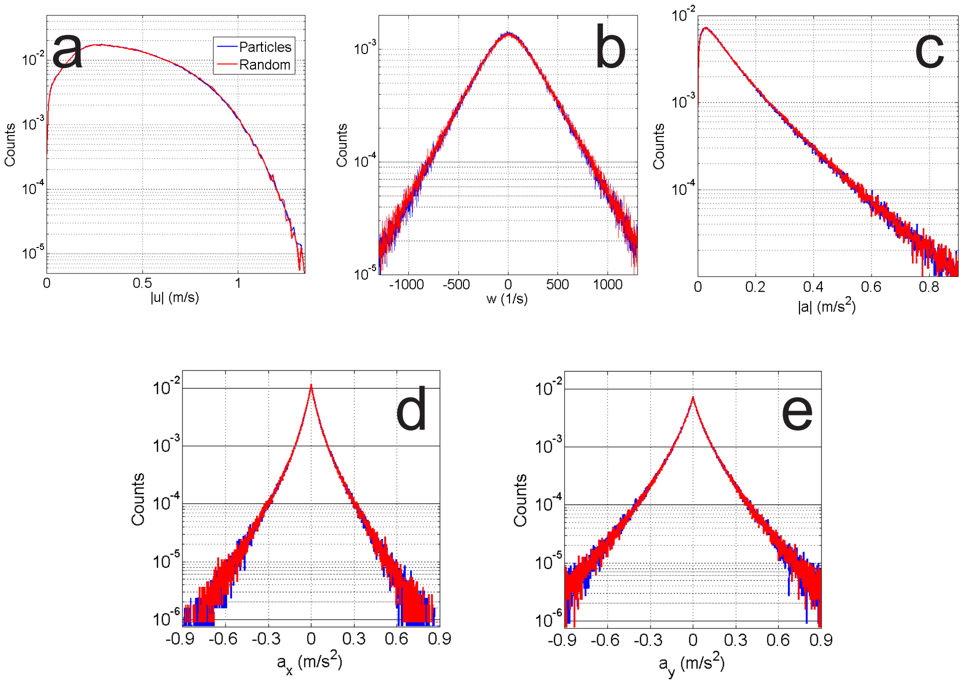

Figure 8.13: Histograms for velocity modulus (a), vorticity (b), Lagrangian acceleration modulus (c), its $z$ component (d) and its $x$ component (e). Blue line is for flow parameters evaluated at the position of inertial particles while the red line is for random positions.

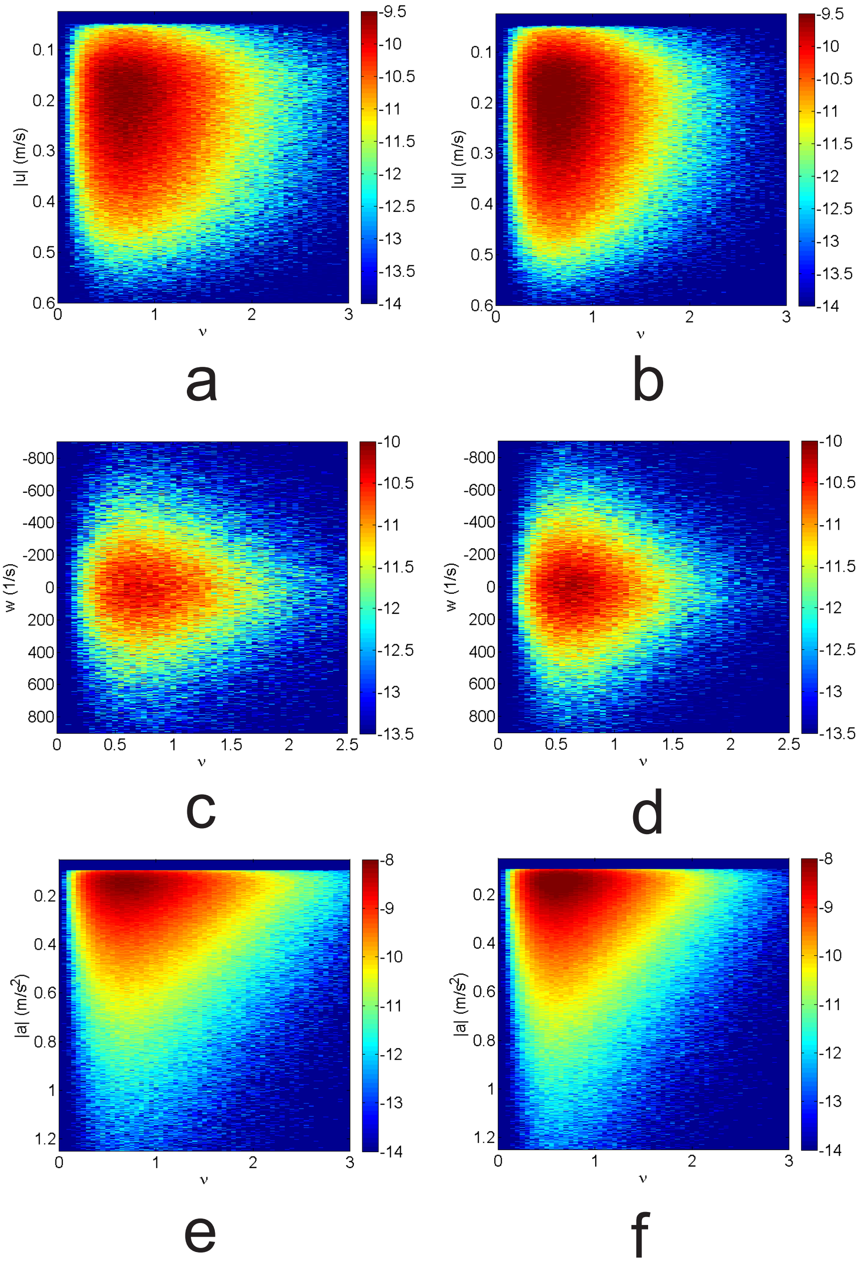

Figure 8.14: Joint histogram for random positions (left) and particle centers (right). The horizontal coordinate represents Voronoï areas $\mathcal{V}$ while the vertical the modulus of velocity (a and b), vorticity (c and d) and the modulus of Lagrangian acceleration (e and f).

dom points. In particular joint PDFs of Voronoï areas and vorticity on one hand and acceleration on the other are both more peaked, towards low vorticity and low acceleration respectively. However none of these trends seem more pronounced one from the other, hence no conclusion can be drawn at this point regarding the better relevance of turbophoresis (preferential sampling of low vorticity regions) or sweep-stick (preferential sampling of low acceleration regions).

The intermediate situation of our particles, where $d_p/\eta \sim 3$, in the limit between point and finite particles is also ambiguous considering the mechanism present for generating clustering. For the $Re_\lambda = 340$ case for which PIV is correctly resolved, this corresponds to Particles with Stokes number of order 1. Coleman *et al.* [20] have shown numerically (in the limit of point particles) that turbophoresis dominates for $St < 1$ while sweep-stick dominates for $St > 1$. In our case ($St \sim 1$) both mechanisms may therefore play a role. It will be interesting in future work to improve the PIV measurements (using dedicated equipment) in order to achieve the same conditional analysis of concentration and velocity fields at larger Reynolds number and hence also larger Stokes number. Also the small amount of clustering ($\sigma_\mathcal{V}$ is always below 0.66, while in the next chapter much higher values are reached) suggests that all these mechanisms are acting in a subtle form.

## 8.5 Conclusions

Preferential concentration of inertial particles with $\Gamma = 1.4$ in the range $2.8 < d_p/\eta < 6.3$ for $340 < Re_\lambda < 810$ and $0.8 < St < 4$ has been studied. This is an interesting case as it represents particles in the limit between point and finite size particles.

Clear evidence of clustering was observed. The Voronoï analysis in this case allowed us to easily identify clusters and voids and analyze their structure. It has been observed that clusters and voids have similar structure. Their PDFs collapse when they are normalized with their mean value and show a maximum for $A_{C,V}/ < A_{C,V} >\sim 0.15$. The typical size of clusters, given for instance by the most probable area of clusters, is found to increase from about $20\eta$ up to $50\eta$ when the stokes number increases from 1 to 4. This is significantly larger than the value of the order of 10 eta reported by Aliseda *et al.*, although a direct comparison is made difficult due to differences in experimental conditions.

The fractal nature of this structures have been verified, with a complex behavior that involves many different populations.

PIV measurements have been successful for the lowest $Re_\lambda$ studied. Some slight but not conclusive effects have been observed when inertial particles are present, where particles seem to explore the regions of lower vorticity and acceleration. At this point this does not allow to discriminate between a dominant turbophoretic effect or a sweep-stick mechanism, although in the range of Stokes number considered (of order 1) both effects might be relevant. Further studies, with better resolved PIV measurements at higher $Re_\lambda$ (and hence larger Stokes numbers) should be instructive.

# Chapter 9

# Preferential concentration of sub-Kolmogorov dense particles in active grid generated turbulence

## 9.1 Introduction

Continuing with our study of preferential concentration in turbulence, in this chapter we will focus on sub-kolmogorov size heavy particles; namely water droplets in the wind tunnel. This chapter is also a continuation of a previous work developed in the same tunnel, by Monchaux and collaborators [68]. Due to experimental limitations these previous studies were limited to moderate Reynolds numbers (up to $Re_\lambda \sim 120$). Using our new active grid, we were able to explore a wider range of Reynolds numbers up to $Re_\lambda \sim 400$. We also present an analysis of the geometry of clusters and voids.

In this chapter we will also analyze exhaustively the compatibility of sweep-stick mechanism with our measurements. Direct numerical simulations of homogeneous isotropic turbulence has been performed in order to check the consistency of this mechanism. A comparison with other models, such as turpophoresis (see chapter 1) is also discussed.

## 9.2 Experimental setup

Experiments are conducted in the wind tunnel SFT1 (see chapter 2). Turbulence is generated with the active grid described in chapter 2 (figure 9.1). In the present work the active grid was driven in a triple random mode: each

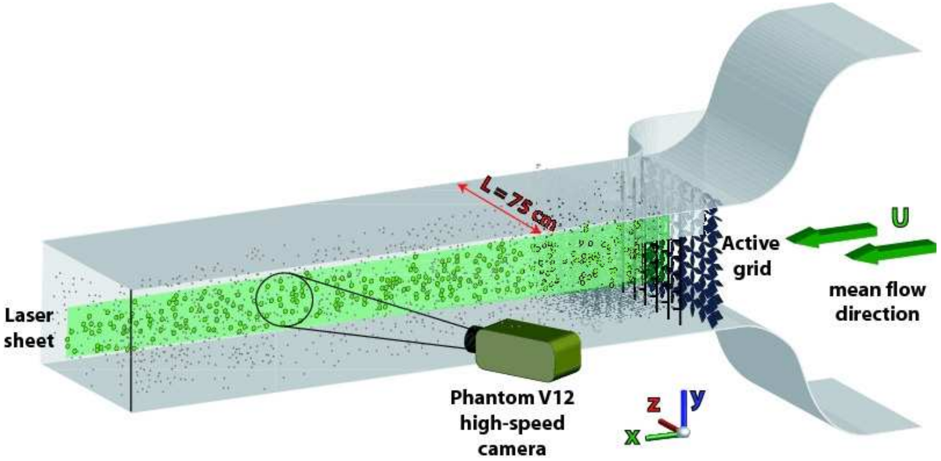

Figure 9.1: Sketch of the experimental setup.

axis has a random rotation rate (within a prescribed range), with random rotation and both (rate and direction) may change randomly in time (within a prescribed time-lag range). In the experiments presented here, the range of prescribed rotation rate was typically between 0.5 Hz and 3 Hz and the time lag between random changes of direction and/or rate was typically between 1 and 3 seconds. The mean velocity of the wind was varied from 3.4 m/s up to 7.6 m/s, corresponding to a range of Reynolds number $Re_\lambda$ from 230 up to 400. Table 9.1 summarizes the main turbulence parameters of the flow generated at the measurement volume location (3 m downstream the active grid) for the 6 mean wind velocities investigated. Besides, figure 9.2a shows a typical turbulent spectrum measured with hot-wire anemometry where a well developed inertial range of scales can be identified. Inertial particles are water droplets generated by 36 injectors (6 × 6 mesh with identical spacing than the grid) located in a transverse plane 15 cm downstream the grid.

As injectors we use single phase industrial spray generators with 0.3 mm nozzles with filtered water pressurized at 40 bars. Figure 9.2b shows the size distribution (in volume) of the generated spray measured at the measurement volume location (3 m downstream the grid), with a Spraytec diffractometer from Malvern (the same used in chapter 7). We have checked that this size distribution is robust and does not depend significantly on the mean wind velocity. As it can be seen on the figure, the size distribution is peaked around a most probable droplet diameter of the order of $D_p \sim 60$ $\mu$m, but is relatively polydisperse.

The water flow rate cumulated over all 36 nozzles is $\Gamma_w = 18$ L/min, giving a volume fraction of water in the range $\phi_v = [5 \cdot 10^{-5} - 2 \cdot 10^{-4}]$ (the lower the average wind velocity, the larger the volume fraction). As explained in chapter 1, we define the droplet Stokes number as the ratio $St = \tau_p/\tau_\eta$, with $\tau_\eta$ the carrier flow dissipation scale estimated from hot-wire anemometry (see table 9.1) and $\tau_p$ the particle viscous relaxation time based on the most probable particle diameter $D_p$ estimated from the diameter distribution function (in figure 9.2b). The Stokes number can be equivalently estimated as $St = (D_p/\eta)^2(1 + 2\Gamma)/36$ with $\eta$ the dissipation scale of the carrier turbulence and $\Gamma = \rho_{water}/\rho_{air}$ the density ratio between the particles and the carrier flow, what in the present case (water particles carried in air) simply gives $St \simeq 46(D_p/\eta)^2$. Note that as droplets diameter is sub-Kolmogorov, the usual point particle estimation is used for the Stokes number. Therefore, as the most probable particle diameter $D_p$ is kept constant and does not depend on flow conditions, varying the carrier flow Reynolds number (and hence varying the dissipation scale $\eta$) also results in a variation of particles Stokes number. Table 9.1 also indicates the particles Stokes number corresponding to each Reynolds number investigated in the present study.

Acquisitions are performed using a Phantom V12 high speed camera operated at 10 kHz and acquiring 12 bits images at a resolution of 1280 pixels × 488 pixels corresponding to a 125 mm (along $x$)× 55 mm (along $y$), though homogeneous illumination conditions (tested *a posteriori* during the post-processing) were actually limited to a smaller visualization window of 70 mm in the streamwise x-direction and 50 mm in the transverse y-direction, which is about half an integral scale. The camera is mounted with a 90 mm macro lens; the view angle with respect to the laser sheet is of the order of 60°, therefore a Scheimpflug mount is used to compensate loss of depth of field. At the given spatial resolution and repetition rate, the onboard memory of our camera (8Gb) allows to record slightly more than $10^4$ images (hence slightly more than one second of recording), which corresponds already to a few integral time scales of the carrier flow. For each experimental configuration we record at least 15 such recordings, thus a set of more than $1.5 \cdot 10^5$ images are recorded for each experiment, though in the present work only a subsample of about $10^4$ statistically independent images have been generally processed. All frames, with the actual temporal resolution of 10kHz have been processed however for the “linear camera” reconstruction method described in section 9.7.

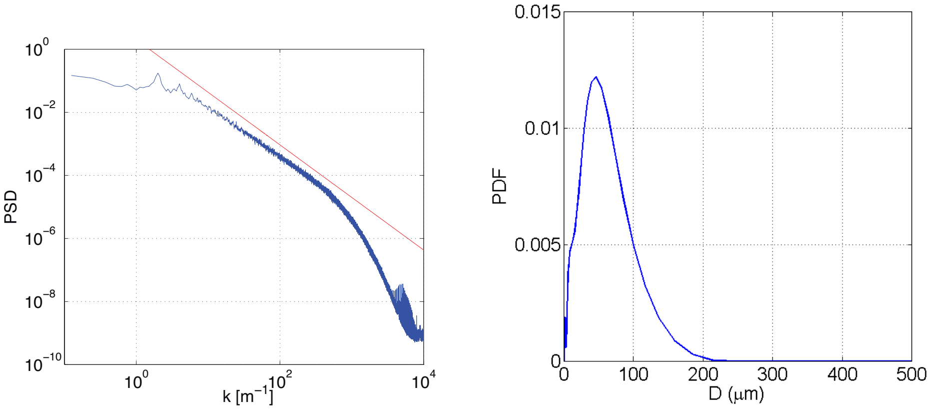

(a) (b)

Figure 9.2: (a) Typical velocity spectrum generated 3 m downstream the active grid. The red solid line indicate a $k^{-5/3}$ power law. (b) Droplet diameter probability density function.

| $Re_\lambda$ | $U$ (m/s) | $L$ (cm) | $\eta$ ($\mu$m) | $\epsilon$ (m$^2$s$^{-3}$) | $St$ |
|---|---|---|---|---|---|
| 234 | 3.4 | 13.0 | 280 | .69 | 2.1 |
| 264 | 4.0 | 13.2 | 240 | 1.2 | 3.3 |
| 295 | 4.8 | 13.5 | 208 | 2.0 | 4.3 |
| 331 | 5.7 | 13.8 | 178 | 3.4 | 5.8 |
| 357 | 6.4 | 14.0 | 160 | 4.7 | 6.6 |
| 400 | 7.6 | 14.3 | 140 | 7.7 | 9.9 |

Table 9.1: Experimental parameters : Reynolds number based on Taylor microscale ($Re_\lambda$), mean wind velocity ($U$), energy injection scale ($L$), dissipation scale ($\eta$), energy dissipation rate per unit mass ($\epsilon$), Stokes number ($St$).

## 9.3 Voronoï analysis of particles spatial distribution

Figure 9.3a shows a typical image of the spatial distribution of particles (the image shown has been corrected for spatial perspective and distorsions). A structuration of the dispersed phase with clusters of droplets and depleted regions is qualitatively evident in this image. To go further in a quantitative analysis of clustering, we have used Voronoï diagrams as in previous chapters. Figure 9.3c presents an example of a calculated Voronoï diagram from the experimental field corresponding to the central region of the image in figure 9.3a, after detection of the particle centers.

Due to illumination inhomogeneity (resulting both from weak lateral blurring due to depth of field limitation, in spite of the use of the Scheimpflug mount, and laser sheet attenuation) we have limited the region of interest for the Voronoï analysis to a central region of the images (corresponding to the yellow rectangle in figure 9.3a) where we have checked that the detection of particles centers is statistically homogeneous over the entire set of $1.5 \cdot 10^5$ images for each experiment (figure 9.3b shows the spatial probability density function of detected particle positions).

As it has been already explained in the two previous chapters, it has been shown in a previous work [68] that a quantitative measure of clustering is given by the analysis of the probability distribution function (PDF) of Voronoï areas compared to that of an exactly random Poisson process (RPP). We recall that no analytical expression is known for the PDF of an RPP, though it is known to be well approximated by a Gamma function [30], however the standard deviation of Voronoï areas (normalized to the average Voronoï area) $\mathcal{V} = \mathcal{A}/\overline{\mathcal{A}}$ for an RPP has a known analytical value $\sigma_{\mathcal{V}}^{RPP} \simeq 0.53$.

## 9.4 Clustering evidence

In this section we present the statistical analysis of Voronoï areas for the different experiments reported in table 9.1. Figure 9.4a presents the probability density function (PDF) of the normalized Voronoï areas $\mathcal{V}$ for all the experiments at different Reynolds numbers and Stokes numbers; we have also superimposed in the figure the distribution expected for a uniform random distribution. As in the previous chapter, the discrepancies with an uniform random process can be clearly seen. Furthermore, the shape of PDF presents the same characteristics, where large Voronoï areas are significantly over-represented compared to the RPP case and areas smaller than $\mathcal{V} \sim 0.5$

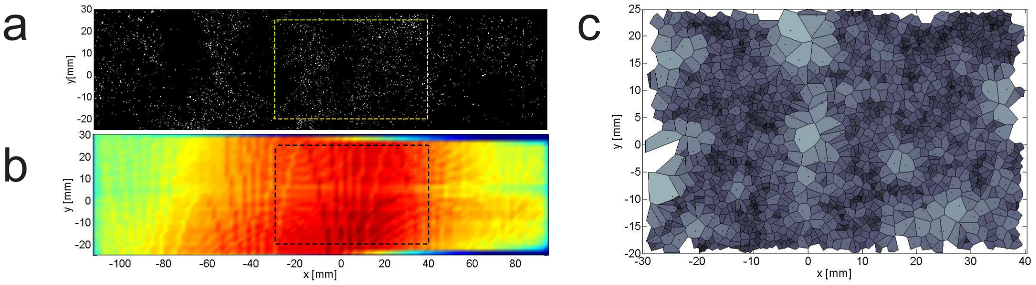

Figure 9.3: (a) Typical raw image of particles. (b) Probability density function of the position of detected particles. (c) Voronoï diagram limited to the region of interest.

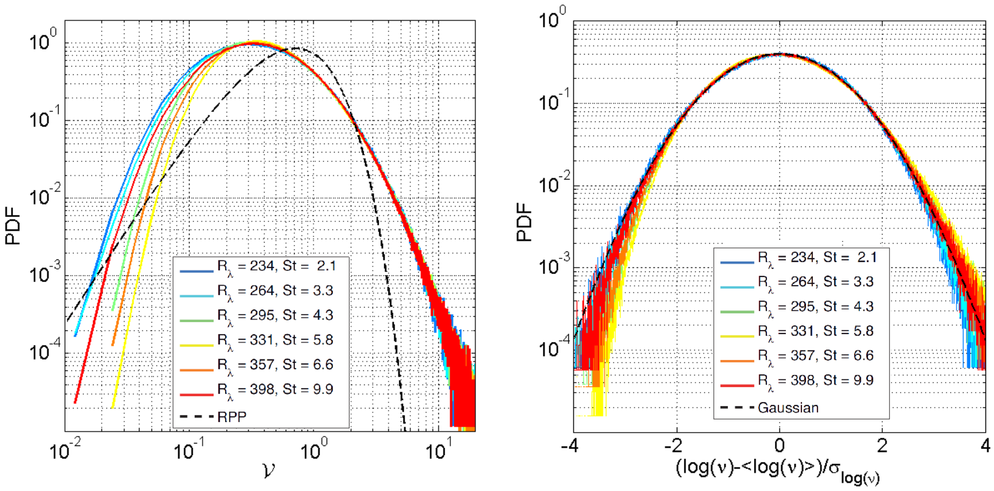

(a)

(b)

Figure 9.4: (a) Probability distribution of normalized Voronoï area $\mathcal{V}$ for experiments at different Reynolds number and Stokes number. (b) Probability distribution function, centered and reduced, of $log(\mathcal{V})$.

are significantly over-represented (indicating the presence of depleted regions and clustering phenomena respectively). In this case the tendencies appear much more pronounced. Figure 9.4a shows an increase of the probability of finding regions with local concentration (given by the inverse of the Voronoï areas) between 2 and several tens of the average concentration. We note however that even if the probability density for very low normalized areas is lower than for the RPP, this has a marginal overall contribution and the integrated probability of finding normalized Voronoï areas below typically 0.5 is significantly larger in our experiments than for an RPP. Besides the position of the maximum of the PDF, corresponding to the most probable Voronoï area is notably lower than for a RPP, indicating the predominance of small areas, hence of overconcetrated regions. Interestingly we also observe that only the left part of the PDF (corresponding to small Voronoï areas, hence highly concentrated regions) appears to be influenced by Reynolds/Stokes number effects while the right part (corresponding to the depleted regions) is extremely robust when experimental parameters are varied. A similar behavior was also reported in the previous chapter and in previous measurements by Monchaux *et al.* [68] at lower Reynolds numbers (with passive grid generated turbulence).

As already observed in the previous chapter and in the previous work by Monchaux *et al.* ([68]), it can be seen in figure 9.4b that the PDF of $log(\mathcal{V})$ is approximately gaussian, at least within he range $\pm 3\sigma_{\log(\mathcal{V})}$. Deviation from lognormality is only observed for small values of $\log(\mathcal{V})$ which are slightly under-estimated (interestingly, contrary to the previous chapter where this value was over-estimated). Therefore, $\sigma_{\mathcal{V}}$ is again a good parameter for quantifying the evolution of particle clustering.

Figure 9.5a shows the evolution of $\sigma_{\mathcal{V}}$ with the Reynolds number $Re_\lambda$ of the carrier flow. As expected by the previous qualitative considerations, $\sigma_{\mathcal{V}}$ exceeds significantly the RPP value $\sigma_{\mathcal{V}}^{RPP} = 0.53$, what reveals the high level of clustering. Interestingly we also note that, though $\sigma_{\mathcal{V}}$ changes by less than 10% over the different experiments, a maximum of clustering is reached for $Re_\lambda \sim 300$.

As discussed previously, carrier flow Reynolds number and Stokes number of carried particles are related in our experiment, since particles are injected with constant size distribution. Therefore, we have plotted in figure 9.5b the evolution of $\sigma_{\mathcal{V}}$ as a function of $St$ (instead of $Re_\lambda$). We have also artificially added the point for $St = 0$, which is expected to represent tracers with $\sigma_{\mathcal{V}}^{RPP} = 0.53$. We have also reported on the same figure previous measurements at lower Reynolds number (from [68]). In this plot, solid lines connect measurements from this previous campaign performed at constant Reynolds number. For guide-eye purpose we have also connected (with a dashed-line)

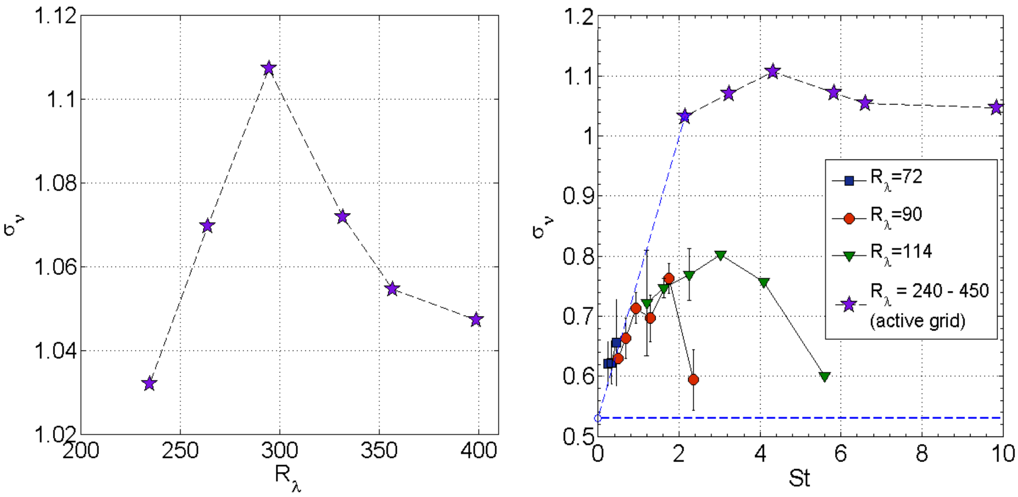

(a) (b)

Figure 9.5: (a) Evolution of the standard deviation of the normalized Voronoï area with Reynolds number. (b) Evolution of the standard deviation of the normalized Voronoï area with Stokes number. We have also reported previous measurements at lower Reynolds number, with the passive grid, by Monchaux *et al.* [68]. We have also manually added the point ($St = 0, \sigma_{\mathcal{V}} = 0.53$).

the measurements from the present study as, though they are not at constant Reynolds number, they all correspond to conditions at much higher Reynolds number than previously. This figure shows a consistent increase of the clustering level with the Reynolds number. It also shows that the maximum of clustering for $Re_\lambda \sim 300$ observed if figure 9.5a may be intrepreted as an optimal Stokes number around 3-4, consistently with observations at lower Reynolds number.

To summarize this section on the diagnosis of clustering, our new measurements confirm the previously reported quasi-lognormal shape of Voronoï area distribution, which is an interesting feature, as the standard deviation $\sigma_{\mathcal{V}}$ of the Voronoï areas can therefore indeed be considered as a good indicator of clustering level. Based on this indicator, the set of new measurements at high Reynolds number combined with the previous measurements at moderate Reynolds number shows that increasing the Reynolds number at constant Stokes number results in a clear increase of clustering level. On the contrary, the new measurements show that when increasing the Reynolds number at constant particle size (and hence at increasing Stokes number) an optimal Reynolds exists for which clustering level is maximal ($Re_\lambda^{max} \sim 300$ in the present study with particles with average diameter around 60 $\mu$m). Optimal clustering is generally observed for Stokes number around unity (which is classically interpreted as an optimal response time of the particles to the turbulent solicitations). This is consistent with the observation that the maximum of clustering level observed at $Re_\lambda \sim 300$ can be reinterpreted as a maximum of clustering for $St \sim 4$. Furthermore considering that clustering increases with $Re_\lambda$, if we take in figure 9.4b the point at $St \sim 4$ and $Re_\lambda \sim 300$ (corresponding to the maximum of clustering we have observed) as reference, one would expect that for the evolution of $\sigma_\mathcal{V}$ as a function of Stokes at constant $Re_\lambda = 300$ points at the right of the reference point (for $St > 4$) will be below the points (stars) in figure 9.5b, while points at the left of the reference point (for $St < 4$), will be above the points in the figure. Therefore, it is likely that the curve representing the evolution of $\sigma_\mathcal{V}$ as a function of Stokes at constant $Re_\lambda \sim 300$ should look more peaked than the dashed-line curve represented in figure 9.5b with a maximum for an optimal Stokes number between 2 and 4, in a range comparable to what was previously observed for $Re_\lambda = 114$. Further experiments, with the active grid generated turbulence, varying particles Stokes number at constant Reynolds number will be performed soon to better address the question of a possible dependency of the optimal Stokes number as a function of Reynolds number.

## 9.5 Cluster geometry

The previous section was dedicated to the diagnosis of the clustering phenomenon. In the present section we address the question of identifying and characterizing the clusters. Clusters and voids are identified with same method as in chapter 8. Figure 9.6a shows the PDFs of the area $A_C$ of clusters, normalized by the average area $< A_C >$. As in the previous chapter, clusters an voids presents similar behavior, therefore only results for the clusters will be shown. Interestingly, all PDFs collapse onto a single curve. Like Monchaux *et al.*, we find that the PDFs of cluster area follow a -2 exponent power law for large areas. However, contrary to Monchaux *et al.* we do observe a clear maximum of these PDFs, with a peak around a most probable area $A_C^{max} = 0.15 < A_C >$, revealing the existence of a characteristic cluster dimension. This is again a strong experimental evidence of a system with a typical cluster area, in contrast to the conclusion by Monchaux *et al.* but in agreement with the earlier work by Aliseda *et al.*.

Figure 9.7a shows how the mean value of cluster area varies with $Re_\lambda$,

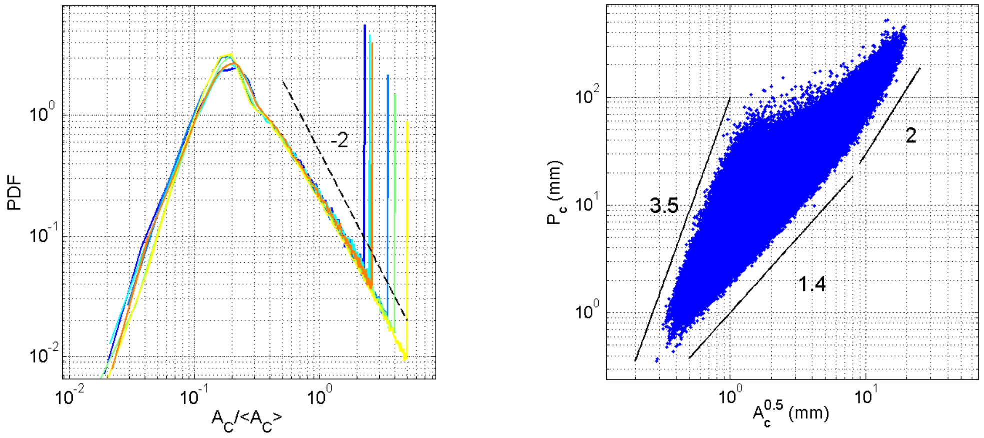

(a) (b)

Figure 9.6: (a) Clusters area PDFs, normalized by the mean area value. (b) Clusters perimeters as a function of the square root of its area.

while 9.7b show the same parameter but as a function of $St$. Both figures show a similar behavior with a minimum around $Re_\lambda = 331$ or $St = 5.8$, slightly bigger than the maximum values obtained for the standard deviation of Voronoï cells in figure 9.4a. As figure 9.6a, shows that the mean value $< A_C >$ is proportional to the most probable clusters area $A_C^{max}$ (*i.e.* the maximum value of the PDFs), although figures 9.7a&b only shows the mean clusters area values, the most probable clusters area has the same trend with both parameters. Figure 9.7 shows that the average cluster area $A_C$ is of the order of a few squared millimeters.

Figure 9.8 shows $\sqrt{< A_C >}/\eta$ as a function of $Re_\lambda$ and $St$. Our experimental results show that typical cluster size ranges from $10\eta$ to $20\eta$. This is in quantitative agreement with the work by Aliseda and co-workers [2]. Working with grid turbulence in a wind tunnel with $Re_\lambda = 75$, and using qualitative inspection, they found that poly-dispersed water droplets form clusters with a typical area of $10\eta$.

In figure 9.8 we also note a net trend of cluster size to increase when Reynolds number grows above 300. Such a behavior is consistent with the observation reported in previous chapter, where the investigated Reynolds number ranged from 340 to 810 and typical cluster size was found to increase from 20 to about $100\eta$ for a similar range of Stokes number. Alltogether, measurements by Aliseda *et al.*, measurements at high $Re_\lambda$ in previous chapter and measurements in the present chapter (figure 9.9), suggest that the typical cluster size relative to $\eta$ may be significantly dependent on Reynolds

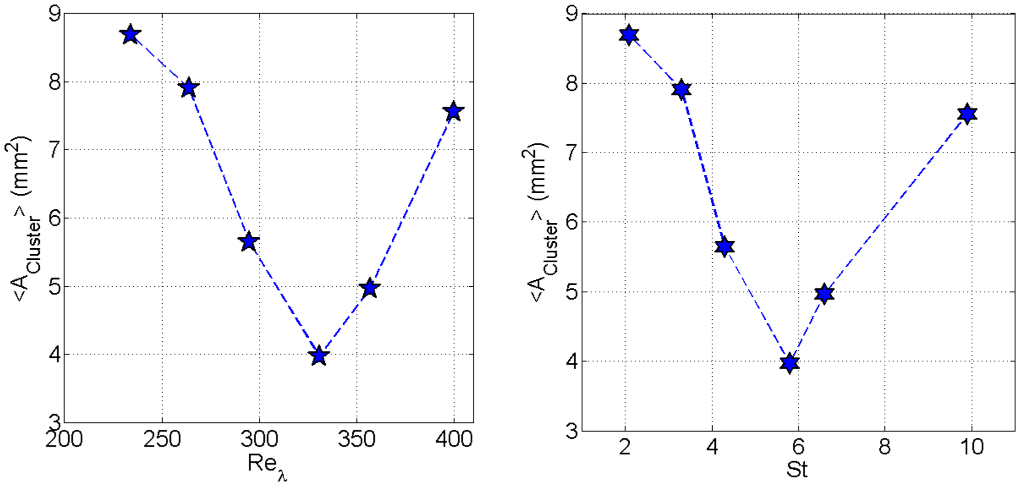

(a) (b)

Figure 9.7: (a) Clusters areas mean value as a function of $Re_\lambda$. (b) Same parameter but as a function of $St$.

number, varying from about $10\eta$ for low/moderate $Re_\lambda$ up to above $100\eta$ for high $Re_\lambda$. This may also indicate that $\eta$ is not the appropriate scale of the flow to characterize cluster dimension.

Figure 9.6b shows clusters perimeters as a function of the square root of its area. The figure shows many different tendencies but the fractional behavior of the exponent evidences the fractal nature of clusters with the presence of several different populations. Moreover, the almost continuum range for this exponent (ranging from $\sim 1.4$ to $\sim 3.1$, similar to those observed in chapter 8) evidence again the extreme complexity of this structures.

## 9.6 Numerical simulations.

### 9.6.1 Motivations

In this section we will use direct numerical simulations (DNS) in order to explore the origins of clustering phenomena. In chapter 1 we detailed the two main mechanisms proposed: turbophoresis and sweep-stick mechanism. These two mechanisms are similar as they propose that particles stick to different points of the flow: low-vorticity (or high strain) regions in a turbophoresis scenario and zero-acceleration points in sweep-stick mechanism. Using DNS we can identify these particular points of the flow, and then com-

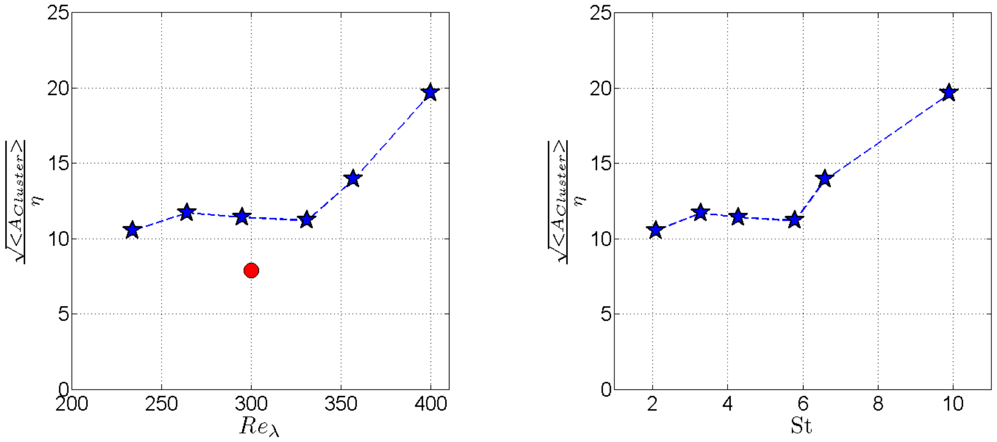

(a) (b)

Figure 9.8: (a) Square root of clusters area's mean value normalized with the dissipation scale $\eta$ as a function of $Re_\lambda$. (b) Same parameter but as a function of $St$. The red circle represents the value obtained numerically in section 9.6 for zero-acceleration points.

pare their clustering properties with the experimental results obtained in the last section.

Considering the large $St$ of the particles investigated, the mechanism that better adjusts to our measurements should be the sweep-stick mechanism [20]. Therefore, DNS has been performed in order to probe the consistency of our results with a sweep-stick mechanism as proposed by Vassilicos and collaborators ([38, 39]). They show numerically very strong correlation in a wide range of scales between distributions of heavy inertial particles on one hand and zero-acceleration points of the carrier velocity field on other hand.

### 9.6.2 Simulation details.

In the present work, DNS has been performed using a pseudo-spectral code, further details of the code composition can be found in [66]. It has been performed in collaboration with Pr. Pablo Mininni, from University of Buenos Aires, for a cube of $N = 512^3$ grid points and a viscosity of $3 \times 10^{-4}$. For assuring a proper resolution of all the turbulent scales it has been checked that $\kappa_\eta/\kappa_{max} \sim 1$, where $\kappa_\eta = (\epsilon/\nu^3)^{1/4}$ and $\kappa_{max}$ is the maximum wave number resolved in simulations. It has been run with random initial conditions and at each step Lagrangian acceleration field has been recorded (figure 9.11a).

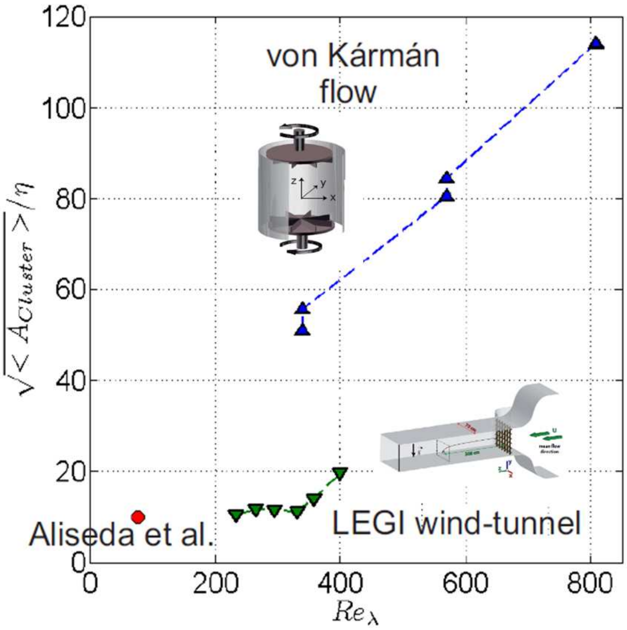

Figure 9.9: Square root of cluster area mean value normalized with the dissipation scale $\eta$ as a function of $Re_\lambda$ for the results obtained in this chapter (green triangles), in the previous chapter (blue triangles) and by Aliseda *et al.* (red circle).

$Re_\lambda$ has been estimated using the same relations as the experimental value (according to [94]). The Reynold number obtained, $Re_\lambda = 300$, is extremely close to the third $Re_\lambda$ in table 9.1 for experiments (also the value that corresponds to the maximum $\sigma_\mathcal{V}$, then the maximum level of clustering achieved in our experiments). Therefore, the numerical zero-acceleration field can be compared with the experimental results showed before. It is also important to remark that no particles are present in the simulations, while we are only interested in studying particular points of the flow.

### 9.6.3 Determination of "zero-acceleration" points.

Considering that PDFs of acceleration magnitude can be approximated by a log-normal distribution (see Mordant et al. [71]) with a standard deviation $\sigma$ (as shown in figure 9.10), a zero acceleration point is defined as a point which has an acceleration modulus of $\sigma/10$ at most (only $\sim 0.1\%$ of the points satisfies this criterion). Strictly speaking this defines small patches of locally

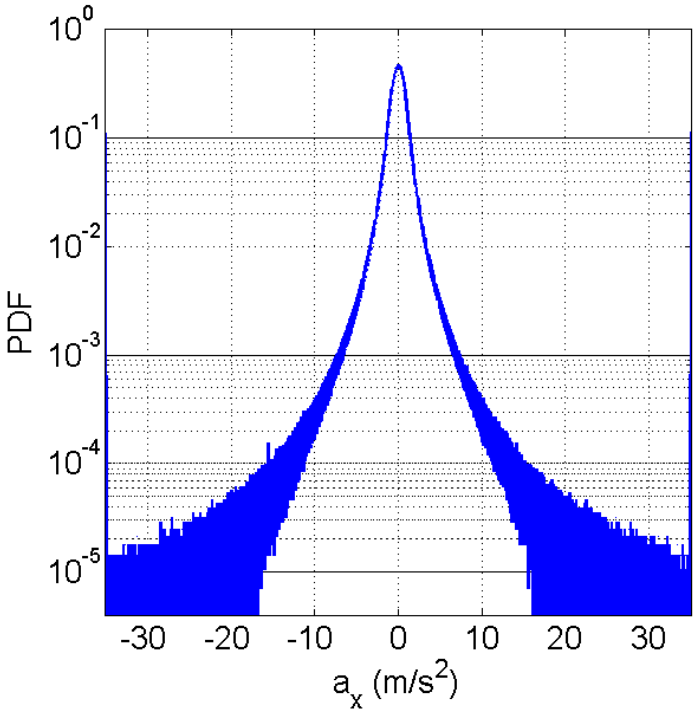

Figure 9.10: Histogram of the acceleration $a_x$ of the flow obtained with DNS. The other components give similar result.

small acceleration rather than actual zero acceleration points. We point out that results presented in this section have been shown to be robust to small variations of the choice of the threshold used to define low acceleration regions. Assuming that the experimental Kolmogorov scale is the same as the numerical one, a conversion to physical parameters can be made, giving the relation 1 *grid point* $\sim$ 80 $\mu$m, and the simulation resolves eddies up to length-scales of $\sim 4$ cm, slightly smaller than the integral scale in the experiments.

Considering that the thickness of the laser sheet in the experiment is of order of 1 mm (which corresponds to about 13 numerical pixels in the simulation), we stack 13 slices of the numerical box to reproduce artificially a plane comparable to the experimental laser sheet. Zero acceleration points are then defined as the center of mass of the low acceleration patches (that can be seen in figure 9.11b), obtained using the criterion that acceleration is smaller than $\sigma/10$ within this slice. After these points have been identified (figure 9.11c), the standard Voronoï analysis can be performed (figure 9.11d).

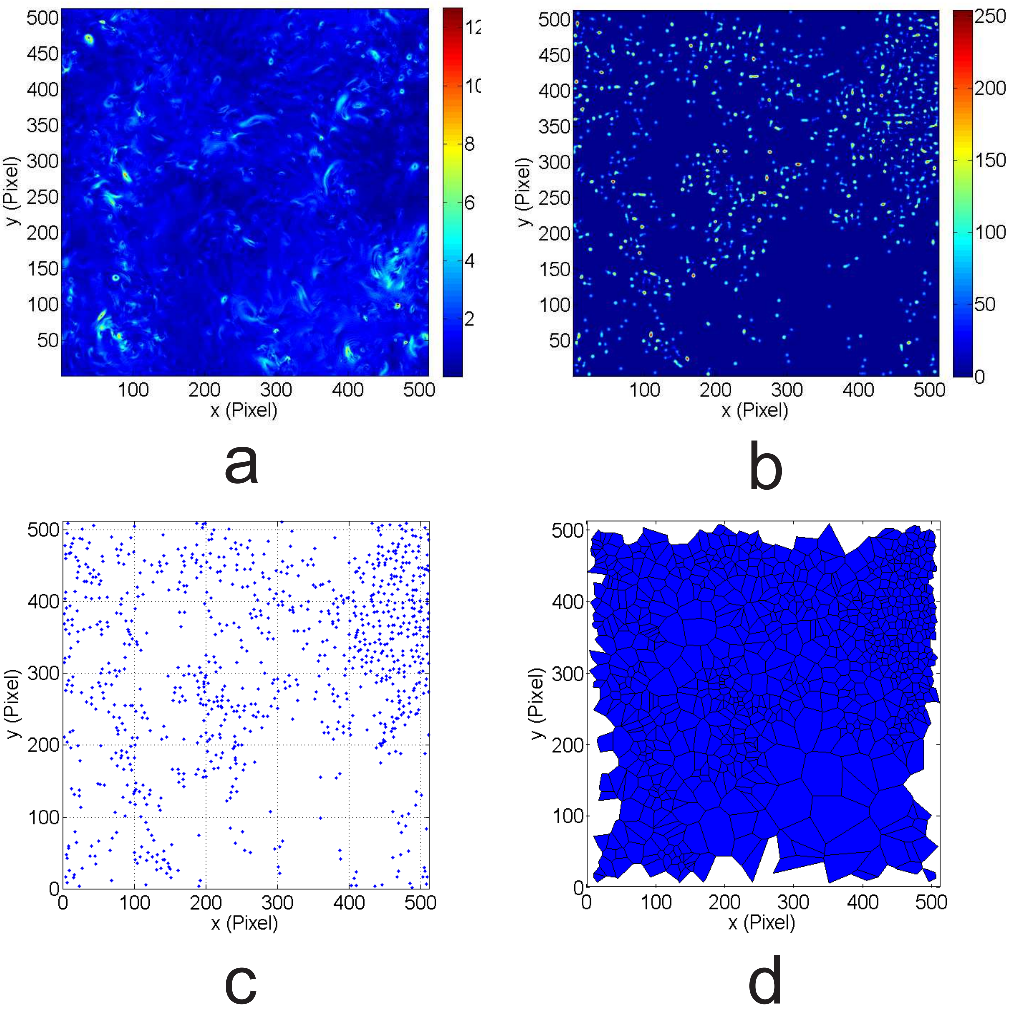

Figure 9.11: (a) Modulus of the Lagrangian acceleration for a cross-section of 512 × 512pixels. (b) Zero-acceleration patches obtained for 13 superposed slides (c) Zero-acceleration points obtained as the centers of mass of patches where acceleration magnitude is below $\sigma/10$. (d) Voronoï tesselation of previous image.

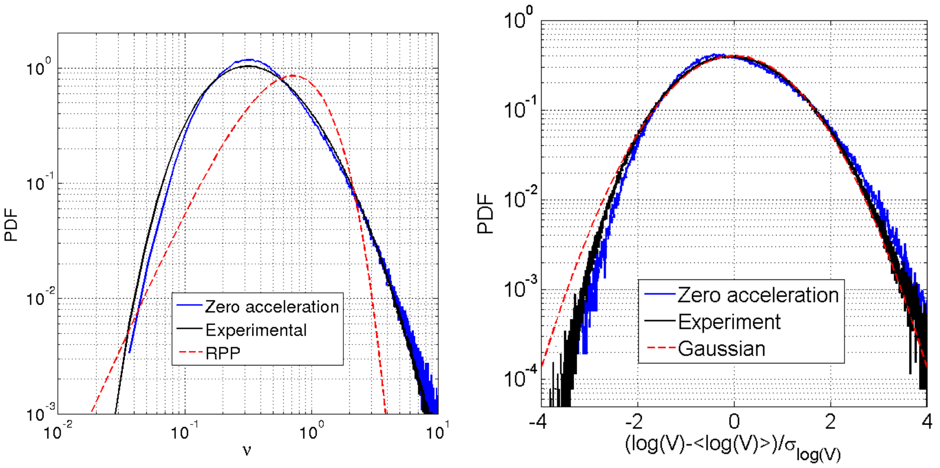

(a) (b)

Figure 9.12: (a) Voronoï cell area PDF normalized by the mean area obtained experimentally (black line) and numerically (blue line). The red dashed line represents a RPP distribution. (b) Probability distribution function, centered and reduced, of $log(\mathcal{V})$ for the same values as before. The red dashed line represents a Gaussian distribution. Al the values are for $Re_\lambda \sim 300$

### 9.6.4 Voronoï analysis of zero-acceleration points.

Figure 9.12a shows the Voronoï area PDF for the droplets in the experiment at the mentioned $Re_\lambda$ (black line) and for the zero acceleration points in the simulation (blue line). The similarity between both curves is remarkable. Figure 9.12b shows the PDF centered and reduced of $log(\mathcal{V})$ obtained again experimentally (black line) and numerically (blue line). Again both curves are extremely similar. This later result is of capital importance because it shows that we have been able, using zero-acceleration points, to reproduce the nature of the structure of particle distributions obtained experimentally. Though the almost perfect superposition of the PDF of $\mathcal{V}$ for particles in experiments and zero acceleration points may appear as somehow fortuitous (in particular the PDF for particles is expected to change with Stokes number for instance), the collapse of the centered-reduced PDF of $log(\mathcal{V})$ is an important observation. This representation has been shown to be robust for all classes of particles. The present observation suggests that it might indeed be reminiscent of the clustering properties of zero-acceleration points in the context of a sweep-stick mechanism.

To go further in the analysis, we investigate the geometry of clusters

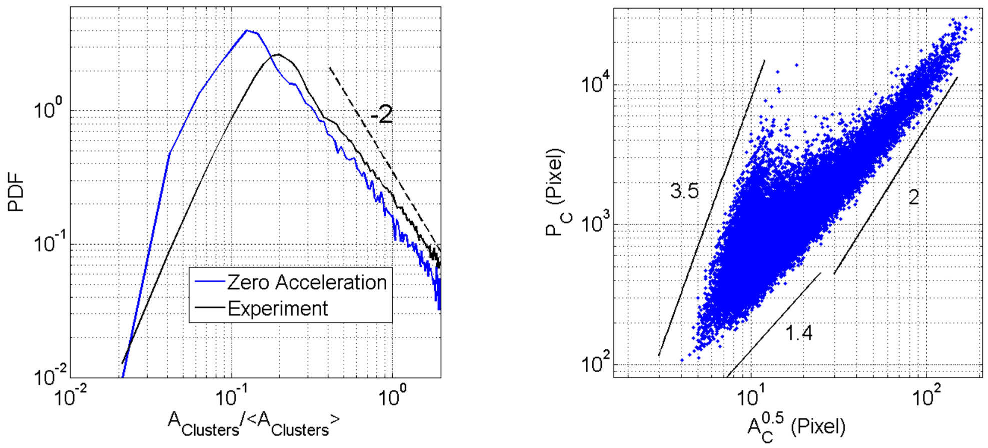

(a) (b)

Figure 9.13: (a) Cluster area PDF obtained experimentally (black line) and numerically (blue line). (b) Clusters perimeters as a function of the square root of its area. Al the values are again for $Re_\lambda \sim 300$

of zero-acceleration points and compare them to experimental results for particles, presented in the previous section. Figure 9.13a shows the same comparison for the PDF of cluster area (normalized with the mean area). Again the numerics reproduces correctly the experimental results, although small clusters are slightly more probable for zero acceleration points than for the particles. In particular the algebraic tail with a $-2$ power law is robustly reproduced. The most probable area is slightly smaller in the numerics. The average area $< A_C >$ for zero acceleration points is found of the order of $8\eta$, hence slightly smaller, but of the same order of magnitude of what has been found in the experiments for clusters of particles.

Figure 9.13b represents clusters perimeters as a function of the square root of its area (only the numerical results are shown in this case), that also shows similar tendencies that the ones appreciated in figure 9.7b for the experiments, evidencing that clusters of zero acceleration points present a fractal structure similar to that of clusters of particles in the experiments.

### 9.6.5 Voronoï analysis of other characteristic points of the turbulent field.

In order to verify the actual relevance of zero-acceleration points to characterize clustering properties of inertial particles, other characteristic points of

|  | Zeros | Mean acceleration | Vorticity | Experiment |
|---|---|---|---|---|
| $\sigma_{\mathcal{V}}$ | 1.19 | 0.77 | 0.76 | 1.11 |
| $\sqrt{< A_{Cluster} >}/\eta$ | 7.87 | 12.25 | 6.63 | 11.41 |

Table 9.2: Cluster area mean value and standard deviation $\sigma_{\mathcal{V}}$ of Voronoï cells for three different quantities: zero-acceleration, mean-acceleration and zero-vorticity points. The corresponding experimental value is showed for comparison.

the flow have been investigated in the exact same manner: the mean acceleration points (*i.e.* points where acceleration is equal to the mean magnitude acceleration) and the zero-vorticity points. The first set should not have any relation with the experimental results, while the second points should be similar considering a turbophoretic effect, responsible for the centrifugation of heavy particles outside the turbulent vortices. Table 9.2 shows the mean cluster area and the standard deviation of Voronoï cells obtained for each configuration. The experimental value of $\sigma_{\mathcal{V}}$ is extremely close to the obtained for the zero-acceleration points, but not with the values for mean acceleration points or zero-vorticity. Figure 9.14a shows the PDFs of Voronoï cell areas $\mathcal{V}$ for all the cases. Zero-acceleration points are the only characteristic points of the flow that correctly fit the experimental data for particles. This situation is confirmed in figure 9.14b, were the centered and reduced PDFs of $\log(\mathcal{V})$ are shown. In this last figure, the fact that the zero-acceleration points are the closest to the experimental distribution means, as mentioned above, that this parameter is the only one capable to reproduce the structure of droplet distribution and the log-normal distribution of particle Voronoï areas, which have been shown in our experiments and in previous experiments by Monchaux et al. [68] to be a robust feature over a wide range of Stokes and Reynolds numbers. This constitutes a determinant support to a zero-acceleration points sweep-stick mechanism scenario. It is also interesting to note that the PDF of $\log(\mathcal{V})$ for zero-acceleration points also reproduces the slight under-representation of small area events compared to the true log-normal distribution, as also observed for the inertial particles in the experiment.

Finally, figure 9.14c shows the PDF of cluster areas for the same numerical points. This figure confirms that the mean-acceleration points are in clear disagreement with experimental results, showing consistently that non-representative parameters do not reproduce the experimental statistics for inertial particles. Remarkably, areas of clusters for zero vorticity points have a distribution almost indistinguishable with what is measured for inertial particles. However, as previously mentioned, the PDF of Voronoï areas for these points does not reproduce satisfactorily the log-normal distribution of inertial particles. Besides, the average value of clusters $< A_C >$ seems to be better represented by clusters of zero-acceleration points than by clusters of zero-vorticity points as indicated in table 9.2.

To summarize, the investigation of characteristic points of a turbulent flow from DNS seems to consolidate the sweep-stick scenario as the relevant mechanism for preferential concentration of particles, at least within the range of parameters accessible in our experiment. Zero-acceleration points reproduce indeed simultaneously the log-normal distribution of Voronoï cells (almost perfectly), the distribution of cluster area and the typical dimension of clusters. It is important to note however that our experiments only considered particles with Stokes numbers relatively large (generally exceeding unity). An interesting point to be addressed in future studies concerns the possible leading role of turbophoresis (and hence of zero-vorticity points) for particles with smaller stokes number, as proposed by Vassilicos *et al.* [20] and as suggested by experimental studies by Gibert *et al.* [37] who find a direct correlation between the location of small and weakly inertial particles and strain dominated regions of the carrier field.

## 9.7 Beyond clustering.

This section briefly discusses some possible extensions of the present work, using a new method to reconstruct large scale concentration fields of particles from the same experimental data presented up to now. We will use the experimental measurements analyzed above for reconstructing a complete spatial field of particles over spatial scales exceeding the actual measurement volume defined by the field of view of the camera. The idea is based on an extension of the classical Taylor hypothesis (commonly used to reconstruct spatial profiles of velocity fields from hot-wire time-series in wind tunnels for instance) applied to high speed imaging. Conceptually, the idea is that if we take images using a high speed lineal camera perpendicular to the main wind stream (the same used in a photocopier, but in this case the camera would be fixed and the flow is moving), and considering that the turbulence is homogeneous and isotropic, it is possible to reconstruct a long spatial field by simply stacking the lines recorded at each time step. Therefore, the field reconstructed is the assembling of the developed turbulence region in the wind tunnel via Taylor hypothesis. In practice, instead of using an actual linear camera (made of just one line of pixels perpendicular to the

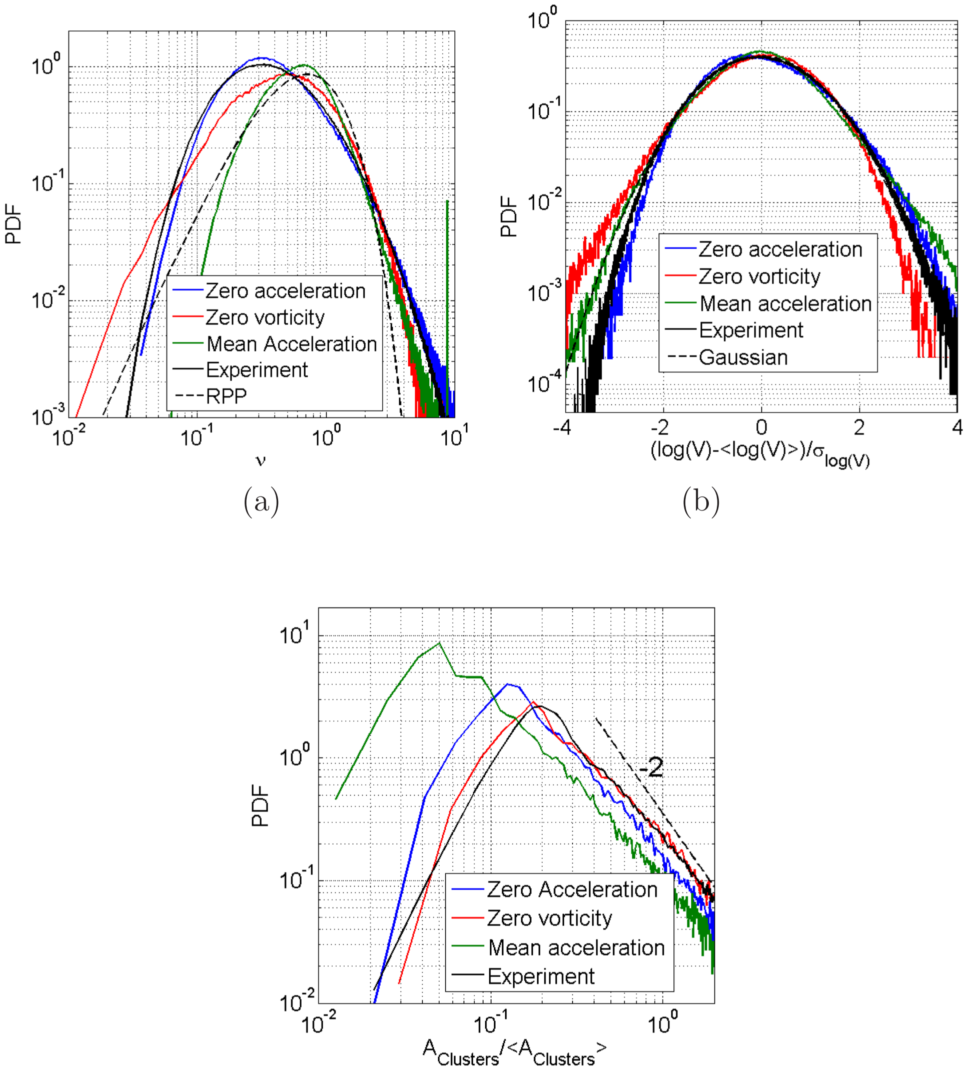

(a) (b)

(c)

Figure 9.14: (a) PDFs of Voronoï cells areas $\mathcal{V}$ for zero-acceleration points (blue line), zero-vorticity points (red) and mean-acceleration point (green). The black line is the corresponding experimental result while the black-dashed line is a RPP distribution. (b) Probability distribution function, centered and reduced, of $\log(\mathcal{V})$ for the same values as before. The black dashed line represents a Gaussian distribution. (c) PDF of the mean value of cluster area for the same cases. Al the values are for $Re_\lambda \sim 300$.

main stream), we use a narrow vertical band of a few pixels from the images recorded and previously described. In the present case having a band of a few pixels is required considering that, at the mean velocity investigated, and at the frame rate $Fs = 10$ kHz at which movies were recorded, the longitudinal displacement of a particle between 2 successive images is of a few pixels. The width of the band used to reconstruct the spatial field with the Taylor hypothesis is therefore chosen precisely to be the equivalent in pixels of the displacement $U/F_s$ between two successive frames. This ensures that no particle is lost in the reconstruction process. With a real lineal camera, it would be simply required to increase the repetition rate.

Figure 9.15 shows how this field is reconstructed, where figure 9.15a&b show two successive raw images taken by the camera at some time $t_0$ and $t_0+\delta t$ with $\delta t = 1/F_s$. Considering that the time between two acquisitions is $\delta t$ and that the mean flow velocity is $U$ (averaged in all time span but spatially only in the region of interest), the distance traveled in the $x$ coordinate by the flow is $\delta t U$. Therefore, a narrow band corresponding to this distance, converted into pixels must be extracted from the first image. We choose the center of each image because there we are sure that good illumination has been achieved, as can be observed in figure 9.3b. Then, using the next image (taken at time $t_0 + \delta t$), we can repeat the same process and assemble the two segments extracted. Repeating this procedure for all the acquisition times, a long spatial field can be obtained (figure 9.15c). This reconstructed field makes the clustering phenomena extremely clear from a simple visual inspection. This large scale field makes it possible to investigate clustering properties at larger scales than those previously accessible by simply looking at the measurement volume. This approach opens many new possibilities of analysis, which we did not have the time to exploit during this thesis. We will show here one of these possibilities, which addresses the question of superclustering (*i.e.* the clustering properties of clusters). For this, let us start by simply repeating the Voronoï analysis previously performed for single images for the large scale reconstructed particle field (as described in section 1.4). Figure 9.15d shows a Voronoï tessellation for a reconstructed field. For each recorded video at each $Re_\lambda$ a field has been reconstructed. In this section we will show the results for $Re_\lambda = 330$.

Figure 9.16 shows results obtained with this technique for $Re_\lambda = 330$ (showed in blue line) compared with the previous results obtained with the standard Voronoï analysis from single images (black line). In figure 9.16a the normalized Voronoï areas $\mathcal{V}$ are exhibited. The agreement is good, except for small Voronoï areas where the standard analysis deviates from the linear camera method. The reason of this discrepancy has been identified to be related to the existence of doublets of particles in the reconstruction method

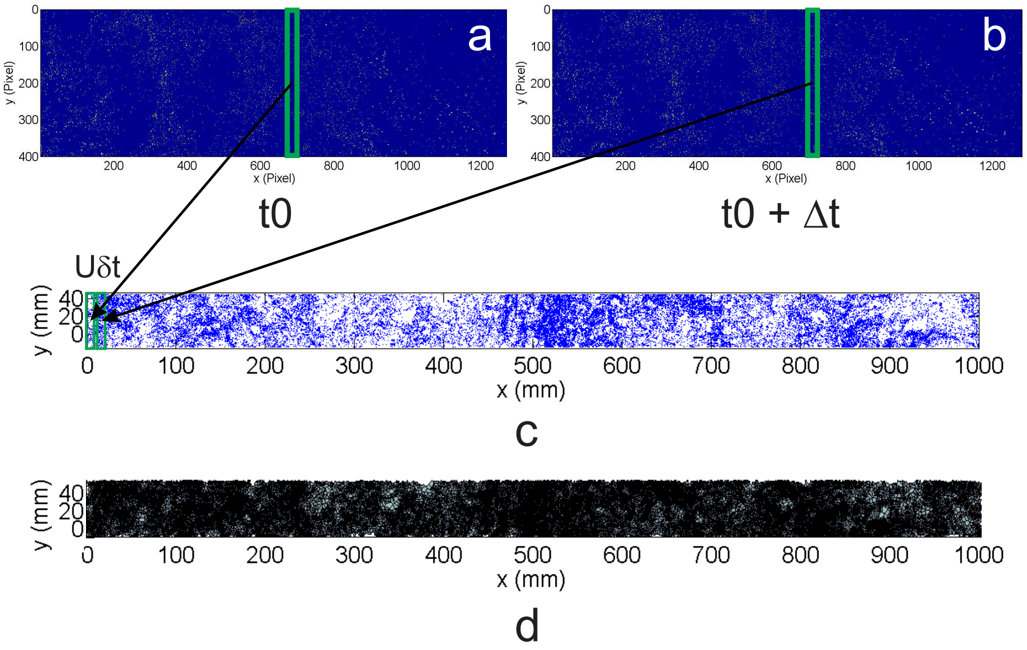

Figure 9.15: (a) Raw image taken with the camera at time $t = t_0$. (b) Raw image taken by the camera at time $t = t_0 + \delta t$. In both images a region with the equivalent length in pixels of $\delta t U$ has been highlighted. (c) Assemblage of the two mentioned regions and final image obtained after reconstructing the field for all the acquisition time. (d) Voronoï tessellation of the image previously obtained

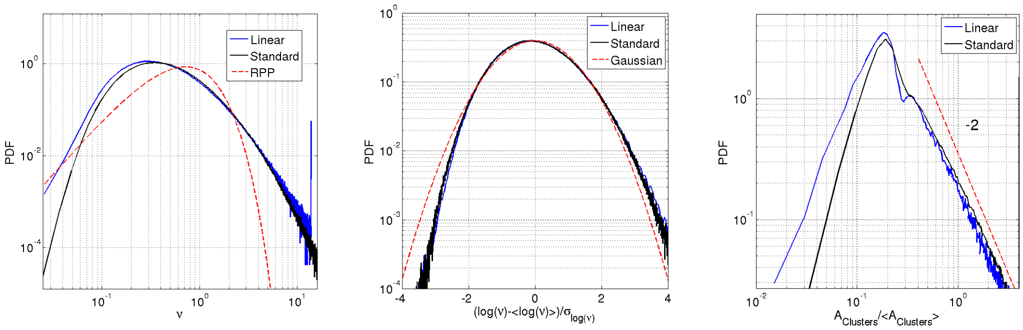

(a) (b) (c)

Figure 9.16: (a) PDF's of Voronoï cells areas $\mathcal{V}$ for the linear camera (blue line) and the standard measurements (black line). The red dashed line represents a RPP distribution. (b) Same comparison for the PDF, centered and reduced, of $log(\mathcal{V})$ for the same parameters as before. The red dashed line represents a Gaussian distribution. (c) PDF of the mean value of cluster area for the same cases. Al the values are for $Re_\lambda \sim 330$.

with the linear camera approach. These doublets appear because of the fluctuations of the velocity field, causing that in some cases particles with a velocity slightly below the average velocity appear twice in the reconstruction process (at the beginning of the band of pixels in one image at a given time step and at the end of the band in the next time step). This doublets tend to introduce artificially small Voronoï areas between the constitutive pairs, responsible for the tail which appears in figure 9.16a for small areas. The data is presently being reprocessed in order to eliminate spurious doublets. At first order this is simply done by replacing pairs of particles with separation below a certain threshold by one particle at the center of mass of the doublets. The threshold has to be chosen in order to suppress most of spurious doublets but to keep most of real nearby particles. In a more sophisticated version, the doublets can be more effectively detected by detecting pairs of particles in the reconstructed field which do not exist in actual images.

However, the existence of these spurious doublets has almost no impact on the reduced-center PDF of $log(\mathcal{V})$ which is indistinguishable for the standard analysis and the linear camera approach (see figure 9.16b). Besides, these pairs do not affect significantly the global geometry of clusters, as they eventually only affect marginally the inner structure of clusters. The analysis of cluster geometry shows indeed that the PDF of cluster area (normalized by the mean) is comparable for the standard analysis and for the linear camera approach (figure 9.16c), except for very small clusters which are also affected by the previously mentioned doublet issue.

## 9.8 Superclustering

An important application of the fields reconstructed in the previous section, is the possibility of studying the statistics of clusters themselves. We have previously studied the individual properties of clusters (related with their area and perimeter), and now, after reconstructing a long spatial field, we can study the collective properties of clusters.

To finish this work we will study the preferential concentration of clusters, therefore, the possibility of the presence of clusters of clusters (*i.e.* superclusters). These structures are widely studied in astrophysics with different techniques such as friends of friends, Voronoï diagrams, among others ([113, 100]).

The procedure for identifying these structures is, conceptually, very simple: using the linear camera reconstructed fields, clusters are identified from the computed Voronoï cells (figure 9.17a) with the same procedure explained in section 9.5. Then, the centers of clusters are identified as the average of local densities (*i.e.* the inverse of Voronoï cells area), as represented in figure 9.17b. Once the centers of mass of clusters are identified, Voronoï tessellations of cluster centers are computed (figure 9.17c) to which we apply the standard analysis in order to diagnose superclustering behavior (figure 9.17d).

For example, figure 9.17a&b represent the PDFs of $\mathcal{V}_{cc}$ (the normalized voronoï areas of centers of clusters) and $\log \mathcal{V}_{cc}$ centered and reduced. The PDF of $\mathcal{V}_{cc}$ clearly shows an important amount of clustering with $\sigma_{\mathcal{V}_{cc}} = 0.95$. Interestingly, figure 9.18b shows that superclusters maintain a quasi-lognormal distribution extremely similar to that observed for clusters. Figure 9.18c shows that the PDF of the area of superclusters has almost an identical shape to that observed for standard clusters in the linear camera reconstruction (figure 9.16c).

Although this is still ongoing work, we show in this thesis the first evidence of these supercluster structures of particles in a turbulent flow. This may be relevant for astrophysical issues, where the origin of superclustering and the role of intergalactic turbulence remains an active field of research.

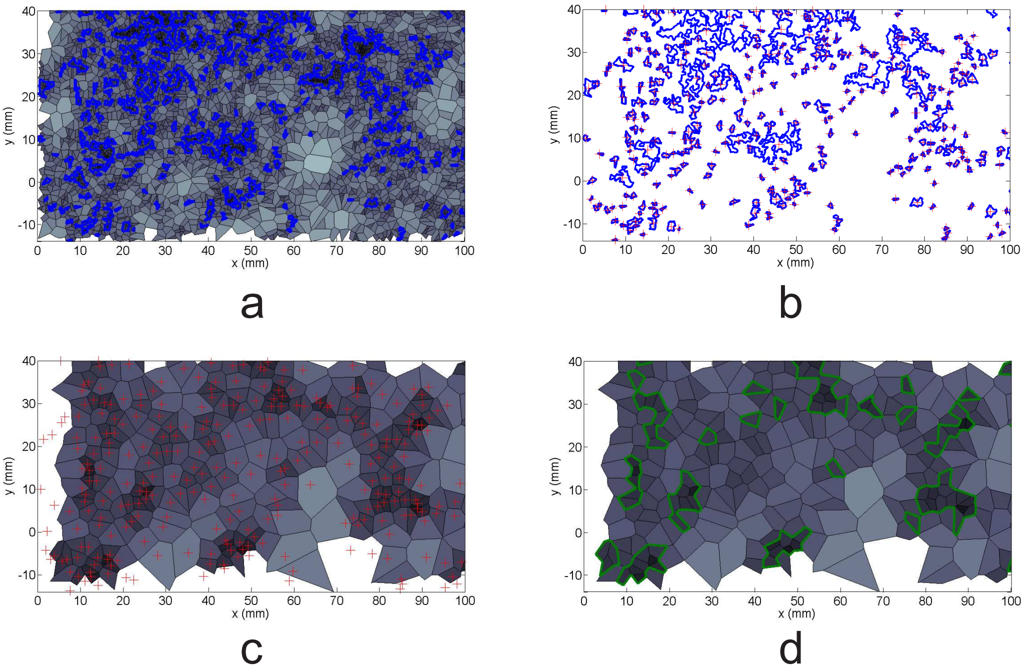

Figure 9.17: Procedure for obtaining superclusters. (a) Clusters are identified from the Voronoï cells obtained from raw images. (b) The centers of clusters are identified as the average of local densities (i.e. the inverse of Voronoï cells area). (c) Voronoï tessellations of clusters centers are computed. (d) Clusters of clusters are identified. Only a section with 5 $\mathrm{cm}^2$ of images is represented for properly identifying Voronoï diagrams.

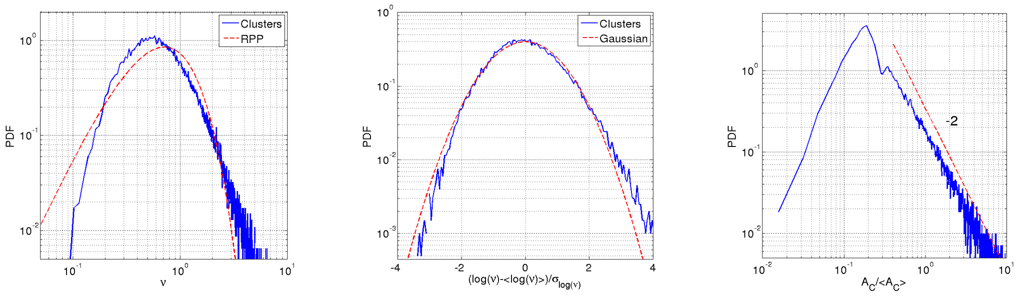

(a) (b) (c)

Figure 9.18: (a) PDF's of Voronoï cells areas $\mathcal{V}_{cc}$ for the superclusters (blue line) and the standard measurements (black line). The red dashed line represents a RPP distribution. (b) Same comparison for the PDF, centered and reduced, of $log(\mathcal{V}_{cc})$ for the same parameters as before. The red dashed line represents a Gaussian distribution. (c) PDF of the mean value of cluster's area for the superclusters. Al the values are for $Re_\lambda \sim 330$.

## 9.9 Discussion and conclusions

We have investigated the preferential concentration of particles of a given size transported in a turbulent flow with varying Reynolds number up to $Re_\lambda \sim 400$. We find clear evidence of particles clustering as Voronoï area PDF strongly deviates from that of a random distribution. Clustering is found to be Reynolds number dependent in highly concentrated regions (left part of Voronoï areas PDF), while large depleted regions appear to be mostly independent of Reynolds number. This is consistent with previous observations at lower Reynolds numbers [68], and can be interpreted as the fact that large depleted regions are mostly associated to large scale structures of the carrier flow, which are not much affected as the Reynolds number is increased. Table 9.1 shows indeed that the large scale of the turbulent flow generated with our active grid remains relatively constant regardless of the Reynolds number, and that as we increase the Reynolds number small scales are further developed and the dissipation scale decreases.

The PDFs of Voronoï areas also show that clustering phenomenon increases the probability of finding regions with local concentration between twice and a few tens the average concentration, while very high concentrations are less probable than a random process. Though a further analysis (in particular regarding to possible biases related to the particle detection procedure) is still required to be fully conclusive, this effect may be reminiscent of specific interactions between particles very close to each other. In previous measurements at lower Reynolds number [68] it has indeed been pointed out that clusters tend to be less over-concentrated when the average concentration increases. Though we have not identified yet the precise mechanism responsible for this phenomenon, it is very likely related to collective effects taking place in the clusters, which tend to repel or to redistribute particles (by a collective increase of their seeding density, as reported by [2], for instance). The low probability of finding very small Voronoï areas observed in the present study may be also reminiscent of a similar phenomenon. Further investigations, at varying seeding density, will help understanding this issue (in the present study we only considered volume fractions of water larger than $3 \cdot 10^{-5}$, experiments in more diluted conditions are planned in the coming months).

The quasi-lognormal structure of Voronoï cells has been corroborated. It is an important feature as it underlines the relevance of the standard deviation of Voronoï cell area as the parameter for quantifying clustering. This work also shows a probable universal character of this behavior, as it has been reproduced via DNS simulations and then observed in superclusters.

A comparison of DNS and experiments shows the consistency of a sweep-stick mechanism since zero-acceleration points of the flow reproduce the statistics of inertial particles. A remarkable similarity between our experiments and simulations has been obtained, using an extremely simple numerical analysis that consists in computing the modulus of Lagrangian acceleration and identifying the zero-acceleration patches by simple thresholding. Furthermore, we have been able to compare the results obtained for zero-acceleration points with other special points (zero-vorticity points and mean-acceleration points). The result shows that the mechanism that better reproduces Voronoï tessellations of inertial particles in our experiments is the sweep-stick mechanism with zero-acceleration points. It is important to note, however, that our experiments only considered particles with relatively large Stokes numbers (generally exceeding unity). An interesting point to be addressed in future studies concerns the possible leading role of turbophoresis (and hence of zero-vorticity points) for particles with smaller Stokes number, as proposed by Vassilicos *et al.* [20] and as suggested by experimental studies by Gibert *et al.* [37] who found a direct correlation between the location of small and weakly inertial particles and strain dominated regions of the carrier field.

Finally, simulating the acquisition of a linear camera using a Taylor hypothesis, several meters long fields of particles have been reconstructed. These fields allow to analyze a complete and unprecedented set of long-scale interactions, such as cluster correlations and the study of superclusters. We have focused on the study of such superclusters. This work presents the first evidence of superclusters of particles in a turbulent flow. Ongoing work will help to understand properly this phenomenon, which certainly consists in a new and exciting feature of fluid-particle interactions. Further analysis based on the large scale reconstructed fields is planed. It includes primarily the investigation of spatial correlation between clusters but also the calculation of velocity fields by PIV correlations between cells defined using Voronoï areas (rather than usual square PIV cells). This can be achieved by reconstructing two particles fields using two bands of pixels per image and considering the correlations between these 2 fields for PIV calculations from particles within clusters. The estimation of such dynamical properties conditioned on clustering properties is of particular importance to shed light into collective mechanisms impacting for instance the settling velocity of particles within clusters as observed by Aliseda *et al.* [2].

# Conclusions

This PhD thesis has covered many features of fluid-particle interactions, ranging from a simple pendulum inmersed in a flow to the presence of superclusters of water droplets in a wind tunnel.

The simplest case studied was a pendulum with a pendulum-blob facing the wind in the wind-tunnel. As the pendulum-blob was a plate, the aerodynamic coefficients as a function of the angle between the plate and the streamwise velocity present a non-trivial behavior, resulting in an hysteresis cycle. We give a simple interpretation of this behavior in terms of a two potential wells description, only requiring to know the angular dependency of the normal drag coefficient of an inclined plate. We investigate the influence of turbulence on the equilibrium of the pendulum in general and on the observed bi-stability in particular. Our results have potentially important fundamental and practical consequences: (i) they extend the attractiveness of the pendulum as a model to investigate generic questions related to bi-stable stochastic processes, (ii) they highlight important fluid dynamic mechanisms, including turbulent drag enhancement and fluid-structure interaction issues.

Then, different instabilities of towed systems has been studied. In chapter 4 we have seen that the wake of a sphere can produce helicoidal motion of a sphere towed by a wire. We found that there exists a particle Reynolds number $Re_p$ threshold for activating this unstable motion. A three-dimensional trajectory was reconstructed with an extremely simple experimental setup, used for characterizing the shape of particle's trajectory.

In chapter 5 we investigate experimentally the equilibrium and the stability of the trajectory of a sphere towed at constant velocity in the wind tunnel at the tip of a cable with unprecedented large length-to-diameter aspect ratio, exceeding $10^4$. Three cases were studied: the cable towed by itself, a light polystyrene particle and a heavy lead particle. Concerning stability issues we find that the heavy lead particle is always towed in stable conditions (within the accessible range of velocities) with only very low energy oscillations related to a weak pendulum like motion. On the contrary, the free end and light sphere cases are shown to become unstable when the towing velocity exceeds a certain threshold. Spectral analysis shows a *flutter* type instability for the sphere, with a dominant oscillatory motion, while the cable alone develops a *divergence* type instability with random fluctuations.

In chapter 6 the same system is studied, but the surrounding flow is turbulent. In this chapter we focus on a comparison with this towed system with freely advected particles in turbulence. Most of theoretical and numerical works for free advected particles in a turbulent flow, which only consider the drag force acting on the particles, fail to predict recent experimental results for the transport of finite size particles. These questions have motivated a series of experiments trying to emphasize the actual role of the drag force by imposing it as an unambiguous leading forcing term acting on a particle in a turbulent background. This is the case of the towed particles studied in this thesis. Our results are consistent with a filtering scenario resulting from the viscous response time of an inertial particle whose dynamics is coupled to the surrounding fluid via the drag

Therefore, depending on several parameters such as the Reynolds number of the particle, the wire or the fluctuations level of the flow, a whole family of instabilities can appear, with no trivial dependencies and important consequences considering different applications of such systems.

Concerning the collective effects, three different flows have been studied: a water tunnel, a von Kármán flow and a wind tunnel. A broad range of $Re_\lambda$, dissipation scales ($\eta$) and particles diameters ($d_p$) and densities ($\rho_p$) has been covered. Using Voronoï diagrams, we have quantified preferential concentration as a function of the Stokes number and the Reynolds number $Re_\lambda$. In chapter 7 and 8 simultaneous PIV measurements complemented the inertial particles acquisitions. The goal was to analyze if the particles tend to stick into special regions of the flow.

In the last chapter also DNS have been performed for comparing with experimental results. A sweep-stick mechanism, in which inertial particles tend to have the same statistics as zero-acceleration points has been proved to be consistent with our results.

Finally, a promising new technique has been presented. Based on the standard measurements, a spatial field has been reconstructed allowing us to acquire a several meters long image of particles. The enormous amount of structures present in the image has evidenced that the clusters are grouped at the same time in bigger clusters (*i.e.* clusters form clusters, that we call superclusters). This new result is still being studied and presents a new and fascinating field for studying particle-flow interactions.

# Bibliography

[1] Ronald J Adrian and Jerry Westerweel. *Particle image velocimetry*, volume 30. Cambridge University Press, 2010.

[2] A Aliseda, Alain Cartellier, F Hainaux, and JC Lasheras. Effect of preferential concentration on the settling velocity of heavy particles in homogeneous isotropic turbulence. *Journal of Fluid Mechanics*, 468(1):77–105, 2002.

[3] Robert A Antonia, RJ Smalley, Tongming Zhou, Fabien Anselmet, and Luminita Danaila. Similarity of energy structure functions in decaying homogeneous isotropic turbulence. *Journal of Fluid Mechanics*, 487(1):245–269, 2003.

[4] Franck Auguste, Jacques Magnaudet, and David Fabre. Falling styles of disks. *Journal of Fluid Mechanics*, 719:388–405, 2013.

[5] P Bagchi and S Balachandar. Effect of turbulence on the drag and lift of a particle. *Physics of Fluids*, 15:3496, 2003.

[6] Promode R Bandyopadhyay, Henry A Leinhos, JDana Hrubes, Norman Toplosky, and Joshua Hansen. Turning of a short-length cable using flapping fin propulsion. *Oceanic Engineering, IEEE Journal of*, 36(4):571–585, 2011.

[7] Alfred Barnard Basset. *A treatise on hydrodynamics*, volume 2. Deighton, Bell and Co., 1888.

[8] J Bec, Luca Biferale, M Cencini, A Lanotte, S Musacchio, and Federico Toschi. Heavy particle concentration in turbulence at dissipative and inertial scales. *Physical review letters*, 98(8):084502, 2007.

[9] Jeremy Bec, Luca Biferale, Guido Boffetta, Antonio Celani, Massimo Cencini, Alessandra Lanotte, S Musacchio, and Federico Toschi. Acceleration statistics of heavy particles in turbulence. *Journal of Fluid Mechanics*, 550(349):10, 2006.

[10] SK Bhattacharyya, CP Vendhan, and K Sudarsan. The finite element method for hydroelastic instability of underwater towed cylindrical structures. *Journal of sound and vibration*, 237(1):119–143, 2000.

[11] Diogo Bolster, Robert E Hershberger, and Russell J Donnelly. Oscillating pendulum decay by emission of vortex rings. *Physical Review E*, 81(4):046317, 2010.

[12] Joseph Boussinesq. *Théorie analytique de la chaleur: mise en harmonie avec la thermodynamique et avec la théorie mécanique de la lumière*, volume 2. Gauthier-Villars, 1903.

[13] Phillip P Brown and Desmond F Lawler. Sphere drag and settling velocity revisited. *Journal of Environmental Engineering*, 129(3):222–231, 2003.

[14] Enrico Calzavarini, Romain Volk, Mickaël Bourgoin, Emmanuel Lévêque, Jean-François Pinton, Federico Toschi, et al. Acceleration statistics of finite-sized particles in turbulent flow: the role of faxén forces. *Journal of Fluid Mechanics*, 630:179, 2009.

[15] L Chen, S Goto, and JC Vassilicos. Turbulent clustering of stagnation points and inertial particles. *Journal of Fluid Mechanics*, 553(1):143–154, 2006.

[16] Young-il Choo and Mario J Casarella. A survey of analytical methods for dynamic simulation of cable-body systems. *Journal of Hydronautics*, 7(4):137–144, 1973.

[17] Marcin Chrust, Gilles Bouchet, and Jan Dušek. Numerical simulation of the dynamics of freely falling discs. *Physics of Fluids*, 25:044102, 2013.

[18] Christophe Clanet. *Sports Physics.* Les éditions de l'École Polytechnique, 2013.

[19] Roland Clift, John R Grace, and Martin E Weber. *Bubbles, drops, and particles.* Courier Dover Publications, 2005.

[20] SW Coleman and JC Vassilicos. A unified sweep-stick mechanism to explain particle clustering in two-and three-dimensional homogeneous, isotropic turbulence. *Physics of Fluids*, 21:113301, 2009.

[21] Gabriel T Csanady. *Turbulent Diffusion in the Environmnet*, volume 3. Springer, 1973.

[22] E De Langre, MP Paidoussis, Olivier Doaré, and Y Modarres-Sadeghi. Flutter of long flexible cylinders in axial flow. *Journal of Fluid Mechanics*, 571(1):371–389, 2007.

[23] Thibaut Deloze, Yannick HOARAU, and Jan DUSEK. Etude numérique des forces agissant sur une sphère en chute libre dans un tube rempli d'un fluide newtonien au repos. *20ème Congrès Français de Mécanique, 28 août/2 sept. 2011-25044 Besançon, France (FR)*, 2011.

[24] Thibaut Deloze, Yannick Hoarau, and Jan Dušek. Transition scenario of a sphere freely falling in a vertical tube. *Journal of Fluid Mechanics*, 711:40, 2012.

[25] AP Dowling. The dynamics of towed flexible cylinders part 1 & 2. *Journal of Fluid Mechanics*, 187(1):507–532, 1988.

[26] T. Doychev and M. Uhlmann. A numerical study of finite size particles in homogeneous turbulent flow. In S. Balachandar and J.S̃inclair Curtis, editors, *ICMF 2010*, Proc. 7th Int. Conf. Multiphase Flow, Tampa, USA, 2010. CDROM.

[27] Guillaume Dupeux, Anne Le Goff, David Quéré, and Christophe Clanet. The spinning ball spiral. *New Journal of Physics*, 12(9):093004, 2010.

[28] S Elghobashi and GC Truesdell. Direct simulation of particle dispersion in a decaying isotropic turbulence. *Journal of Fluid Mechanics*, 242(3):655–700, 1992.

[29] Patricia Ern, Frédéric Risso, David Fabre, and Jacques Magnaudet. Wake-induced oscillatory paths of bodies freely rising or falling in fluids. *Annual Review of Fluid Mechanics*, 44:97–121, 2012.

[30] Járai-Szabó Ferenc and Zoltán Néda. On the size distribution of poisson voronoi cells. *Physica A: Statistical Mechanics and its Applications*, 385(2):518–526, 2007.

[31] John R Fessler, Jonathan D Kulick, and John K Eaton. Preferential concentration of heavy particles in a turbulent channel flow. *Physics of Fluids*, 6(11):3742–3749, 1994.

[32] L Fiabane, R Zimmermann, R Volk, J-F Pinton, and M Bourgoin. Clustering of finite-size particles in turbulence. *Physical Review E*, 86(3):035301, 2012.

[33] O Flachsbart. Messungen an ebenen und gewölbten platten. *Ergebnisse der Aerodynamischen Versuchsanstalt zu Göttingen*, 4:96–100, 1932.

[34] Uriel Frisch. Turbulence. *Turbulence, by Uriel Frisch, pp. 310. ISBN 0521457130. Cambridge, UK: Cambridge University Press, January 1996.*, 1, 1996.

[35] Manuel Garcia-Villalba, Aman G Kidanemariam, and Markus Uhlmann. Dns of vertical plane channel flow with finite-size particles: Voronoi analysis, acceleration statistics and particle-conditioned averaging. *International Journal of Multiphase Flow*, 46:54–74, 2012.

[36] Renée Gatignol. The faxen formulae for a rigid particle in an unsteady non-uniform stokes flow. *J. Mec. Theor. Appl*, 1(2):143–160, 1983.

[37] Mathieu Gibert, Haitao Xu, and Eberhard Bodenschatz. Where do small, weakly inertial particles go in a turbulent flow? *Journal of Fluid Mechanics*, 698:160–167, 2012.

[38] Susumu Goto and JC Vassilicos. Self-similar clustering of inertial particles and zero-acceleration points in fully developed two-dimensional turbulence. *Physics of Fluids*, 18:115103, 2006.

[39] Susumu Goto and JC Vassilicos. Sweep-stick mechanism of heavy particle clustering in fluid turbulence. *Physical review letters*, 100(5):054503, 2008.

[40] Carine Guivier-Curien, Valérie Deplano, and Eric Bertrand. Validation of a numerical 3-d fluid–structure interaction model for a prosthetic valve based on experimental piv measurements. *Medical engineering & physics*, 31(8):986–993, 2009.

[41] Sighard F Hoerner. *Fluid-dynamic drag: practical information on aerodynamic drag and hydrodynamic resistance.* Hoerner Fluid Dynamics, 1965.

[42] Holger Homann, Jeremie Bec, et al. Finite-size effects in the dynamics of neutrally buoyant particles in turbulent flow. *Journal of Fluid Mechanics*, 651:81, 2010.

[43] Holger Homann, Jérémie Bec, and Rainer Grauer. Effect of turbulent fluctuations on the drag and lift forces on a towed sphere and its boundary layer. *arXiv preprint arXiv:1012.5205*, 2010.

[44] M Horowitz and CHK Williamson. The effect of reynolds number on the dynamics and wakes of freely rising and falling spheres. *Journal of Fluid Mechanics*, 651:251, 2010.

[45] M Jenny, J Dušek, and G Bouchet. Instabilities and transition of a sphere falling or ascending freely in a newtonian fluid. *Journal of Fluid Mechanics*, 508(1):201–239, 2004.

[46] KD Jensen. Flow measurements. *Journal of the Brazilian Society of Mechanical Sciences and Engineering*, 26(4):400–419, 2004.

[47] YW Jun, KR Hall, AG Bennett, and PD Bridges. Optimal guidance for airborne cable pickup system. *AIAA paper*, pages 84–1893, 1984.

[48] JW Kamman and TC Nguyen. Modeling towed cable system dynamics. Technical report, DTIC Document, 1990.

[49] Aman G Kidanemariam, Clemens Chan-Braun, Todor Doychev, and Markus Uhlmann. Direct numerical simulation of horizontal open channel flow with finite-size, heavy particles at low solid volume fraction. *New Journal of Physics*, 15(2):025031, 2013.

[50] Louis Vessot King. On the convection of heat from small cylinders in a stream of fluid: determination of the convection constants of small platinum wires, with applications to hot-wire anemometry. *Proceedings of the Royal Society of London. Series A*, 90(622):563–570, 1914.

[51] Andrey Nikolaevich Kolmogorov. The local structure of turbulence in incompressible viscous fluid for very large reynolds numbers. In *Dokl. Akad. Nauk SSSR*, volume 30, pages 299–303, 1941.

[52] Hendrik Anthony Kramers. Brownian motion in a field of force and the diffusion model of chemical reactions. *Physica*, 7(4):284–304, 1940.

[53] Gregor Kühn. *Untersuchungen zur Feinsedimentdynamik unter Turbulenzeinfluss*. Univ.-Verlag Karlsruhe, 2007.

[54] Arthur La Porta, Greg A Voth, Alice M Crawford, Jim Alexander, and Eberhard Bodenschatz. Fluid particle accelerations in fully developed turbulence. *Nature*, 409(6823):1017–1019, 2001.

[55] PP Lalu and KP Narayanan. Effect of bending rigidity of marine cable on the dynamic stability of two-part underwater towing system. *International Journal of Engineering Science*, 3, 2011.

[56] Marcel Lesieur. *Turbulence in fluids*, volume 84. Springer, 2008.

[57] Georges Lespinard. *Contribution à l'étude de la transition en couche limite: effet de l'aspiration pariétale.* PhD thesis, Facult des Sciences de l'Universit de Grenoble, 1968.

[58] Ho-Gon Lim, Jin-Hee Park, and Seung-Cheol Jang. Development of a swing check valve model for a low velocity pipe flow prediction. *Nuclear engineering and design*, 236(10):1051–1060, 2006.

[59] H Makita and K Sassa. Active turbulence generation in a laboratory wind tunnel. In *Advances in Turbulence 3*, pages 497–505. Springer, 1991.

[60] Paul Manneville. *Instabilities, chaos and turbulence*, volume 1. Imperial College Pr, 2010.

[61] Martin R Maxey and James J Riley. Equation of motion for a small rigid sphere in a nonuniform flow. *Physics of Fluids*, 26:883, 1983.

[62] Nicolas Mazellier. *Dynamique spatio-temporelle du champ de vorticité en turbulence.* PhD thesis, Université Joseph Fourier, 2005.

[63] KL McElhaney. An analysis of check valve performance characteristics based on valve design. *Nuclear engineering and design*, 197(1):169–182, 2000.

[64] Rabindra D Mehta. Aerodynamics of sports balls. *Annual Review of Fluid Mechanics*, 17(1):151–189, 1985.

[65] R Mei. Velocity fidelity of flow tracer particles. *Experiments in Fluids*, 22(1):1–13, 1996.

[66] Pablo D Mininni, Duane Rosenberg, Raghu Reddy, and Annick Pouquet. A hybrid mpi–openmp scheme for scalable parallel pseudospectral computations for fluid turbulence. *Parallel Computing*, 37(6):316–326, 2011.

[67] S Mittal and P Saxena. Prediction of hysteresis associated with the static stall of an airfoil. *AIAA journal*, 38(5):933–935, 2000.

[68] Romain Monchaux, Mickaël Bourgoin, and Alain Cartellier. Preferential concentration of heavy particles: A voronoï analysis. *Physics of Fluids*, 22:103304, 2010.

[69] Romain Monchaux, Mickael Bourgoin, and Alain Cartellier. Analyzing preferential concentration and clustering of inertial particles in turbulence. *International Journal of Multiphase Flow*, 40:1–18, 2012.

[70] Nicolas Mordant, Alice M Crawford, and Eberhard Bodenschatz. Experimental lagrangian acceleration probability density function measurement. *Physica D: Nonlinear Phenomena*, 193(1):245–251, 2004.

[71] Nicolas Mordant, Alice M Crawford, and Eberhard Bodenschatz. Three-dimensional structure of the lagrangian acceleration in turbulent flows. *Physical review letters*, 93(21):214501, 2004.

[72] Nicolas Mordant, Pascal Metz, Olivier Michel, and J-F Pinton. Measurement of lagrangian velocity in fully developed turbulence. *Physical Review Letters*, 87(21):214501, 2001.

[73] Nicolas Mordant, Jean-François Pinton, and Olivier Michel. Time-resolved tracking of a sound scatterer in a complex flow: Nonstationary signal analysis and applications. *The Journal of the Acoustical Society of America*, 112:108, 2002.

[74] Thomas J Mueller. The influence of laminar separation and transition on low reynolds number airfoil hysteresis. *Journal of Aircraft*, 22(9):763–770, 1985.

[75] L Mydlarski and Z Warhaft. On the onset of high-reynolds-number grid-generated wind tunnel turbulence. *Journal of Fluid Mechanics*, 320:331–368, 1996.

[76] Ramesh Natarajan and Andreas Acrivos. The instability of the steady flow past spheres and disks. *Journal of Fluid Mechanics*, 254(1):323–344, 1993.

[77] Alan M Nathan. Analysis of knuckleball trajectories. *Procedia Engineering*, 34:116–121, 2012.

[78] Douglas Neill, Dean Livelybrooks, and Russell J Donnelly. A pendulum experiment on added mass and the principle of equivalence. *American Journal of Physics*, 75:226, 2007.

[79] Isaac Newton. Principia mathematica. *Newton's principia (ed. F. Cajori)*, 1964.

[80] CC Ni and RJ Hansen. An experimental study of the flow-induced motions of a flexible cylinder in axial flow. *Journal of Fluids Engineering*, 100:389, 1978.

[81] Martin Obligado and Mickaël Bourgoin. An experimental investigation of the equilibrium and stability of long towed cable systems. *New Journal of Physics*, 15(4):043019, 2013.

[82] Martin Obligado, Mahrane Missaoui, Romain Monchaux, Alain Cartellier, and Mickaël Bourgoin. Reynolds number influence on preferential concentration of heavy particles in turbulent flows. In *Journal of Physics: Conference Series*, volume 318, page 052015. IOP Publishing, 2011.

[83] AM Oboukhov. Some specific features of atmospheric turbulence. *J. Fluid Mech*, 13(1):77–81, 1962.

[84] CR Ortloff and J Ives. On the dynamic motion of a thin flexible cylinder in a viscous stream. *Journal of Fluid Mechanics*, 38(04):713–720, 1969.

[85] Carl Wilhelm Oseen. *Über die Stoke'sche Formel und über eine verwandte Aufgabe in der Hydrodynamik:...* Almqvist & Wiksell, 1911.

[86] Nicholas T Ouellette, Haitao Xu, Mickaël Bourgoin, and Eberhard Bodenschatz. Small-scale anisotropy in lagrangian turbulence. *New Journal of Physics*, 8(6):102, 2006.

[87] MP Paidoussis. Dynamics of flexible slender cylinders in axial flow. *J. Fluid Mech*, 26(part 4):717–736, 1966.

[88] MP Paidoussis. Dynamics of cylindrical structures subjected to axial flow. *Journal of sound and vibration*, 29(3):365–385, 1973.

[89] MP Païdoussis. *Fluid-Structure Interactions: Slender Structures and Axial Flows – Vol. 2.* Elsevier, 2003.

[90] MP Païdoussis, E Grinevich, D Adamovic, and C Semler. Linear and nonlinear dynamics of cantilevered cylinders in axial flow. part 1: physical dynamics. *Journal of fluids and structures*, 16(6):691–713, 2002.

[91] MB Pinsky and AP Khain. Turbulence effects on droplet growth and size distribution in cloudsa review. *Journal of aerosol science*, 28(7):1177–1214, 1997.

[92] Leonard Pode. Tables for computing the equilibrium configuration of a flexible cable in a uniform stream. Technical report, David Taylor Model Basin, 1951.

[93] REG Poorte and A Biesheuvel. Experiments on the motion of gas bubbles in turbulence generated by an active grid. *Journal of Fluid Mechanics*, 461(1):127–154, 2002.

[94] Stephen B Pope. *Turbulent flows*. Cambridge university press, 2000.

[95] Scott L Post and John Abraham. Modeling the outcome of drop–drop collisions in diesel sprays. *International Journal of Multiphase Flow*, 28(6):997–1019, 2002.

[96] Vivek N Prakash, Yoshiyuki Tagawa, Enrico Calzavarini, Julián Martínez Mercado, Federico Toschi, Detlef Lohse, and Chao Sun. How gravity and size affect the acceleration statistics of bubbles in turbulence. *New Journal of Physics*, 14(10):105017, 2012.

[97] Johnny E Quisenberry and AS Arena. Dynamic simulation of low altitude aerial tow systems. In *AIAA Atmospheric Flight Mechanics Conference and Exhibit*, 2004.

[98] Nauman M Qureshi, Unai Arrieta, Christophe Baudet, Alain Cartellier, Yves Gagne, and Mickaël Bourgoin. Acceleration statistics of inertial particles in turbulent flow. *The European Physical Journal B*, 66(4):531–536, 2008.

[99] Nauman M Qureshi, Mickaël Bourgoin, Christophe Baudet, Alain Cartellier, and Yves Gagne. Turbulent transport of material particles: an experimental study of finite size effects. *Physical review letters*, 99(18):184502, 2007.

[100] Massimo Ramella, Walter Boschin, Dario Fadda, and Mario Nonino. Finding galaxy clusters using voronoi tessellations. *arXiv preprint astro-ph/0101411*, 2001.

[101] Lord Rayleigh. On the irregular flight of a tennis ball. *Messenger of Mathematics*, 7:14–16, 1877.

[102] LF Richardson. Weather prediction by numerical process cambridge university press. *Cambridge, England*, page 219, 1922.

[103] BJ Rothschild and TR Osborn. Small-scale turbulence and plankton contact rates. *Journal of Plankton Research*, 10(3):465–474, 1988.

[104] Haniu Sakamoto and H Haniu. A study on vortex shedding from spheres in a uniform flow. *ASME, Transactions, Journal of Fluids Engineering*, 112:386–392, 1990.

[105] Juan PLC Salazar, Jeremy De Jong, Lujie Cao, Scott H Woodward, Hui Meng, and Lance R Collins. Experimental and numerical investigation of inertial particle clustering in isotropic turbulence. *Journal of Fluid Mechanics*, 600(1):245–256, 2008.

[106] Günter Schewe. On the force fluctuations acting on a circular cylinder in crossflow from subcritical up to transcritical reynolds numbers. *Journal of Fluid Mechanics*, 133(1):265–285, 1983.

[107] François G Schmitt and Laurent Seuront. Intermittent turbulence and copepod dynamics: increase in encounter rates through preferential concentration. *Journal of Marine Systems*, 70(3):263–272, 2008.

[108] Lionel Schouveiler, Christophe Eloy, and Patrice Le Gal. Flow-induced vibrations of high mass ratio flexible filaments freely hanging in a flow. *Physics of Fluids*, 17:047104, 2005.

[109] C Semler, JL Lopes, N Augu, and MP Païdoussis. Linear and nonlinear dynamics of cantilevered cylinders in axial flow. part 3: nonlinear dynamics. *Journal of fluids and structures*, 16(6):739–759, 2002.

[110] DE Sgarioto, P Williams, and PM Trivailo. Remote payload transportation using an aircraft-towed flexible cable system. *ANZIAM Journal*, 47:C231–C244, 2006.

[111] H Siebert, S Gerashchenko, A Gylfason, K Lehmann, LR Collins, RA Shaw, and Z Warhaft. Towards understanding the role of turbulence on droplets in clouds: In situ and laboratory measurements. *Atmospheric Research*, 97(4):426–437, 2010.

[112] Fotis Sotiropoulos and Iman Borazjani. A review of state-of-the-art numerical methods for simulating flow through mechanical heart valves. *Medical & biological engineering & computing*, 47(3):245–256, 2009.

[113] Volker Springel, Simon DM White, Adrian Jenkins, Carlos S Frenk, Naoki Yoshida, Liang Gao, Julio Navarro, Robert Thacker, Darren Croton, John Helly, et al. Simulations of the formation, evolution and clustering of galaxies and quasars. *Nature*, 435(7042):629–636, 2005.

[114] Kyle D Squires and John K Eaton. Preferential concentration of particles by turbulence. *Physics of Fluids A: Fluid Dynamics*, 3:1169, 1991.

[115] Katepalli R Sreenivasan. On the universality of the kolmogorov constant. *Physics of Fluids*, 7(11):2778–2784, 1995.

[116] K Sudarsan, SK Bhattacharyya, and CP Vendhan. An experimental study of hydroelastic instability of flexible towed underwater cylindrical structures. In *Proceedings of the International Confernece on Offshore Mechanics and Artic Engineering*, pages 73–80. American Society of Mechanical Engineers, 1997.

[117] Yoshiyuki Tagawa, Julián Martínez Mercado, Vivek N Prakash, Enrico Calzavarini, Chao Sun, Detlef Lohse, et al. Three-dimensional lagrangian voronoi analysis for clustering of particles and bubbles in turbulence. *Journal of Fluid Mechanics*, 693:201–215, 2012.

[118] Geoffrey Taylor. Analysis of the swimming of long and narrow animals. *Proceedings of the Royal Society of London. Series A. Mathematical and Physical Sciences*, 214(1117):158–183, 1952.

[119] Chan-Mou Tchen. *Mean value and correlation problems connected with the motion of small particles suspended in a turbulent fluid.* PhD thesis, TUDelft, 1947.

[120] Hendrik Tennekes and John Leask Lumley. *A first course in turbulence.* The MIT press, 1972.

[121] Vassilios E Theodoracatos and DE Calkins. An experimental study of elastohydrodynamics of towed flexible cylinders aided by video image processing. *Ocean engineering*, 13(6):587–619, 1986.

[122] GS Triantafyllou and C Chryssostomidis. Stability of a string in axial flow. *Journal of energy resources technology*, 107(4):421–425, 1985.

[123] DJ Tritton. Experiments on the flow past a circular cylinder at low reynolds numbers. *J. Fluid Mech*, 6(4):547–567, 1959.

[124] Nicolaas Godfried Van Kampen. *Stochastic processes in physics and chemistry*, volume 1. North holland, 1992.

[125] CHJ Veldhuis, A Biesheuvel, and D Lohse. Freely rising light solid spheres. *International Journal of Multiphase Flow*, 35(4):312–322, 2009.

[126] P Villedieu and J Hylkema. Modeles numériques lagrangiens pour la phase dispersée dans les propulseursa poudre. *Rapport technique ONERA*, 2000.

[127] R Volk, Enrico Calzavarini, G Verhille, Detlef Lohse, N Mordant, J-F Pinton, and Federico Toschi. Acceleration of heavy and light particles in turbulence: comparison between experiments and direct numerical simulations. *Physica D: Nonlinear Phenomena*, 237(14):2084–2089, 2008.

[128] R Volk, N Mordant, G Verhille, and J-F Pinton. Laser doppler measurement of inertial particle and bubble accelerations in turbulence. *Europhysics Letters*, 81(3):34002, 2008.

[129] Romain Volk, Enrico Calzavarini, E Leveque, Jean-Francois Pinton, et al. Dynamics of inertial particles in a turbulent von kármán flow. *Journal of Fluid Mechanics*, 668:223–235, 2011.

[130] Romain Volk, R, Delphine Chareyron, and Jean-François Pinton. Mesures d'accélération lagrangienne dans un écoulement anisotrope par vélocimétrie laser doppler étendue. *20ème Congrès Français de Mécanique, 28 août/2 sept. 2011-25044 Besançon, France (FR)*, 2011.

[131] Greg A Voth, Arthur la Porta, Alice M Crawford, Jim Alexander, and Eberhard Bodenschatz. Measurement of particle accelerations in fully developed turbulence. *Journal of Fluid Mechanics*, 469(1):121–160, 2002.

[132] CY Wei and SN Kukureka. Evaluation of damping and elastic properties of composites and composite structures by the resonance technique. *Journal of materials science*, 35(15):3785–3792, 2000.

[133] Bernhard Westrich and Ulrich Förstner. Sediment dynamics and pollutant mobility in rivers (sedymo): assessing catchment-wide emission-immission relationships from sediment studies. bmbf coordinated research project sedymo (2002–2006). *Journal of Soils and Sediments*, 5(4):197–200, 2005.

[134] Paul Williams, Daniel Sgarioto, and Pavel M Trivailo. Constrained path-planning for an aerial-towed cable system. *Aerospace Science and Technology*, 12(5):347–354, 2008.

[135] Haitao Xu and Eberhard Bodenschatz. Motion of inertial particles with size larger than kolmogorov scale in turbulent flows. *Physica D: Nonlinear Phenomena*, 237(14):2095–2100, 2008.

[136] Robert Zimmermann, Yoann Gasteuil, Mickael Bourgoin, Romain Volk, Alain Pumir, and Jean-François Pinton. Rotational intermittency and turbulence induced lift experienced by large particles in a turbulent flow. *Physical review letters*, 106(15):154501, 2011.

[137] G Zocchi, P Tabeling, J Maurer, and H Willaime. Measurement of the scaling of the dissipation at high reynolds numbers. *Physical Review E*, 50(5):3693, 1994.